THERMALLY ACTIVATED MINIATURIZED COOLING SYSTEM

A Dissertation
Presented to
The Academic Faculty

By

Matthew Delos Determan

In Partial Fulfillment
Of the Requirements for the Degree
Doctor of Philosophy in Mechanical Engineering

Georgia Institute of Technology

August 2008

THERMALLY ACTIVATED MINIATURIZED COOLING SYSTEM

Approved By:

Dr. Srinivas Garimella, Chairman
G. W. Woodruff School of Mechanical Engineering
Georgia Institute of Technology

Dr. Mark Allen
School of Electrical and Computer Engineering
Georgia Institute of Technology

Dr. Sheldon Jeter
G. W. Woodruff School of Mechanical Engineering
Georgia Institute of Technology

Dr. Tom Fuller
School of Chemical and Biomolecular Engineering
Georgia Institute of Technology

Dr. William Wepfer
G. W. Woodruff School of Mechanical Engineering
Georgia Institute of Technology

Date Approved: April 16, 2008

Dedication

To my wife, Jenny.

Acknowledgements

I would like to thank my advisor and mentor, Dr. Srinivas Garimella, for his support and encouragement through out the process of this work. I would also like to thank the many members of the Sustainable Thermal Systems Laboratory, both current and former. In particular, I would like to thank Jesse Killion, Tim Ernst, Lalit Bohra, Akhil Agarwal, Todd Bandhauer, Vishwanath Subramaniam, Ulf Andresen and Chris Goodman. Each of these individuals provided useful insights during some phase of this project. Their willingness to listen and offer suggestions was greatly appreciated.

I would also like to thank my committee members: Dr. Mark Allen, Dr. Tom Fuller, Dr. Sheldon Jeter and Dr. William Wepfer. Their comments and suggestions provided guidance during the course of this work.

Table of Contents

List of Tables

List of Figures

Nomenclature

Symbols

a	Aspect Ratio, [-]
A	Area, [m^2]
AC	Absorption Cycle
B	Battery
Bo	Boiling Number, [-]
C	Chisholm Parameter, [-]
Co	Convection Number, [-]
COP	Coefficient of Performance, [-]
c_p	Constant Pressure Specific Heat, [kJ/kg-K]
D	Diameter, [m, mm, μm]
f	Friction Factor, [-]
f(,)	Function of (,)
F_{FL}	Fluid Surface Parameter, [-]
FC	Fuel Cell
G	Mass Flux, [kg/m^2-s]
GAX	Generator Absorber Heat Exchange
h	Specific Enthalpy, [kJ/kg]
h_{LV}	Specific Latent Heat of Vaporization, [kJ/kg]

HX	Heat Exchanger
IC	Internal Combustion
IP	Ice Pack
k	Conductivity, [W/m-K]
L	Length, [m, mm, μm]
LHV	Lower Heating Value, [kJ/kg]
LMTD	Log Mean Temperature Difference, [K, °C]
m	Extended Surface Parameter, [1/m]
$\dot{m}$	Mass Flowrate, [kg/s]
P	Pressure, [kPa]
q	Vapor Quality, [-]
q”	Heat Flux, [W/m^2]
$\dot{Q}$	Heat Transfer Rate, [W, kW]
R	Thermal Resistance, [K/W]
Re	Reynolds Number, [-]
s	Specific Entropy, [kJ/kg-K]
t	thickness, [m, mm, μm]
T	Temperature, [°C]
UA	Overall Heat Transfer Conductance, [W/K, W/°C]
$\dot{V}$	Volume Flowrate, [m^3/s]
VCC	Vapor Compression Cycle
w	width, [m, mm, μm]
$\dot{W}$	Work Transfer Rate, [W, kW]

We	Weber Number
x	Ammonia Mass Concentration, [-]
X	Martinelli Parameter, [-]

Greek Symbols

α	Heat Transfer Coefficient, [W/m^2-K]
Δ	Change, Difference
ε	emmisivity, [-]
η	Efficiency, [-, %]
η_f	Single Fin Efficiency, [-]
η_T	Overall Surface Efficiency, [-]
μ	Dynamic viscosity, [kg/m-s]
ρ	Density, [kg/m^3]
σ	surface Tension, [N/m]
σ	Stefan-Boltzmann Constant [5.67×10^{-8} W/m^2-K^4]
ϕ^2	Two Phase Multiplier, [-]
φ	Angle, [°]

Subscripts and Superscripts

Abs	Absorber
Array	Array of Fins
C	Cold
ch, channel	Channel

Con, Cond	Condenser
Coolant	Coolant
cr	Critical
CS	Concentrated Solution
Des	Desorber
DS	Dilute Solution
e	Heated Equivalent
Evap	Evaporator
f, Fin	Heat Exchanger Fin
flow	Flow Direction
h	Hydraulic, heated
H	Hot
high	High Pressure
In	Inlet
l	Liquid
lo	Liquid Only
loss	Losses
Low	Low Pressure
net	Net Value
Out	Outlet
Pump	Pump
r	Reduced
Rec	Rectifier

Ref	Refrigerant
Reflux	Reflux
RHX	Refrigerant Heat Exchanger
S	Surface
Sur	Surroundings
sat	Saturated Condition
SHX	Solution Heat Exchanger
Sol	Solution
T	Total
tp	Two-Phase
v, Vap	Vapor
w	Water
wall	Heat Exchanger Wall

Summary

A comprehensive study of a miniaturized thermally activated cooling system was conducted. This study represents the first work to conceptualize, design, fabricate and successfully test a thermally activated cooling system for mobile applications. Thermally activated systems have the ability to produce useful cooling from waste heat streams or directly from the combustion of liquid fuels. Numerous concepts of miniaturized or mobile, active cooling systems exist in the literature but up to this point, successful fabrication and testing has not been documented.

During this study, a breadboard absorption heat pump system was fabricated from off the shelf or in-house, custom-built components. The breadboard system was used to validate the feasibility of operating an absorption heat pump with a cooling capacity of about 300 W. Subsequently, a flexible and scalable design methodology for designing miniaturized absorption heat pumps was developed. A miniaturized, 300 W nominal cooling capacity ammonia/water absorption heat pump cycle with overall dimensions of 200 × 200 × 34 mm and a mass of 7 kg was then fabricated and tested.

The unique ammonia water absorption heat pump system developed in this study utilized microchannel (D_h = 306 μm) heat exchangers to facilitate the miniaturization of the system. The system was fabricated using a manufacturing process that allowed all of the heat exchangers to be integrated into a single component. The fluid channels for each individual heat exchanger were chemically etched on 0.5 mm thick stainless steel sheets

and then 40 sheets were joined together in a diffusion bonding process. The overall dimensions of the heat and mass exchanger portion of the system are 200 × 200 × 34 mm with a mass of 7 kg.

Testing of the absorption heat pump was conducted over a range of heat sink temperatures ($20 \leq T \leq 35°C$) and desorber thermal input rates ($500 \leq \dot{Q}_{Des} \leq 800$ W). Evaporator coolant heat duties in the study ranged from 136 to 300 W, while system COPs ranged from 0.247 to 0.434. At a nominal rating condition of 35°C heat sink temperature, the maximum thermal input of 800 W produced a cooling effect of 230 W. This represents a cycle COP of 0.29. Analysis of the experimental data indicated that future work should focus on improved desorber and rectifier designs to improve refrigerant purity. It is estimated that a system similar to the one in this study, with all fluid connections made internal to the system, could achieve the same cooling capacity with a system mass of 2.5 – 3.5 kg in an envelope of 120 × 120 × 25 mm.

The results of this study are the first experimental data on any miniaturized or mobile absorption heat pump. This study also presents a detailed design methodology for future mobile thermally activated heat pumps of varying capacities.

1 Introduction

A thermally activated mobile cooling system with a cooling capacity of 200-1000 Watts would be useful for numerous applications. Users of Nuclear-Biological-Chemical protective clothing would benefit from personal cooling systems by extending mission durations as well as increasing worker productivity. Bishop *et al*. (1995) provided a review of the studies on heat stress of individuals working in protective clothing. Individuals in military style protective clothing were unable to sustain metabolic work rates of 475 W in 31°C ambient temperature for longer than 90 minutes due to substantial increases in body core temperatures. Individuals performing the same tasks in normal work clothing had reached a sustainable equilibrium core temperature. Including rest periods during the work periods provided no increase in total sustainable work time. The need for mobile cooling systems is illustrated by the reduced physical performance of individuals in protective clothing. Automobile comfort cooling systems powered by waste heat from the engine cooling fluid or exhaust gas could reduced the power requirements of the air conditioning system and thereby increase overall fuel efficiency of the vehicle. Researchers have investigated the use of personal cooling systems to alleviate heat induced symptoms of certain diseases such as multiple sclerosis (Ku *et al.*, 1999). As the sizes of electronic systems continue to decrease and the power consumption increases, there will be an increased need for high heat flux cooling of

components. A thermally activated cooling system would enable mobile cooling of these electronic devices.

The limited cooling capacities and excessive mass for long duration current mobile cooling systems are the major factors that limit their widespread use. Thermally activated cooling systems such as absorption heat pumps, can take advantage of the high specific energy of liquid fuels to minimize the total mass of the system and its energy source. The incorporation of microchannel heat and mass exchanges also leads to significant reductions in the volume and mass of the system.

1.1 Mobile Cooling System Comparison

To illustrate the differences in the required mass of various mobile cooling systems, a comparison of the energy source-to-cooling efficiency and system mass for the different systems was conducted. The systems considered include: Ice Packs (IP), a Lithium-Ion battery powered Vapor Compression Cycle (B-VCC), a Fuel Cell powered Vapor Compression Cycle (FC-VCC), a miniature Internal Combustion engine powered Vapor Compression Cycle (IC-VCC), and an Absorption Cycle (AC). The required cooling capacity for this comparison was established at 300 W for a duration of 8 hours.

The ice packs represent the simplest cooling method. Each kilogram of ice will provide 334 kJ of latent cooling and approximately 83 kJ of sensible cooling (to 20°C) for a total specific cooling capacity of 417 kJ/kg of ice. A total of 20.7 kg of ice would be required to provide the 300 W of cooling for 8 hours.

Vapor compression cycles are attractive for cooling or refrigeration systems because of their high Coefficient of Performance (COP). A schematic of a vapor compression cycle is shown in Figure 1-1. A high pressure stream of liquid refrigerant

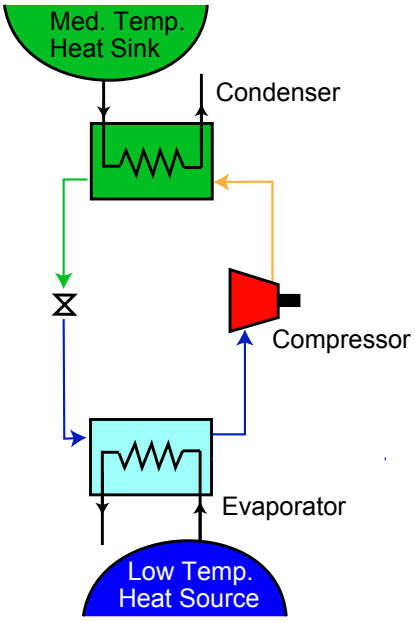

Figure 1-1 Vapor Compression Heat Pump Schematic

exits the condenser and then expands to a lower pressure through a throttling device. As the refrigerant passes through the evaporator, it receives energy from the low temperature heat source, eventually exiting as a superheated vapor. A compressor returns the refrigerant vapor to the higher pressure of the condenser, with a corresponding increase in the saturation temperature of the refrigerant. The refrigerant temperature is now greater than that of the medium temperature heat sink, so it may reject energy to that sink in order to return to the condensed liquid state.

Vapor compression cycles are simple and their operation is well understood; unfortunately they require a substantial work input in the form of shaft power. They also rely on synthetic refrigerants, most of which have significant global warming potential. For this comparison, the COP of a miniature vapor compression cycle operating between a sink temperature of 35°C and a source temperature of 5°C was estimated to be 2, which

results in a required input power of 150 W. The mass of the vapor compression cycle was estimated to be 1.8 kg (Ernst and Garimella, 2007).

Lithium-Ion batteries could be used to provide the electrical power for the motor that drives the vapor compression cycle. Lithium-Ion batteries have a specific energy of 450 kJ/kg (Kiehne, 2003). To provide the required 150 W of input power for 8 hours would require 9.6 kg of batteries. The required electrical motor is estimated to weigh 0.3 kg.

For the fuel cell powered vapor compression system, a direct methanol fuel cell was used for the comparison. Small fuel cells in this power range have a specific power of approximately 30 W/kg (DOE, 2006). A fuel cell to provide the required 150 W of electrical energy would weigh approximately 5 kg and the electrical motor is estimated to weigh 0.3 kg. Based on the Gibbs function of formation of the reactants and products, the maximum theoretical work output of a DMFC is 21,923 kJ/kg of methanol. With an assumed fuel cell efficiency of 50%, the required mass flow rate of methanol is 0.05 kg/hr and the total mass of fuel for the 8 hours would be 0.4 kg.

Internal combustion engines have high specific power and are widely used for mobile applications. The small scale engine and vapor compression cycle developed and demonstrated by Ernst and Garimella (2007, 2008) had a total system efficiency, based on fuel energy usage to evaporator cooling duty, ranging from 8.0 to 15.2 percent. The mass of the small scale engine, drive train and starting system used in that study was 1.6 kg. The fuel was a mixture of 88 percent methanol and 12 percent lubricating oil. Small-scale engines typically use oil in the fuel to lubricate the moving parts, rather than have a separate oil circulation system that would add substantially to the system mass. Methanol

has a lower heating value of 19,920 kJ/kg. With a system performance of 15%, a methanol flowrate of 0.36 kg/hr and an oil flow rate of 0.05 kg/hr is required. For the 8 hour cooling duration, this results in a total methanol mass of 2.9 kg and oil mass of 0.4 kg.

Among the systems under consideration, absorption cycles have the unique ability to directly convert thermal energy into a source of cooling. The energy does not need to be transformed into electrical or mechanical energy. A schematic of a single-effect absorption heat pump is shown in Figure 1-2.

The condenser and evaporator of an absorption heat pump function in the same manner as those in the vapor compression cycle. A high pressure, condensing refrigerant rejects heat to the medium temperature heat sink while the low pressure, evaporating refrigerant in the evaporator receives heat from the low temperature heat source. The compressor of the vapor compression cycle is replaced in absorption cycles with a liquid solution pump, absorber, desorber, and a solution heat exchanger. As the refrigerant vapor enters the absorber, it is absorbed in a liquid solution. This exothermic absorption process releases heat that must be rejected to the medium temperature heat sink. Once the refrigerant vapor has been absorbed in the liquid solution, it is pumped to the required condensing pressure. Pumping, rather than compressing, the refrigerant significantly reduces the required work input to the system. A high temperature heat source is required to supply heat to the desorber to separate the refrigerant from the solution. The refrigerant then flows to the condenser. The remaining solution returns to the absorber via the solution heat exchanger which is used to internally recuperate energy to increase system efficiency.

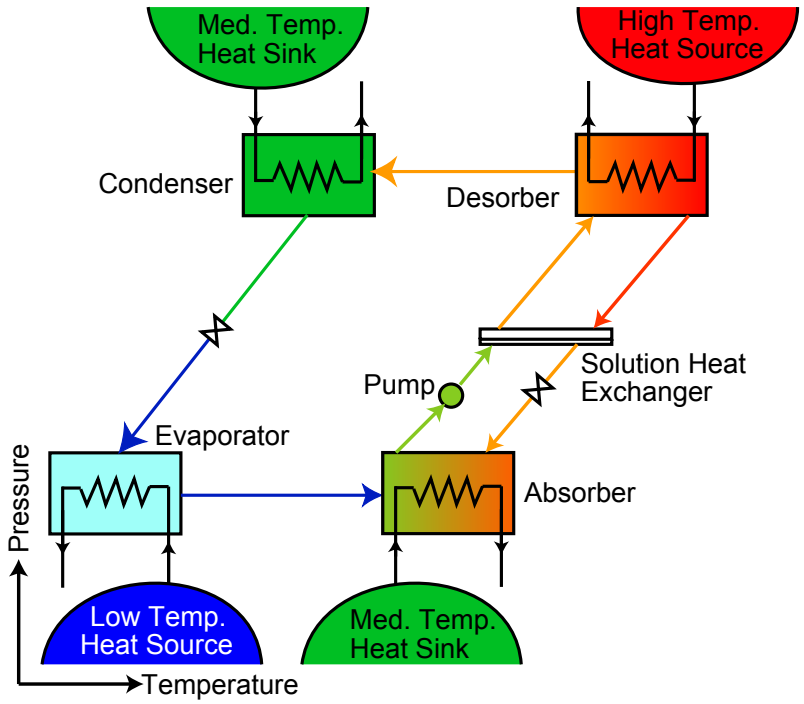

Figure 1-2 Single-Effect Absorption Heat Pump Schematic

An absorption cycle using kerosene (LHV = 43,300 kJ/kg) as a fuel with a typical COP of 0.4 would require only 0.06 kg/hr of fuel for the required 300 W cooling capacity. Absorption cycles do require the use of a pump to circulate the working fluids but the electrical requirements of the pump are generally a small fraction of the total energy required. For the 8 hours of cooling being considered, an electrical requirement of 2 percent of the input thermal power could be satisfied with 1 kg of batteries. The mass of a production version of a miniaturized absorption system, including the mass of the solution pumps is estimated to be 5 kg.

Figure 1-3 illustrates the mass breakdown for the various systems considered as mobile cooling technologies for the case of a 300 W cooling load and 8 hr cooling duration. The internal combustion engine driven vapor compression cycle and the

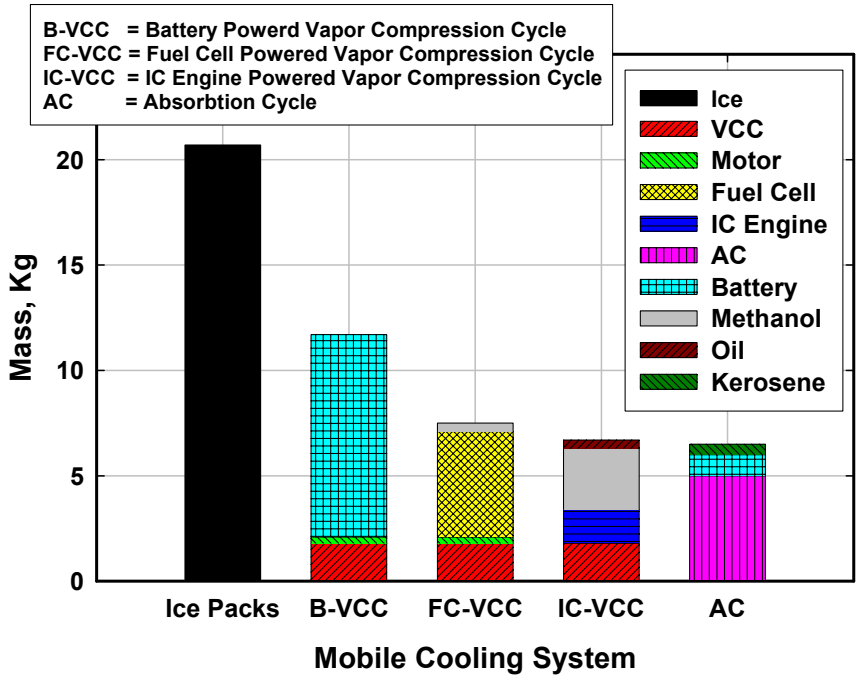

Figure 1-3 Mobile Cooling System Mass Comparison, 300 W Cooling Capacity, 8 Hour Duration

absorption heat pump represent the least massive systems in this comparison. The internal combustion engine however, has many moving parts and can be excessively loud. The lubricating oil used in small scale engines is typically exhausted with the combustion products necessitating an oil trap or the incorporation of an internal lubrication system that would increase the mass of the system.

The absorption heat pump appears to be the system with the greatest potential for providing long duration mobile cooling. The absorption system is also the only cycle that can utilize waste heat to produce cooling.

In the current study, a novel miniaturized thermally activated heat pump was designed and fabricated using state of the art manufacturing techniques. Microchannel heat exchangers with channel hydraulic diameters of 306 μm were employed to achieve the significant weight reduction required to produce a system that is viable as a mobile cooling system. The experimental system developed during this study provides nominal cooling loads of 300 W with heat rejection to a high temperature heat sink in a compact package. Scaling of the system will allow extension to both smaller systems for portable electronics cooling, and larger systems for automobile cooling systems.

1.2 Dissertation Organization

This dissertation is organized as follows:

- Chapter 2 is a review of the prior work in the literature that involves miniaturized mobile cooling systems as well as absorption heat pump technology and microchannel heat transfer and pressure drop.
- Chapter 3 describes the development of a breadboard test facility for the cycle testing of a miniaturized thermally activated heat pump. The testing and data acquisition procedures are outlined and the data analysis and the corresponding uncertainties are discussed.
- Chapter 4 presents the details of the microchannel heat exchanger fabrication techniques as well as the cycle and component design procedures.
- Chapter 5 presents the testing of the packaged microchannel heat pump. Cycle data analysis and uncertainties are presented. Performance of the major components is compared with the original design calculations.

- Chapter 6 presents the important results and conclusions of the study and provides recommendations for future work in this area.

2 Literature Review

A review of the relevant mobile cooling, absorption, and microchannel heat and mass transfer literature is presented here.

2.1 Mobile Cooling

Mobile cooling devices can broadly be classified as passive or active cooling devices. Passive cooling systems consume no power while they are providing the cooling effect, although they require a secondary system to return the system to its initial state. Active cooling systems consume power as they provide the cooling effect. Mobile cooling systems have potential uses in many fields including automotive cooling, electronics cooling, man-portable microclimate cooling systems, as well as medical applications.

2.1.1 Passive Mobile Cooling

The simplest mobile cooling devices use a material that undergoes a phase change to provide the cooling effect. A common phase-change cooling system for personnel consists of ice packs worn in a vest. Body heat is removed as the ice melts. Epstein *et al.* (1986) studied the use of ice packs, and several other cooling methods, for auxiliary cooling. They found that the ice packs provided the greatest cooling rate of 140 W. Because the mass of these systems scales directly with the required cooling capacity, they can become burdensome if long periods of cooling are required. Close contact of skin

with ice can result in lowered skin temperature, resulting in discomfort as well as vasoconstriction that reduces the blood flow to the outer surface of the body and reduces the heat dissipation rate. The study by Cheuvront *et al.* (2003) attempted to avoid this negative physiological response by applying the cooling effect in an intermittent fashion.

Adsorption or solid desiccant cooling systems have also been used for mobile cooling. Grzyll and Bladerson (1997) used a calcium oxide desiccant to adsorb water vapor. The resulting evaporation of the water removed energy from a circulating water loop and provided 150 W of cooling for 4 hours. While this system was simple, it was massive (19.9 kg) and the desiccant must be dried or replaced after each use.

Several investigations of phase-change cooling devices for mobile electronics have been conducted. Alawadhi and Amon (2003) studied the use of phase change material for the cooling of wearable computers. The goal was to extend the operating time of the computers before the acceptable operating temperatures were exceeded. A numerical model was developed that accurately predicted the experimental melting time of the phase change material.

Tan and Tso (2004) investigated a cooling system for mobile electronic devices that utilized the phase change material n-eicosane. The incorporation of the phase-change material leads to an extended operating time before the system temperature exceeds the allowable limit by providing a finite thermal reservoir. Unfortunately this also means there will be an extended period of time without this cooling capability while the phase change material returns to its original state.

The characteristically low thermal conductivities of phase change materials can lead to over heating of the electronics before the entire mass of phase change material has

melted, thus underutilizing its thermal capacity. The work done by Akhilesh *et al*. (2005) provided a design procedure for coupling the base material of the electronic device with the phase change material in such a way as to maximize the allowable operating time.

Although phase-change cooling systems provide a simple cooling system, they are limited due to the intermittent nature of their operation. They require replacement of the desiccant material, or an external cooling system to return the phase-change material to its initial state. In the case of electronics cooling with phase-change material, the cooling effect is used only in intermittent bursts during extreme IC activity and heat dissipation to the ambient slowly returns the material to its original condition. Phase-change materials are unable to provide the necessary cooling for steady state operation of high heat flux mobile electronic devices. For short duration cooling needs, these systems may be well suited. For continuous cooling needs, and for cooling applications at sub-ambient temperatures, an active system is required.

2.1.2 Active Mobile Cooling

While passive or intermittent cooling techniques are often used for their simplicity, they lack the capacity for extended periods of cooling. Active cooling systems can provide the needed capacity but at a cost of added complexity and weight. Miniature electrically driven vapor compression cycles have been studied, mainly for electronics cooling, but also for mobile personal cooling devices.

Ashraf *et al.* (1999) designed a vapor compression cooling system fabricated on silicon wafers. The intended application was, "an integrated heat removal system for electronics or photonic chips or modules." The cooling system was to be driven by a centrifugal compressor with the input power from a variable capacitance motor, both of

which were to be fabricated on the silicon wafers. Shannon *et al*. (1999) developed a miniature vapor compression heat pump for use as a personal microclimate cooling device. The proposed refrigeration cycle is driven by a diaphragm compressor. Each device is sized to provide 3 W of cooling. Multiple systems would be operated together to provide the total desired cooling effect. The major focus of the work was the design and development of the diaphragm compressor. A fully functioning prototype was not constructed, so no experimental results of the cooling system were presented.

While various electrically driven vapor compression systems have been investigated for mobile use, the major obstacle is the power source to drive the cycle. Current battery technology does not provide the required specific energy to make portable cooling from batteries feasible. Lithium-ion batteries have a specific energy in the range of 125 W-h/kg or 450 kJ/kg (Kiehne, 2003). The weight of miniature fuel cells also makes this technology unacceptable as a power source for mobile cooling. Portable fuel cells for consumer electronics currently have a specific power of only 30 W/kg (DOE, 2006). The combustion of a liquid hydrocarbon fuel can provide the large specific energy, and energy density required for successful miniaturization of cooling systems. In contrast to the low specific energies of batteries and fuel cells, kerosene, a fuel which is readily available throughout the world, has a lower heating value (LHV) of 43.3×10^3 kJ/kg. Various thermally activated cooling systems have been investigated to take advantage of the large specific energy of liquid fuels, or the availability of waste heat.

Rahman (1996) investigated the use of a Brayton cycle to provide mobile cooling for soldiers. Ambient air is compressed by a centrifugal compressor. A portion of this air is then mixed with a fuel and burned in a combustion chamber. The combustion

products then expand through a turbine that provides power to the compressor and an electrical generator. The remaining portion of the pressurized air flows through a heat exchanger where it is cooled. It then expands through a turbine to a low temperature. During the expansion of this air, some water vapor is condensed. The system would provide cold air for cooling, as well as potable water and electrical power. The system was designed to cool 8.5×10^{-3} m^3/s of ambient air to 26.7 C at two separate design conditions of 35°C, 74% relative humidity and 48.9°C, 50% relative humidity. The amount of useful cooling of the individual this provides was not discussed. The system is estimated to have dimensions of $0.47 \times 0.279 \times 0.368$ m. No estimate of the mass of the system is given. This system would require a compressor and two turbines that must by carried by the user. No prototype was developed in this study, and no experimental results were presented.

Salim (2004) proposed a thermally activated mobile ejector refrigeration system for use in automobile cooling. The required cooling capacity was 7 kW at an ambient temperature of 43.3°C. The system used waste heat from the engine cooling fluid, (90°C) and from the exhaust gas (220 – 990°C depending on driving conditions) to drive the refrigeration cycle. A high pressure vapor stream is expanded through a convergent-divergent nozzle to induce a secondary flow of refrigerant from the evaporator. While the system still requires power to drive a pump, it is a small fraction of the power that is required to drive the compressor in current automobile vapor compression systems. A thermodynamic model of the proposed system was described and the predicted COPs of 0.5-1.04 were reported for several heat input methods. No experimental results were reported.

Gordon *et al.* (2002) proposed a coupling of thermoelectric and adsorption devices that would allow cooling of personal computers and microelectronics. This pairing minimizes the number of moving parts required in a cooling system. They developed a model to investigate the dynamics of the batch cooling process that is inherent in adsorption chillers. While the efficiencies of both thermoelectric and adsorption systems are each quite low, the COP_{net} claimed by the authors was approximately 1.0 for their reference cooling case of 10 W/cm^2. The total cooling capacity of the system and the ambient conditions were not reported, but the absorber temperature approached 20°C during cycles indicating an ambient lower than that. No experimental results were obtained in this study.

Wang *et al.* (2004a) analyzed a combination Rankine power cycle and vapor compression cycle for use as a portable cooling system. The high COP of the vapor compression cycle is utilized while also taking advantage of the heat-actuation provide by the incorporation of a Rankine power cycle. The coupling of the systems is achieved through an integrated expander/compressor and the use of the same working fluid in both the power and refrigeration cycle. A thermodynamic model of the system is developed and the effects of varying several cycle parameters on system COP are presented. They system analyzed had a cooling capacity of 150 W at an evaporating temperature of 7°C and a condensing temperature of 40°C. The basic cycle COP for this study was 0.83. A parametric study was conducted and the effects of boiler superheat, condensing temperature, evaporating temperature and expander/compressor efficiency on COP were analyzed. With a 100°C superheat, the system COP was 1.3. The key component, the

expander/compressor is claimed to be in development but no experimental results are reported.

Ernst and Garimella (2007, 2008) designed and fabricated a vapor compression refrigeration system for completely autonomous mobile cooling of an individual. The cooling system was driven by a miniature internal combustion engine linked to a miniature reciprocating piston compressor. The working fluid was R-134a. The condenser was an air-coupled aluminum microchannel heat exchanger. The evaporator was integrated into a vest to provide cooling to the torso of an individual. The system provided a cooling capacity of 230 W at an ambient temperature of 43.3°C with an overall, fuel-to-cooling efficiency of 10.2%. The 4.4 kg system with a fuel supply of 1.8 kg would be able to provide the cooling capacity stated above for 5.7 hours. The exhaust gases and noise generated from the small internal combustion engine are some drawbacks of this technology.

Absorption cycles have also been studied for their potential use as miniaturized mobile cooling systems. Drost (1999) described a man-portable absorption heat pump for use as a microclimate cooling system. The proposed cooling system was a single-effect water/lithium bromide absorption heat pump with a water cooled absorber and condenser. One of the systems described would use a thermoelectric device to provide some of the required electrical power. The potential performance of the various components was discussed and an estimate of 4 to 5 kg in an envelope of 20 x 22 x 8 cm was given for a system with 350 W of cooling capacity. It is not clear, however, whether this system was ever successfully fabricated as no experimental results were presented.

While absorption systems have a lower COP than vapor compression cycles, they have several distinct advantages that can be useful in mobile applications. Their ability to provide continuous cooling with a heat input significantly reduces the need for electrical power and the associated batteries. Miniaturized pumps are readily available, unlike the miniature compressors or turbines that would be required for other thermally activated systems.

2.2 Absorption Heat Pumps

Much of the work on absorption systems has focused on evaluating increasingly complex cycle configurations in order to increase system COP. A common method of increasing system COP is to cascade several absorption heat pumps together so that the reject heat from one is the input heat for the next. Figure 2-1 is a schematic of a double-effect absorption heat pump. The system shown has an additional desorber, absorber, solution heat exchanger and solution pump. In this configuration, the concentrations in the solution streams are adjusted to allow the reject heat from the high temperature absorber to be used to heat the low temperature desorber. The term double-effect indicates that each unit of input heat is used twice to generate refrigerant vapor. There are numerous other multi-effect system configurations that can be used to increase system efficiency or increase the attainable temperature lifts.

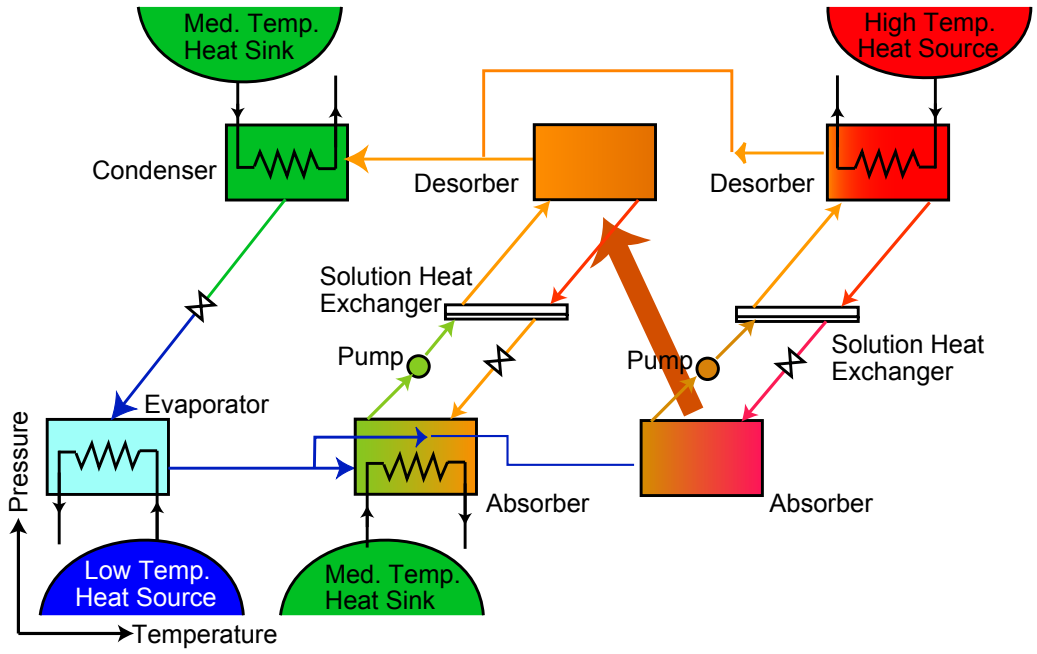

Figure 2-1 Double-Effect Absorption Heat Pump Schematic

Gommed and Grossman (1990) evaluated the performance of a single-effect as well as 3 double-effect water/lithium bromide absorption heat pumps. For each of the systems, the effects of various system temperatures on the COP were discussed. DeVault and Marsala (1990) studied several triple-effect cycles at a standard rating condition. The tripe-effect cycle had a COP of 1.41 while the single-effect baseline cycle had a COP of 0.77. The triple-effect cycle also had the added benefit of operating at a lower pressure than the corresponding double-effect cycle. Ivester and Shelton (1994) investigated a triple-effect ammonia/water system that had the potential to yield a COP of 1.50. Ziegler and Alefeld (1994) predicted that a quadruple-effect system would have a COP of 2.0. They used a superposition principle with the known cycle performance of elementary

cycles to estimate the COPs of more complex cycles. This method is not restricted to any specific cycle configuration or fluid pair.

Garimella *et al.* (1997) investigated the use of two sets of working fluids in a triple-effect absorption cycle. The working fluids studied were ammonia-water in both the upper and lower cycles, and ammonia-water in the upper cycle and ammonia-sodium thiocyanate in the lower cycle. A realistic gas burner model was included to account for flue gas losses. The reported cooling mode COPs for several control schemes at 35°C were approximately 0.8. The analysis concluded that, due to several practical considerations concerning intermediate fluid flow arrangements, the COP of the triple effect cycle was essentially the same as a double-effect cycle with equivalent heat exchanger size. However, the triple-effect cycle accomplished this with a substantially lower high cycle maximum pressure.

Another method of increasing cycle COP is to recuperate some energy from the hot portions of the absorber to power the cool portion of the generator. Such a system operates on a Generator Absorber Heat Exchange (GAX) cycle. Garimella *et al.* (1996) analyzed such a GAX system with the cycle components coupled to the conditioned space through secondary hydronic fluid loops as would be necessary to avoid having ammonia circulating through the conditioned space. They found the cooling COP to be 0.925 at an ambient temperature of 35°C. Performance maps covering the entire range of ambient operating temperatures (-30°C to 46.1°C) were also developed

Experimental studies of absorption cycles have also focused on using internal heat recovery to increase system COP. Serpente et al. (1994) designed and built a 2 kW water/lithium bromide absorption system. The design process included using general

heat transfer correlations to size components. The experimental COP ranged from 0.642 to 0.743. A direct gas fired, ammonia/water system, built by Treffinger (1996) was used as a domestic water heater. Experimental heating mode COP values of 1.4 – 1.7 were reported. Erickson *et al*. (1996) demonstrated an ammonia/water GAX absorption system with a 21.2 kW cooling load, with a COP of 1.05 at an ambient temperature of 27.8°C.

The miniaturization of absorption components has been studied by Garimella (1999, 2004) although not to the small scale required for mobile applications. These miniaturization studies have focused on developing smaller components for residential scale heating and cooling applications by using small, 1.58 mm diameter tubes. Meacham and Garimella (2002, 2003) investigated the use of this technology for the absorber component in an ammonia/water absorption heat pump. They conducted experiments on the microchannel, falling film, ammonia/water absorber and found that incomplete wetting of the tubes reduced the performance. An updated design (Meacham and Garimella, 2004) resulted in better performance using an improved solution distribution device. Determan and Garimella (2005) successfully demonstrated that the same component could be used as the desorber in an absorption system with only minor modifications to the liquid distribution system.

The majority of absorption studies have focused on increasingly complex cycles to increase the system COP. Increasing COP through system complexity comes at the price of increased number of components, and therefore increased mass. For mobile applications, where compactness and mass are critical design factors, this increased complexity may not be warranted. The reduced fuel consumption of a marginally more

efficient system would have to offset the increased fixed mass of the larger physical system. As was demonstrated earlier in Figure 1-3, the mass of the fuel of an absorption cycle is already a very small fraction (~8%) of the total system mass.

The design choice between working fluids for absorption heat pumps is driven by operating conditions and fluid properties. Many fluid pairs have been considered for absorption cycles but the two main fluid pairs (refrigerant/absorbent) remain water/lithium bromide and ammonia/water. The critical fluid characteristics for absorption fluid pairs are discussed by Herold *et al*. (1996). Water/lithium bromide systems have the advantage of using a non-volatile absorbent. This means the refrigerant vapor generated in the desorber is pure and does not require rectification before entering the condenser. Water, however, has a sub-atmospheric vapor pressure at the evaporating temperatures required. Vacuum operation of a system requires an auxiliary non-condensable gas removal system. Careful monitoring of the concentrations in water/lithium bromide systems is required to avoid crystallization issues. The large specific volume of water at the low pressures causes excessive pressure drop in miniaturized systems, which in turn introduces large saturation temperature penalties. For comparison, at a temperature of 5°C, water has a saturation pressure of 0.87 kPa and a vapor specific volume of 147 m^3/kg while the saturation pressure of ammonia is 516 kPa and the vapor specific volume is 0.24 m^3/kg.

Ammonia/water systems operate at pressures well in excess of atmospheric conditions, eliminating the need for a non-condensable purge system. The absorbent in this fluid pair, water, is a volatile substance and therefore a rectifier must be included to purify the refrigerant stream. Small amounts of water in the refrigerant stream can cause

large temperature glides in the evaporator which can significantly reduce system performance. Ammonia can create adverse health consequences if humans are exposed to it in large enough concentrations, so precautions must be taken to avoid exposure. Several common heat exchanger materials, aluminum and copper, are incompatible with ammonia/water systems, so carbon steel or stainless steel are the materials of construction for these systems. While the lower thermal conductivity of stainless steel compared to aluminum and copper can be a concern in macroscale heat exchangers, it can be advantageous in microchannel heat exchangers by suppressing axial conduction (Hong *et al.*, 1999; Schubert *et al.*, 2001). Also, for prototype units such as the one under consideration in the present study, a stainless steel system eliminates the possibility of corrosion of the components due to frequent exposure to the atmosphere during shake-down testing.

2.3 Microchannel Heat Transfer and Pressure Drop

The miniaturization of a thermo-fluid device such as an absorption heat pump requires an understanding of the state of the art in single phase, boiling and condensation heat transfer and pressure drop in microchannels. Kandlikar *et al.* (2005) provides a convenient compilation of the relevant material in these areas of research.

A comparison of the investigations of single-phase heat transfer and fluid flow in microchannels was presented by Sobhan and Garimella (2001). The reported correlations and trends of friction factor and average Nusselt number in microchannels were compared with classical correlations for conventional channels. They found little agreement between the studies and concluded that improperly accounting for factors such as entrance and exit effects, surface roughness, channel dimensions and experimental

uncertainty could result in the reported deviations from conventional predictions. Liu and Garimella (2004) conducted heat transfer and pressure drop experiments and numerical simulations of single-phase flows in microchannels ($244 < D_h < 974$ μm). They concluded that conventional correlations adequately predict the heat transfer and pressure drop in microchannels as small as 244 μm for Reynolds numbers up to 2000. Consequently, the friction factor and Nusselt number correlations for flows in channels of various geometries compiled by Kakac *et al.* (1987) can be used with reasonable accuracy.

Boiling in small channels has been studied recently for its applications to cooling of high heat flux electronics. The prediction of heat transfer coefficients in small channels is complicated by the difference in flow patterns from those encountered in conventional size tubes. Useful correlations for the accurate design of microchannel evaporators are still in their infancy and should not be expected to provide results with low uncertainty.

Warrier *et al.* (2002) conducted experiments on flow boiling of the fluid FC-84 in parallel channels with hydraulic diameters of 0.75 mm at varying mass fluxes (557-1600 kg/m^2-s) and heat fluxes (0-5.99 W/cm^2). The correlations available in the literature were unable to accurately predict the experimental results. Correlations of heat transfer coefficient with boiling number, and either the subcooling parameter or quality were developed for the subcooled boiling region and the saturated boiling region.

In the first part of a two part study, Qu and Mudawar (2003a) evaluated 11 correlations (6 developed for conventional channels, and 5 developed specifically for mini- and microchannels) to predict flow boiling heat transfer coefficients from their own

experiments of water boiling in 349 μm hydraulic diameter channels. They found that all of the correlations they evaluated provided poor results. The best results, with a mean absolute error of 19.3%, were provided by the correlation from Yu *et al.* (2002) and did not correctly predict the trend of heat transfer coefficient with quality. In the second part of the study, Qu and Mudawar (2003b) argue that while nucleate boiling may dominate the heat transfer in microchannels with refrigerants, the greater surface tension and contact angles associated with water cause an abrupt transition to annular flow, thus bypassing the nucleate boiling dominated region. They developed an annular flow model to predict the heat transfer coefficient. Their new model was able to predict the heat transfer coefficients from their earlier experiments with a mean absolute error of 13.3%.

Kandlikar and Steinke (2003) and Kandlikar and Balasubramanian (2004) have presented a correlation for flow boiling in microchannels that is a modification of the earlier correlation by Kandlikar (1990) for flow boiling in conventional tubes. For flows with all-liquid Reynolds numbers greater than 100, nucleate boiling and convective boiling heat transfer coefficients are calculated, with the larger of the two being used to represent the flow. For flows with all liquid Reynolds numbers less than 100, only the nucleate boiling correlation is used.

Garimella (2006) has provided a comprehensive review of the research on flow regimes, void fraction, pressure drop, and heat transfer coefficients for condensation in minichannels. The heat transfer correlation developed by Shah (1979) is based on a large data set of conventional sized tubes and provides reasonable estimates for mini and microchannels. Very few studies of condensation in channels with $D_h < 1$ mm have been conducted.

The two-phase pressure drop correlations for conventional channels by Lockhart and Martinelli (1949), Chisholm (1973) and Fridel (1980) have been used, or modified for use with, mini and microchannels. Based on their experiments of air-water flows in 1-4 mm tubes, Mishima and Hibiki (1996) suggested a modification of the Chisholm parameter based on the diameter of the tubes. The work of Garimella *et al*.(2002; 2003; 2005) resulted in flow-regime-based pressure drop models for condensation of R134a in 0.4-5 mm channels.

The condensation heat transfer studies that have been conducted on small channels (Garimella and Bandhauer, 2001; Wang and Rose, 2004; Wang *et al.*, 2004b; Shin and Kim, 2005; Bandhauer *et al.*, 2006) have been almost exclusively conducted with R-134a as the working fluid.

2.4 Research Needs

There is a need for mobile cooling technology in areas ranging from electronics cooling, to microclimate air conditioning, to treatment of chronic medical conditions. Current passive cooling technologies fail to provide the required heat removal rates and have limited applications due to the intermittent nature of the systems. Fully autonomous, electrically powered, active cooling systems suffer from low battery specific energy that requires the use of bulky and massive battery packs. Active, thermally powered cooling systems could provide continuous cooling from small enough packages to truly enable many mobile applications. While there have been several proposed thermally activated mobile cooling systems, few have been fabricated or experimentally validated. Fabrication and experimental validation of miniaturized cooling systems is essential to advance the state of mobile cooling technology.

The current status of microchannel heat and mass exchanger technology provides the opportunity to use these devices to enable the miniaturization of heat pumps. Coupling microchannel heat and mass exchangers with macro scale pumps utilizes the heat transfer benefits of the microchannels while avoiding the challenges of micro fabrication of pumps, compressors, turbines and fans. Demonstration of a fabrication technique that allows the creation of multiple heat and mass exchangers, and entire heat transfer systems with a single joining process would lead to reduced manufacturing inputs.

2.5 Research Objectives

The objectives of this study are as follows:

- Design and fabricate a flexible breadboard test facility for cycle validation of a miniaturized, thermally activated heat pump.
- Using the flexible breadboard test facility, demonstrate a miniaturized, single-effect ammonia/water absorption heat pump with cooling loads of 150-300 watts.
- Utilizing the experience of the miniature cycle demonstration and current microchannel heat and mass transfer technology, design and fabricate an integrated, multiple component heat pump into a single packaged unit by taking advantage of advanced manufacturing techniques. Demonstrate the creation of multiple heat and mass exchangers in a single joining process.
- Experimentally evaluate the cooling performance of the miniature packaged heat pump to confirm the viability of the mobile, thermally activated ammonia/water absorption cooling system.

The approach used to achieve these objectives, and the results from this approach, are documented in the following chapters.

3 Breadboard Test Facility Design and Testing

A single-effect, ammonia/water absorption heat pump was designed, fabricated and tested using a flexible breadboard test facility. This experimental system was used to investigate the feasibility of operating a small-scale absorption heat pump. This chapter outlines the design and testing of this system. Descriptions of the individual components of the system are presented, and a representative data point is evaluated.

3.1 Test Facility Design and Fabrication

For initial validation of the suitability of an ammonia/water absorption heat pump for miniaturization, a bench top breadboard system was designed and fabricated. The objective of the breadboard system was to demonstrate that operation of a small-scale ammonia/water absorption heat pump is possible and also to evaluate system components.

A schematic of the system is shown in Figure 3-1. Concentrated ammonia/water solution leaving the absorber [1] is pumped through the solution cooled rectifier and the solution heat exchanger, recuperating heat rejected from those parts of the system. The pre-heated concentrated solution [4] then enters the desorber. An electrically powered cartridge heater provides the necessary heat input, $\dot{Q}_{Des}$. An electrical heater is used in place of a gas burner to simplify the construction and operation of this demonstration unit as well as to enable more accurate measurement of the input power.

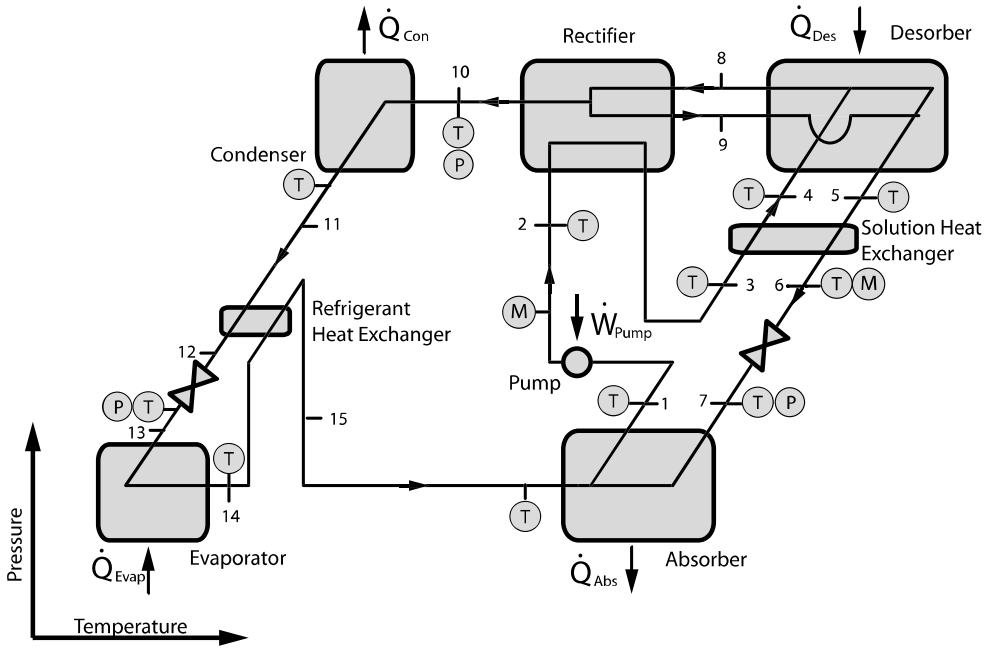

Figure 3-1 Breadboard System Schematic

Inside the desorber, gravity is used to separate the vapor and liquid. The vapor [8] enters the solution-cooled rectifier where excess water vapor is condensed, thus increasing the ammonia concentration of the vapor. This purification of the refrigerant vapor limits the temperature glide in the evaporator and is essential to efficient cycle operation. The reflux [9] is mixed with the dilute solution leaving the desorber [5] which then flows through the solution heat exchanger to preheat the concentrated solution stream. The dilute solution [6] then flows through a pressure reducing valve and enters the absorber [7]. After the refrigerant vapor exits the rectifier [10], it enters the condenser where the heat of condensation, $\dot{Q}_{Con}$, is rejected to the ambient air. The condensed liquid ammonia refrigerant [11] then flows through a sight glass so that a liquid condition can be verified. After flowing through a recuperative heat exchanger,

the liquid refrigerant [12] flows through a pressure reducing valve and then enters the evaporator [13].

As the refrigerant evaporates, the water circulating through the evaporator is cooled, thus providing the cooling effect, $\dot{Q}_{Evap}$. After exiting the evaporator [14], the refrigerant vapor flows through the recuperative refrigerant heat exchanger and then enters the absorber [15]. The refrigerant heat exchanger is necessary due to the large temperature glide of the evaporating refrigerant at high qualities. The otherwise unutilized latent heat of evaporation of the last liquid to evaporate is used to reduce the enthalpy of the refrigerant stream entering the expansion device. As the refrigerant vapor and the dilute solution mix in the absorber, the liquid solution begins to absorb the vapor. The absorption of the ammonia releases a large amount of heat, $\dot{Q}_{Abs}$, which must be rejected to the ambient. Once the vapor is fully absorbed into the liquid, it flows into the solution receiver tank, and then flows to the solution pump [1].

A thermodynamic model of the absorption system was developed using Engineering Equation Solver (EES) software (Klein, 2006). This model allowed parametric analysis of the flow conditions and heat exchanger sizes, and assisted in establishing the operating conditions of the experimental system. To fully describe the operating conditions, several input variables and assumptions about the state of the working fluids are required. The refrigerant vapor outlet from the rectifier [10] was assumed to be at a saturated vapor state. The dilute solution outlet from the desorber [5] was assumed to be at a saturated liquid state. The state of the reflux [9] was determined by assuming that it is a saturated liquid. The operating pressures and concentrations at various locations in the cycle are then dictated by mass and species balances, the ambient

temperature and the heat exchange performance of the various components. This model was used to estimate the required sizes of all of the components.

The breadboard test facility was fabricated in a configuration that enabled easy installation or removal of the components. Figure 3-2 shows a photograph of the test facility. This flexibility in the test facility allowed modifications to the system to be completed in an expedited manner while also providing ample space for the

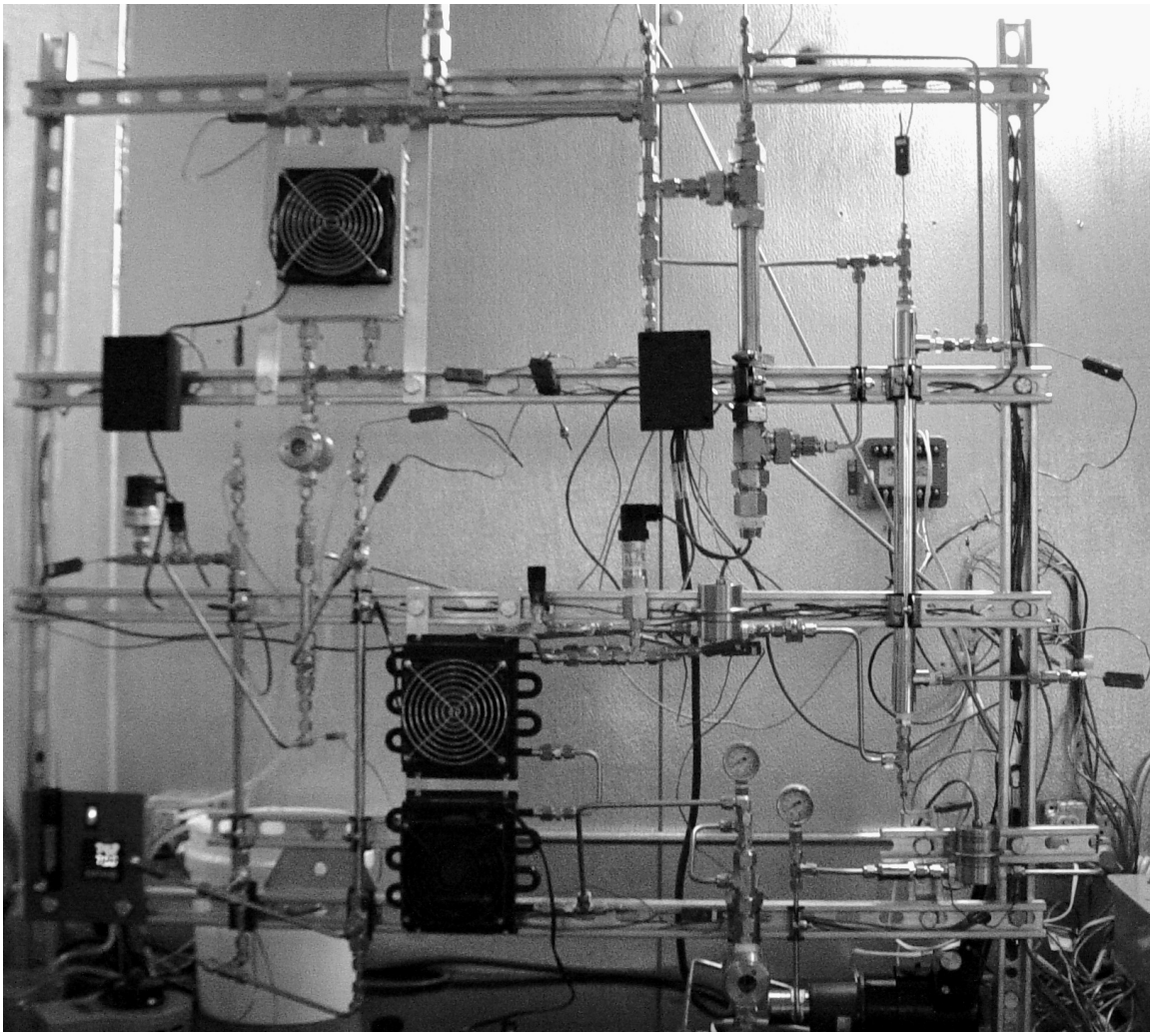

Figure 3-2 Breadboard System Photograph

instrumentation required.

The 1.2 × 1.2 × 0.3 m test facility was constructed inside the 2.7 × 4.0 × 2.4 m environmental chamber shown in Figure 3-3. The chamber and its associated HVAC system are capable of simulating ambient air conditions from 15 to 60°C for air coupled heat rejection experiments. A water circulation system was also installed for liquid-coupled heat rejection experiments. A tank of water simulates the thermal mass of a cooling load and is maintained at a specified temperature by an immersed electrical resistance heater controlled by an Extech Instruments (48VTR) PID control circuit. The water in this tank is circulated by a LAING centrifugal pump (SM-1212-26) through the evaporator where it is cooled. The electrical power input to the generator is controlled with a Staco Energy variable voltage transformer (3PN1010B).

Figure 3-3 Environmental Chamber Photograph

Using the heat exchanger estimates from the EES model, components were selected from suppliers or were fabricated in-house. Table 3-1 lists the heat exchanger type, size and manufacturer for all of the heat exchangers in the final version of the breadboard system. Table A-1 through Table A-8 in Appendix A provide the dimensional details of all of the heat exchangers used in the final breadboard system configuration. Table A-9 through Table A-22 provide details on the other components.

Table 3-1 Breadboard System Heat Exchangers

Component	Type	Heat Transfer Area	Manufacturer	Model #
Absorber	Finned Tube	0.376 m^2 × 2	Lytron	4105G1SB
Condenser	Finned Tube	0.277 m^2	In-house	NA
Solution Heat Exchanger	Shell and Tube	0.11 m^2	Exergy	00540-3
Refrigerant Heat Exchanger	Tube-in-Tube	3.8×10^{-3} m^2	In-house	NA
Evaporator	Tube-in-Tube	18.4×10^{-3} m^2	In-house	NA
Desorber	Immersion Heater, 1000 W	NA	Watlow	L6EX16B
Rectifier	Tube-in-Tube	4.6×10^{-3} m^2	In-house	NA

The absorber used in the breadboard system is shown in Figure 3-4. Two identical heat exchangers were connected in series to provide the required heat transfer area. In this figure, the fan has been removed from the upper heat exchanger to reveal the tube passes and the fins. The dilute solution and refrigerant vapor flow into the absorber at the top tube connection labeled A and the concentrated solution flows out of the bottom tube connection at B. The air flows through the absorber in a cross-flow orientation with respect to the solution.

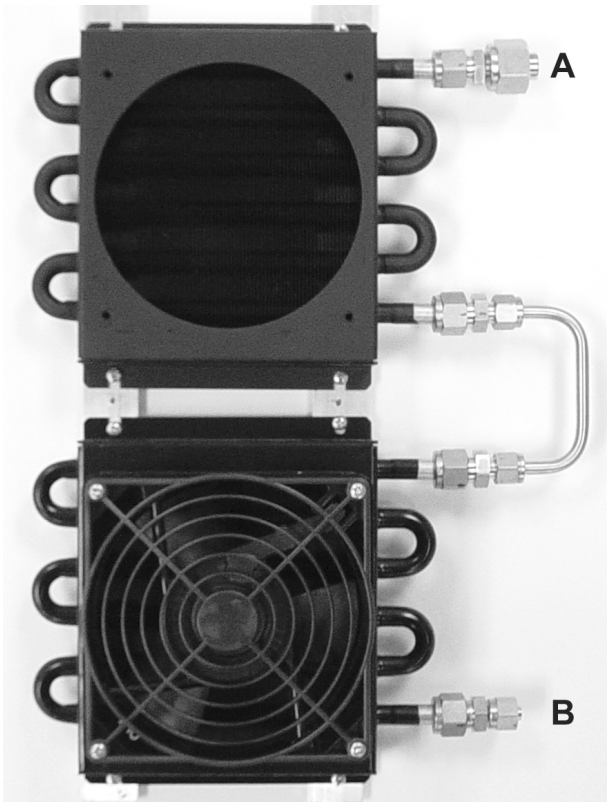

Figure 3-4 Breadboard System Absorber Photograph

The condenser used in the breadboard system is shown in Figure 3-5. In this photograph, the fan has been removed (and is shown adjacent to the condenser) to reveal the tubes and fins. The condenser was fabricated in-house due to a lack of commercial small-scale, air-coupled heat exchangers that could withstand the required system pressures and were also constructed of materials that are compatible with ammonia. The refrigerant vapor enters the condenser through the tube connections at A and the liquid refrigerant exits at the bottom tube connections labeled B. The air is in cross-flow with respect to the refrigerant.

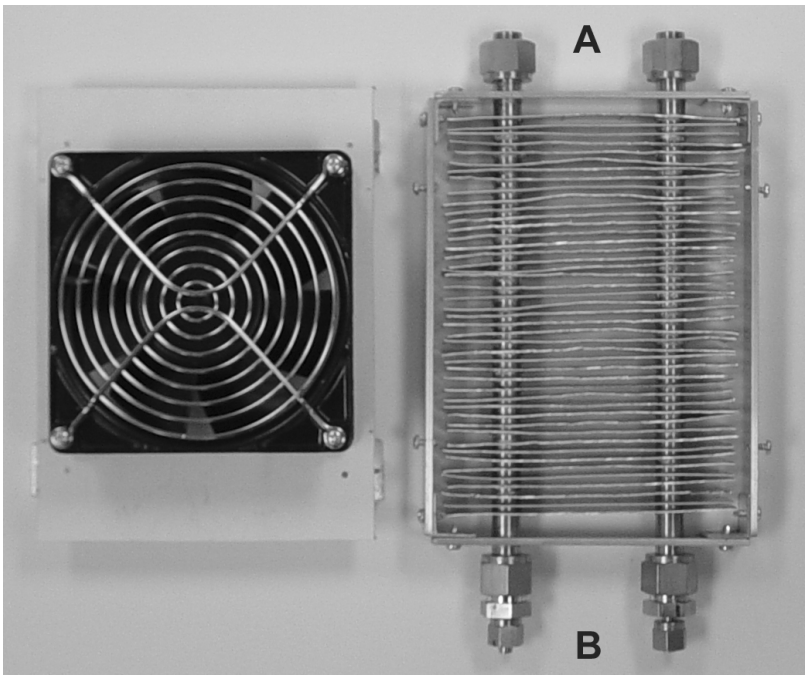

Figure 3-5 Breadboard System Condenser Photograph

The solution heat exchanger used in the breadboard system testing is shown in Figure 3-6. The dilute solution enters the heat exchanger at the tube connection labeled A in the photograph and flows on the tube side of this shell-and-tube heat exchanger. The dilute solution exits at B. The concentrated solution enters at C and flows through the shell side of the heat exchanger until it exits at D.

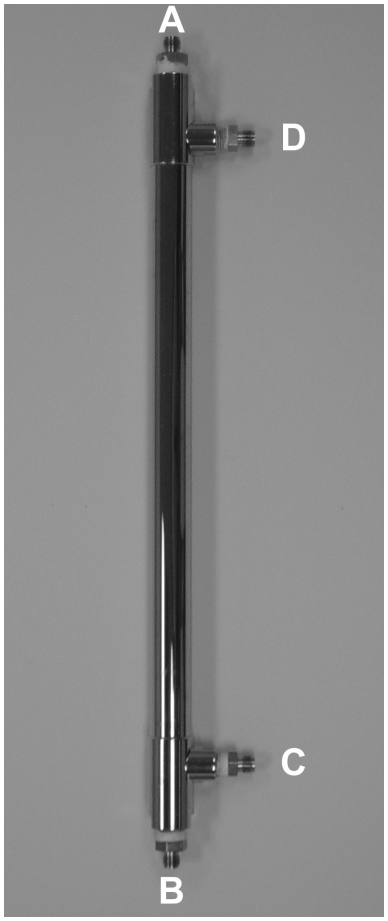

Figure 3-6 Breadboard System Solution Heat Exchanger Photograph

The refrigerant heat exchanger is shown in Figure 3-7. It is a tube-in-tube heat exchanger that was fabricated in-house. The high pressure refrigerant stream enters the inner tube at A and exits at B. The low pressure refrigerant stream enters at C and flows through the annulus side of the heat exchanger, counter-current to the high pressure refrigerant, until it exits at D.

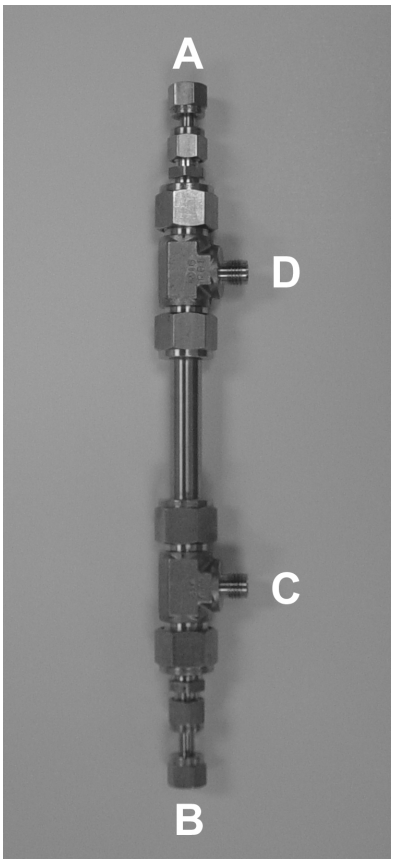

Figure 3-7 Breadboard System Refrigerant Heat Exchanger Photograph

The heat exchangers used for the evaporator are shown in Figure 3-8. Two tube-in-tube heat exchangers were used in series for the evaporator. Splitting the evaporator in this manner allowed the addition of thermocouples into the refrigerant and coolant streams at the middle of the evaporator to monitor the evaporation process in two segments. The refrigerant entered the annulus side of the first evaporator at A and exited at B. The refrigerant entered the annulus side of the second evaporator at C and exited at D. The coolant stream entered the tube side of the second evaporator at E and exited at F and then entered the first evaporator at G and exited at H.

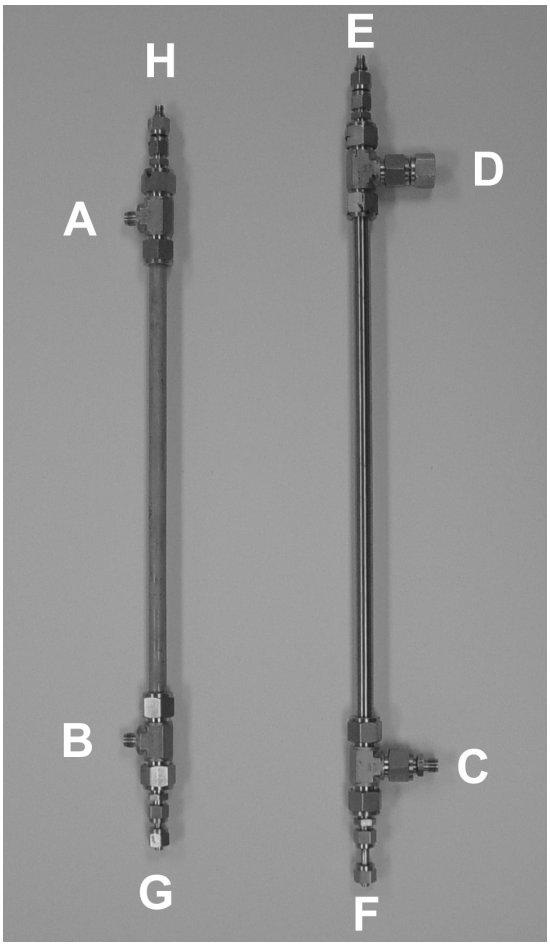

Figure 3-8 Breadboard System Evaporator Photograph

The desorber for the breadboard system is shown in Figure 3-9, as well as an illustration of the desorber depicting the internal configuration. The concentrated solution entered the desorber at A. The tube supplying the concentrated solution extends into the desorber to a level below the refrigerant exit to ensure the solution does not flow along the inner surface of the desorber and collect in the vapor outlet port. The dilute solution exits at B where it mixes with the reflux from the rectifier while the impure refrigerant vapor exits the desorber at C. An electrical resistance immersion heater,

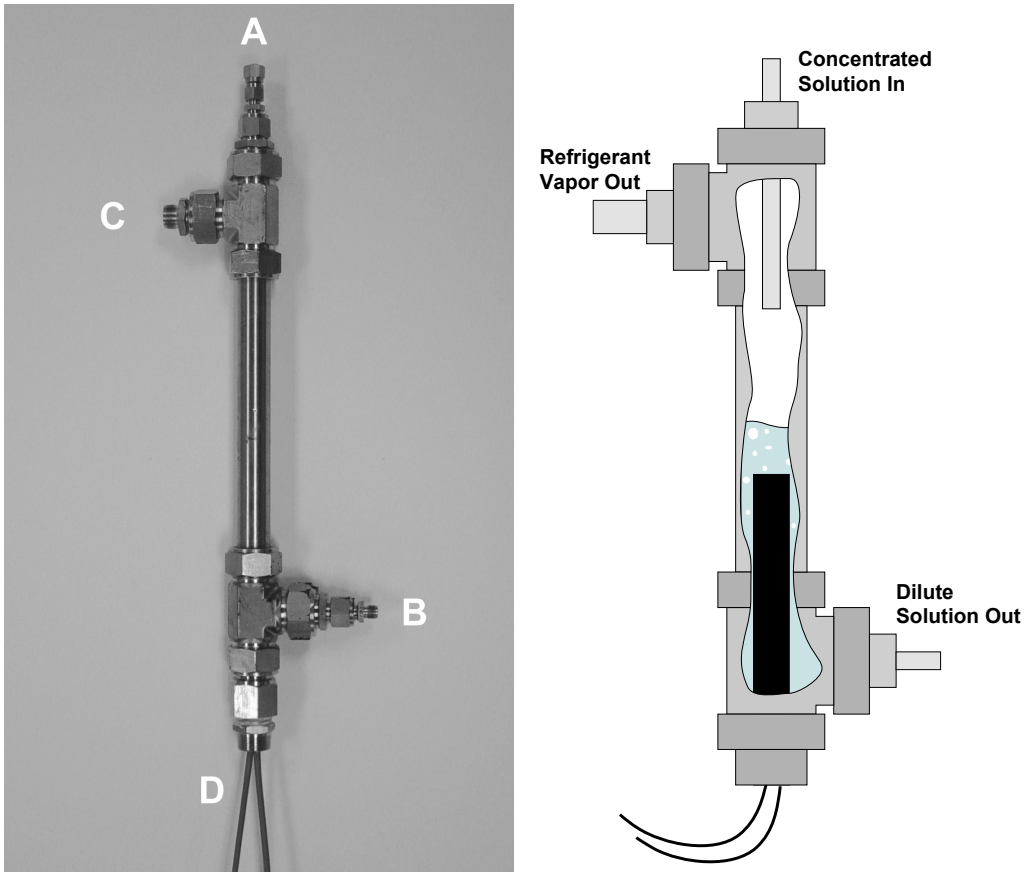

Figure 3-9 Breadboard System Desorber Photograph and Illustration

inserted into the bottom of the desorber at D, supplied the heat input to separate the refrigerant vapor from the solution.

The rectifier used in the breadboard system is shown in Figure 3-10. The rectifier is a tube-in-tube heat exchanger. The impure refrigerant enters the annulus side at A and flows in counter-flow to the concentrated solution. The purified refrigerant vapor exits the rectifier at B. The reflux exits the bottom of the rectifier at C. The concentrated solution used as the cooling source enters the tube side of the heat exchanger at D and exits at E.

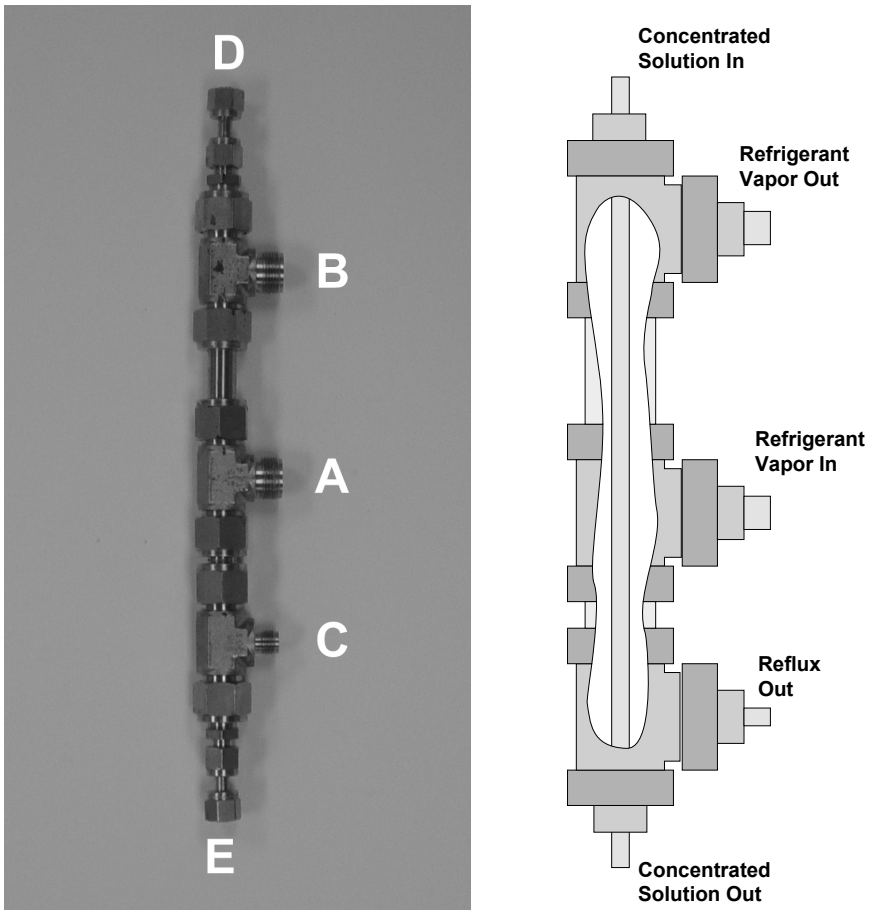

Figure 3-10 Breadboard System Rectifier Photograph and Illustration

3.2 Testing Procedure

Prior to charging the system with ammonia and water, the entire system is leak tested by pressurizing the system with nitrogen to 500 kPa and inspecting each of the tube fittings with a bubble leak detection solution. After all fittings have been inspected, the entire solution loop is evacuated with a rotary vane vacuum pump (J.B. Industries, Model: DV-85N) to an absolute pressure of 20 Pa. After the evacuation was complete, the system was charged with 0.3 kg of distilled water. The required mass of water is

determined by the system internal volume, the majority of which is the solution sump. After several charges and discharges of the fluids, 0.3 kg of water was found to provide an adequate liquid level in the solution sump for the range of testing done in this study. Ammonia was then charged to the desired concentration. The amount of ammonia charged into the system depended on the desired operating concentrations.

Testing begins with setting the desired ambient air temperature of the environmental chamber. Once the ambient conditions have been achieved and the flow regulating valves set to their required positions, the water coolant pump and the condenser and absorber fans are started. The power input to the generator is slowly increased as the system pressures are monitored. Once a steady flow is established in the dilute solution line from the generator to the absorber, the solution pump is started. Frequent checks and adjustments of system pressure, solution flowrates, input power and valve positions provide the required control to achieve the desired test conditions. The water coolant flow rate is established based on the competing requirements of having an adequate temperature change to reduce experimental uncertainties while still maintaining sufficiently high heat transfer coefficients in the evaporator. Air flow rates through the condenser and absorber are fixed based on the fan size and the pressure drop of the heat exchangers.

Operation of such a small scale system presented several challenges. Matching the flowrates of the concentrated solution, dilute solution and refrigerant to achieve steady state required constant adjustments of the solution pump and the control valves. Sight glasses installed at the solution sump upstream of the pump and downstream of the condenser allowed fluid inventories in those portions of the system to be monitored and

greatly decreased the difficulty of operation. Several positive feedback loops inherent in absorption systems also required special attention during testing. As high side pressures begin to drop, the concentrated solution flowrate increases, supplying more cold solution to the desorber, which further lowers the high side pressure. If the absorber pressure begins to rise due to increasing vapor input from the evaporator, the dilute solution flow rate tends to decrease, thus reducing the available solution to absorb the vapor. This tends to further increase the absorber pressure. Both of these events result in increasing fluid inventory in the desorber and, if corrective control actions are not taken, cause the eventual flooding of the condenser with ammonia/water solution. These pressure variations are most prevalent during start-up of the system or during transition between test points.

3.3 Data Acquisition

Temperature, pressure and volume flow rate measurement locations are indicated on Figure 3-1. All temperature measurements were made with type T (copper/constantan) thermocouples (Omega, TMQSS-062G-6, ±0.5°C). Pressure measurements at the absorber inlet and condenser inlet were made with WIKA pressure transducers (S-10, ±0.25% F.S.). Pressure measurements at the evaporator inlet were made with a WIKA pressure transducer (ECO-1, ±0.5% F.S.). The concentrated and dilute solution flow rates were measured with DEA Engineering Company flowmeters (FMTE20, ±0.5% of reading). The power input to the generator was measured with an Ohio Semitronics wattmeter, (PC5-019E, ±0.5% F.S.). All electrical signal measurements were recorded with an IOTech Personal DAQ/56-PDQ2 data acquisition system connected to a personal computer via USB. The water coolant flow rate was

measured with a Key Instruments rotameter (MR3000, ±4.0% F.S.) and measurements were recorded by hand. During testing, critical temperature and pressure readings were displayed as a function of time to ensure steady-state operation is achieved before recording the data points. Each temperature, pressure, flowrate and power measurement was recorded in 60 consecutive scans over a 210 second period. The recorded values are averaged and then used for post acquisition confirmation of operating conditions.

3.4 Data Analysis and Uncertainty

The analysis of a sample data point taken during the testing of the breadboard test facility is outlined here. The data are analyzed using Engineering Equation Solver (Klein, 2006), and the uncertainties in calculated quantities due to measurement uncertainties are estimated using the procedure from Taylor and Kuyatt (1994). For a calculated quantity Y, its uncertainty, U_Y, is given by:

$$U_Y = \sqrt{\sum_i \left(\frac{\partial Y}{\partial X_i} \right)^2 U_{X_i}^2} \tag{3.1}$$

where the measured variables are given by X_i and their uncertainties are U_{X_i}.

The complete analysis and uncertainty calculations are outlined in Table A-23 in Appendix A. For this representative data point, the ambient temperature was 22.6±0.5°C and the input power to the generator was 931±7.5 W. The high side pressure was 1669±8.6 kPa and the low side pressure was 403±8.6 kPa. The temperature of the saturated dilute solution stream leaving the desorber was 120.4±0.5°C. Using the temperature-pressure relation for a saturated liquid to calculate the properties at this state leads to an ammonia concentration of 32.7±0.2%. The measured volume flow rate of the

dilute solution stream was 140.5±0.7 mL/min, which results in a mass flow rate of $2.01\times10^{-3}\pm1.0\times10^{-5}$ kg/s. The temperature of the refrigerant vapor leaving the rectifier was 73.7±0.5°C. At this saturated state, the refrigerant concentration was calculated to be 99.3±0.03% ammonia. The refrigerant entering the absorber was at 49.3±0.5°C, the dilute solution was at 57.9±0.5°C, and the exiting concentrated solution was 42.0±0.5°C. A mass and species balance calculation on the absorber resulted in a concentrated solution stream ammonia concentration of 44.1±0.4%. The volume flowrate of the concentrated solution stream was 174.0±0.9 mL/min, which resulted in a mass flowrate of $2.42\times10^{-3}\pm1.0\times10^{-5}$ kg/s. The difference between the concentrated and dilute solution flowrates resulted in a refrigerant flowrate of $0.41\times10^{-3}\pm1.2\times10^{-5}$ kg/s.

At the outlet of the condenser, the liquid refrigerant temperature was 40.9±0.5°C. After flowing through the refrigerant heat exchanger and expanding through the pressure reduction valve, the pressure and temperature were 409.4±3.4 kPa and -1.0±0.5°C, respectively. It should be noted that while the other components on the high and low sides of the system are assumed to be at their respective constant pressures, the pressure at the inlet of the evaporator is measured independently due to the sensitivity of the refrigerant enthalpy calculation to slight pressure changes at this point. The temperature of the refrigerant at the exit of the evaporator was 11.6±0.5°C. The mass flowrate of the refrigerant and the change in enthalpy from the inlet to the exit of the evaporator resulted in a heat transfer rate of 360±75 W. The mass flowrate of water coolant was $21.0\times10^{-3}\pm1.7\times10^{-4}$ kg/s. The inlet and outlet evaporator coolant temperatures were 16.2±0.5°C and 12.3±0.5°C respectively, which yielded a water-side heat transfer rate of 339±68 W. The 6% difference between the refrigerant and water-side heat transfer rates can be attributed

to minor heat losses/gains to the ambient. The COP of this demonstration system, based on the evaporator cooling water heat duty and the desorber heat input, was 0.36±0.07.

The test results from the breadboard system have demonstrated the feasibility of using a miniaturized ammonia/water absorption heat pump as a mobile cooling system. The results also provided several key insights into the testing of such small systems. The breadboard system was an air-coupled heat pump to demonstrate its potential as a completely autonomous mobile cooling system. The inability to accurately measure the small air flowrates of the absorber and condenser made validation of the operating conditions of those components impossible. While accurate energy balances on these components were not necessary to confirm the cooling load, or the system efficiency, they would have been useful during testing to isolate discrepancies between the operating state and the design state.

4 Microchannel System Development

The breadboard test facility described in the previous chapter confirmed that operation of a small scale absorption heat pump was possible. This chapter describes the design and fabrication of a novel miniaturized heat pump system utilizing microchannel heat exchangers. For this system, liquid coupling was used instead of air coupling to yield a much more compact system. Liquid coupling also enabled more accurate measurements of coupling fluid heat duties. The unique fabrication technique utilized to produce the system is outlined in this chapter. The design of the cycle, as well as the individual component design and configuration, is presented. Finally, the tradeoffs between efficient system packaging and experimental requirements are addressed.

4.1 Manufacturing Techniques

The manufacturing techniques used to build the packaged microchannel system allow multiple microchannel heat exchangers to be fabricated at the same time in a single structure. The microchannels were first formed on 304L stainless steel shims by a wet chemical etching process. The shims were then diffusion bonded together to form the device. By placing shims with different channel configurations in an alternating pattern, the fluid streams of each heat exchanger are allowed to come into close thermal contact.

The type 304L stainless steel used for the shims contains 18% Chromium, 9% Nickel, 1.5% Manganese, and 0.02% Carbon by weight, with the balance being Iron.

Low carbon stainless steels are the preferred stainless steels for diffusion bonding as well as most other welding or joining applications. The corrosion resistance of the stainless steel is not affected by the chemical etching or diffusion bonding process. The corrosion resistance of stainless steel is due to a passivation layer that forms on the surface of chromium bearing alloys. Stainless steels exposed to air are always in a passive condition. The passivation layer can be enhanced by exposure to oxidizing solutions or an electrochemical technique (Dillon, 1995). The microchannel system was fabricated by an outside vendor, VACCO Industries. The steps in the manufacturing process are outlined in the following sections. Images of the manufacturing process are available in section B.2 of Appendix B.

4.1.1 Photochemical Etching

The steps in the etching process are depicted in Figure 4-1. The photochemical etching process began with cleaning the stainless steel with a mild alkaline liquid cleaner in an immersion bath to remove any oils, greases, metal working fluids or other contaminants on the surface. The shims were then cleaned with hydrochloric acid to remove any scale or oxides on the surface of the metal.

A photosensitive material (photoresist) was then applied to both sides of the shim. The photo resist material used in the production of the device in this study was a dry film, negative resist. The portions of the resist exposed to UV light cure and protect the underlying steel during the etching process. The thickness of the photoresist material was chosen to balance the competing requirements of feature precision and durability of the photoresist during the etching process. Thinner photoresist would enable greater accuracy of etched features but may not be able to withstand the etching process if long

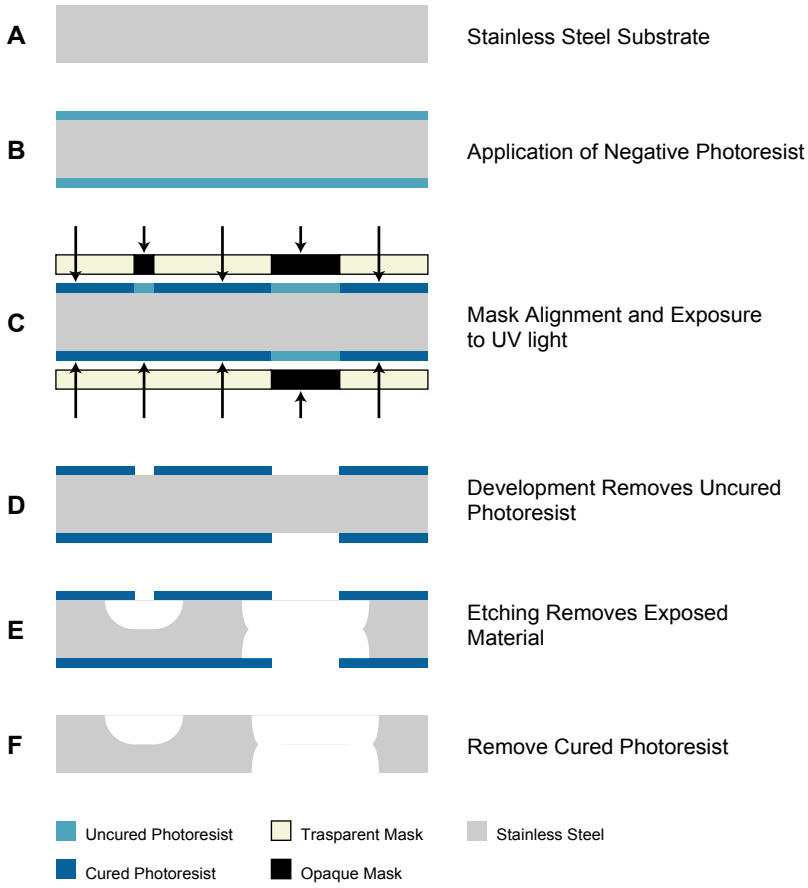

Figure 4-1 Steps in the Photochemical Etching Process

etch times are required. The thickness of the photoresist used in the production of the device in this study was 38 μm (0.0015 in).

A mask containing the image of the required flow channels was created for both sides of each of the two shim designs. The mask was a Polyethylene Terephthalate film with opaque sections representing the areas to be etched and transparent sections representing areas were the photo resist should remain to protect the base material from the etching chemicals. Alignment of the front and back masks is critical to ensure features match up on both sides of the steel.

The arrangement of the steel, photoresist and mask was then exposed to ultra violet light to cure the photoresist. The uncured photoresist was then removed in a developing process. The metal with the cured photoresist was then passed through the etching process. A ferric chloride solution was used as the etchant. This acid solution removed the exposed metal and formed the channels and holes in the steel. The etch rate was controlled by the temperature, spray pressure and acid concentration. Typical etch rates for this process were 12 μm/min. Once the shim is removed from the etching process, the remaining photoresist material is removed. During the etching process the parts remained connected to the process sheets by several tabs. Leaving the parts tabbed to the sheet ensured consistent etching for all of the parts. After the photoresist material was removed, the individual parts were removed from the process sheet. The photoresist application and the etching process were conducted in a clean room to reduce the risk of dust contamination which could cause manufacturing defects during the etching process.

4.1.2 Diffusion Bonding

The diffusion bonding process began with cleaning the shims and an inspection to ensure there were no burrs or foreign objects on the material. The shims were coated with a nickel plating (99.3% pure nickel) in an electroless nickel plating procedure. The thickness of the nickel deposited during this step was 1.27-2.54 μm. The nickel coating was applied to aid in creating a hermetic seal during the diffusion bonding process.

The shims and end plates were then arranged in the correct order and proper alignment of the shims was carefully monitored. Two pins were inserted into alignment holes in the front end plate. All of the shims and the back end plate each have one alignment hole and one alignment slot. This alignment scheme allows the steel shims to

lie flat, even if there are minor inconsistencies in the position of the alignment holes. It also allows the steel to expand and contract due to thermal expansion during the bonding process without causing buckling or delimitation while achieving alignment tolerances of ±0.05 mm.

The assembled system was then placed in a hot press vacuum furnace, Figure 4-2. The evacuation removed any air from between the shims as well as from the voids within the assembled shims. The system was then raised to an elevated temperature (~1000°C) in the vacuum conditions and a load was applied to the system to raise the interfacial stress between adjoining components to the required value (~10 MPa). The system remained at these conditions for a sufficient period of time (~5 hours) for the bonding process to occur. During the bonding process, the surface asperities on contacting surfaces begin to deform plastically. The deformation continues until the pores between the surfaces have been eliminated. The atoms from adjacent surfaces can then diffuse

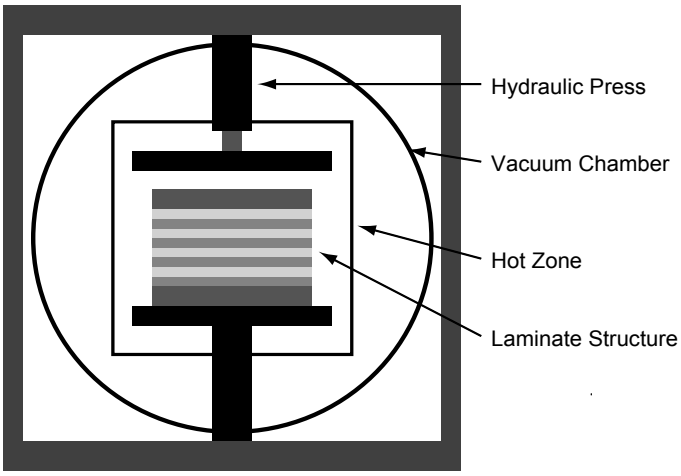

Figure 4-2 Hot Vacuum Press for Diffusion Bonding

across the interface, allowing the grain boundaries to reorganize in the interface region. This process forms a bond with a strength approaching the yield strength of the bulk material. The nickel coating diffuses into the bulk stainless steel. Type 304L stainless steel contains 9% nickel by weight; the addition of the small amount of nickel from the plating does not greatly affect the bulk properties of the steel. A similar bonding process has been used (Schubert *et al.*, 2001; Henning *et al.*, 2004; Pfeifer *et al.*, 2004; Brandner *et al.*, 2006) to form single microchannel heat exchangers, miromixers and reactors.

4.1.3 Manufacturing Constraints

The design of the individual components was affected by the constraints on channel geometry imposed by the manufacturing techniques used. The double-sided etching process imposed a constraint of using only one channel depth for all of the channels. The material of the shim could be etched from both sides, creating a hole through the entire material, or the material could be etched from one side, creating a channel depth of ½ the thickness of the shim. Because all of the channels for each component were fabricated on the same shim during a single etching process, this constraint was applied to all of the channels in the system. The channel width, however, could be modified for each component. In order to limit the design variables for this prototype system, only a single channel size was used for most components.

4.2 Cycle Design Calculations

A cycle model was developed in EES to estimate the required component sizes for the microchannel system. A schematic of the cycle is shown in Figure 4-3.

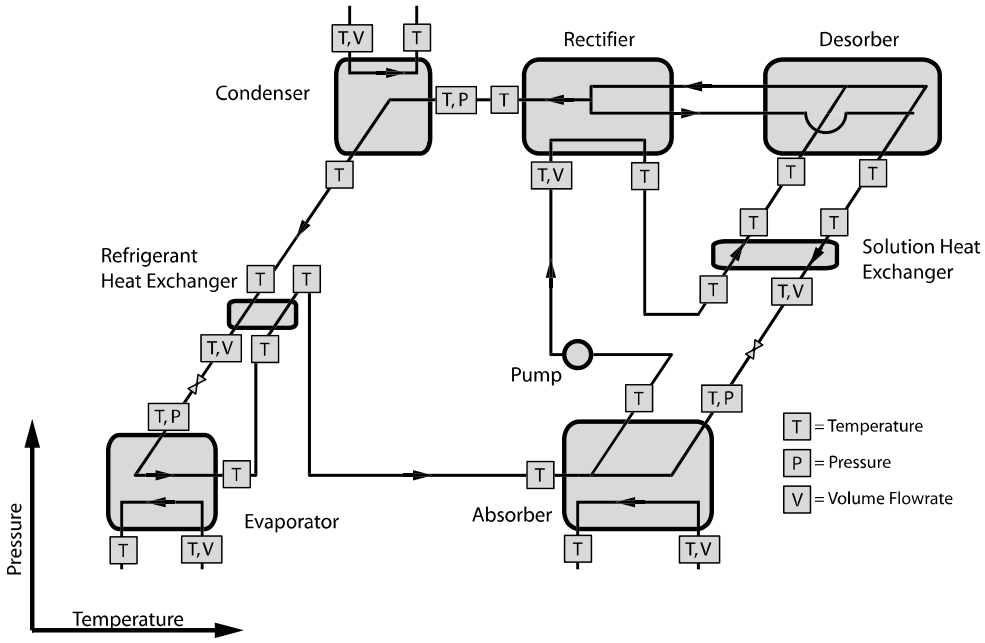

Figure 4-3 Microchannel System Schematic

A thermodynamic model for the system was developed by choosing a design point for the cycle with a heat sink temperature of 37°C and a thermal power input of 800 W. For the design point calculation, the concentrated solution mass flowrate was set to 2.7×10^{-3} kg/s and its ammonia mass fraction was assumed to be 0.37. The flow rates and concentration were based on the desired cooling capacity of 300 W and the ambient and heat source temperatures. Section 5.2 explains the relationship between ambient temperature, heat source temperature, heat sink temperatures and cycle concentrations in more detail. The high and low side operating pressures were set at 1600 and 400 kPa, respectively. The concentrated solution flows through the desorber where a fraction of the solution evaporates. An energy balance on the desorber fixes the outlet enthalpy.

$$\dot{Q}_{Des,Sol} = \dot{m}_{cs} \cdot \left(h_{Des,Out} - h_{Des,In} \right) \tag{4.1}$$

The stream exits the desorber as a two-phase mixture and is then allowed to separate due to buoyancy. The outlet temperature and vapor quality are fixed by the pressure, concentration and enthalpy.

$$T_{Des,Out} = f\left(P_{Des}, x_{cs}, h_{Des,Out}\right) \tag{4.2}$$

$$q_{Des,Out} = f\left(P_{Des}, x_{cs}, h_{Des,Out}\right) \tag{4.3}$$

The desorber outlet temperature and quality for the design point are 128.2°C and 14.3% respectively. Using saturation assumptions, the ammonia concentration of the liquid and vapor were calculated.

$$x_{Des,Out,Vap} = f\left(T_{Des,Out}, P_{Des}, q = 1\right) \tag{4.4}$$

$$x_{Des,Out,Liq} = f\left(T_{Des,Out}, P_{Des}, q = 0\right) \tag{4.5}$$

The resulting liquid and vapor concentrations were 28.5% and 87.6%, respectively. A vapor concentration this low would cause severe temperature glide penalties in the evaporator. Figure 4-4 illustrates the effects of low refrigerant ammonia concentration on the evaporator temperature profile. For a representative cooling application at 5°C, a refrigerant stream with an ammonia concentration of 87.6% can only utilize a quality range of 0 – 0.4. A refrigerant stream with a concentration of 98.0% can utilize a quality range of 0 – 0.9. This exploitable quality range has a direct effect on evaporator cooling capacity and therefore system COP.

In order to ensure an adequately pure ammonia refrigerant stream, the vapor stream must be cooled in the rectifier to strip off extra water vapor. The design outlet

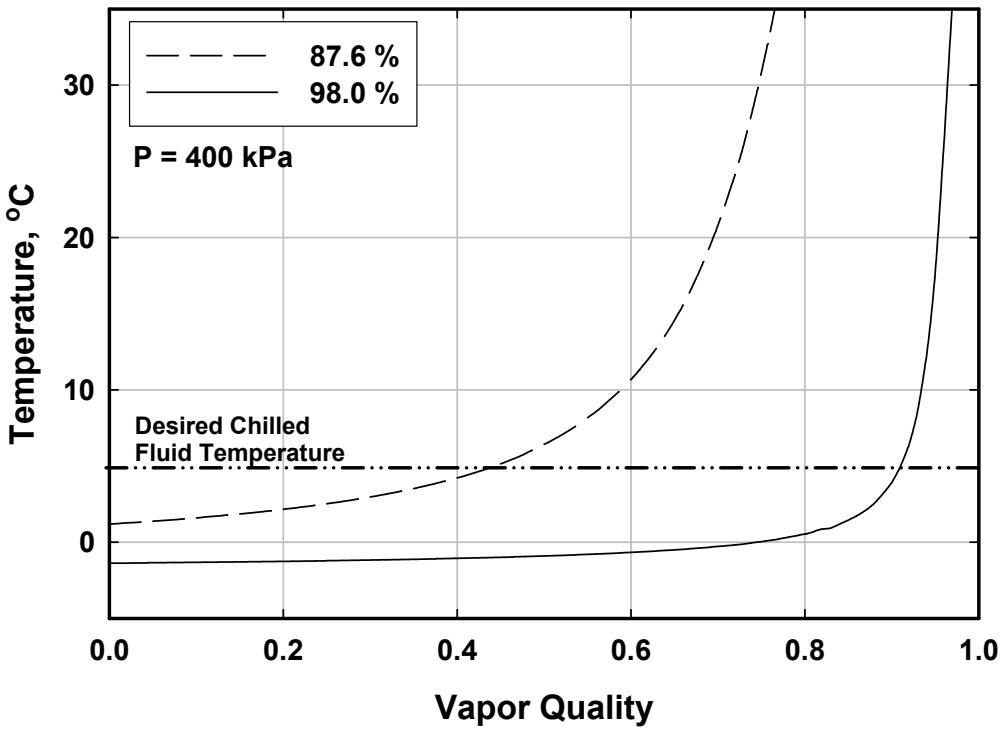

Figure 4-4 Refrigerant Concentration Effect on Evaporator Temperature Glide

temperature of the saturated vapor stream leaving the rectifier was set to be 85°C to provide an ammonia concentration of 98.4%.

The reflux liquid that is condensed out of the refrigerant stream in the rectifier flows back into the separation chamber where it mixes with the dilute solution before exiting the desorber. The reflux liquid is approximately a 50% mixture of ammonia and water. To maximize the refrigerant mass flowrate, the reflux is allowed to remain in contact with the vapor to raise its temperature. This will result in decreasing its ammonia content and adding to the vapor-phase refrigerant concentration and flowrate. The reflux re-entering the separation chamber was assumed to be in thermal equilibrium with the

refrigerant vapor entering the rectifier. An energy balance on the rectifier shows that a cooling load of 152 W is required.

$$\dot{Q}_{Rec} = \dot{m}_{Rec,ref,Out} \cdot h_{Rec,ref,Out} + \dot{m}_{Rec,reflux,Out} \cdot h_{Rec,reflux,Out} - \dot{m}_{Rec,vap,in} \cdot h_{Rec,vap,in} \tag{4.6}$$

To provide the required cooling, the concentrated solution stream leaving the solution pump was used as the cooling source for the rectifier. This solution is at a temperature of 50.8°C. An energy balance yields the outlet enthalpy of the concentrated solution.

$$h_{Rec,CS,Out} = h_{Rec,CS,In} - \frac{\dot{Q}_{Rec}}{\dot{m}_{CS}} \tag{4.7}$$

Combined with the concentration and pressure, this fixed the state point and yielded a solution outlet temperature of 63.6°C from the rectifier.

Mass and species balances on the rectifier yield the refrigerant and reflux mass flowrates.

$$\dot{m}_{Rect,In} = \dot{m}_{ref} + \dot{m}_{reflux} \tag{4.8}$$

$$\dot{m}_{Rect,In} \cdot x_{Rect,In} = \dot{m}_{ref} \cdot x_{ref} + \dot{m}_{reflux} \cdot x_{reflux} \tag{4.9}$$

The resulting refrigerant and reflux flowrates were 0.3×10^{-3} kg/s and 6.0×10^{-5} kg/s, respectively. The reflux mixes with the remaining liquid solution in the separation chamber in the bottom of the rectifier and exits towards the solution heat exchanger. Mass and species balances on this mixing process yield the dilute solution flowrate and concentration.

$$\dot{m}_{DS} = \dot{m}_{des,liq,out} + \dot{m}_{reflux} \tag{4.10}$$

$$\dot{m}_{DS} \cdot x_{DS} = \dot{m}_{des,liq,out} \cdot x_{des,liq,out} + \dot{m}_{reflux} \cdot x_{reflux} \tag{4.11}$$

The resulting dilute solution flowrate and concentration were 2.37×10^{-3} kg/s and 28.5%, respectively. The mass flowrates and the concentrations of all solution and refrigerant streams are now fixed. The refrigerant vapor leaving the rectifier flows to the condenser. The refrigerant outlet of the condenser was assumed to be 2°C sub-cooled. At the condensing pressure of 1600 kPa and the refrigerant concentration of 98.4%, this results in a temperature of 39.6°C. With the inlet and outlet states fixed, the condenser heat load was calculated.

$$\dot{Q}_{Cond} = \dot{m}_{ref} \cdot \left(h_{Cond,ref,Out} - h_{Cond,ref,In} \right) \tag{4.12}$$

Based on reject heat load and coolant temperature rise considerations, the condenser cooling water flowrate was set at 17.8×10^{-3} kg/s, and the inlet temperature was the design heat sink temperature of 37°C. An energy balance yields the condenser water outlet temperature of 42.6°C.

$$\dot{Q}_{Cond} = \dot{m}_{w,cond} \cdot c_{p,w} \left(T_{Cond,w,in} - T_{Cond,w,out} \right) \tag{4.13}$$

After leaving the condenser, the refrigerant flows through the refrigerant heat exchanger where it is further cooled by the refrigerant leaving the evaporator. The outlet temperature of the high pressure side of this heat exchanger was set to 30.2°C. The corresponding heat load was found to be 15 W.

$$\dot{Q}_{RHX} = \dot{m}_{ref} \left(h_{RHX,high,In} - h_{RHX,high,Out} \right) \tag{4.14}$$

The expansion of the refrigerant through the expansion valve is assumed to be isenthalpic.

$$h_{Evap,ref,in} = h_{RHX,high,Out} \tag{4.15}$$

This resulted in an evaporator inlet temperature of -1.4°C. The evaporator outlet temperature was fixed at 8.6°C. The heat load of the evaporator was then calculated.

$$\dot{Q}_{Evap} = \dot{m}_{ref}\left(h_{Evap,ref,Out} - h_{Evap,ref,In}\right) \tag{4.16}$$

With the evaporator heat load of 354 W, a chilled water flowrate of 24×10^{-3} kg/s was set to maintain a sufficient temperature drop in the chilled water. The chilled water inlet temperature was specified as 9°C, and the chilled water outlet enthalpy, and thus temperature was calculated from an energy balance.

$$\dot{Q}_{Evap} = \dot{m}_{w,Evap}\left(h_{Evap,w,out} - h_{Evap,w,in}\right) \tag{4.17}$$

With the evaporator refrigerant outlet state fixed and the refrigerant heat exchanger load calculated from equation (4.14) the state of the low pressure outlet of this heat exchanger could be determined from an energy balance.

$$\dot{Q}_{RHX} = \dot{m}_{ref}\left(h_{RHX,low,Out} - h_{RHX,low,In}\right) \tag{4.18}$$

The low pressure refrigerant leaving the refrigerant heat exchanger was at 18°C. This state point is also the absorber refrigerant inlet condition. Once the state points in the refrigerant loop had been fixed, the remaining state points in the solution circuit could be determined.

The concentrated solution inlet to the solution heat exchanger was determined by the outlet of the rectifier, which was found to be 63.6°C. The concentrated solution outlet of the solution heat exchanger is assumed to have a temperature of 109°C. This

fixes the outlet state of the solution heat exchanger as well as its heat load. An energy balance yields the dilute solution outlet state of the solution heat exchanger.

$$h_{SHX,DS,Out} = \frac{\dot{m}_{CS}}{\dot{m}_{DS}}\left(h_{SHX,CS,In} - h_{SHX,CS,Out}\right) + h_{SHX,DS,in} \tag{4.19}$$

The resulting dilute solution outlet temperature was 75.7°C. The solution expansion valve is assumed to be isenthalpic.

$$h_{SHX,DS,Out} = h_{Abs,DS,In} \tag{4.20}$$

The inlet conditions to the absorber are thus fixed and the outlet was assumed to be 4.8°C sub-cooled. The absorber heat load was then calculated.

$$\dot{Q}_{Abs} = \dot{m}_{Ref} \cdot h_{Abs,Ref,In} + \dot{m}_{DS} \cdot h_{Abs,DS,In} - \dot{m}_{CS} \cdot h_{Abs,CS,Out} \tag{4.21}$$

The resulting absorber heat load for the design point was 748 W.

The state points obtained from these design calculations are listed in Table B-3 in Appendix B. Once the state points were fixed, the heat transfer rates of each component were also fixed. In order to calculate the required heat exchanger size, the UA-LMTD method was used.

$$\dot{Q} = UA \cdot LMTD \tag{4.22}$$

The UA LMTD method is valid for heat exchangers where the heat capacity rates, $\dot{m} \cdot c_p$, of the two fluid streams are constant along the length of the heat exchanger. While this is not strictly valid for the ammonia/water streams in these heat exchangers, the method can still be used to provide useful results. The heat transfer rate, LMTD and UA of each component in the design point calculation are listed in Table 4-1. The next step in the

design process was to determine the geometry for each heat exchanger that meets the required UA values from the cycle analysis and also could be fabricated with the manufacturing techniques discussed above.

Table 4-1 Component Design Point Calculation Results

Component	Q, W	UA, W/K	LMTD, K
Absorber	748	38	19.7
Condenser	414	29	14.3
SHX	562	37	15.3
RHX	15	0.7	21.6
Evaporator	354	160	2.21
Rectifier	152	3.2	47.8

4.3 Component Design Calculations

The required size (overall heat transfer conductance, UA) of each component was determined from the cycle model. The specific fluid channel configuration of the components was determined by estimating the overall heat transfer resistance of each individual component. For this first prototype device, mass transfer resistances were not included in the analysis. A diagram of the cross section of a typical microchannel heat exchanger that can be fabricated with the photochemical etching and diffusion bonding process is shown in Figure 4-5

The hot and cold fluids flow through the channels on alternating shims, in a counter flow arrangement. The analysis of each heat exchanger begins by considering the section outlined in Figure 4-5 and shown in detail in Figure 4-6.

The wet chemical etching process creates rounded rectangular channels. During the etching process, the etchant acts laterally as well as vertically, removing material

under the edge of the cured photoresist, creating rounded features as shown in Figure 4-5 and Figure 4-6.

The heat exchanger can be modeled as two sets of fin arrays, each extending into separate flows, and separated by a solid wall. However, the fin arrays are of different shape. The fin arrays represent a thermal resistance that is modeled as:

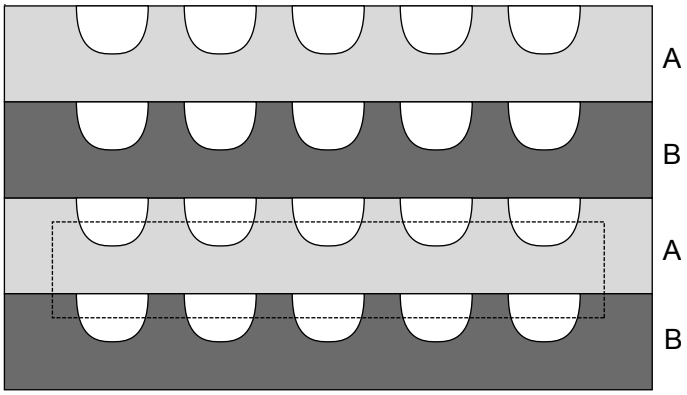

Figure 4-5 Illustration of Typical Heat Exchanger Cross Section

Figure 4-6 Illustration of Channel Extended Surface Detail

$$R_{\text{Fin Array}} = \frac{1}{\eta_T \cdot \alpha \cdot A_T} \tag{4.23}$$

Where A_T is the total heat transfer area of the fin array, α is the heat transfer coefficient of the fluid, and η_T is the overall surface efficiency of the fin array.

$$\eta_T = 1 - \frac{N \cdot A_f}{A_T}\left(1 - \eta_f\right) \tag{4.24}$$

The fin shapes produced by this manufacturing process are not standard profiles for extended surface heat exchangers. However, as a conservative approximation, a straight fin with a uniform cross section and an adiabatic tip condition is used here for the calculation of fin efficiency. The individual fin efficiency, η_f, is given by (Incropera and DeWitt, 2002):

$$\eta_f = \frac{\tanh(m \cdot L_{fin})}{m \cdot L_{fin}} \tag{4.25}$$

where L is the length of the fin (half the channel height), and m is defined below.

$$m = \sqrt{\frac{\alpha \cdot 2}{k \cdot t_{fin}}} \tag{4.26}$$

Here, k is the thermal conductivity of the fin, and t_{fin} is the thickness of the fin. For the combination of fin geometry and heat transfer coefficients of interest in this study, it can be shown that the fin efficiency approaches a value of 1 for all components. Figure 4-7 shows the variation of fin efficiency with heat transfer coefficient for a stainless steel rectangular fin with a thickness of 500 μm and a length of 127 μm. This thickness represents the thinnest portion of the fins used in this study. Use of a larger fin width will result in even greater fin efficiencies. For the range of heat transfer coefficients

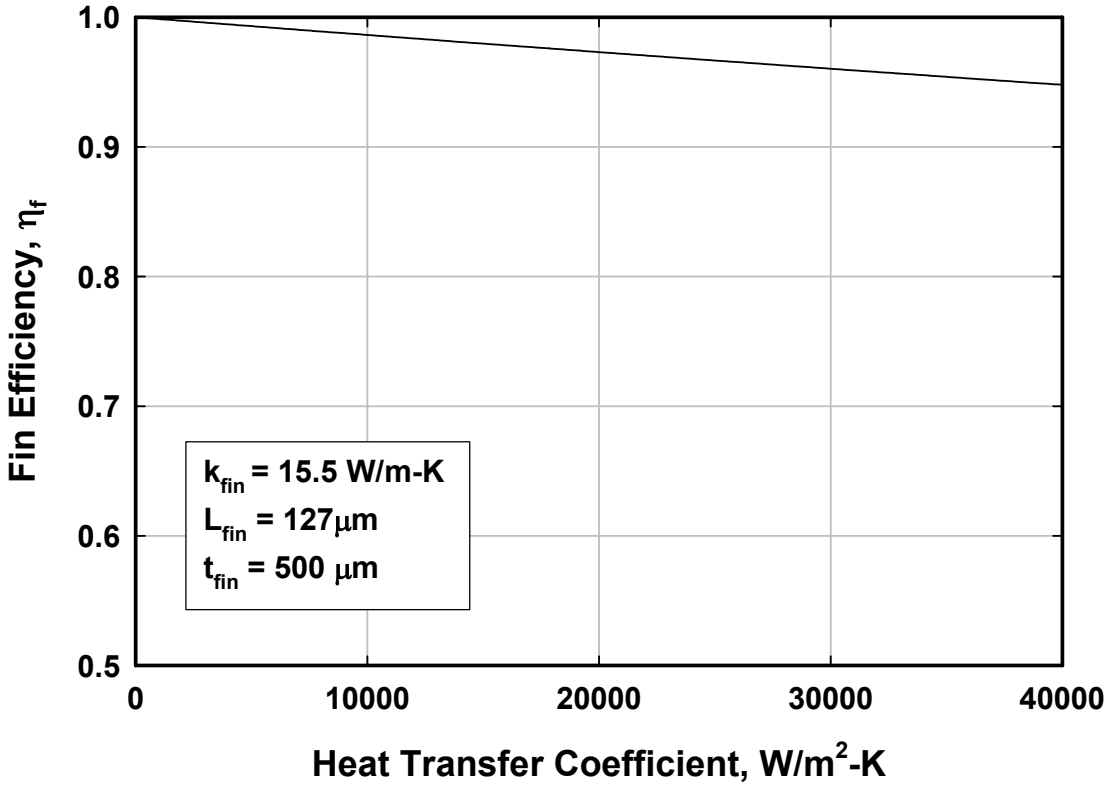

Figure 4-7 Fin Efficiency Estimates for Expected Operating Envelope

encountered in this design process (380 - 38,000 W/m^2-K), the fin efficiencies approach unity and the entire area of the channel walls can be treated as prime surface.

This procedure was used to calculate the thermal resistance of the fin arrays in the hot and cold fluids, $R_{\text{Fin Array, H}}$, and $R_{\text{Fin Array, C}}$. The heat transfer coefficient for each of the streams was determined from applicable correlations.

The thermal resistance of the wall was determined by:

$$R_{\text{wall}} = \frac{t_{wall}}{k_{\text{wall}} \cdot w \cdot L_{\text{flow}}} \tag{4.27}$$

Here, t_{wall} is the thickness of the wall, k_{wall} is the thermal conductivity of the heat exchanger material, w is the width of the fin arrays in contact with each other for the entire heat exchanger, and L_{flow} is the length of the heat exchanger in the flow direction. The overall thermal resistance was then calculated as:

$$R_T = R_{\text{Fin Array, H}} + R_{\text{wall}} + R_{\text{Fin Array, C}} \tag{4.28}$$

The UA value of the heat exchanger was then calculated.

$$UA = \frac{1}{R_T} \tag{4.29}$$

The log mean temperature difference for a counter flow heat exchanger is:

$$LMTD = \frac{\left(T_{H,in} - T_{C,out}\right) - \left(T_{H,out} - T_{C,in}\right)}{\text{Ln}\left[\frac{\left(T_{H,in} - T_{C,out}\right)}{\left(T_{H,out} - T_{C,in}\right)}\right]} \tag{4.30}$$

The required heat transfer rate, log mean temperature difference, and UA value were determined from the cycle analysis. This leaves the channel width, channel length, and number of channels as design variables. This procedure was used to design the absorber, condenser, solution heat exchanger, refrigerant heat exchanger, and evaporator. In order to simplify the design procedure for this prototype, a single channel size was used for all of these components. A shim thickness of 0.5 mm (0.02 in) was chosen based on availability and for the range of channel sizes that could be fabricated on it. With a channel etch depth of half the shim thickness and a channel width of 0.5 mm, the nominal channel hydraulic diameter for this prototype is 306 μm, with a channel horizontal transverse pitch of 1 mm and vertical pitch of 0.5 mm. These dimensions are shown on Figure 4-8.

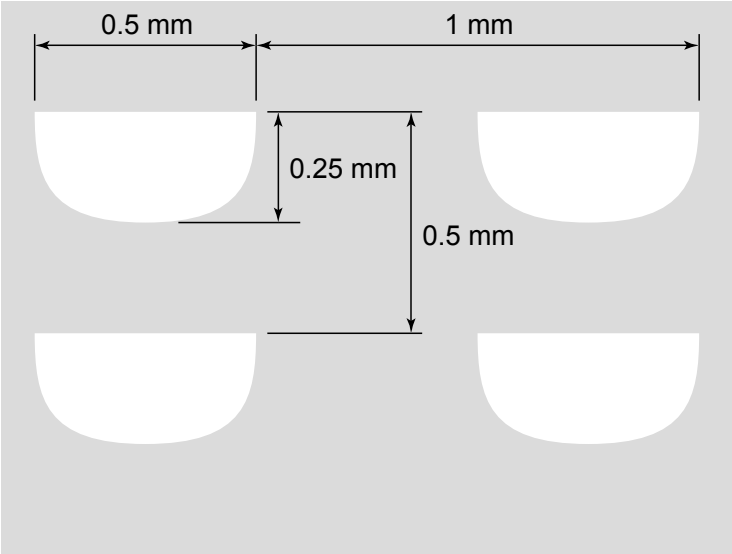

Figure 4-8 Illustration of Heat Exchanger Cross-Section with Nominal Channel Dimensions

4.3.1 Absorber

The absorber design inlet and outlet conditions are listed in Table 4-2 The cooling water is a single-phase laminar flow (Re = 390). The heat transfer coefficient and friction factor are estimated using the correlations reported in (Kakac *et al.*, 1987) for flow in a circular sector duct with a cross section that sweeps an angle of 2φ.

$$\frac{\alpha \cdot D_h}{k} = 2.0705 \cdot \left(1 + 2.2916 \cdot \varphi - 2.5682 \cdot \varphi^2 + 1.4815 \cdot \varphi^3 - 0.3338 \cdot \varphi^4\right) \qquad (4.31)$$

Table 4-2 Absorber Design Conditions

	Solution	Refrigerant	Cooling water
Mass flowrate	2.37×10^{-3} kg/s (Inlet)	0.33×10^{-3} kg/s	20.89×10^{-3} kg/s
Pressure	400 kPa	400 kPa	101 kPa
Inlet Temperature	73.2°C	18.0°C	37.0°C
Outlet Temperature	50.4°C		45.6°C
Q	748 W		
LMTD	19.7°C		
$UA_{required}$	38 W/K		

$$f \cdot \mathrm{Re} = = 48 \cdot \left(1 + 0.5059 \cdot \varphi - 0.3948 \cdot \varphi^2 + 0.1875 \cdot \varphi^3 - 0.0385 \cdot \varphi^4\right) \tag{4.32}$$

The ammonia/water solution enters the absorber as a two-phase flow with a vapor quality of 0.1 and leaves as a sub-cooled liquid. The correlation from Shah (1979) for condensation in tubes is used to estimate the two-phase heat transfer coefficient.

$$\alpha_{tp} = \alpha_{lo}\left[\left(1-q\right)^{0.8} + \frac{3.8x^{0.76}\cdot\left(1-q\right)^{0.04}}{P_r^{0.38}}\right] \tag{4.33}$$

$$\alpha_{lo} = 0.023\,\mathrm{Re}_{lo}^{0.8}\,\mathrm{Pr}_l^{0.4} \times \frac{k_l}{D_h} \tag{4.34}$$

This correlation was originally developed for larger diameter tubes and for single component fluids. Therefore, its application to a two-component fluid flowing through small hydraulic diameter channels represents only an approximation. However, for an initial design exercise for this prototype, this correlation is deemed sufficient. Using these heat transfer coefficient estimates and the procedure outlined in section 4.3, the number and the length of the channels was determined. The pressure drop was estimated using the procedure of Mishima and Hibiki (1996).

$$\left(\frac{dP}{dz}\right)_{tp} = \phi_l^2 \cdot \left(\frac{dP}{dz}\right)_l \tag{4.35}$$

The two phase multiplier is given by:

$$\phi_l^2 = 1 + \frac{C}{X} + \frac{1}{X^2} \tag{4.36}$$

Where X is the Martinelli parameter:

$$X = \left[\frac{(dP/dz)_l}{(dP/dz)_v} \right]^{1/2} \tag{4.37}$$

And the C parameter depends on the size of the channel:

$$C = 21\left(1 - e^{-319 \cdot D_h}\right) \tag{4.38}$$

The results of the absorber design calculations are outlined in Table 4-3.

Table 4-3 Absorber Design Calculation Results

	Solution	Cooling water
Channels per Shim	12	12
$L_{channel}$	50 mm	50 mm
G	115 kg/m^2-s	887 kg/m^2-s
α	10,100 W/m^2-K	8400 W/m^2-K
$R_{fin\ Array}$	6.4 K/kW	7.7 K/kW
R_{wall}	0.7 K/kW	
UA	67 W/K	
ΔP	6.5 kPa	11 kPa

Pictures of the absorber shims are shown in the following figures. Figure 4-9 shows shim A while Figure 4-10 shows shim B. The dilute solution enters the device in header A and the refrigerant vapor enters at header C. The refrigerant vapor initially flows on a channel on shim B until it is introduced into each individual channel on shim A via the vapor injection holes. This is done to help ensure a more even distribution of vapor among the channels. After the vapor and solution are combined, they flow together through the channels on shim A to header B where the concentrated solution is removed. The cooling water for the absorber enters at header D and flows through the channels on shim B, counter-current to the solution, and exits the device from header E.

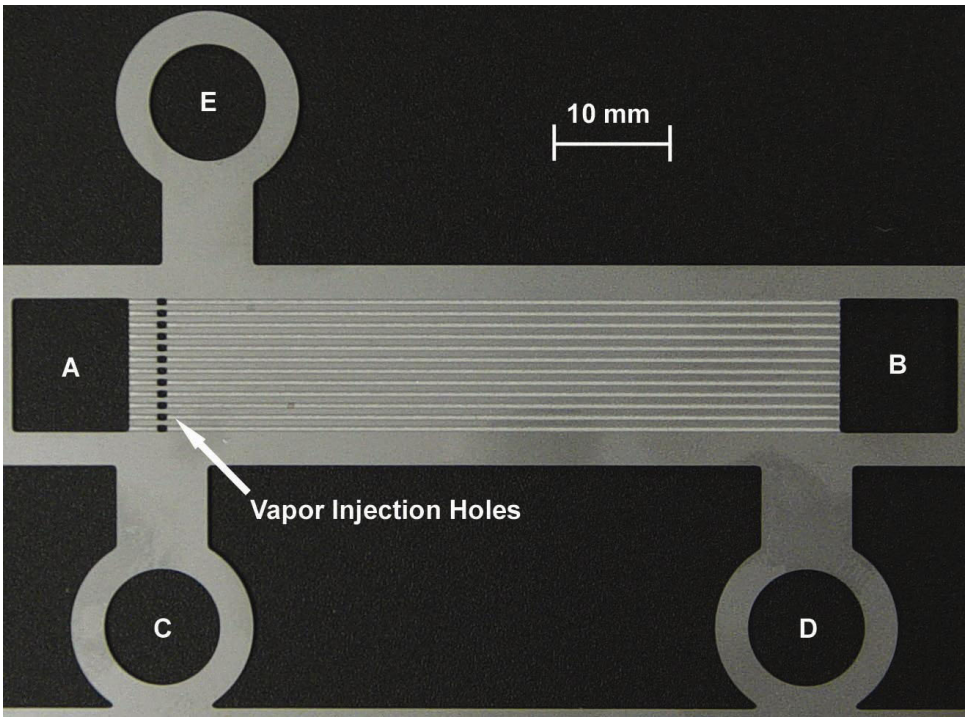

Figure 4-9 Absorber Photograph, Shim A

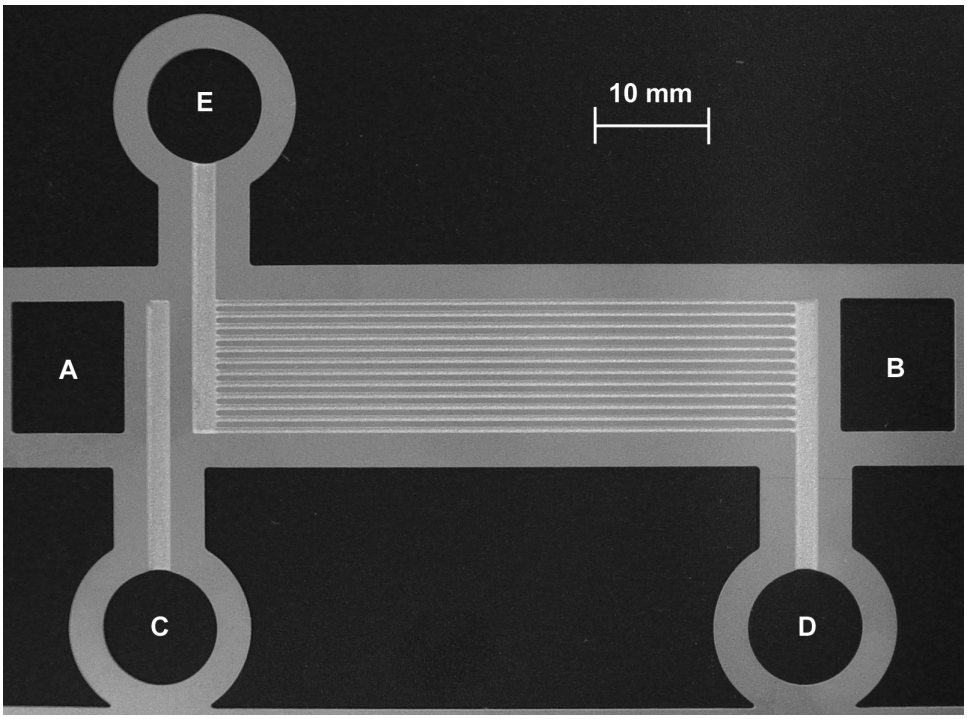

Figure 4-10 Absorber Photograph, Shim B

4.3.2 Condenser

The condenser design inlet and outlet conditions are listed in Table 4-4.

Table 4-4 Condenser Design Conditions

	Refrigerant	Cooling water
Mass flowrate	0.33×10^{-3} kg/s	17.8×10^{-3} kg/s
Pressure	1600 kPa	101 kPa
Inlet Temperature	85°C	37.0°C
Outlet Temperature	39.61°C	42.6°C
Q	414 W	
LMTD	14.3°C	
$UA_{required}$	29 W/K	

The cooling water flow is single-phase and laminar (Re = 500). The mean heat transfer coefficient and pressure drop estimates for the cooling water are calculated using equations (4.31) and (4.32) respectively. The refrigerant side enters the condenser as a saturated vapor and leaves the condenser as a sub-cooled liquid. The mean heat transfer coefficient was estimated using the Shah (1979) correlation at a representative quality of 0.4 to account for the non-linear variation of vapor quality with condenser length. The total pressure drop was estimated by using the Mishima and Hibiki (1996) procedure to calculate the greatest pressure gradient in the heat exchanger and applying that to the total length. The results of the design calculations are outlined in Table 4-5.

Table 4-5 Condenser Design Calculation Results

	Refrigerant	Cooling water
Channels per Shim	8	8
$L_{channel}$	60 mm	60 mm
G	20.8 kg/m^2-s	1130 kg/m^2-s
α	3700 W/m^2-K	8400 W/m^2-K
$R_{fin\ Array}$	20.5 K/kW	9.7 K/kW
R_{wall}	0.88 K/kW	
UA	32W/K	
ΔP	0.6 kPa	17 kPa

Figure 4-11 shows shim A of the condenser while Figure 4-12 shows shim B. The refrigerant vapor enters in header A and flows through the channels on shim A to header B where it exits. The cooling fluid enters the device at header C and flows through the channels on shim B, counter-current to the refrigerant, until it exits the condenser from header D.

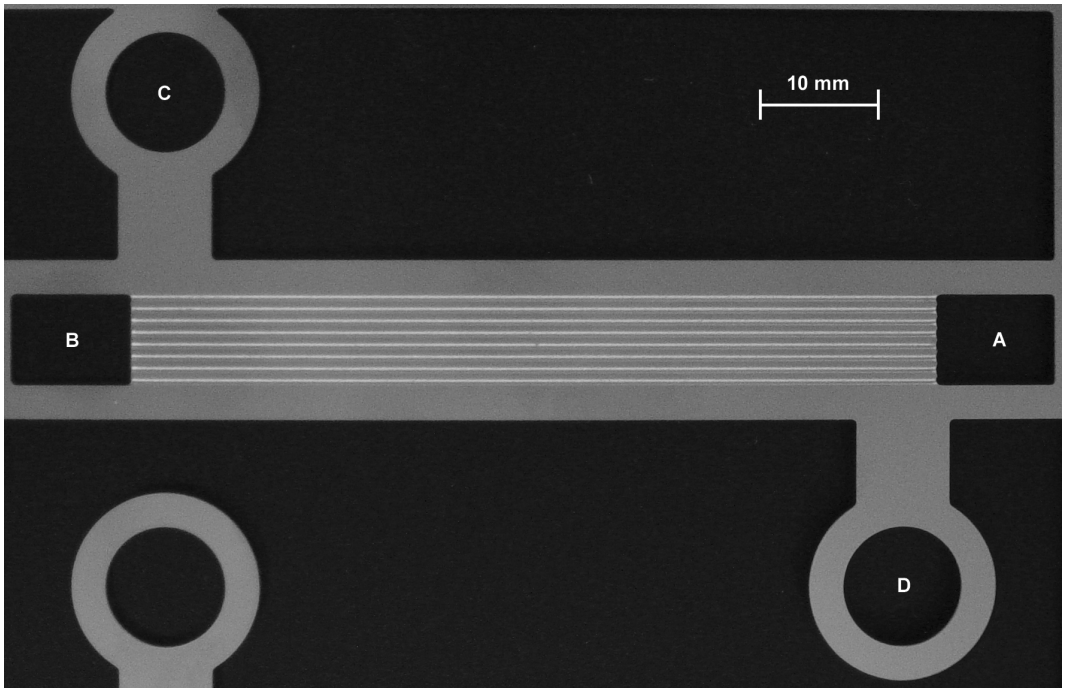

Figure 4-11 Condenser Photograph, Shim A

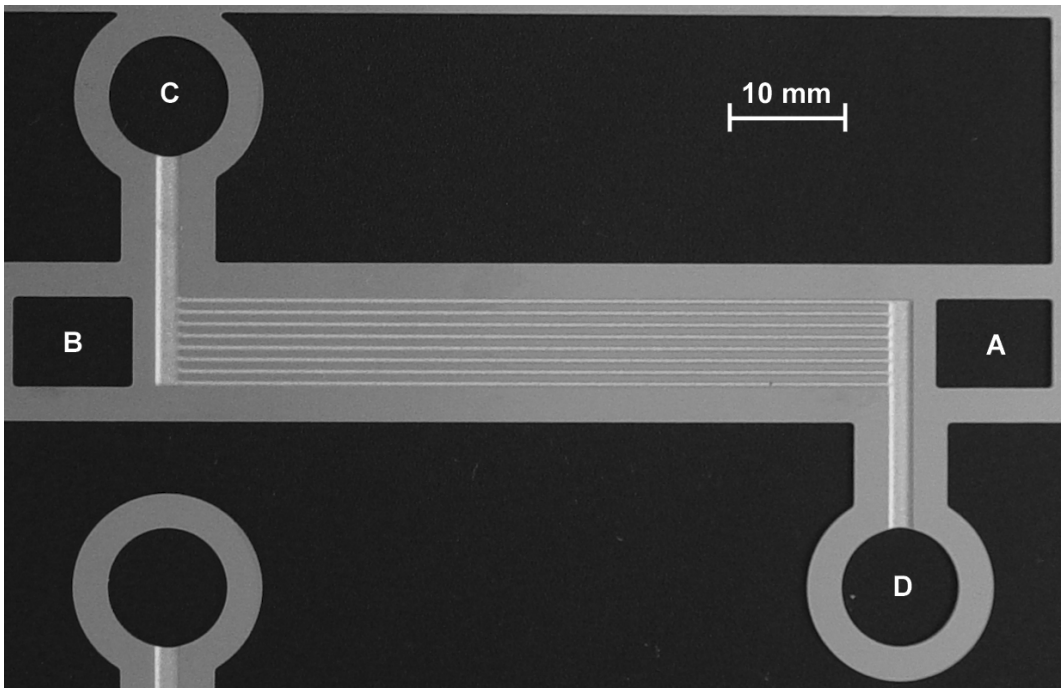

Figure 4-12 Condenser Photograph, Shim B

4.3.3 Solution Heat Exchanger

The solution heat exchanger design inlet and outlet conditions are listed in Table 4-6.

Table 4-6 Solution Heat Exchanger Design Conditions

	Concentrated Solution	Dilute Solution
Mass flowrate	2.7×10^{-3} kg/s	2.37×10^{-3} kg/s
Pressure	1600 kPa	1600 kPa
Inlet Temperature	63.7°C	128.2°C
Outlet Temperature	109°C	75.7°C
Q	562 W	
LMTD	15.3°C	
$UA_{required}$	37 W/K	

Both the concentrated and the dilute solution flows are single-phase and laminar (Re_{CS} = 119, Re_{DS} = 122). The mean heat transfer coefficient and the pressure drop estimates for both flows are calculated using equations (4.31) and (4.32). The results of the design calculations are outlined in Table 4-7.

Table 4-7 Solution Heat Exchanger Calculation Results

	Concentrated Solution	Dilute Solution
Channels per Shim	10	10
$L_{channel}$	40 mm	40 mm
G	137.5 kg/m^2-s	120.8 kg/m^2-s
α	7300 W/m^2-K	7600 W/m^2-K
$R_{fin\ Array}$	13.3 K/kW	12.8 K/kW
R_{wall}	1.1 K/kW	
UA	37 W/K	
ΔP	0.5 kPa	0.4 kPa

Pictures of the solution heat exchanger are shown in the following figures. Figure 4-13 shows shim A of the solution heat exchanger and Figure 4-14 shows shim B. The concentrated solution enters at header A and flows through the channels on shim A to header B. The dilute solution enters the device at header C and flows through the channels on shim B to header D where it exits.

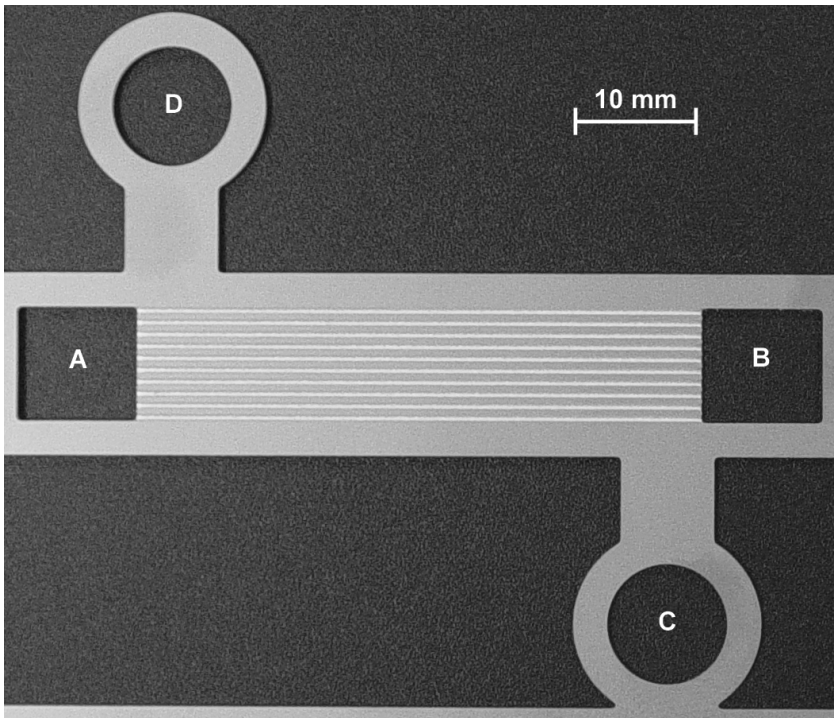

Figure 4-13 Solution Heat Exchanger Photograph, Shim A

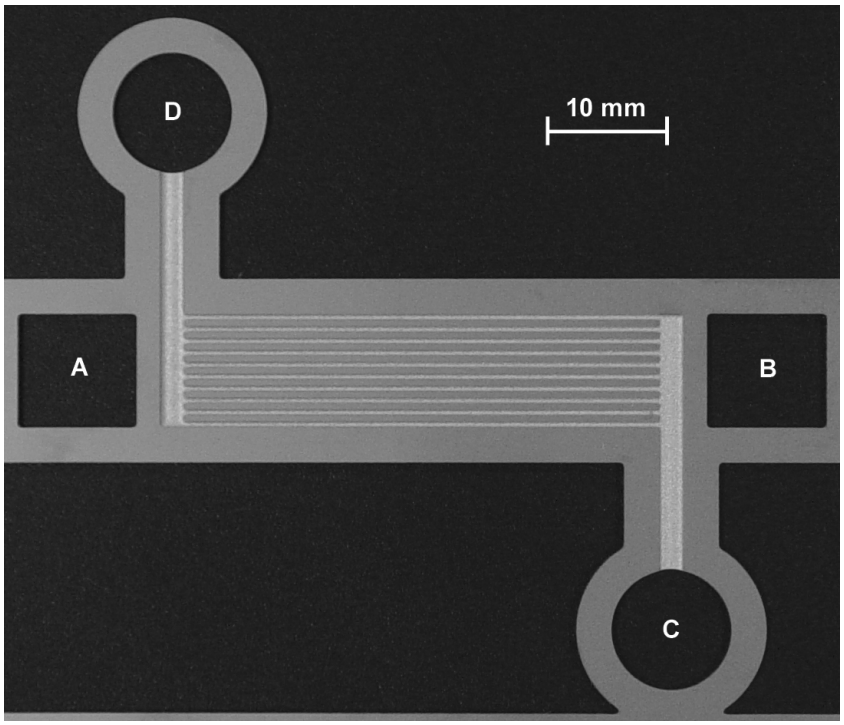

Figure 4-14 Solution Heat Exchanger Photograph, Shim B

4.3.4 Refrigerant Heat Exchanger

The refrigerant heat exchanger design inlet and outlet conditions are listed in Table 4-8. The high pressure side of the refrigerant heat exchanger is a sub-cooled liquid stream. The low pressure side is a very high quality, essentially fully vapor stream. Therefore both streams are treated as single-phase laminar flows (Re_{High} = 71, Re_{Low} = 1008) and the mean heat transfer coefficient and the pressure drop are calculated using equations (4.31) and (4.32). The results of the design calculations are outlined in Table 4-9.

Table 4-8 Refrigerant Heat Exchanger Design Conditions

	High Pressure	Low Pressure
Mass flowrate	0.33×10^{-3} kg/s	0.33×10^{-3} kg/s
Pressure	1600 kPa	400 kPa
Inlet Temperature	39.6°C	8.6°C
Outlet Temperature	30.2°C	18.0°C
Q	15 W	
LMTD	21.6°C	
$UA_{required}$	0.7 W/K	

Table 4-9 Refrigerant Heat Exchanger Calculation Results

	High Pressure	Low Pressure
Channels per Shim	5	5
$L_{channel}$	40 mm	40 mm
G	33.3 kg/m^2-s	33.3 kg/m^2-s
α	6100 W/m^2-K	380 W/m^2-K
$R_{fin\ Array}$	32 K/kW	515 K/kW
R_{wall}	2.1 K/kW	
UA	1.8 W/K	
ΔP	0.1 kPa	1.4 kPa

Figure 4-15 and Figure 4-16 show shim A and shim B of the refrigerant heat exchanger, respectively. The high pressure refrigerant enters the device at header A and flows through the channels on shim B to header B. The low pressure refrigerant enters at header C and flows through the channels on shim A until it reaches header D where it exits the device.

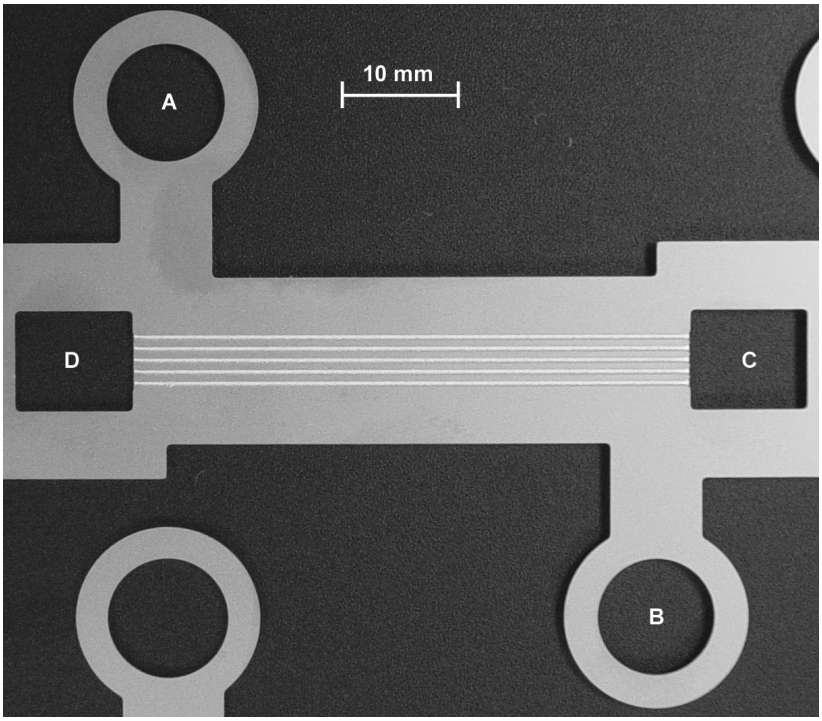

Figure 4-15 Refrigerant Heat Exchanger Photograph, Shim A

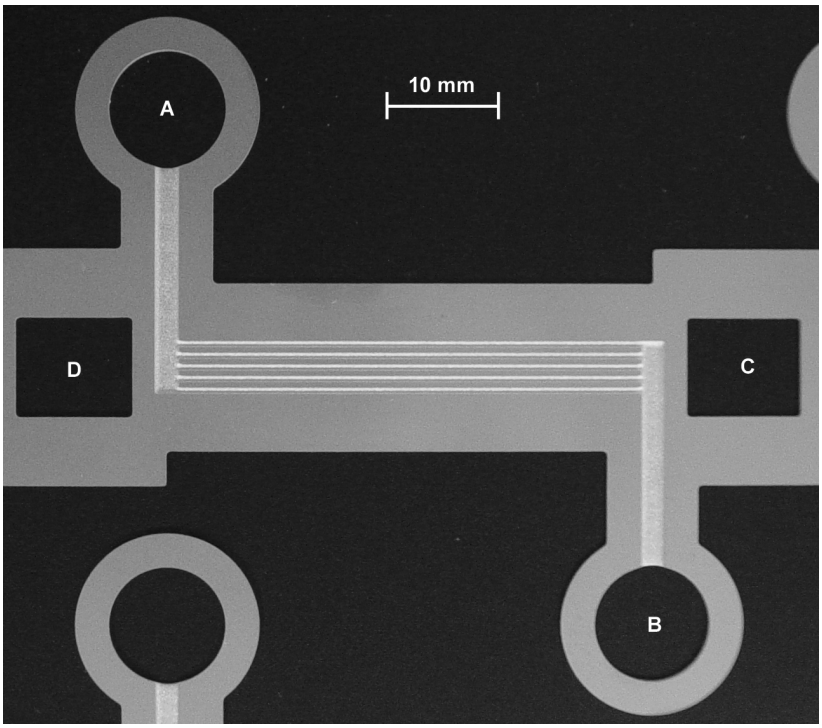

Figure 4-16 Refrigerant Heat Exchanger Photograph, Shim B

4.3.5 Evaporator

The evaporator design inlet and outlet conditions are listed in Table 4-10. The coupling fluid flowrate was chosen to maintain a sufficient temperature difference between the inlet and outlet to limit experimental uncertainty.

Table 4-10 Evaporator Design Conditions

	Refrigerant	Coupling Fluid
Mass flowrate	0.33×10^{-3} kg/s	24×10^{-3} kg/s
Pressure	400 kPa	101 kPa
Inlet Temperature	-1.4°C	9°C
Outlet Temperature	8.6°C	5.5°C
Q	354 W	
LMTD	2.2°C	
$UA_{required}$	160 W/K	

The coupling fluid is a single-phase, laminar flow (Re = 175). The mean heat transfer coefficient and the pressure drop are calculated using equations (4.31) and (4.32). The refrigerant stream enters the evaporator at a low quality, (0.12) and leaves at a high quality (0.94). The heat transfer coefficient is calculated using the correlation from Kandlikar *et al.* (2003; 2004). For deep laminar flows, ($Re_{LO} \leq 100$) such as those encountered in this evaporator, the heat transfer coefficient is calculated as:

$$\alpha_{TP} = 0.6683 \cdot \mathrm{Co}^{-0.2} \left(1-q\right)^{0.8} \cdot \alpha_{LO} + 1058.0 \cdot \mathrm{Bo}^{0.7} \left(1-q\right)^{0.8} \cdot F_{Fl} \cdot \alpha_{LO} \qquad (4.39)$$

where α_{LO} is the single-phase all-liquid heat transfer coefficient. The Convection number, Co is defined as:

$$\mathrm{Co} = \left[\frac{\left(1-q\right)}{q}\right]^{0.8} \left[\frac{\rho_v}{\rho_l}\right]^{0.5} \qquad (4.40)$$

The boiling number, Bo is defined as:

$$\mathrm{Bo} = \frac{q''}{G \cdot h_{LV}} \qquad (4.41)$$

Where q'' is the heat flux, G is the mass flux and h_{LV} is the latent heat of vaporization. For stainless steel, the fluid surface parameter, F_{Fl} has a value of 1. The mean heat transfer coefficient for the evaporating stream is calculated at a representative quality of 0.7 to account for the non-linear variation of vapor quality with evaporator length. The pressure drop was estimated using the procedure of Mishima and Hibiki (1996) at the location of the greatest pressure gradient and applying that gradient to the entire channel length to produce a conservative estimate of the required pressure drop. The results of the evaporator design calculations are outlined in Table 4-11.

Table 4-11 Evaporator Calculation Results

	Refrigerant	Coupling Fluid
Channels per Shim	15	15
$L_{channel}$	80 mm	80 mm
G	11.1 kg/m^2-s	815 kg/m^2-s
α	38000 W/m^2-K	7006 W/m^2-K
$R_{fin\ Array}$	0.8 K/kW	4.2 K/kW
R_{wall}	0.3 K/kW	
UA	185 W/K	
ΔP	1.2 kPa	32 kPa

Shim A of the evaporator is show in Figure 4-17 and shim B is shown in Figure 4-18. The refrigerant enters the evaporator at header A and flows through the channels on shim A. The refrigerant exits the evaporator at header B. The chilled fluid enters the evaporator at header C and flows through the channels on shim B until it reaches header D where it exits the device.

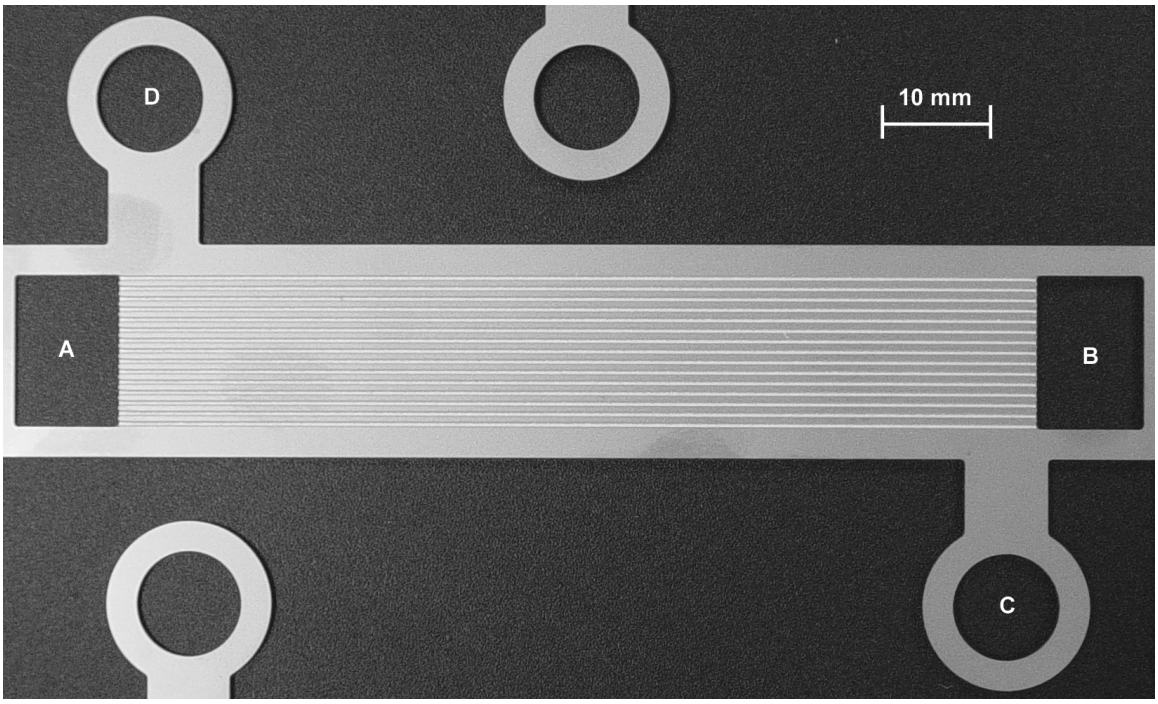

Figure 4-17 Evaporator Photograph, Shim A

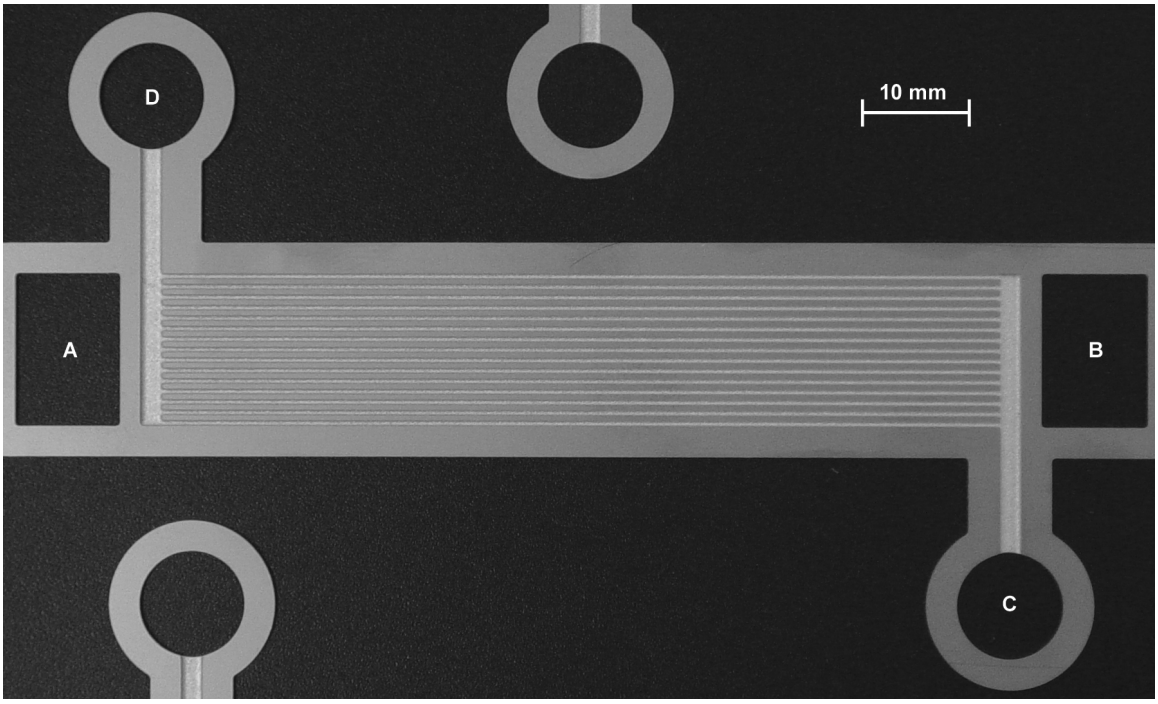

Figure 4-18 Evaporator Photograph, Shim B

4.3.6 Desorber

The solution inlet and outlet design conditions of the desorber are listed in Table 4-12.

Table 4-12 Desorber Design Conditions

	Solution
Mass flowrate	2.7×10^{-3} kg/s
Pressure	1600 kPa
Inlet Temperature	109°C
Outlet Temperature	128.2°C
Q	800 W
Outlet Vapor Quality	0.143

The solution enters the desorber as a saturated liquid and leaves as a low quality (~0.14) two phase mixture. The desorber is heated by eight 150 W electrical cartridge heaters for a maximum heat input of 1200 W. Each shim has 4 solution channels for a total of 160 channels. The channels are 55 mm in length, providing a heat transfer area of 11.3×10^{-3} m^2. At the design condition of 800 W desorber heat input rate, the average wall heat flux is 70.7 kW/m^2, and at the maximum heat input rate of 1200 W, the average wall heat flux is 106.1 kW/m^2. The critical heat flux for the desorber is estimated using the correlation for parallel mini/microchannels from (Qu and Mudawar, 2004).

$$\frac{q''_{cr}}{G\cdot h_{lv}} = 33.43\left(\frac{\rho_v}{\rho_l}\right)^{1.11} \mathrm{We}^{-0.21}\left(\frac{L}{d_e}\right)^{-0.36} \tag{4.42}$$

Where the L is the length of the channels, the Weber number, We is defined as

$$\mathrm{We} = \frac{G^2 L}{\sigma \rho_f} \tag{4.43}$$

and d_e is the heated equivalent diameter of the channels.

$$d_e = \frac{4A_{ch}}{P_h} \tag{4.44}$$

The maximum design heat flux of the desorber is well below the estimated critical heat flux for the desorber of 3.1 MW/m^2. The pressure drop is estimated using the procedure of Mishima and Hibiki (1996) at the location of the greatest pressure gradient. The results of the desorber design calculations are outlined in Table 4-13.

The geometry of the desorber, shown in Figure 4-19, is the same on both shim A and shim B. The concentrated solution enters the desorber at header A and flows through the channels on both shim A and shim B until it enters header B, which is also the inlet to the rectifier. The electrical resistance heaters are inserted in the 8 circular holes and provide the required heat input. Two insulating cavities reduce the conduction of heat into header A to prevent vapor generation in the header which could cause uneven distribution of the fluid among the channels.

Table 4-13 Desorber Calculation Results

	Solution
Channels per Shim	4
$L_{channel}$	55 mm
G	171.9 kg/m^2-s
q''_{design}	70.7 kW/m^2
q''_{max}	106.1 kW/m^2
q''_{cr}	3.1 MW/m^2
ΔP	3.5 kPa

Figure 4-19 Desorber Photograph

4.3.7 Rectifier

The rectifier acts like a distillation column to purify the ammonia refrigerant stream leaving the desorber by condensing a portion of the flow. The vapor phase of the

solution stream leaving the desorber has an ammonia concentration of 88%. This low concentration of ammonia would cause large temperature glide penalties in the evaporator as previously shown in Figure 4-4. In order to increase system efficiency, the refrigerant stream must have an ammonia concentration approaching 100%. To enhance internal heat recuperation in the system, the concentrated solution stream leaving the solution pump is used to provide the cooling in the rectifier. The design inlet and outlet conditions of the rectifier are listed in Table 4-14.

Table 4-14 Rectifier Design Conditions

	Vapor	Reflux	Concentrated Solution
Mass flowrate, in	0.387×10^{-3} kg/s		2.7×10^{-3} kg/s
Mass flowrate, out	0.327×10^{-3} kg/s	60.0×10^{-6} kg/s	2.7×10^{-3} kg/s
Pressure	1600 kPa	1600 kPa	1600 kPa
x, inlet	0.88		0.37
x, outlet	0.98	0.29	0.37
Inlet Temperature	128.2°C		50.8°C
Outlet Temperature	85°C	128.2°C	63.6°C
Q	152 W		
LMTD	47.7°C		
$UA_{required}$	3.2W/K		

With a design pressure of 1600 kPa, the concentration of the saturated vapor refrigerant stream leaving the rectifier is fixed at 0.98 by choosing an outlet temperature of 85°C. The liquid reflux and the vapor stream are assumed to be in thermal equilibrium so the temperature of the reflux leaving the rectifier is equal to the temperature of the vapor entering the rectifier. In order to facilitate the approach to this equilibrium, 4 trays are included in the rectifier to hold the liquid reflux so that it can have adequate time to interact with the vapor before returning to the desorber.

The heat transfer coefficient of the concentrated solution is calculated from the correlation reported by Kakac *et al.* (1987) for laminar flow (Re_{CS} = 212) in a channel of rectangular cross section with an aspect ratio of *a*.

$$\frac{\alpha \cdot D_h}{k} = 8.235 \times \left(\begin{array}{c} 1 - 2.0421 \times a + 3.0853 \times a^2 - 2.4765 \times a^3 \\ + 1.0578 \times a^4 - 0.1861 \times a^5 \end{array} \right) \tag{4.45}$$

The heat transfer coefficient on the refrigerant side is estimated using the laminar film condensation correlation from Sadasivan and Lienhard (1987).

$$\alpha = 0.943 \left[\frac{g \rho_l \left(\rho_l - \rho_v \right) k_l^3 h'_{fg}}{\mu_l \left(T_{sat} - T_s \right) L} \right]^{1/4} \tag{4.46}$$

Only the area of the single wall in thermal contact with the concentrated solution was used in this calculation. The heat and mass transfer area associated with the trays is not included in this calculation in order to produce a more conservative result. The additional area of the trays will further enhance the performance of this component. The results of the rectifier design calculations are given in Table 4-15.

Table 4-15 Rectifier Calculation Results

	Concentrated Solution	**Refrigerant Vapor**
Channels per Shim	1	NA
$L_{channel}$	38 mm	NA
G	300 kg/m^2-s	NA
α	5900 W/m^2-K	8000 W/m^2-K
$R_{Thermal}$	49.1 K/kW	157.8 K/kW
R_{wall}	86.61 K/kW	
UA	3.4 W/K	
ΔP	1.6 kPa	NA

The geometry of the rectifier, Figure 4-20 is the same on both shim A and shim B. The two-phase mixture of impure refrigerant vapor and dilute solution are present in header A after leaving the desorber channels. Buoyancy separates the vapor which flows upwards through the trays of the rectification column. Pure refrigerant vapor leaves the device at header B.

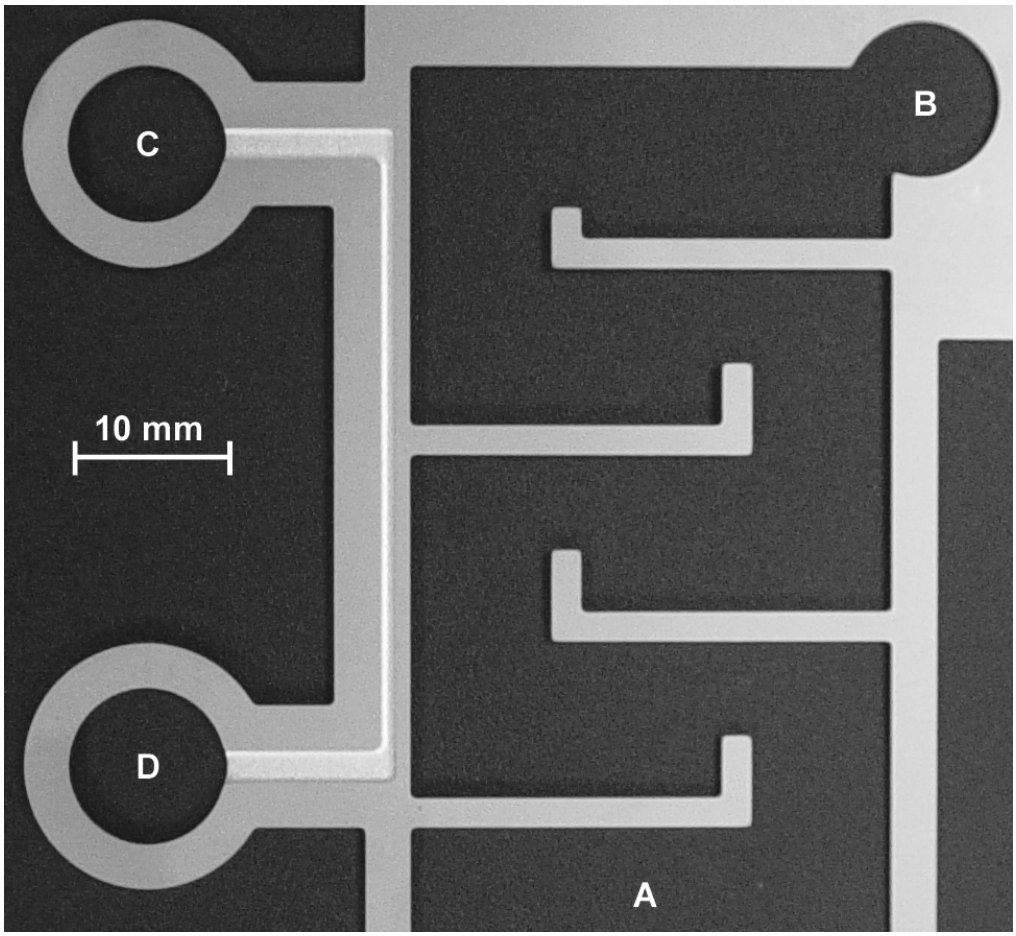

Figure 4-20 Rectifier Photograph

The reflux collects in the trays and flows back to header A where it mixes with the dilute solution. The dilute solution is removed from header A. The cooling is provided by the concentrated solution which has just left the solution pump entering at header C. The concentrated solution flows through the channels on both shim A and shim B to header D where it exits. Due to the limited number of concentrated solution fluid channels that could be brought into close contact with the rectification chamber, the fluid channels used in this component have a width of 1 mm to reduce the mass flux and thus pressure drop to an acceptable value.

4.4 Packaging and Bonding Considerations

Simultaneous design calculations of all of the components lead to a packaged system configuration with a total of 40 shims. Twenty of shim design A and twenty of shim design B are stacked in an alternating configuration. Figure 4-21 shows the component layout on shim A while Figure 4-22 shows the layout of the components on shim B for the fabricated microchannel system.

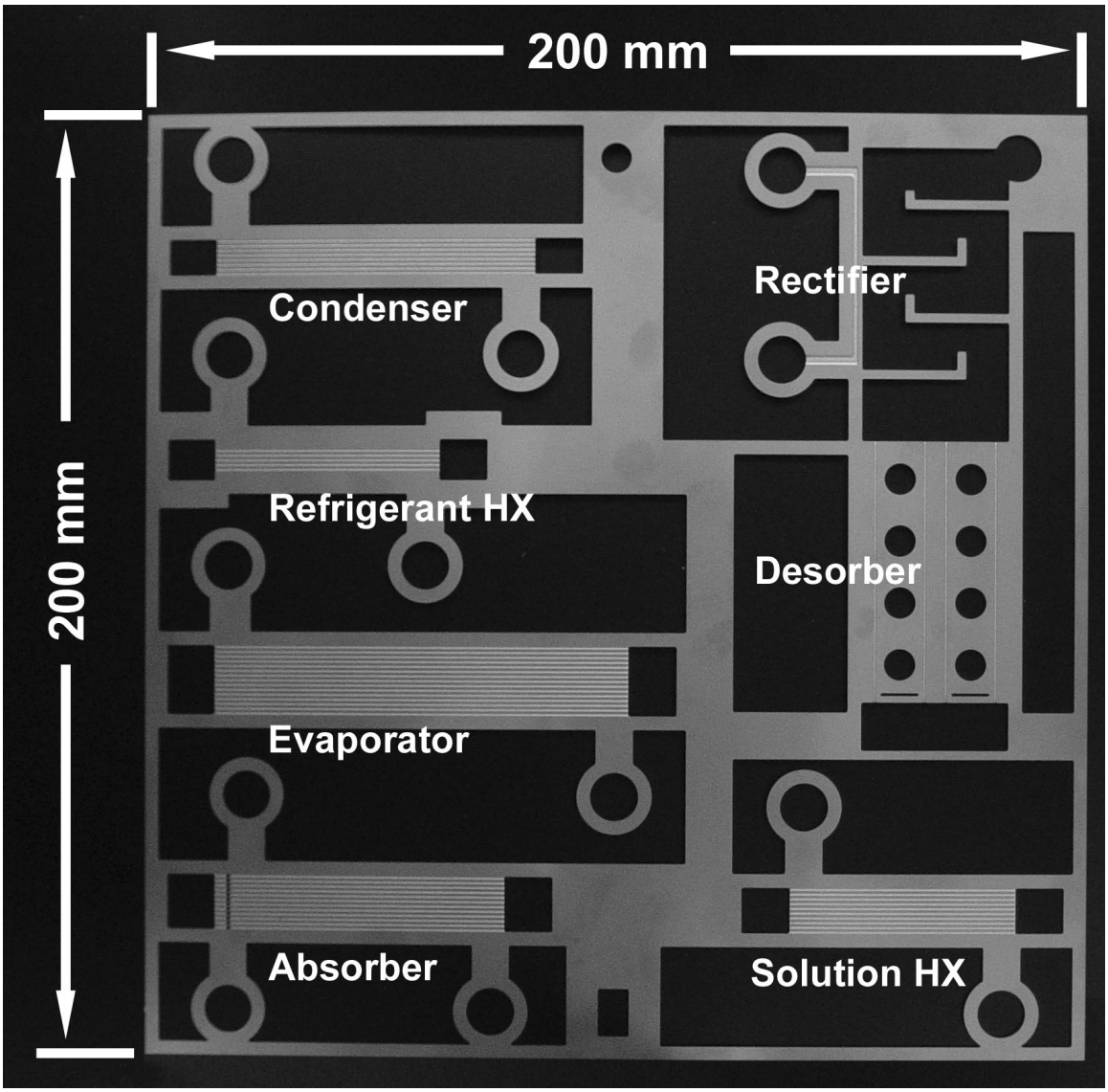

Figure 4-21 Photograph of Shim A

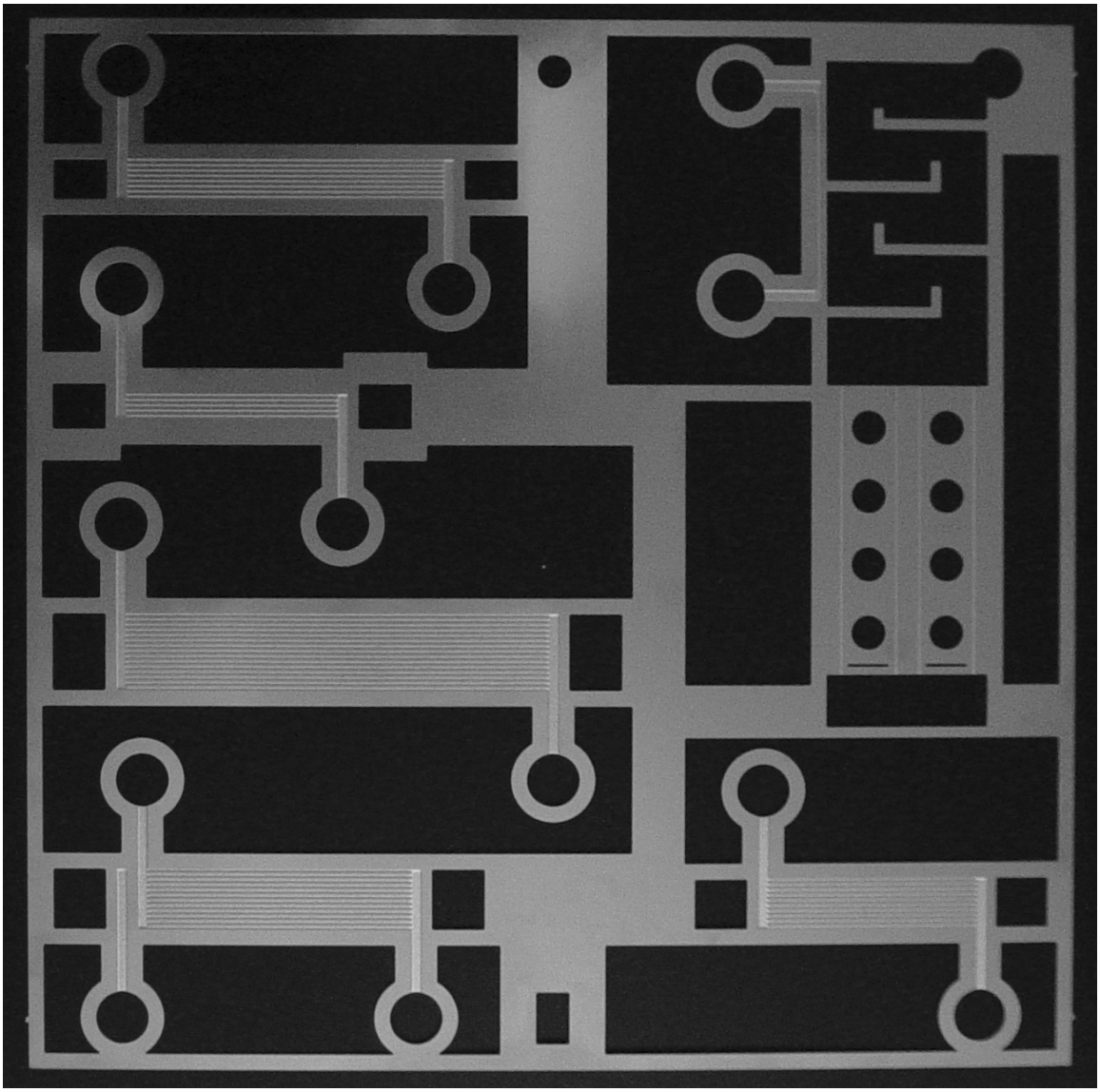

Figure 4-22 Photograph of Shim B

The headers for the fluids flowing on shim A are rectangular to ensure the flow length for each channel is identical in order to minimize flow maldistribution among the many parallel channels. For fluids flowing through the channels on shim B, the fluid inlet and outlet headers are on opposite sides of each device to minimize flow maldistribution.

As the fluid channels on shim B pass into the heat exchanger core through the necked region shown in Figure 4-23, they create an area where the bonding pressure will not be transmitted directly through the stacked shims during the diffusion bonding process. A similar area is present below the channels on shim A as they enter the heat exchanger core from the headers, but the fluid distribution channel on shim B is much wider than the individual channels, so it represent the critical bonding point.

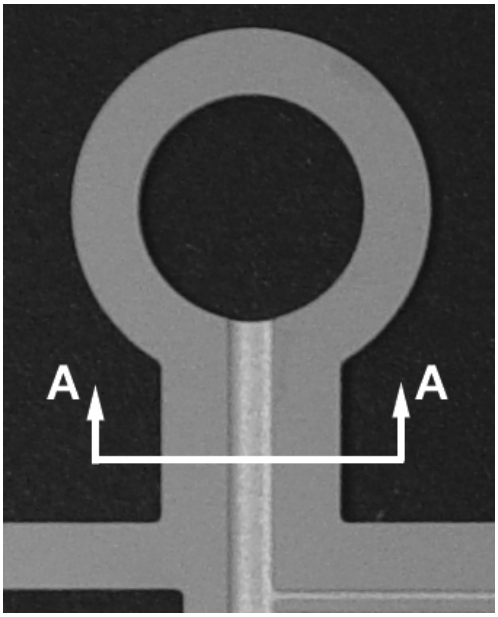

Figure 4-23 Photograph of Typical Header for Shim B Fluids

Figure 4-24 shows an illustration of cross section AA from Figure 4-23. The bonding pressure must be transmitted laterally underneath the channels on shims B to ensure a hermetic seal at the critical bonding point, labeled 1 in this figure. Paul *et al*. (2006) numerically and experimentally investigated the acceptable channel widths for which bonding would occur in stainless steel, diffusion bonded heat exchangers. For the shim thickness of interest in this study, (0.508 mm) they found that channel spans of up

to 3 mm would still create acceptable bonding conditions. The channel widths in this critical necked region were limited to 2 mm for this study to ensure bonding.

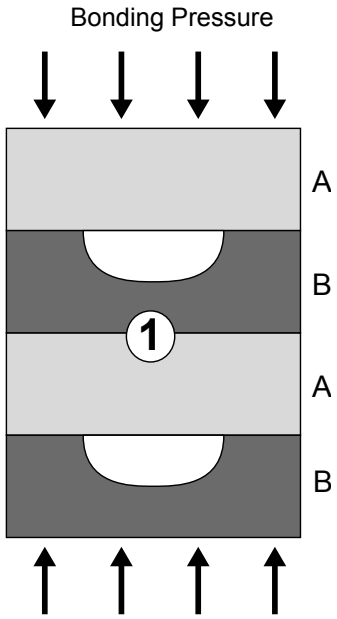

Figure 4-24 Cross Section A from Figure 4-23 Showing the Critical Bonding Point in Diffusion Bonded Heat Exchanger

In order to minimize the mass and volume of the packaged system, it is desirable to place the components closely together. The limiting factors in the spacing of the components are:

- the ability to make the required external fluid connections
- the extraneous conduction of heat between components
- maintaining sufficient structural supports to ensure the integrity of the shims during the manufacturing process.

The minimum acceptable center-to-center distance between adjacent fluid headers was determined by estimating the required space to make fluid connections. Based on this consideration, the minimum distance was chosen to be 20 mm. This distance ensures adequate space for the required fluid connection fittings as well as the tools required to install them.

The extraneous conduction of heat between the components was estimated by analyzing the microchannel system using the commercial Finite Element Analysis (FEA) code ANSYS (ANSYS, 2007). Analyzing this system requires a 3-Dimensional conduction analysis due to the heat conduction paths through the shims and as well as the end plates. The geometry was simplified for this analysis by removing the fluid channels in each component and the fluid connections in the end-plates. The shims are treated as plates without the fluid channels but with the insulating voids between components. The endplates are treated as solid plates. All of the shims as well as the end plates are

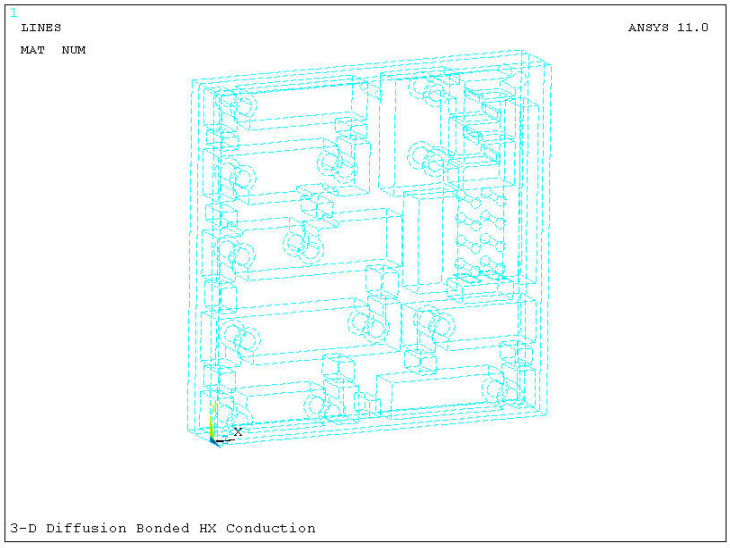

Figure 4-25 3-Dimensional Conduction Analysis Geometry

treated as a single solid volume. An illustration of the modeled geometry is shown in Figure 4-25.

For this 3-Dimensional conduction analysis, the system is modeled using a 3-D, thermal solid element (SOLID90) with the maximum element edge length of surface elements set to 5 mm. A tetrahedral element shape was chosen to enable free meshing of the solid. The resulting mesh is shown in Figure 4-26. Further refinement of the mesh resulted in negligible changes in the results.

Constant temperature boundary conditions were applied to areas in contact with the fluids, using the design temperatures for all of the components. The exterior surfaces as well as the interior areas of the evacuated voids were assigned zero heat flux boundary

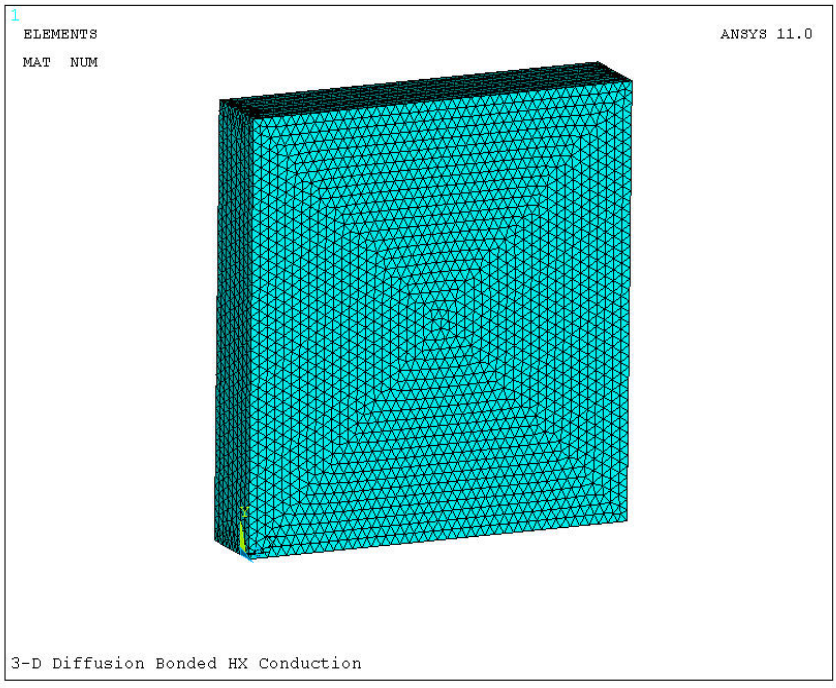

Figure 4-26 3-Dimensional Conduction Analysis Mesh Generated by ANSYS

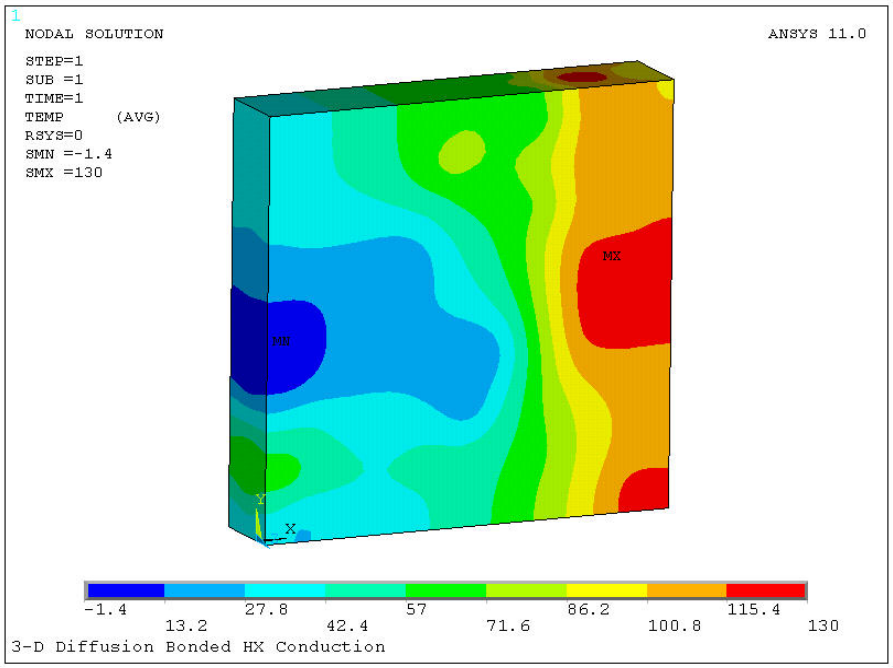

Figure 4-27 3-Dimensional Conduction Analysis Temperature Contours

conditions. Radiation effects were neglected in this analysis. Material properties in this model were assumed to be isotropic. Figure 4-27 shows the resulting temperature contours of the 3-dimensional, steady-state conduction analysis.

The maximum temperature occurs near the exit of the desorber while the minimum temperature is located at the inlet of the evaporator. Analysis of the heat flux at the section shown in Figure 4-28 indicated that a total of approximately 60 W will be conducted from the desorber, rectifier and solution heat exchanger to the other surrounding components at the design condition.

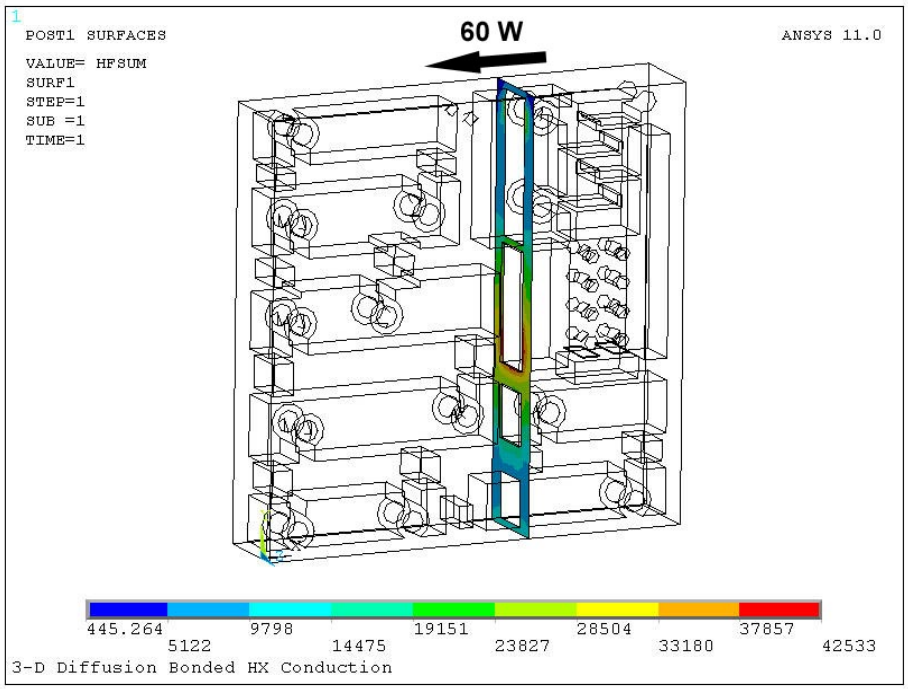

Figure 4-28 3-Dimensional Conduction Analysis Section Heat Flux

The amount of energy conducted between components could be reduced further by decreasing the size of the interconnections, spacing the components further apart or reducing the thickness of the endplates. The interconnections, however, are required to insure the integrity of the components during the manufacturing processes. Spacing the components further apart would significantly increase the mass of the system as well exceeded the limits on overall dimensions set by the diffusion bonding furnace. The thickness of the endplates is set by the requirement of providing threaded taps for the fluid conditions as well as the fixture needs for alignment of the components during the diffusion bonding. With those constraints in mind, this amount of extraneous conduction,

while not negligible, was deemed acceptable. Subsequent designs can consider modifications that reduce this parasitic conduction.

In this prototype, the components are spaced relatively far apart as a result of the need to have external fluid connections for each inlet and outlet of every component. The space required to make the external fluid connections was the driving factor in the size and mass of this system. Without the requirement to bring the fluids in and out for experimental reasons, the majority of the fluid connections on the solution streams could be made internally, substantially reducing the size and mass of the entire system.

Figure 4-29 shows several photographs of the Microchannel Absorption heat pump after the final diffusion bonding of the system. The overall dimensions of the packaged system are 200 × 200 × 34 mm. The component has a mass of 7 kg. The solution pump and fluid connections are external to this envelope.

Before testing of the system was started, all components were tested individually for leaks to the exterior of the system as well as for cross leaks between opposite sides of the heat exchangers. Test fittings were installed on each component and a small amount

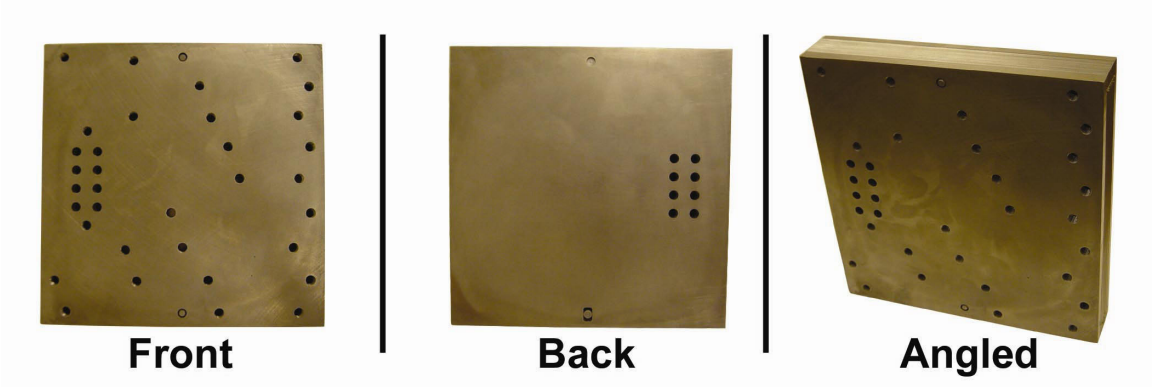

Figure 4-29 Microchannel System Photographs

of a detectable gas, R-134a, was introduced into one of the components. A refrigerant leak detector was then used to search for leaks in the system. The refrigerant leak detector (TIF, Model TIFZX-1) has two sensitivity minimum threshold settings of 15 g/year and 3 g/year of refrigerant. There were no detectable leaks in any component of the system to the exterior of the device. There were no detectable cross-leaks between sides of any of the components at the less sensitive setting of 15 g/year. The absorber, condenser, refrigerant heat exchanger, evaporator and the solution heat exchanger all had detectable cross leaks at the most sensitive setting of the leak detector of 3 g/year. All of these heat exchangers have critical bonding areas as shown in Figure 4-24. The desorber and rectifier do not have these critical bonding areas and had no detectable leaks. While the level of cross-leaks detected in the components would not be acceptable in a production version of a heat pump because of the long service life required, the leaks were not significant enough to prevent testing of this prototype. Even after testing for several weeks with the same charge, no detectable loss of fluids was observed. At these small leakage rates, it would take months before significant amounts of fluid were lost.

5 Microchannel System Testing and Experimental Results

This chapter presents a description of the test facility, experimental procedures, and results from the testing of the prototype absorption heat pump system. The system level, as well as individual component level, data analysis is presented.

5.1 Test Facility Description

The microchannel system was installed in the test facility used for testing of the breadboard system. The system plumbing was modified to accommodate the new system. Figure 5-1 is a plumbing schematic of the solution and refrigerant lines of the test facility. In this illustration, a drawing of Shim B is used to help illustrate the connections into the internal heat exchangers. The channels on Shim A are not visible. During the initial shake down testing of the system, several difficulties were encountered. The concentrated solution flowrate oscillated quite significantly due to the positive displacement pump and the system feedback issues discussed in section 3.2. The rectifier would occasionally flood causing system crashes due to water passing into the refrigerant stream. The solution cooled rectifier made consistent and independent control of the rectifier very difficult.

To provide better control of the rectifier, the cooling method was switched from the solution cooled scheme of the original design, to an externally cooled scheme. In the externally cooled scheme, the rectifier is cooled by fluid at the same temperature as the

absorber and condenser. While this change reduced the overall performance of the cycle, it enabled significantly more stable operation of the system. The major consequence of this change was a reduction in the required cooling capacity of the absorber.

During the initial testing of the device, the consistent control of the concentrated solution flowrate continued to plague the system. Small variations in the pressure difference between the high and low pressure sides of the system would cause significant swings in solution flowrate. In order to dampen these fluctuations, a back pressure regulator was installed as shown in Figure 5-1. A detailed illustration of the back pressure system is presented in Figure 5-2. The backpressure regulator allows the operator to set a maximum discharge pressure of the pump, independently of the pump speed control. If the discharge pressure exceeds the set value, the regulator opens and bleeds the excess flow back to the low pressure side of the system. The operator can use the pump speed control to set a coarse value of the flowrate and then use the concentrated solution control valve to fine tune the flowrate. While this arrangement does not completely remove the fluctuations, it reduces them to a manageable level.

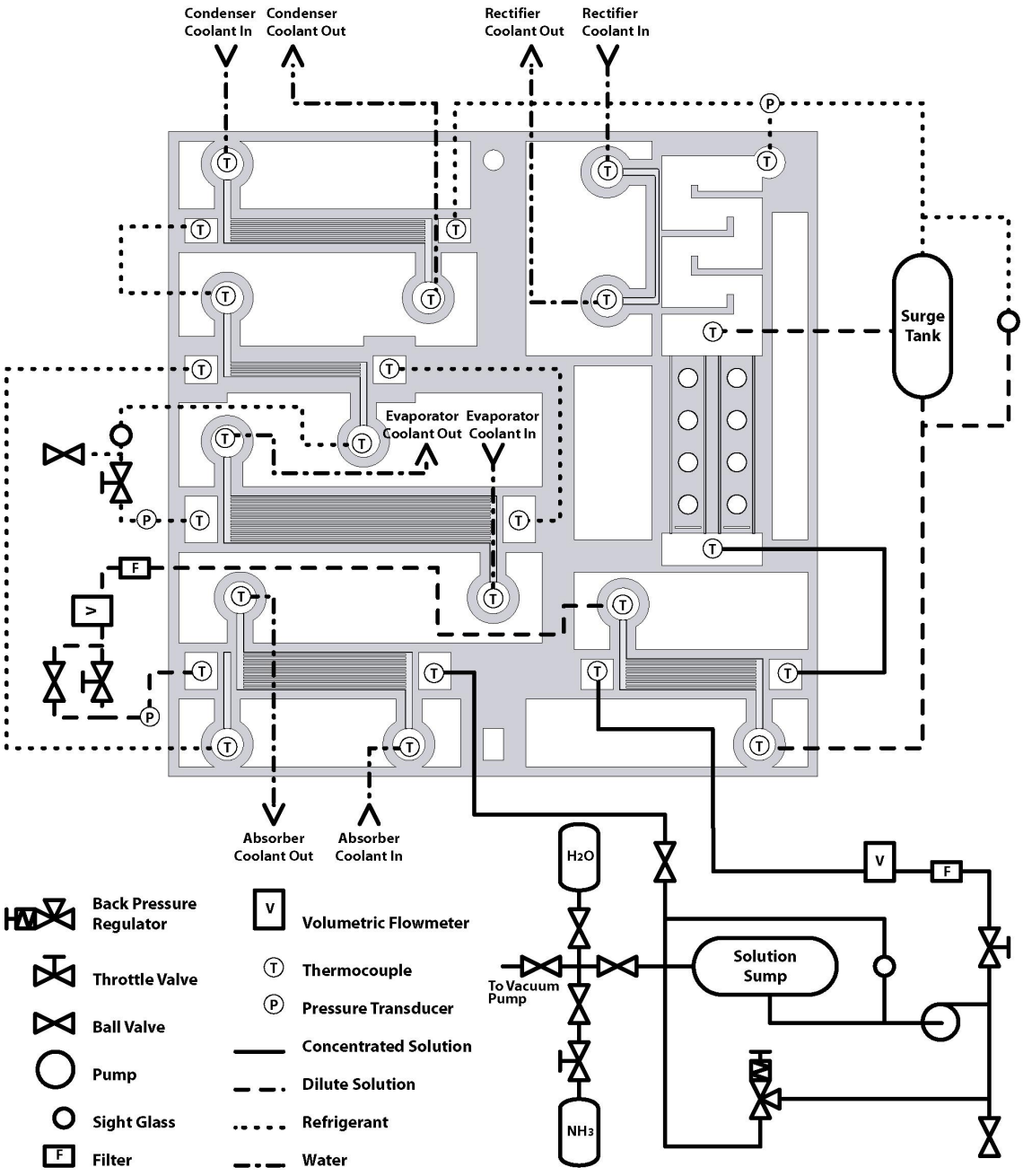

Figure 5-1 Microchannel System Test Facility Solution-Refrigerant Plumbing Schematic

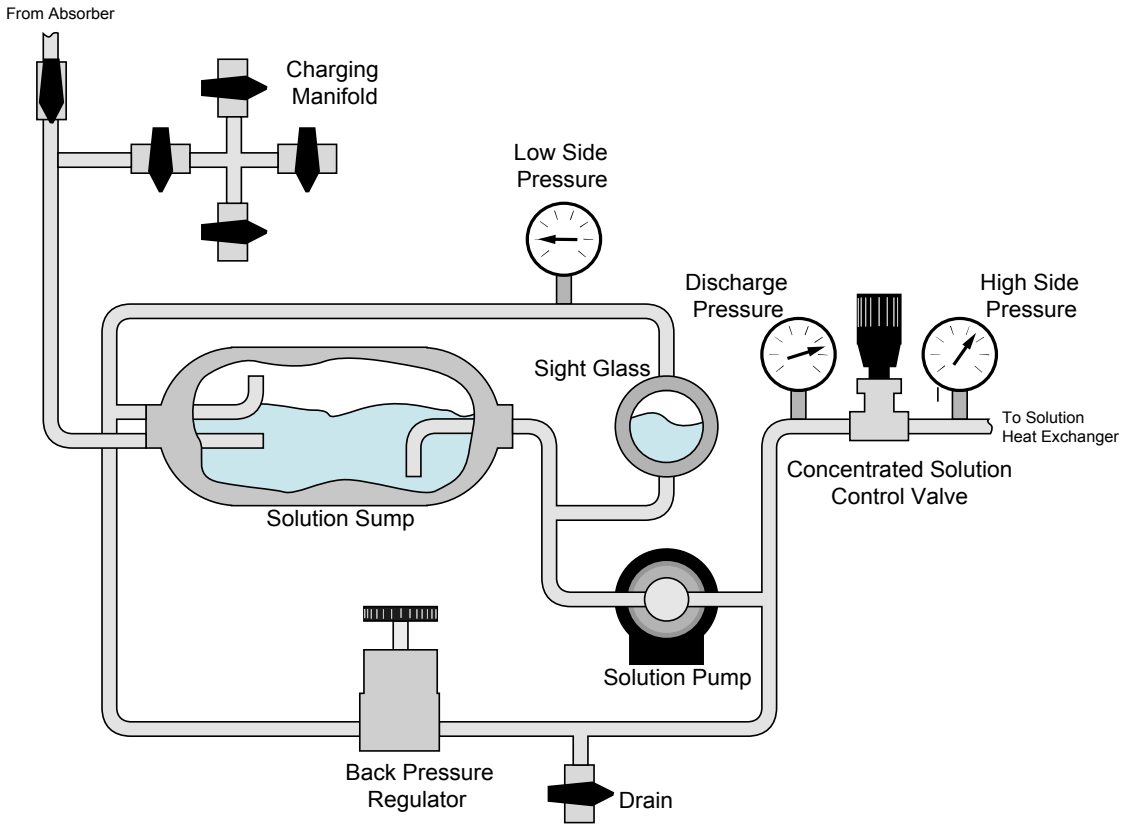

Figure 5-2 Illustration of the Solution Sump, Sight Glass, Solution Pump, Back Pressure Regulator and Concentrated Solution Control Valve.

A surge tank was added to the desorber/rectifier to eliminate the rectifier flooding issues. A detailed illustration of the surge tank is shown in Figure 5-3. The tank allowed excess dilute solution to leave the rectifier, rather than flooding it. The sight glass in parallel with the surge tank allowed the operator to see the exact level of solution in the tank and rectifier. The vertical position of the sight glass was set to ensure the liquid surface was visible when the liquid level was at the appropriate level in the rectifier.

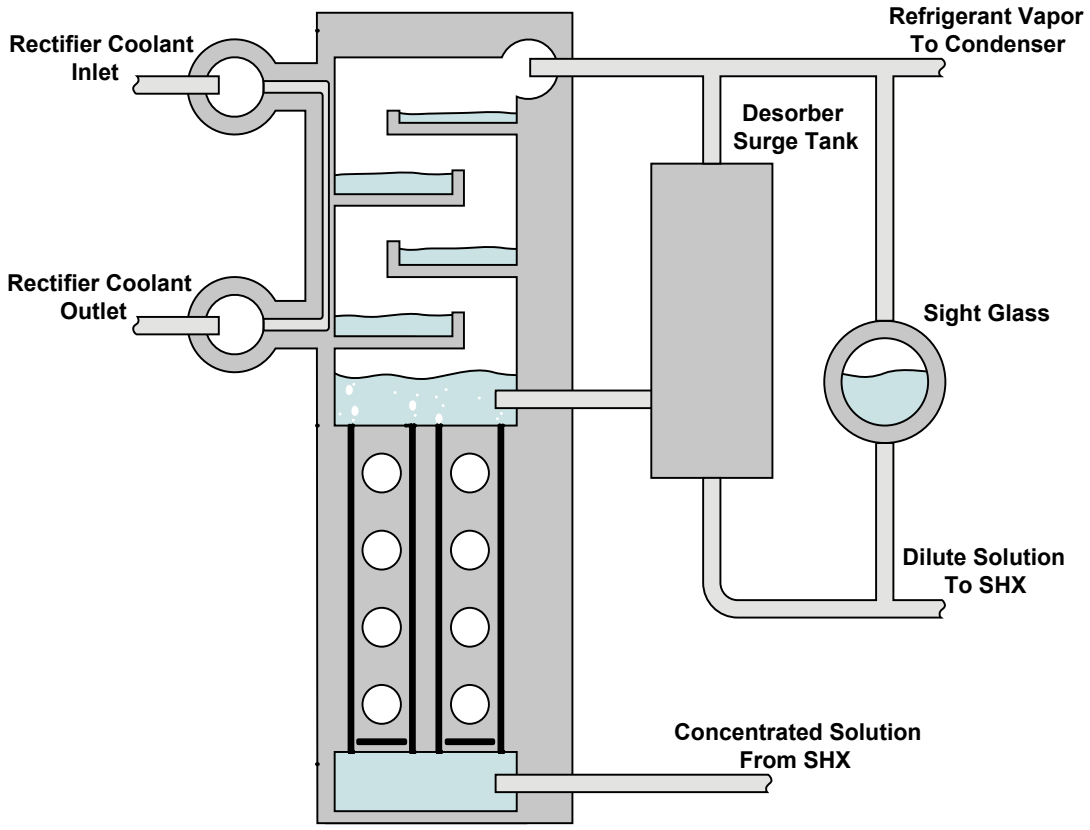

Figure 5-3 Illustration of Rectifier Surge Tank and Sight Glass

The plumbing schematic of the auxiliary cooling loops is show in Figure 5-4. The absorber, condenser and rectifier are cooled by water drawn from the same tank which is simulating the ambient temperature. A single pump (LIANG, Model SM-1212-26) powers the three coolant circuits. After flowing through a 20 micron filter, the flow branches into individual circuits where the flowrate can be adjusted by control valves on the rotameters (Key Instruments, Model 3L22). A throttling valve in a bypass line allows control of the total flowrate and pump head. Once the coolant lines return from the test facility, they recombine and then pass through a plate heat exchanger (FlatPlate, Model FP5x12-10) before returning to the water tank. Building chilled water is used to cool the

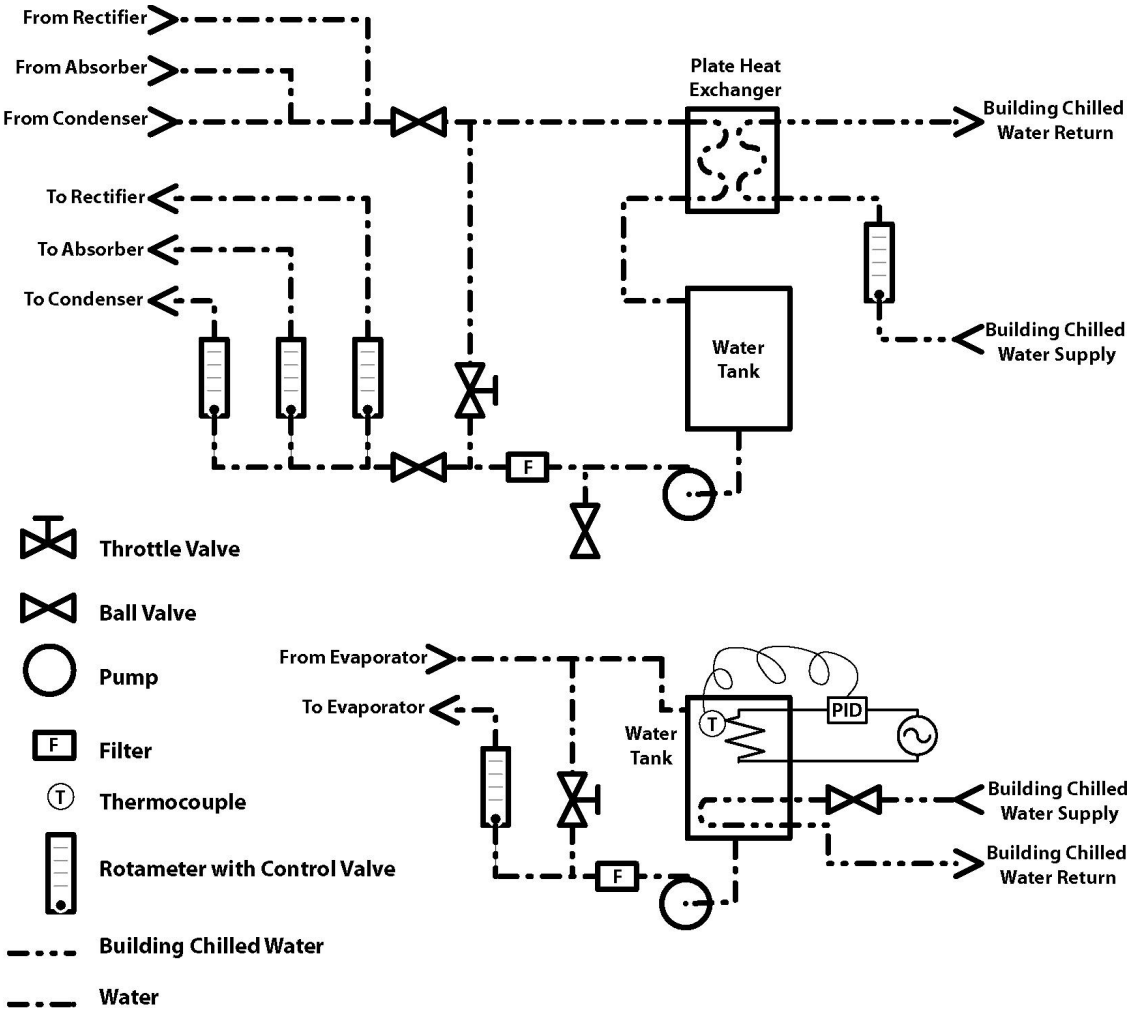

Figure 5-4 Plumbing Schematic for Auxiliary Water Loops

water in the plate heat exchanger. Adjusting the building chilled water flowrate allows control of the water temperature in the tank.

The evaporator chilled water is conditioned in a separate tank. Water is drawn from the tank by a pump (LIANG, Model SM-1212-26) and passes through a 20 micron filter before reaching the rotameters (Key Instruments, Model 3L22) with a control valve for setting the required flowrate. After being chilled in the absorption cycle, the water returns to the water tank. A throttle valve in a bypass line provides control of the total

pump flowrate and head. An electrical immersion heater controlled by a PID controller provides the necessary heat input to maintain the water tank at the desired temperature. Building chilled water can be passed through a coil of copper tubing in the bottom of the tank to reduce the water temperature to the desired point prior to testing in order to avoid excessively long start up times. The building chilled water can also be used to provide an additional cooling load on the tank during test conditions when the PID controller has difficulties maintaining a constant temperature due to small evaporator cooling capacity.

Eight, 150 Watt electrical resistance cartridge heaters (Watlow, Model E1E43-L12) provide the heat input to the desorber. The heaters are controlled by a manual variable voltage transformer. This arrangement allows heat input rates of 0-1200 W. The heaters and the inside of the heater holes were covered with a thermally conductive paste (Omega, OT-201, k = 2.3 W/m-K) to ensure good thermal contact between the heaters and the shims. During installation of the electrical resistance cartridge heaters, a misalignment of the holes in the front plate prevented full insertion of three of the eight heaters. The cartridge heaters have a non-heated zone at each end. In order for the heated section of the cartridge to be in contact with the shims, it must pass fully through the back plate, shims and the front plate. Figure 5-5 illustrates the heater insertion problem. The misalignment of the holes has been greatly exaggerated to illustrate the problem. Due to the one of a kind prototype nature of the system, it was decided not to attempt to re-drill the holes in the front plate. The process of re-drilling the holes could have caused irreparable damage to the device by causing delamination of the shims. The misalignment of the heaters will cause some of the heat input to be transferred directly to the back plate and then lost to ambient. This will cause a reduction in the overall COP of

the cycle. The portion of the heaters not in contact with the shims due to the insertion problem is approximately 10% of the entire heated length of all of the heaters. Figure 5-6 shows a photograph of the electrical heaters after insertion into the system. The heaters that are in the misaligned holes are visible and labeled. The thermal paste is also visible in the photograph.

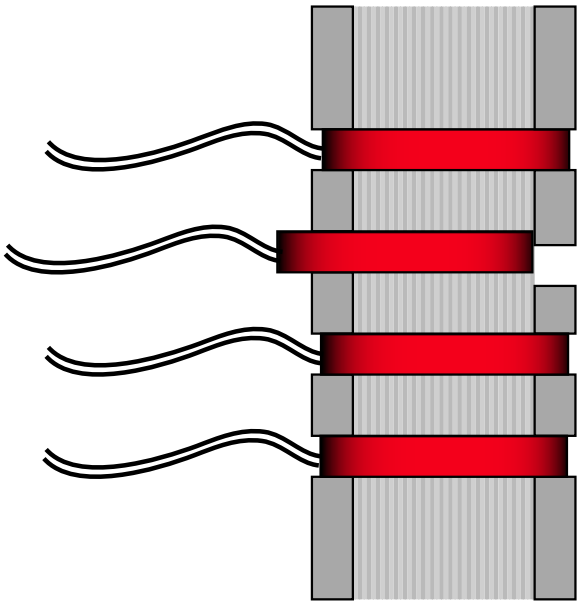

Figure 5-5 Illustration of Heater Insertion (misalignment is greatly exaggerated)

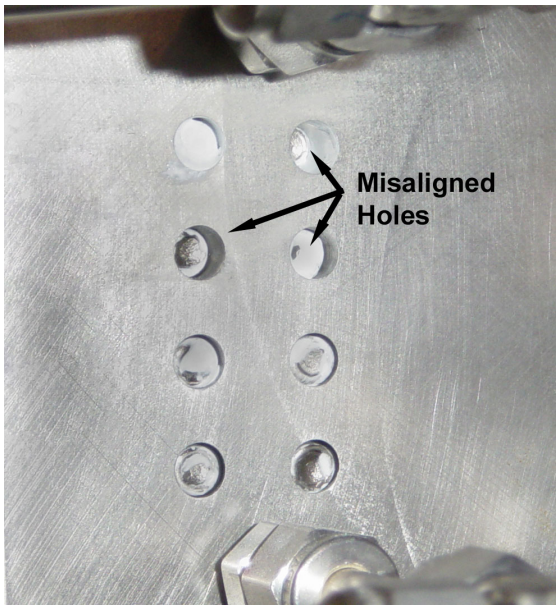

Figure 5-6 Photograph of Electrical Heaters in Misaligned Holes

After the microchannel system was completely installed in the test facility, the fluid connections were leak checked by pressurizing the system to 500 kPa with compressed air. Each fitting was individually inspected with a bubble leak detection solution. The system was then left at pressure for 24 hours, and the system pressure was monitored to ensure there were no leaks. Figure 5-7 is a photograph of the microchannel heat pump system installed in the test facility after all plumbing and electrical connections were made. During testing, the system and the connecting plumbing are insulated to reduce heat loss to the ambient.

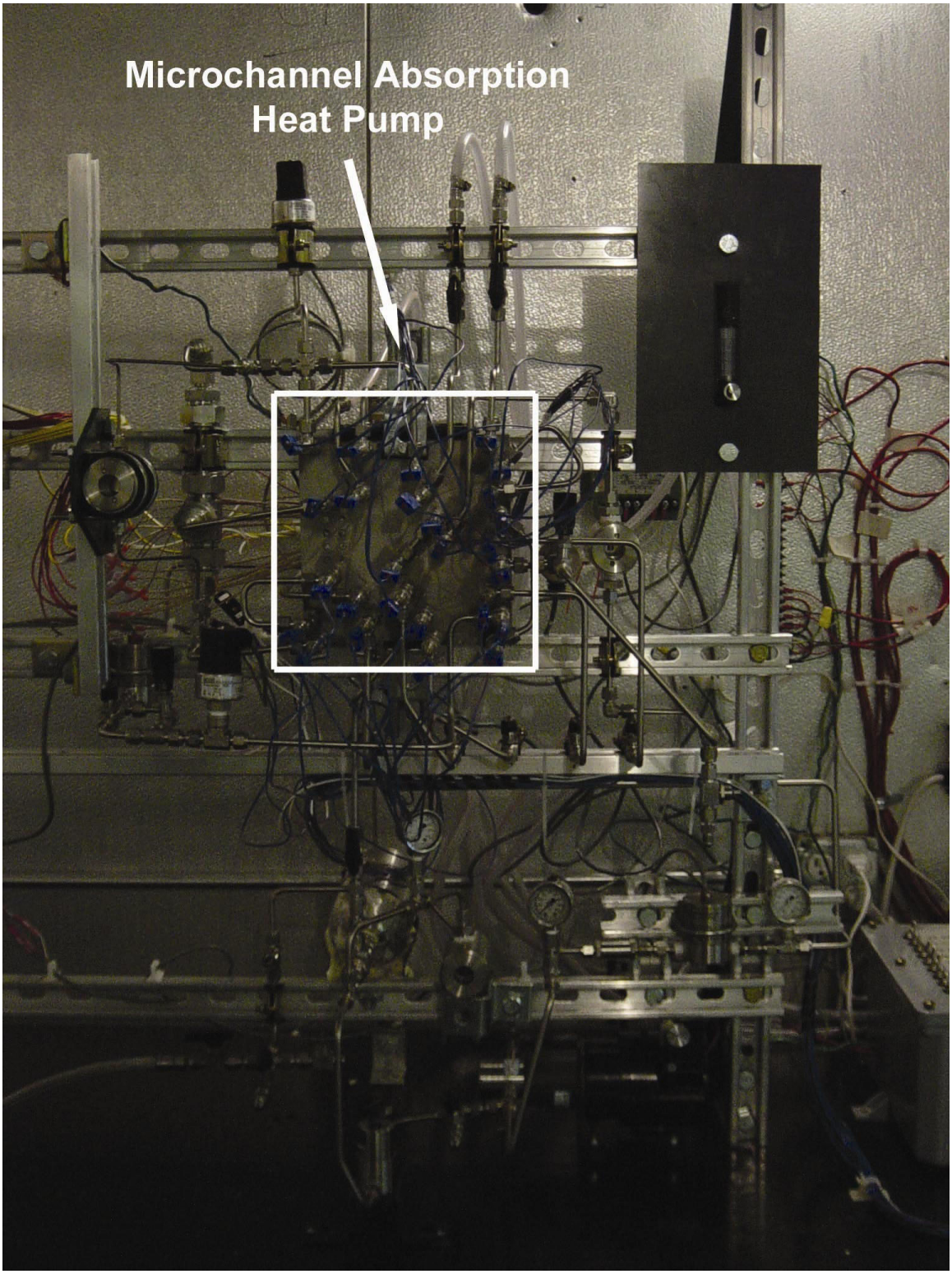

Figure 5-7 Photograph of Microchannel Absorption Heat Pump Installed in Test Facility

Charging the system with the working fluids requires that the system be evacuated. A vacuum pump (J.B. Industries, Model: DV-85N) was used to remove air from the system and the charging manifold as shown in Figure 5-1. They system was evacuated to an absolute pressure of 20 Pa. Distilled water was then degassed by boiling the water for 30 minutes. The distilled water container was then connected to the charging port and the pressure difference between atmosphere and the system forced the water into the system. Approximately 300 grams of water was required. The large size of the solution sump in this system made the operation of the system relatively insensitive to the exact charge of water in the system. Ammonia was then charged to the desired concentration for the tests. The total mass of ammonia charged varied between approximately 120 and 450 grams. Between tests, ammonia could be added as required to adjust the operation concentrations.

5.2 Testing and Data Acquisition

To initiate a test, the building chilled water is first turned on and set to the desired temperature. The coolant pumps are then turned on and the water flowrates in the absorber, condenser, rectifier and evaporator are adjusted to the desired values. The PID controller in the evaporator loop is set to maintain a constant 12.8°C at the evaporator chilled water inlet. The building chilled water can be used to reduce the temperature of the evaporator chilled water if necessary. The desired temperature of the absorber, condenser and rectifier coolant is set by adjusting the flowrate of the building chilled water through the plate heat exchanger. This flowrate is constantly adjusted by the operator as the required cooling capacity of the plate heat exchanger changes as the system approaches a steady operating condition.

Next, the backpressure regulator is set to a low pressure. The solution pump is then turned on and a steady flow of solution is set. The heat input to the desorber is slowly increased and the system pressures are monitored. As the high side pressure increases, adjustments are made to the backpressure value, the pump speed and the solution control valve to maintain steady operation. As vapor generation in the desorber begins, the refrigerant and solution expansion valves are adjusted to maintain the proper levels of dilute solution and refrigerant in their respective sight glasses. Even after the system reaches a steady operating condition, the system must be closely monitored as small perturbations in the state points can push the system into unstable operation.

The flowrate of the evaporator chilled water is set to achieve an outlet temperature of 7.2°C. The evaporator water inlet and outlet temperatures were set at 12.8 and 7.2°C (55 and 45°F) for all experiments on the microchannel system because that is a standard water chiller operation condition and provides a sufficient temperature difference to limit experimental uncertainty in the calculated evaporator cooling capacity.

The operating pressures and the solution concentrations in the absorption cycle are determined by several outside constraints. For a water chilling application where the desired outlet temperature of the chilled fluid is 7.2°C (45°F) a typical evaporator temperature would be 5°C. The heat transfer performance of the specific evaporator will determine how much lower the refrigerant evaporating temperature needs to be than the desired chilled water outlet temperature. The maximum low side pressure is determined by the intersection of a 5°C isotherm and the 100% ammonia isotere. This is illustrated in Figure 5-8 which is a plot of the saturation pressure and saturated solution temperature of ammonia-water mixtures. The refrigerant stream in an ammonia water absorption

cycle will have some small water content but as can be seen on the figure, the isoteres are closely spaced at the pure ammonia side of the figure, so assuming pure ammonia for this overview of the operating conditions is sufficient. The intersection of the maximum low-side pressure line with the ambient temperature line indicates the maximum concentration for the concentrated solution. Higher concentrations would be beneficial in the desorber to produce a more pure refrigerant stream with a smaller rectification heat load. However, increasing the concentration above what is indicated in the figure would result in incomplete absorption of the refrigerant vapor in the absorber, no matter how large it is. Further allowances must be made to allow for heat exchanger temperature differences and several degrees of sub-cooling at the absorber solution outlet, so the maximum allowable concentration is reduced further.

The intersection of the ambient temperature line with the 100% ammonia isostere indicates the outlet of the condenser and sets the minimum high side pressure. At pressures lower than this, the refrigerant saturation temperature is below the ambient and the refrigerant stream would not fully condense before passing through the expansion valve.

The dilute solution concentration is set by several factors: the temperature of the driving heat source, the circulation ratio of the solution, and the capability of the rectifier. As the temperature of the driving heat source increases, the generator can lower the concentration of the dilute solution further, given that the rectifier can adequately purify the less pure vapor that would be generated. For a fixed refrigerant flow rate and concentrated solution concentration, a decreasing circulation rate in the solution circuit leads to a lower dilute solution concentration.

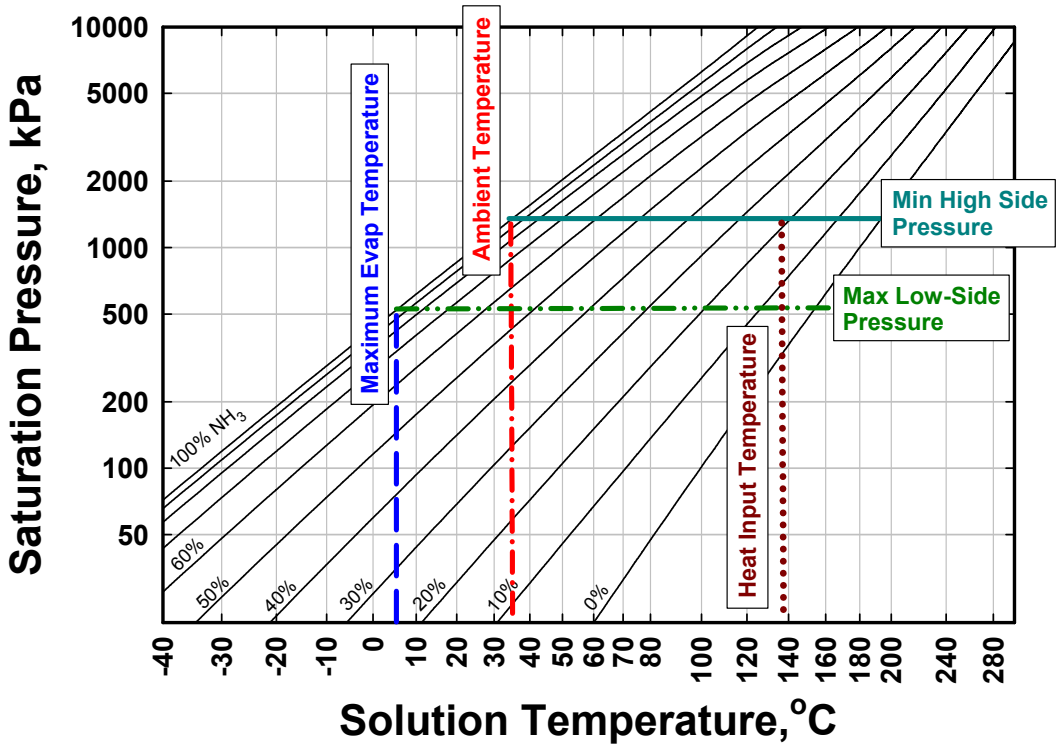

Figure 5-8 Cycle Operating Conditions

The desorber in this study is a co-flow device. As the refrigerant vapor is generated in the desorber, it flows along with the solution stream to the exit of the desorber. This flow arrangement means the vapor leaving the generator is at a high temperature and a relatively low concentration. It would be preferable to have the vapor in counter-flow with the solution stream so that the vapor would be at a lower temperature and a higher concentration when it leaves the desorber. The counter-flow arrangement is not currently amenable to microchannel designs so this flow arrangement was not attempted in this device.

The main control of the concentrated solution concentration in the experimental system is the amount of ammonia charged into the system. The concentration can be checked by running several experiments and analyzing the data at saturated states in the system. If additional ammonia is required, it is added between tests. The low-side and high-side pressures are controlled by adjusting the solution and refrigerant expansion valves, along with the backpressure regulator and the pump speed. Closing the refrigerant expansion valve increases the pressure difference between the high pressure and low pressure sides of the heat pump. Closing the dilute solution valve will cause the low-side pressure to rise because the refrigerant vapor entering the absorber does not have an adequate amount of liquid solution to be absorbed into. The pump and backpressure valve are used to maintain sufficient liquid flow from the low pressure and high pressure sides. Increasing the concentrated solution flowrate will lower the high-side pressure by decreasing the amount of vapor that is generated in the desorber.

The locations of the temperature, pressure and flowrate measurements are indicated in Figure 5-1 and Figure 5-4. Details of the microchannel experimental facility components are listed in Table B-4 through Table B-22. All thermocouple measurements were made with type T thermocouples, which have an uncertainty of ±0.5°C. The pressure measurements were made with WIKA pressure transducers (ECO-1, ±0.5% of span). Solution flowrates were measured with DEA Engineering Company flowmeters (FMTE20, ±0.5% of reading). The power input to the generator was measured with an Ohio Semitronics wattmeter, (PC5-019E, ±0.5% F.S.). The water coolant flowrates were measured with Key Instruments flowmeters (MR3000, ±4.0% F.S.). All voltage signal measurements were recorded with a National Instruments SCXI

signal conditioning and data acquisition system. Two SCXI-1102 modules, each with 32 channels, were housed in a SCXI-1000 chassis. Electrical connections were made to the SCXI-1102 modules via SCXI-1303 isothermal terminal blocks with built in reference junction for cold-junction compensation of thermocouple measurements. The signal conditioning system was connected to a PC via a DAQCard-6036E data acquisition card. Frequency measurements were recorded with an IOTech Personal DAQ/56 data acquisition system connected to a personal computer via USB. Both the National Instruments and the IOTech data acquisition systems were controlled with a LabVIEW (version 7.1) Virtual Instrument. A graphical user interface was developed to display all operating temperatures and pressures during testing. The LabVIEW VI also displayed the heat input to the generators and the heat transfer rates of the absorber, condenser, rectifier, and evaporator water loops.

During testing, data are continuously recorded every 0.2 seconds for every measurement device. During data reduction, a 2 minute section of data is taken from the raw data at a point when the system has reached a steady operating condition. The recorded data for the 2 minute section are averaged and the results are used for the data analysis of the test point.

5.3 System Level Data Analysis

An analysis of a single test point is presented here for illustration of the data reduction. The details of the cycle data analysis and uncertainty calculations can be found in Table B-23 in Appendix B. The uncertainty propagation is calculated using the procedure of Taylor and Kuyatt (1994). The calculations were conducted using EES

(Klein, 2006). The properties of water and ammonia/water mixtures supplied with EES were used for these calculations

The absorber coolant inlet temperature for this test point was 30.2±0.5°C and the electrical input to the desorber heaters was 708.9±7.5 W. The dilute solution leaving the rectifier was at a saturated condition at a temperature of 115.4±0.5°C. The system high-side pressure was 1304±17.4 kPa. Based on these measured quantities, the calculated concentration of the dilute solution was 0.299±0.003. The measured dilute solution volumetric flowrate was 64.8±0.3 ml/min. The dilute solution density, based on the dilute solution concentration, system high side pressure, and the solution heat exchanger outlet temperature of 47.7±0.5°C, was 880.8±1.2 kg/m^3. The dilute solution mass flowrate was $9.51\times10^{-4}\pm4.9\times10^{-6}$ kg/s.

The refrigerant vapor temperature leaving the rectifier was 102.2±0.5°C. At this saturated vapor condition, the refrigerant concentration was calculated to be 0.946±0.002. The concentrated solution volumetric flowrate was 88.2±0.4 ml/min. The temperature of the concentrated solution inlet to the solution heat exchanger was 36.3±0.5°C, the system high side pressure was 1304±17.4 kPa, and the density was calculated to be 838.4±1.5 kg/m^3. The calculated concentrated solution mass flowrate was $1.23\times10^{-3}\pm5.4\times10^{-6}$ kg/s. A mass and species balance on the solution circuit yielded a refrigerant mass flowrate of $2.8\times10^{-4}\pm6.2\times10^{-6}$ kg/s and a concentrated solution concentration of 0.447±0.004. The evaporator refrigerant inlet temperature and pressure were -1.3±0.5°C and 375.3±3.45 kPa, respectively. The calculated evaporator inlet enthalpy was 510.1±169.8 kJ/kg. The evaporator outlet refrigerant temperature was 16.8±0.5°C and the enthalpy, based on the pressure, temperature and concentration, was 1115±7.2 kJ/kg. The refrigerant outlet

temperature is greater than the evaporator chilled water inlet temperature due to internal conduction from the desorber. The refrigerant flowrate and the evaporator inlet and outlet enthalpies were used to calculate the refrigerant evaporator heat duty of 170±48 W. The uncertaintiy in this heat duty is large due to the small variation in temperature with enthalpy at low qualitys of ammonia/water mixtures. This calculation is also impeded by the conduction of heat from the desorber into the refrigerant outlet header. The refrigerant outlet temperature is actuall higher than the inlet temperatue of the chilled water due to this conduction. An alternative method to calculate the refrigerant heat duty is to use the enthalpy of the refrigerant before the expansion valve and assume an isenthalpic expansion. The refrigerant outlet temperature from the high pressure side of the refrigerant heat exchanger was 22.6±0.5°C and the refrigerant enthalpy was 66.4±2.7 kJ/kg. Using this in place of the evaporator inlet condition, the evaporator refrigerant heat duty was calculated to be 295±7 W. This calculation has a much lower uncertainty due to the difference in slope of the enthalpy versus temperature graphs of a condensed liquid and a low quality, high concentration, two-phase mixture of ammonia and water. It does not take into account any losses in the expansion process or heat gains through the tubing between the expansion valve and the inlet of the evaporator. The measured evaporator chilled water flowrate was 631±101 mL/min. The chilled water inlet temperature was 12.5±0.5°C and the density was 999.4±0.1 kg/m^3. The calculated chilled water mass flowrate was $10.5\times10^{-3}\pm1.7\times10^{-3}$ kg/s. The chilled water outlet temperature was 7.1±0.5°C. The chilled water inlet and outlet enthalpies were 52.8±2.1 kJ/kg and 30.1±2.1 kJ/kg respectively. The calculated evaporator chilled water heat duty was 239±49 W. The difference between the calculated chilled water heat duty and the

refrigerant evaporator heat duty calculated using the refrigerant state at the inlet of the expansion valve was 56 W or 23% of the water-side heat duty. To calculate a system COP, the water-side heat duty was used. Given the uncertainty in the refrigerant-side calculations as well as the heat losses and gains to the system, the water-side calculations were considered more appropriatefor indicating system performance. The water-side heat duty also represents the useful amount of cooling that the system produced. Using the evaporator chilled water heat duty, the system COP was calculated as 0.34±0.07.

The cycle analysis outlined above was conducted for all the 109 test points recorded during the testing of the microchannel heat pump. Figure 5-9 depicts the

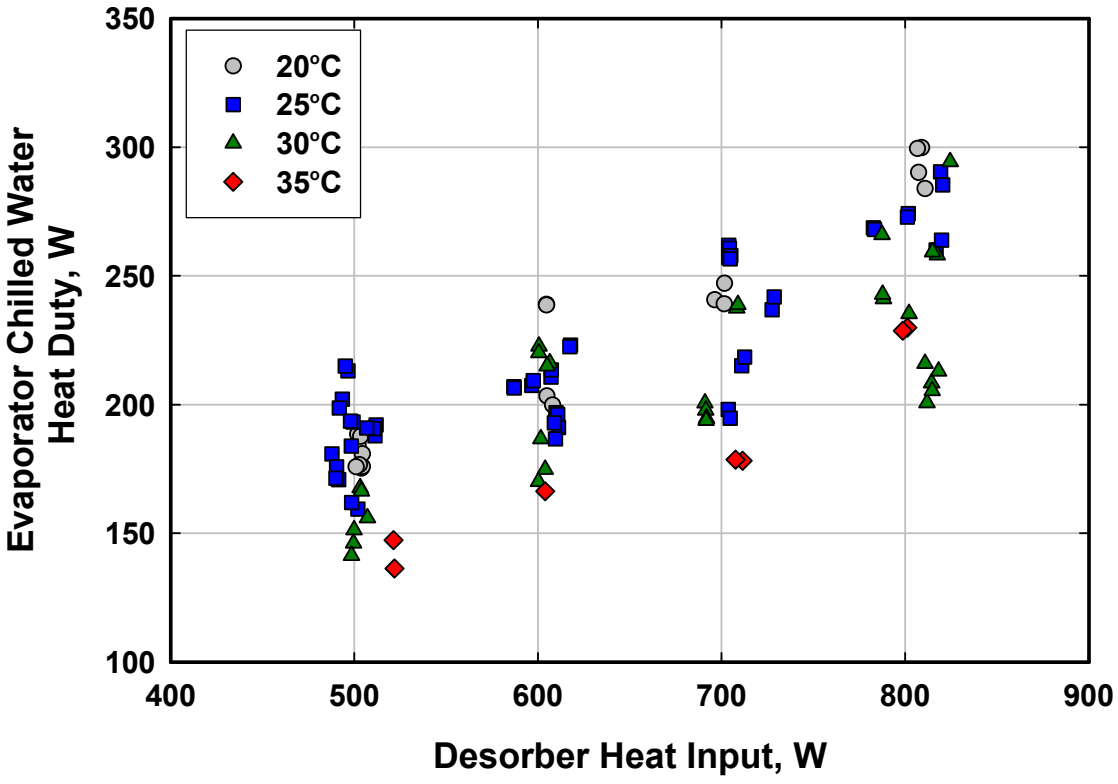

Figure 5-9 Evaporator Chilled Water Heat Duty versus Desorber Heat Input

variation in the evaporator chilled water heat duty with desorber heat input as well as with the nominal absorber coolant inlet temperature.

The evaporator chilled water cooling capacity represents the useful amount of cooling that is produced by the system. The results indicate a fairly smoothly increasing cooling capacity at all of the absorber coolant temperatures. As the desorber heat input increases, the amount of vapor that can be generated in the desorber increases, leading to larger refrigerant flow rates and thus higher cooling capacities. The increasing absorber coolant temperature at the fixed chilled water conditions leads to higher temperature lifts

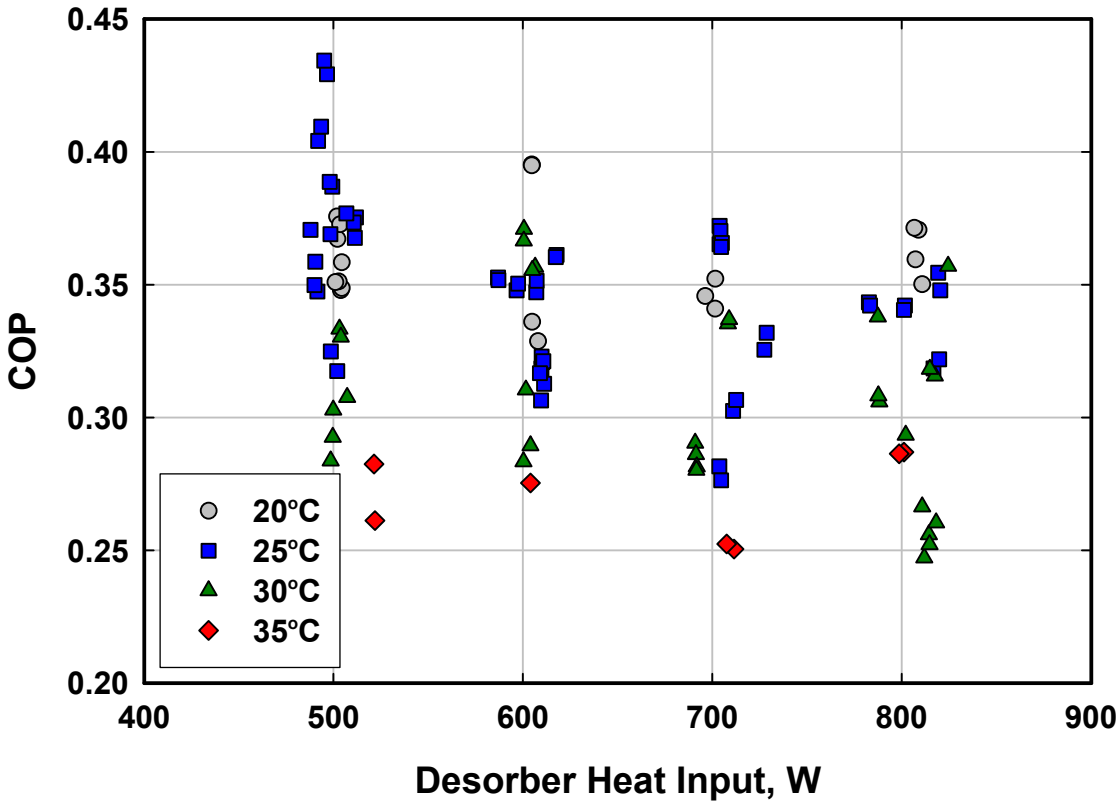

Figure 5-10 System COP versus Desorber Heat Input

and reduces the capacity of the system as it would with any chiller or heat pump system.

Figure 5-10 shows the variation of system COP with the desorber heat input. The system exhibits fairly flat trends in COP with increasing desorber heat input at constant absorber coolant temperatures. This indicates that the system is fairly robust over the range of operating conditions tested. The maximum nominal desorber heat input tested was 800 Watts. While the COP trends from 500 to 800 W are flat, extrapolating them past 800 Watts is not advisable for the current system because of the steep decline in refrigerant purity at higher desorber heat input rate.

Figure 5-11 shows the variation in refrigerant ammonia concentration with

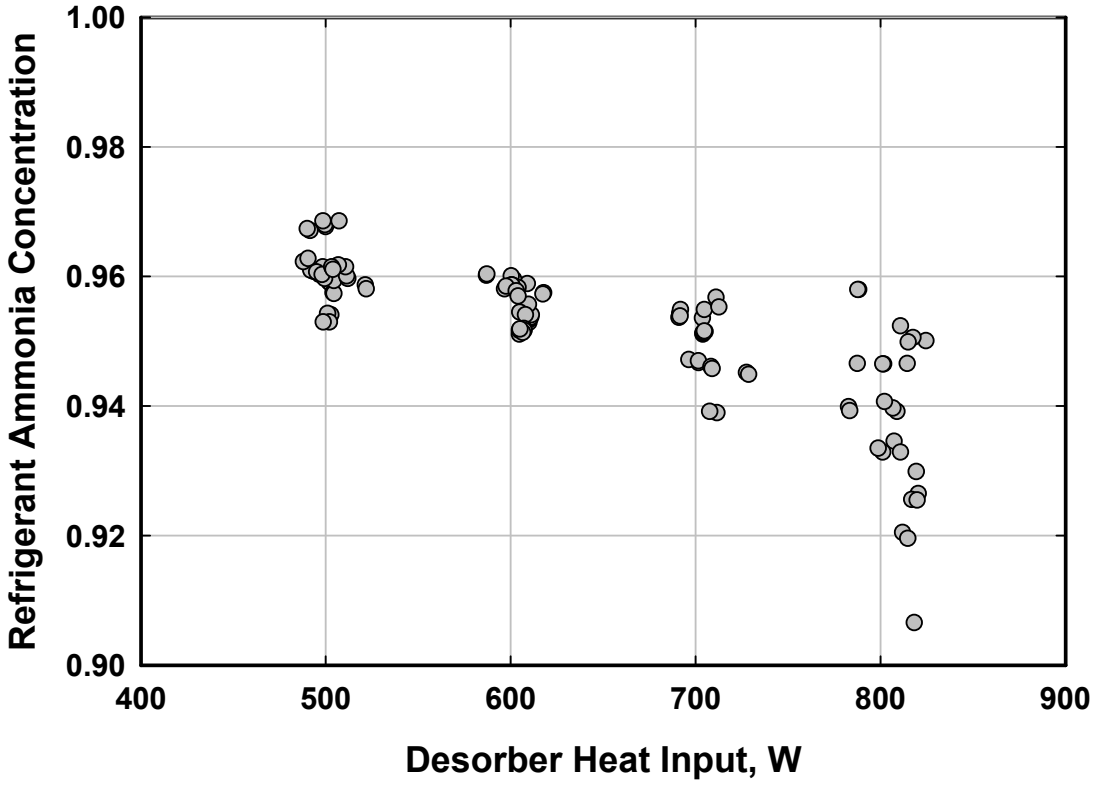

Figure 5-11 Refrigerant Ammonia Concentration versus Desorber Heat Input

desorber heat input rate. The concentration decreases with increasing heat input rate and begins to drop sharply above 800 Watts. In general, as the thermal input to the desorber increases, the solution flowrate increases, the temperature of the solution leaving the desorber increases, and the concentration of the vapor leaving the desorber decreases, requiring significantly more rectification to purify the refrigerant. As discussed in Section 4.2 and shown in Figure 4-4, obtaining a very pure refrigerant stream is necessary to obtain high operating COPs. In order to adequately purify the refrigerant stream, the rectifier must lower the temperature of the refrigerant stream. For example, at a pressure of 1600 kPa, and a temperature of 100°C the saturated vapor leaving the rectifier is 96.4% ammonia, but at a temperature of 75°C, it is 99.2%. The refrigerant concentrations for this prototype ranged from a high of 0.969 at 500 W to a low of 0.907 at 800 W. Although the system performed well with these concentrations, they are somewhat low for normal operation of an ammonia water absorption heat pump. The design point for the system had a refrigerant concentration of 98% at a desorber heat input of 800 W. In order to further increase the efficiency and increase the total cooling capacity by operating the system at higher desorber heat input rates, a more effective rectifier, or counter-current desorption leading to a higher rectifier inlet concentration is needed. As the prototype exists, operation of the system at desorber heat inputs above 800 W was not possible due to the significant reduction in refrigerant concentration at those operating conditions.

Figure 5-12 illustrates the decreasing trend of evaporator chilled water heat duty with the increasing heat sink temperature, represented by the absorber coolant inlet temperature. The system COP versus the absorber coolant inlet temperature is shown in

Figure 5-13. As the heat sink temperature increases, the cooling capacity as well as the system COP diminish. As the temperature lift of the system increases the system efficiency declines.

Figure 5-14 shows the variation of COP with the concentrated solution flowrate and desorber heat input. Although not precise, several trends are visible. Increasing the thermal input requires that the solution flowrate be increased in order to maintain stable operation of the cycle. Over all of the conditions as well as within each subgroup, increasing the solution flowrate leads to a decrease in the cycle COP. As the solution flowrate increases at a constant desorber heat input, the fraction of energy that goes to sensible heating of the solution increases and the fraction used to produce refrigerant vapor decreases. The energy used to produce vapor is useful in producing the cooling effect in the evaporator, while the sensible heating of the solution is essentially wasted. The solution heat exchanger is used to recuperate this otherwise wasted heat within the cycle but not all of it can be saved and this leads to the decreasing COP with increasing solution flowrate.

Increasing the size of the solution heat exchanger as well as returning to a solution cooled rectifier will all help reduce this effect by increasing the internal recuperation of heat within the system. The wide variation of COP in Figure 5-14 at similar desorber heat input, especially 500 W, and similar solution flowrate is mainly due to the variation in heat sink temperature as well as slight variations in operating variables such as concentrations.

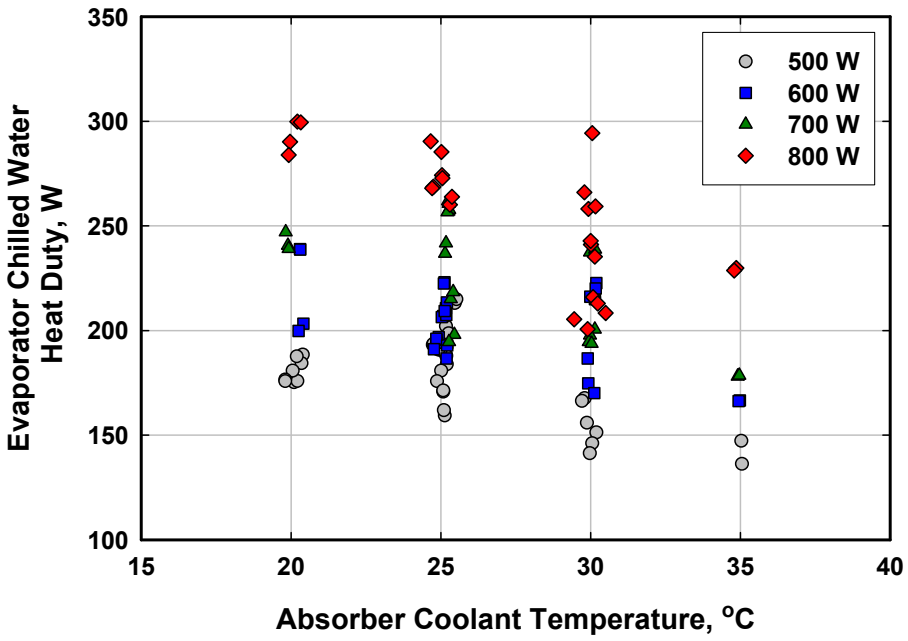

Figure 5-12 Evaporator Chilled Water Heat Duty versus Absorber Coolant Inlet Temperature

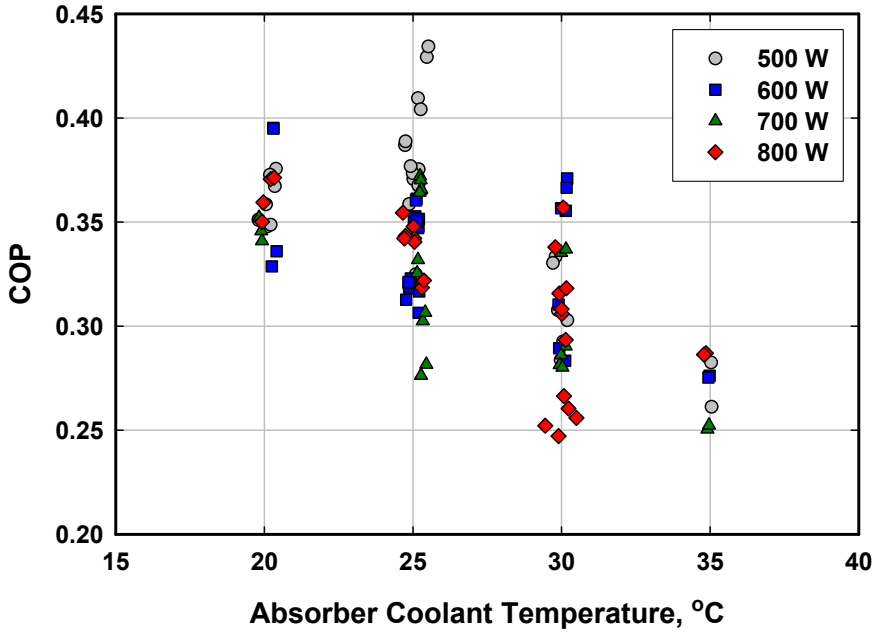

Figure 5-13 System COP versus Absorber Coolant Inlet Temperature

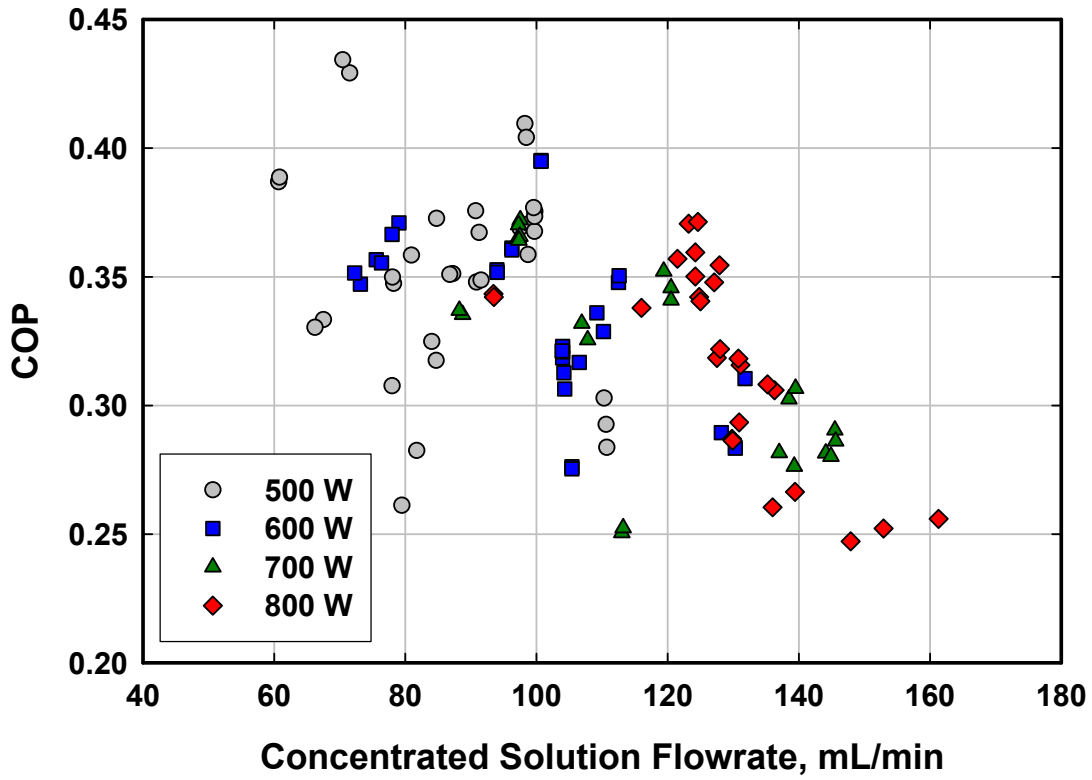

Figure 5-14 System COP versus Concentrated Solution Flowrate

At a standard chiller rating condition of 35°C heat sink temperature, and a desorber heat input of 800 W, the evaporator chilled water cooling capacity was 230 W. This represents a cycle COP of 0.29. This performance is lower than the cycle design condition of 354 W of cooling and a COP of 0.44. The reduction in system performance was due to several factors including, the low performance of the rectifier, the transition from the solution cooled rectifier to an externally cooled rectifier, internal conduction between the components, and heat losses/gains to/and from the ambient.

5.4 System Heat Losses

Accounting for all of the energy paths in the system proved to be very difficult. The internal conduction of heat between the components results in uneven heat balances between the hot and cold sides of heat exchangers. The small total heat duty of the system also means that heat loss to the ambient will not be an insignificant fraction. Figure 5-15 illustrates the heat losses from the system. The heat losses were calculated by summing the heat inputs to the system at the desorber and evaporator and subtracting the rejected heat from the absorber, condenser, and rectifier.

$$\dot{Q}_{Loss} = \dot{Q}_{Des} + \dot{Q}_{Evap} - \dot{Q}_{Abs} - \dot{Q}_{Cond} - \dot{Q}_{Rect} \tag{5.1}$$

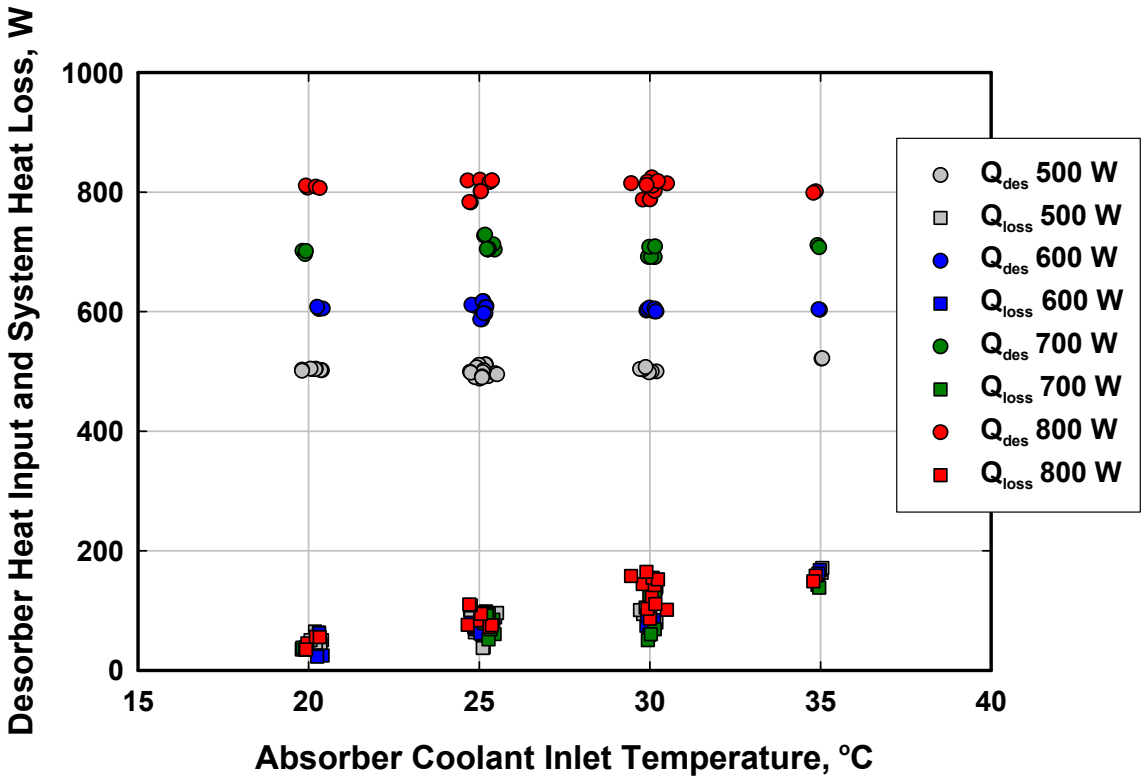

Figure 5-15 Desorber Heat Input and System Heat losses

The coolant side heat duty was used for the absorber, condenser, rectifier and evaporator for the calculation of the heat losses. The heat losses from the system show virtually no dependence on the heat input at the desorber but rather show a very linear increase with the heat sink temperature. As the heat sink temperature increases, the operating points on the Cycle Operating Conditions graph, Figure 5-8, shift up and to the right. This causes the average temperature of the system to increase and thus increase the heat losses to the ambient room air. During testing at nominal conditions of 700 W desorber heat input and 30°C heat sink temperature, surface temperatures of the insulated system were monitored with an infrared thermometer (GenTech, ±1.0°C). Figure 5-16 is a photograph of the test facility with the insulation installed to reduce heat losses to the ambient. A free convection and radiation heat loss estimation calculation was conducted (details in Table C-1 in Appendix C). For these conditions, the estimated heat loss from the system was approximately 72 W. This falls within the range of heat losses calculated from the experimental results as shown on Figure 5-15. A major contributor to the heat loss was the tubing and fittings that connect the various components, which accounted for approximately 38% of the total heat loss. Internal connection of the components would eliminate this significant heat loss.

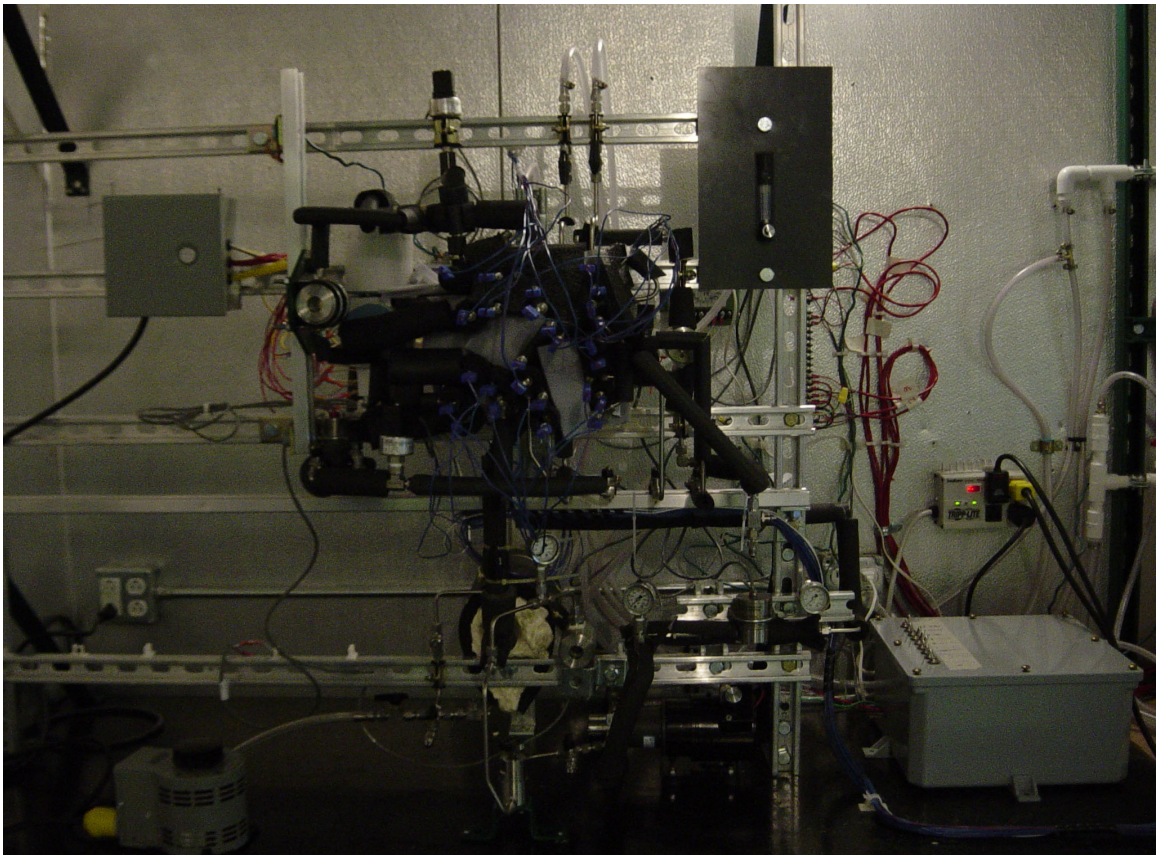

Figure 5-16 Photograph of Insulated Test Facility.

5.5 Component Data Analysis

The following sections present the results of heat transfer analysis of the experimental results for each of the major components of the microchannel heat pump system. In order to compare the experimental performance of the components with the original design conditions, the heat transfer rate, log mean temperature difference, and UA of the absorber, condenser, solution heat exchanger, evaporator and rectifier were calculated. The following sections outline the heat transfer analysis of a sample data point. The data point used for these calculations is the same one used previously for the

cycle analysis. The details of the heat transfer analysis are outlined in Table B-24 of Appendix B.

5.5.1 Absorber

The absorber coolant flow rate was 16.8×10^{-3} kg/s, with inlet and outlet temperatures of 30.2 and 35.0°C, respectively. The heat transfer rate of the coolant is calculated from the coolant flowrate and the inlet and outlet enthalpies.

$$\dot{Q}_{Abs,Coolant} = \dot{m}_{Abs,Coolant}\left(h_{Abs,Coolant,Out} - h_{Abs,Coolant,In}\right) \tag{5.2}$$

The resulting absorber coolant heat transfer rate was 337 W. The dilute solution inlet temperature was 42.4°C, the refrigerant inlet temperature was 25.7°C, and the concentrated solution outlet temperature was 34.3°C. The concentrated solution outlet saturation temperature was 38.73°C. The solution side heat transfer rate was determined from the solution and refrigerant flowrates and enthalpies.

$$\dot{Q}_{Abs,Sol} = \dot{m}_{DS}\cdot h_{Abs,DS,In} + \dot{m}_{Ref}\cdot h_{Abs,Ref,In} - \dot{m}_{CS}\cdot h_{Abs,CS,Out} \tag{5.3}$$

The solution side heat transfer rate was 428 W. The difference between the coolant and solution side heat transfer rates can be attributed to the internal conduction between components. The average of the solution and coolant heat duties is 382 W. The average value is used for evaluating the performance of the absorber.

The log mean temperature difference of the absorber was calculated using the coolant temperatures, the dilute solution inlet temperature and the concentrated solution outlet saturation temperature. The saturation temperature is used because it produces a better estimate of the average temperature difference in the absorber than the actual subcooled outlet temperature would.

$$LMTD_{Abs} = \frac{\left(T_{Abs,DS,In} - T_{Abs,Coolant,out}\right) - \left(T_{Abs,CS,out,Sat} - T_{Abs,Coolant,In}\right)}{\mathrm{Ln}\left[\frac{\left(T_{Abs,DS,In} - T_{Abs,Coolant,out}\right)}{\left(T_{Abs,CS,out,Sat} - T_{Abs,Coolant,In}\right)}\right]} \tag{5.4}$$

The UA of the heat exchanger is then calculated from the Q and the LMTD.

$$UA_{Abs} = \frac{\dot{Q}_{Abs}}{LMTD_{Abs}} \tag{5.5}$$

The LMTD for the example test point was 8.0°C and the UA was 47.7 W/K.

Figure 5-17 shows the variation of the absorber heat duty, UA and LMTD with desorber heat input as well as the heat sink temperature for all of the data points. The

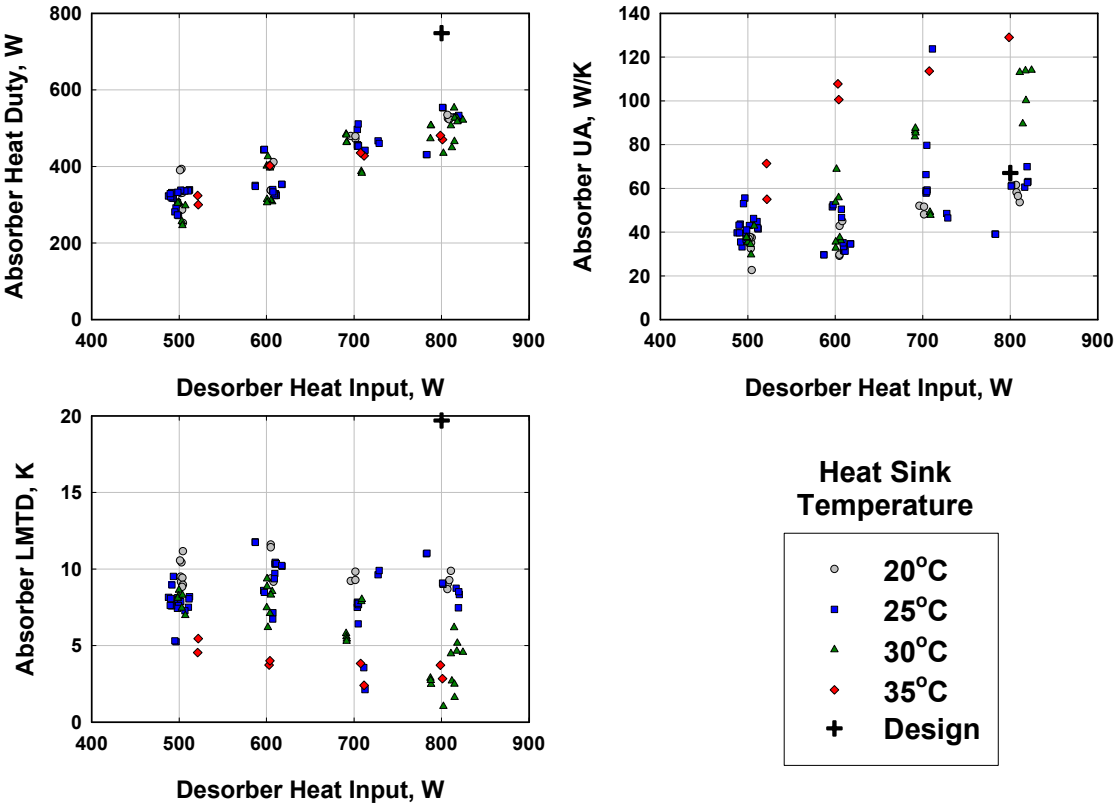

Figure 5-17 Absorber Heat Duty, UA, and LMTD versus Desorber Heat Input

absorber heat duty increases with desorber heat input as would be expected while there is little variation with heat sink temperature. The actual absorber heat capacities are significantly less than the design condition. This is due to the transition to an externally cooled rectifier rather than a solution cooled rectifier. The heat that would have been recuperated internally with the solution cooled rectifier would have ultimately been rejected to the heat sink via the absorber.

There is an increasing trend in the absorber UA with desorber heat input as well as heat sink temperature. The increasing UA with desorber heat input is caused by the increasing solution flowrates at those conditions. As the solution flowrate increases, the average solution velocities and therefore the heat transfer coefficient also increase. As seen in Figure 5-17, the absorber UAs span a range above and below the design condition of 67 W/K but at much lower LMTD than it was designed for due to the lower heat duties.

5.5.2 Condenser

The condenser performance was evaluated in a similar manner as the absorber. The coolant side heat transfer rate is determined from the water flowrate and inlet and outlet enthalpies.

$$\dot{Q}_{Cond,Coolant} = \dot{m}_{Cond,Coolant}\left(h_{Cond,Coolant,Out} - h_{Cond,Coolant,In}\right) \tag{5.6}$$

The coolant inlet and outlet temperatures were 30.3 and 35.2°C respectively. The condenser coolant heat transfer rate for the example test point was 339 W. The refrigerant side heat transfer rate is determined from the refrigerant flowrate and the condenser refrigerant inlet and outlet enthalpies. The enthalpies are determined from the

solution properties using the high side pressure, 1304 kPa, the refrigerant concentration, 0.946 and the inlet and outlet temperatures, 94.8 and 31.4°C. The liquid refrigerant saturation temperature at the outlet of the condenser was 35.6°C.

$$\dot{Q}_{Cond,Ref} = \dot{m}_{Ref}\left(h_{Cond,Ref,In} - h_{Cond,Ref,Out}\right) \tag{5.7}$$

The refrigerant heat transfer rate of the condenser for the example calculation is 382 W. The condenser heat transfer rate used to analyze the performance of the component is the average of the coolant and refrigerant heat transfer rates, 360 W. Internal conduction between the components causes the difference between the coolant and refrigerant heat transfer rates. The LMTD of the condenser is calculated as follows:

$$LMTD_{Cond} = \frac{\left(T_{Cond,Ref,Out,Sat} - T_{Cond,Coolant,Out}\right) - \left(T_{Cond,Ref,Out,Sat} - T_{Cond,Coolant,In}\right)}{\mathrm{Ln}\left[\frac{\left(T_{Cond,Ref,Out,Sat} - T_{Cond,Coolant,Out}\right)}{\left(T_{Cond,Ref,Out,Sat} - T_{Cond,Coolant,In}\right)}\right]} \tag{5.8}$$

For calculating the condenser LMTD, the actual refrigerant inlet and outlet temperature are replaced with the saturated liquid temperature of the refrigerant. This modification is used to account for the large temperature glide in the early portions of the condenser, which leads to the refrigerant temperature being close to the saturated liquid temperature through most of the condenser length. This modification gives a better estimate of the average temperature difference in the condenser. The condenser heat transfer rate and LMTD are used to calculate the condenser UA.

$$UA_{Cond} = \frac{\dot{Q}_{Cond}}{LMTD_{Cond}} \tag{5.9}$$

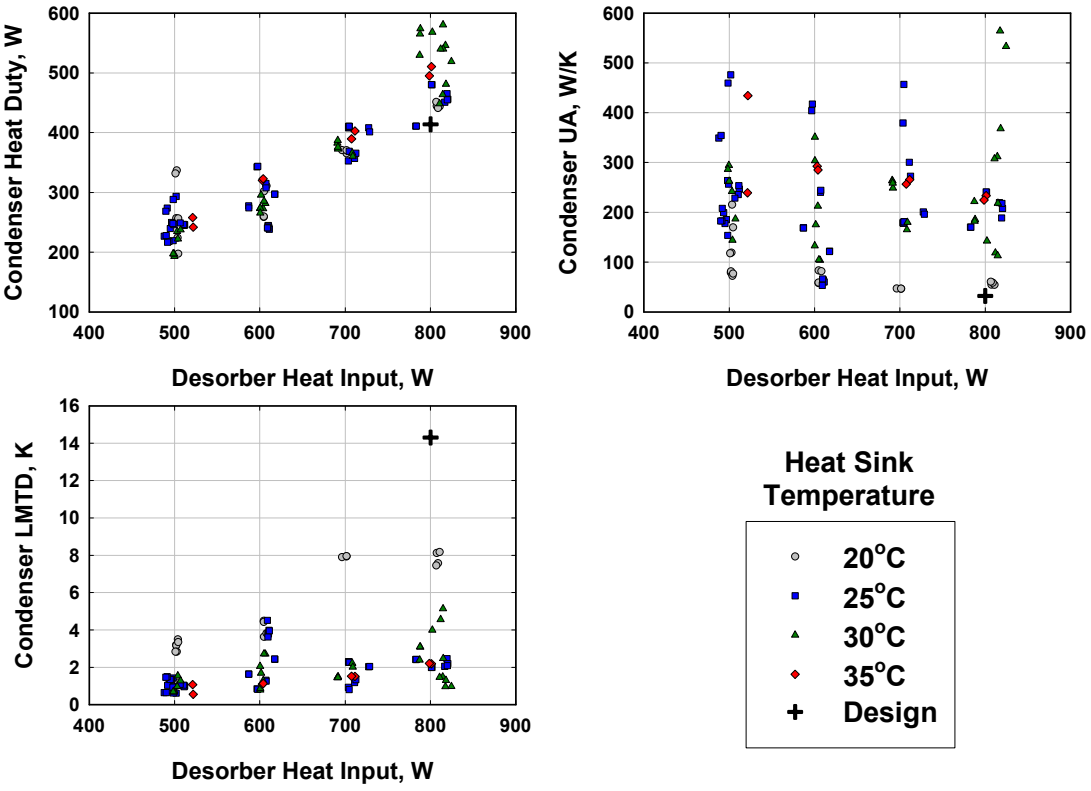

Figure 5-18 Condenser Heat Duty, UA, and LMTD versus Desorber Heat Input

The LMTD and UA for the sample calculation were 2.0°C and 179.7 W/K. The LMTD and UA for the design point were 14.3°C and 32 W/K respectively. Figure 5-18 shows the condenser heat transfer rate, LMTD and UA versus the desorber heat input rate.

The condenser performed very effectively over the entire range of operating conditions. Due to the poor performance of the rectifier, the refrigerant inlet temperature was higher than originally designed, and the temperature glide of the refrigerant was much more than originally anticipated. This, combined with the use of the liquid refrigerant saturation temperature to calculate the experimental LMTD lead to lower LMTDs than the design value and consequently higher experimental UA values.

5.5.3 Solution Heat Exchanger

The dilute solution inlet and outlet temperatures were 111.6°C and 47.7°C, respectively, while the concentrated solution inlet and outlet temperatures were 36.3°C and 89.8°C, respectively. The solution heat exchanger concentrated solution and dilute solution heat transfer rates were calculated as follows.

$$\dot{Q}_{SHX,CS} = \dot{m}_{CS} \cdot \left(h_{SHX,CS,Out} - h_{SHX,CS,In} \right) \tag{5.10}$$

$$\dot{Q}_{SHX,DS} = \dot{m}_{DS} \cdot \left(h_{SHX,DS,In} - h_{SHX,DS,Out} \right) \tag{5.11}$$

The concentrated solution heat transfer rate for the example test point was 386 W, while the dilute solution heat transfer rate was 268 W. The substantial difference in the concentrated solution and dilute solution heat transfer rates is due to the internal conduction between components and heat losses to the ambient. The dilute solution inlet to the solution heat exchanger is the highest temperature in the cycle and therefore more susceptible to heat losses. The inlet header for the concentrated solution is also near the desorber and so there is unaccounted for conduction into the solution heat exchanger. The heat transfer rate used for the analysis of the component is the average of the dilute solution and concentrated solution values. The log mean temperature difference of the solution heat exchanger is calculated as follows:

$$LMTD_{SHX} = \frac{\left(T_{SHX,DS,In} - T_{SHX,CS,Out} \right) - \left(T_{SHX,DS,Out} - T_{SHX,CS,In} \right)}{\mathrm{Ln}\left[\frac{\left(T_{SHX,DS,In} - T_{SHX,CS,Out} \right)}{\left(T_{SHX,DS,Out} - T_{SHX,CS,In} \right)} \right]} \tag{5.12}$$

The UA of the solution heat exchanger is calculated using the heat transfer rate and the LMTD.

$$UA_{SHX} = \frac{\dot{Q}_{SHX}}{LMTD_{SHX}} \tag{5.13}$$

The LMTD for the example calculation was 16.0°C and the UA was 20.4 W/K. The design point LMTD and UA were 15.3°C and 37 W/K, respectively. Figure 5-19 shows the solution heat exchanger heat transfer rate, UA and LMTD for all of the data points in this study.

The design point heat transfer rate, LMTD and UA are also plotted on the graphs in Figure 5-19. The solution heat exchanger performed very near its design point. The effectiveness of the solution heat exchanger is defined as:

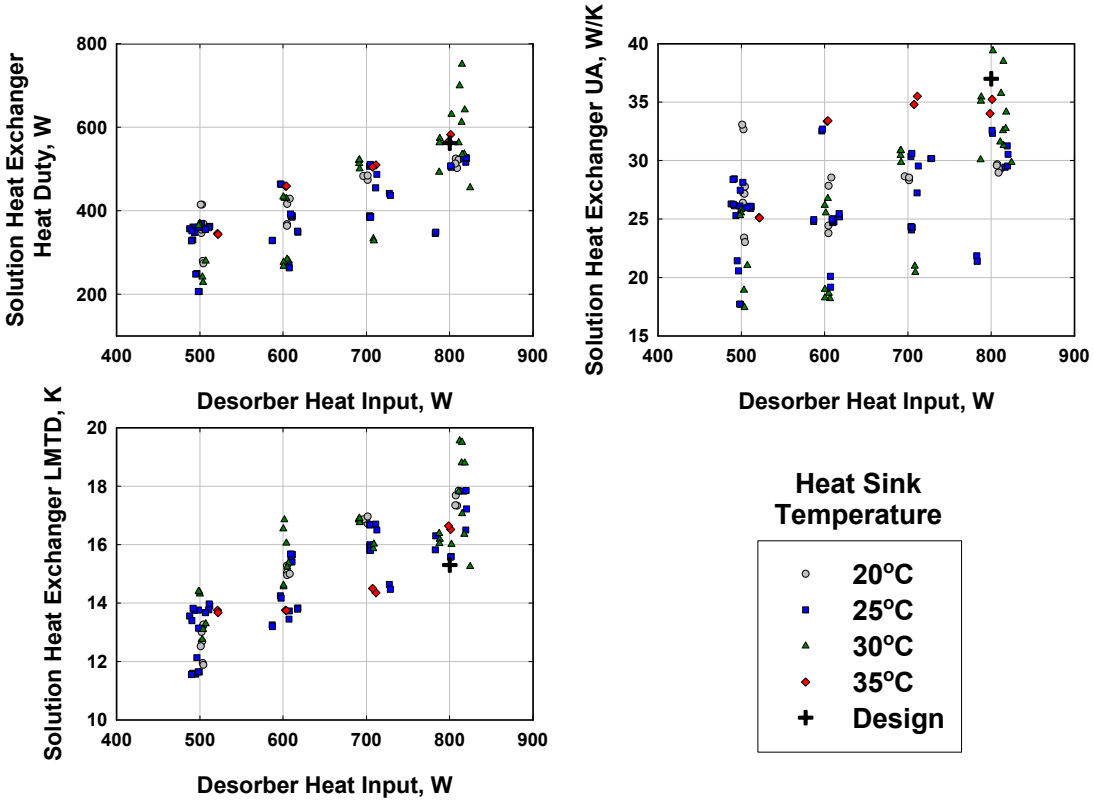

Figure 5-19 Solution Heat Exchanger Heat Duty, UA, and LMTD versus Desorber Heat Input

$$\varepsilon_{SHX} = \frac{T_{SHX,DS,In} - T_{SHX,DS,Out}}{T_{SHX,DS,In} - T_{SHX,CS,In}} \tag{5.14}$$

The effectiveness of the solution heat exchanger is plotted versus concentrated solution volume flowrate in Figure 5-20.

5.5.4 Evaporator

The evaporator coolant inlet and outlet temperatures were 12.5°C and 7.1°C, respectively. The refrigerant inlet temperature was -1.3°C, while the outlet was 16.8°C. The evaporator chilled water and refrigerant heat duties were calculated as follows.

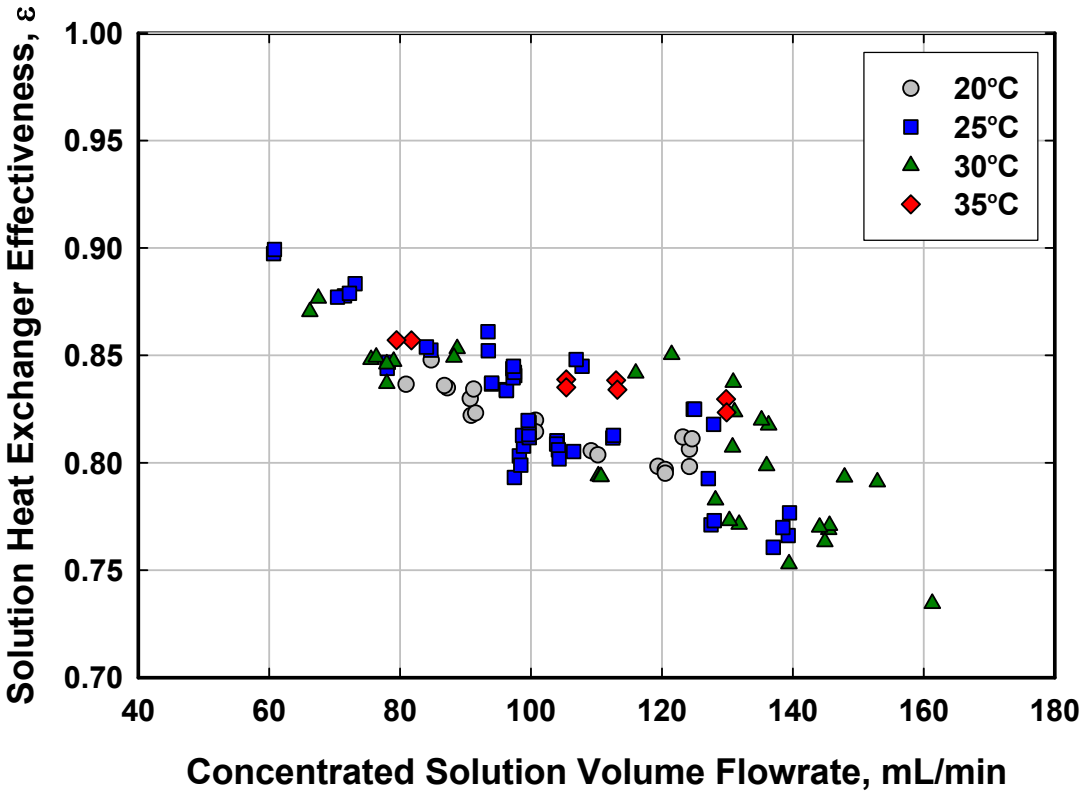

Figure 5-20 Solution Heat Exchanger Effectiveness versus Concentrated Solution Flowrate

$$\dot{Q}_{Evap,Coolant} = \dot{m}_{Evap,Coolant} \cdot \left(h_{Evap,Coolant,Out} - h_{Evap,Coolant,In} \right) \tag{5.15}$$

$$\dot{Q}_{Evap,Ref} = \dot{m}_{Ref} \cdot \left(h_{Evap,Ref,Out} - h_{Evap,Ref,In} \right) \tag{5.16}$$

The evaporator coolant and refrigerant heat duties for the sample calculation are 239 W and 170 W respectively. Due to the uncertainty associated with the evaporator refrigerant heat duty calculation, the chilled water heat duty was used to describe the performance of the evaporator. The LMTD for the evaporator was calculated as follows:

$$LMTD_{Evap} = \frac{\left(T_{Evap,Coolant,In} - T_{Evap,Ref,In} \right) - \left(T_{Evap,Coolant,Out} - T_{Evap,Ref,In} \right)}{\mathrm{Ln}\left[\frac{\left(T_{Evap,Coolant,In} - T_{Evap,Ref,In} \right)}{\left(T_{Evap,Coolant,Out} - T_{Evap,Ref,In} \right)} \right]} \tag{5.17}$$

To provide a better estimate of the average temperature difference in the evaporator, the refrigerant inlet temperature is used in place of the refrigerant outlet temperature to account for the large temperature rise at higher refrigerant vapor qualities. This modification represents the case of an evaporator with a fluid undergoing constant temperature phase change. Due to the internal conduction of heat from the desorber to the evaporator, the evaporator refrigerant outlet temperature was higher than the coolant inlet temperature. The evaporator UA is calculated as follows.

$$UA_{Evap,Coolant} = \frac{\dot{Q}_{Evap}}{LMTD_{Evap}} \tag{5.18}$$

For the sample calculation, the evaporator LMTD and UA were 10.9°C and 21.9 W/K, respectively. The design point LMTD and UA were 2.2°C and 185 W/K, respectively. Figure 5-21 shows the experimental evaporator heat duty, UA and LMTD for all of the experiments.

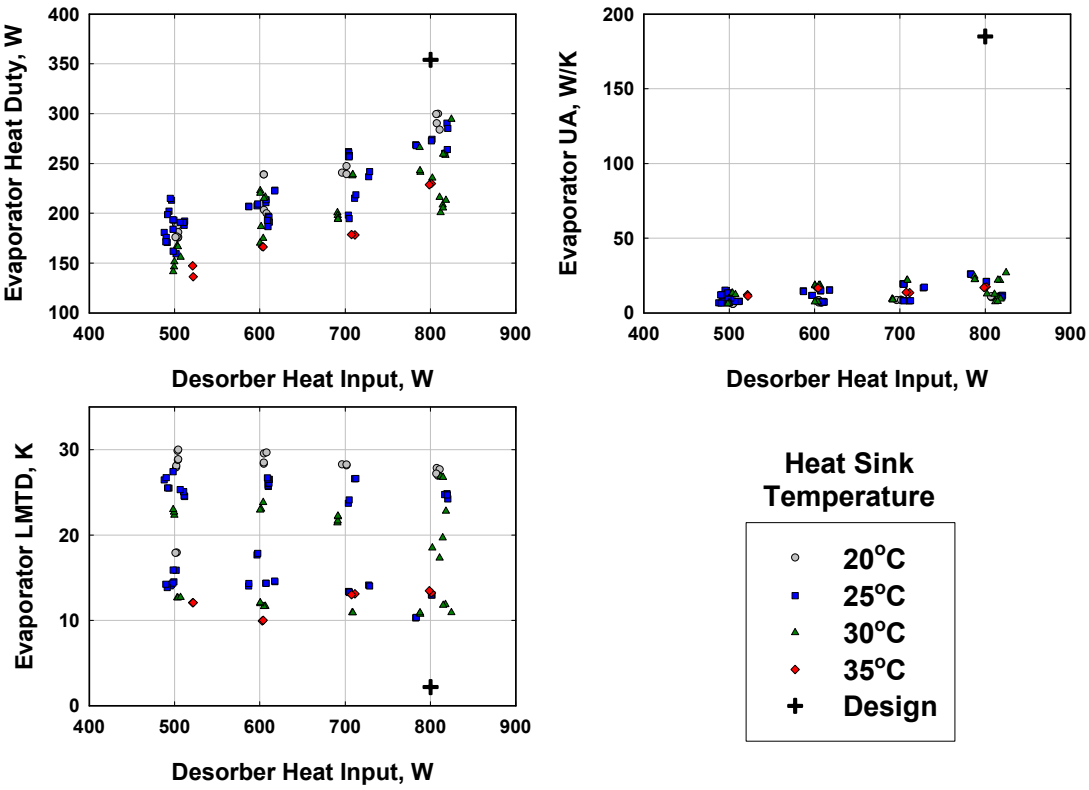

Figure 5-21 Evaporator Heat Duty, UA, and LMTD versus Desorber Heat Input

The evaporator heat duty was lower than the design conditions due to the lower than expected refrigerenat concentration, ambient heat losses/gains, and the internal conduction between components. The large range in LMTD for a set desorber heat input and constant heat sink temperature is caused by differences in the concentrated solution concentrations. Increasing the concentrated solution concentration increases the saturation temperature of the absorber outlet which determines the low side operating pressure and thus the evaporating temperature of the refrigerant in the evaporator. Interestingly, the large variability in the evaporator temperature difference did not affect the evaporator cooling capacity or COP significantly. This was due to the original design of the evaporator requiring a small temperature difference and hence a very large UA

value. The calculation of the experimental LMTD value used the refrigerant inlet temperature at the inlet and outlet of the evaporator, leading to a larger LMTD and a smaller UA than the design condition.

5.5.5 Rectifier

The rectifier coolant inlet and outlet temperatures were 30.1°C and 36.5°C, respectively. The rectifier coolant heat duty was calculated as follows.

$$\dot{Q}_{Rec,Coolant} = \dot{m}_{Rec,Coolant}\left(h_{Rec,Coolant,Out} - h_{Rec,Coolant,In}\right) \tag{5.19}$$

For the example calculation, the rectifier heat duty was 139 W. The LMTD was calculated using the coolant inlet and outlet temperatures as well as the refrigerant outlet, 102.2°C, and the dilute solution outlet temperature, 115.4°C.

$$LMTD_{Rec} = \frac{\left(T_{Rec,DS,Out} - T_{Rec,Coolant,Out}\right) - \left(T_{Rec,Ref,Out} - T_{Rec,Coolant,In}\right)}{\mathrm{Ln}\left[\frac{\left(T_{Rec,DS,Out} - T_{Rec,Coolant,Out}\right)}{\left(T_{Rec,Ref,Out} - T_{Rec,Coolant,In}\right)}\right]} \tag{5.20}$$

The overall conductance was calculated from the heat duty and the LMTD.

$$UA_{Rec} = \dot{Q}_{Rec} / LMTD_{Rec} \tag{5.21}$$

The LMTD and UA for the sample data point were 75.4°C and 1.8 W/K. The design point LMTD and UA were 47.7°C and 3.4 W/K, respectively. Figure 5-22 illustrates the rectifier heat duty, UA and LMTD for all of the experimental data points. Even though the rectifier was tested with an externally coolant instead of the solution coolant as it was designed, the design points are still used for comparison. Although the rectifier heat duty was very near the design point, it still failed to provide the required purification of the

refrigerant stream. This indicates that the reflux was actually being sub-cooled inside the rectifier but was not coming to a thermal equilibrium with the vapor stream.

The purity of the refrigerant did not cause cycle operation problems due to the once-through flow arrangement of the evaporator, but it does incur a COP penalty. The water vapor carried along with the refrigerant required a significant amount of energy to convert from liquid to vapor in the desorber. This water then passes through the evaporator as a liquid, failing to produce any useful cooling effect.

Of the major components in the system, the absorber, solution heat exchanger, and condenser functioned very close to, or better than their design conditions. The rectifier, while it provided adequate purification of the refrigerant stream at lower

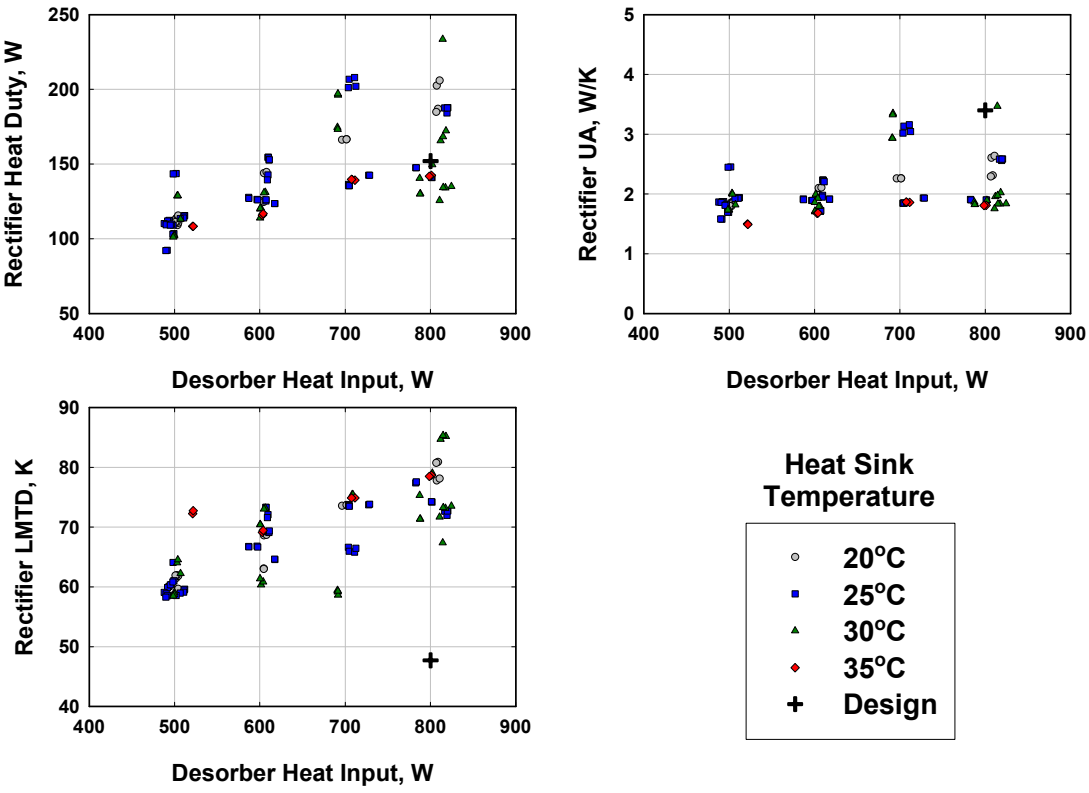

Figure 5-22 Rectifier Heat Duty, UA, and LMTD versus Desorber Heat Input

desorber heat input rates, was unable to purify the vapor at higher heat input rates. This limited the testing of the system to desorber heat duties of 800 W and less.

6 Conclusions and Recommendations

6.1 Conclusions

A comprehensive study of a miniaturized thermally activated cooling system was conducted. This study represents the first work to conceptualize, design, fabricate and successfully test a thermally activated cooling system for mobile applications. Thermally activated systems have the ability to produce useful cooling from waste heat streams or directly from the combustion of liquid fuels. Numerous concepts of miniaturized or mobile, active cooling systems exist in the literature but up to this point, successful fabrication and testing has not been documented.

During this study, a breadboard absorption heat pump system was fabricated from off the shelf or in-house, custom-built components. The breadboard system was used to validate the feasibility of operating an absorption heat pump with a cooling capacity in the range of 300 W. The breadboard system was used to evaluate the necessary components such as fluid control valves and pumps for use in a small scale absorption heat pump.

A methodology was outlined for designing the miniaturized absorption heat pump. The thermodynamic cycle analysis was presented and the heat exchanger sizing calculations were reported. This design method can be used by engineers, with the necessary adjustments for any different flow geometries that are incorporated, for designing future generations of miniaturized absorption heat pumps.

The unique ammonia water absorption heat pump system in this study utilized microchannel (D_h = 306 μm) heat exchangers to facilitate the miniaturization of the system. The system was fabricated using a manufacturing process that allowed all of the heat exchangers to be integrated into a single component. The fluid channels for each individual heat exchanger were chemically etched on 0.5 mm thick stainless still sheets and then 40 sheets were joined together in a diffusion bonding process. While this manufacturing method introduced several challenges to the experiments, it was necessary to demonstrate the potential for further reducing the system mass. The overall dimensions of the heat exchanger portion of the system are 200 × 200 × 34 mm with a mass of 7 kg.

Testing of the absorption heat pump was conducted over a range of heat sink temperatures ($20 \leq T \leq 35$°C) and desorber thermal input rates ($500 \leq \dot{Q}_{Des} \leq 800$ W). Evaporator inlet and outlet coolant temperatures were maintained at nominal values of 12.8 and 7.2°C, respectively to simulate expected operating conditions. Evaporator coolant heat duties in the study ranged from 136 to 300 W, while system COPs ranged from 0.247 to 0.434. At a nominal rating condition of 35°C heat sink temperature, the maximum thermal input of 800 W produced a cooling effect of 230 W. This represents a cycle COP of 0.29.

The cycle analysis indicated that poor vapor rectification at the highest thermal input rates limited the operating range of the system. The co-flow desorption process in the microchannels limits the refrigerant outlet concentrations to lower values than would be attainable in counter-flow desorbers.

The results of this study are the first experimental data of any miniaturized or mobile absorption heat pump. This study also presents a detailed design methodology for future mobile thermally activated heat pumps of varying capacities.

6.2 Recommendations

The present study is a major advance in the field of miniaturized energy systems, specifically absorption heat pumps and mobile cooling systems. However, due to the nature of a study involving a first prototype, there is room for further advancement in follow on work. Also, during the course of this work there were several branches of research that could not be fully explored due to various constraints. The following are recommendations for future work that will enhance the understanding and utility of miniaturized cooling systems.

During the design phase of the project, experimental necessity dictated that every fluid connection between components was made external to the system. This constraint required excessive spacing of the fluid connections to allow room for the fittings that would need to be attached to the system as well as the tools to attach them. Internal fluid connections would significantly reduce the systems mass by substantially reducing the spacing between components. Reducing the spacing of the components would allow smaller bridges between components on the individual sheets which provide the required structural support during the manufacturing process. Reducing or eliminating the bridges would reduce the internal conduction of heat between components. Reducing the overall size of the system and eliminating the external tubing will also reduce heat losses to the ambient.

The inability of the rectifier to sufficiently purify the refrigerant stream at desorber heat inputs above 800 Watts limited the range of conditions that could be tested. Even at the lower heat input rates, the refrigerant concentration was only modestly purified. In future prototypes, an improved design of the rectifier is warranted. New flow geometers should be considered to further enhance the heat and mass transfer between the reflux liquid and the refrigerant vapor. Another option to reduce the load on the rectifier is to incorporate a liquid-vapor counter flow desorber into the device. This would increase the concentration of the vapor leaving the desorber, thus reducing the need for rectification. Incorporation of such a flow scheme in a microchannel device may prove quite challenging.

The desorber and rectifier combination proved to be such a critical component in this system that it may warrant investigations of these components separate from the rest of the cycle in order to isolate and overcome the challenges they present. The original design of the prototype in this study used a solution cooled rectifier. This did not allow sufficient control of the rectifier cooling load for stable operation of the system, so it was replaced with an external cooling fluid. This modification reduced the amount of beneficial internal heat recovery in the system, thereby causing a reduction in the COP. Future designs should again attempt to use a solution cooled rectifier and should also attempt to take advantage of the internal conduction paths in the system rather than only attempting to eliminate them. Most deviations from the simplest absorption cycle configuration are attempts to recuperate heat internal to the absorption system so there is no reason the conduction paths in future devices can not be used to advantage.

The stable control of the system during testing was an operational challenge. The unique dynamics of absorption systems demand a closer investigation and integration of control systems into this energy system. For mobile absorption cycles to be used successfully in the field by unskilled operators, a very robust control scheme must be included with the system. This would require automated control of solution and refrigerant expansion valves as well as the solution pump. Long duration laboratory testing would also benefit from an independent control system.

Transition of the miniaturized absorption heat pump from laboratory prototype to commercial waste heat recovery system requires the incorporation of a fluid stream to provide the heat input to the desorber. For example, the waste heat from a vehicle engine would be in the form of engine coolant or exhaust gas. In this study, electrical resistance heaters were used to simplify the experimental facilities. Future work should incorporate more realistic coupling to the waste heat source.

The heat exchanger design process in this study considered the heat exchanger as a single area with the heat transfer coefficient evaluated at a representative location. Detailed segmental analysis of each of the components would contribute to more accurate designs for future devices. The segmental approach would limit the effects of the non-constant heat capacities of the fluid streams on the heat exchanger calculations and provide improved designs. Consideration of the mass transfer resistances in appropriate components would also enhance the design process. The heat exchangers in this prototype were all fabricated with similar channel dimensions. In future prototypes, the exact channel dimensions of each component should be optimized for producing the most

compact overall system. The number of channels for either side of every heat exchanger could be customized to increase component and system efficiency.

With respect to the manufacturing techniques used in this work, a systematic investigation of diffusion bonding of heat exchangers is required to determine suitable channel configurations. The channel configuration used in this study was based on prior work in the literature on diffusion bonding and proved inadequate. The cross leakage between sides of heat exchangers experienced in this study was very small but will need to be reduced in any commercial applications. Destructive testing of the heat exchangers at elevated pressures will also increase the knowledge of the design limits of diffusion bonded heat exchangers. Investigation of the use of interface materials in diffusion bonding is also warranted.

Further work would also benefit from the development of new measurement techniques. Analysis of the operating conditions of the system relies on saturation assumptions to determine concentrations. In situ measurement of ammonia concentrations for real-time analysis and elimination of saturation assumptions would greatly enhance the results of future work. The uncertainty of small heat duty measurement needs to be addressed to enhance investigations of further miniaturization of absorption systems.

It is estimated that a system similar to the one in this study which incorporates the recommendations listed here including making all fluid connections internal to the sytem, could achieve the same cooling capacity, with a system mass of 2.5 – 3.5 kg in a envelope of 120 × 120 × 25 mm.

Appendix A Breadboard Experimental Facility Details

A.1 Breadboard Experimental Component Details

Table A-1 Absorber Details

Characteristic	Value
Heat Exchanger Type	Finned Tube
Flow Configuration	Cross Flow
Tube Material	Stainless Steel
Fin Material	Copper
Manufacturer	Lytron Inc.
Model #	4105G1SB
Quantity	2
Tube Diameter	9.525 mm
Tube Wall Thickness	0.71 mm
Tube Passes	6
Tube Pitch	21.84 mm
Fin Thickness	0.19 mm
Fin Width	19.82 mm
Fin Length	139.7 mm
Number of Fins	76
Air Side Heat Transfer Area	0.376 m^2
Overall Heat Exchanger Dimmensions	194 × 167 × 33 mm

Table A-2 Solution Heat Exchanger Details

Characteristic	Value
Heat Exchanger Type	Shell and Tube
Flow Configuration	Counter Flow
Material	Stainless Steel
Manufacturer	Exergy, Inc.
Model #	00540-3
Tube Outside Diameter	2.4 mm
Tube Wall Thickness	0.25 mm
Tube Length	406 mm
Tube Count	37
Shell Outside Diameter	25 mm
Baffle Count	13
Heat Transfer Area	0.11 m^2

Table A-3 Desorber Details

Characteristic	Value
Heater Type	Nickel-Chromium Resistance Wire Immersion Heater
Sheath Material	Stainless Steel
Manufacturer	Watlow
Model #	L6EX16B
Diameter	15.875 mm
Length	159 mm
Volts	120
Watts	1000

Table A-4 Rectifier Details

Characteristic	Value
Heat Exchanger Type	Tube-in-Tube
Flow Configuration	Counter Flow
Material	Stainless Steel
Manufacturer	In-House
Inner Tube Outside Diameter	6.35 mm
Inner Tube Wall Thickness	0.89 mm
Inner Tube Length	230 mm
Outer Tube Outside Diameter	12.7 mm
Outer Tube Wall Thickness	0.89 mm
Heat Transfer Area	4.59×10^{-3} m^2

Table A-5 Condenser Details

Characteristic	Value
Heat Exchanger Type	Finned Tube
Flow Configuration	Cross Flow
Tube Material	Stainless Steel
Fin Material	Aluminum
Manufacturer	In-House
Tube Outside Diameter	12.7 mm
Tube Wall Thickness	0.89 mm
Tube Passes	2 Parallel Tubes
Tube Pitch	72.4 mm
Fin Thickness	0.8 mm
Fin Width	25.4 mm
Fin Length	127 mm
Number of Fins	45
Air Side Heat Transfer Area	0.277 m^2
Overall Heat Exchanger Dimmensions	180 × 127 × 25.4 mm

Table A-6 Evaporator 1 Dimensional Details

Characteristic	Value
Heat Exchanger Type	Tube-in-Tube
Flow Configuration	Counter Flow
Material	Stainless Steel
Manufacturer	In-House
Inner Tube Outside Diameter	6.35 mm
Inner Tube Wall Thickness	0.89 mm
Inner Tube Length	435 mm
Outer Tube Outside Diameter	12.7 mm
Outer Tube Wall Thickness	2.1 mm
Heat Transfer Area	8.7×10^{-3} m^2

Table A-7 Evaporator 2 Dimensional Details

Characteristic	Value
Heat Exchanger Type	Tube-in-Tube
Flow Configuration	Counter Flow
Material	Stainless Steel
Manufacturer	In-House
Inner Tube Outside Diameter	6.35 mm
Inner Tube Wall Thickness	0.89 mm
Inner Tube Length	485 mm
Outer Tube Outside Diameter	12.7 mm
Outer Tube Wall Thickness	0.89 mm
Heat Transfer Area	9.7×10^{-3} m^2

Table A-8 Refrigerant Heat Exchanger Dimensional Details

Characteristic	Value
Heat Exchanger Type	Tube-in-Tube
Flow Configuration	Counter Flow
Material	Stainless Steel
Manufacturer	In-House
Inner Tube Outside Diameter	6.35 mm
Inner Tube Wall Thickness	0.89 mm
Inner Tube Length	190 mm
Outer Tube Outside Diameter	12.7 mm
Outer Tube Wall Thickness	0.89 mm
Heat Transfer Area	3.8×10^{-3} m^2

Table A-9 Solution Pump Details

Characteristic	Value
Manufacturer	Tuthill Corporation
Pump Type	Magnetic Coupled External Gear Pump
Model Number	DGS.38EEET1NN37000
Serial Number	A31503
Wetted Materials	Stainless Steel, PEEK, Teflon
Maximum Flowrate	76 L/hr
Maximum Differential Pressure	1720 kPa
Temperature Range	-46°C to 176°C
Motor Type	Variable Speed Brushless DC
Motor Voltage	24 VDC
Motor Power	75 W
Maximum Speed	4600 RPM

Table A-10 DC Power Supply Details

Characteristic	Value
Manufacturer	International Power
Model Number	CC
Input	120 VAC
Output	24 VDC
Max Temperature	50°C

Table A-11 Data Acquisition Hardware Details

Characteristic	Value
Manufacturer	IOTech
DAQ Model Number	Personal DAQ/56
DAQ Serial Number	262048
Expansion Module Model Number	PDQ2
Expansion Module Serial Number	260689

Table A-12 Refrigerant and Solution Expansion Valve Details

Characteristic	Value
Manufacturer	Swagelok
Valve Type	S Series Needle Metering Valve
Model Number	SS-SS4-VH-NE
Wetted Materials	Stainless Steel, Neoprene, Teflon, Glass Filled PTFE
Temperature Range	-23°C to 121°C
Maximum Working Pressure	13.7 MPa
Orifice Size	0.81 mm
C_V Range	0.0001 to 0.004

Table A-13 Concentrated Solution Flowmeter Details

Characteristic	Value
Manufacturer	DEA Engineering
Flowmeter Type	Nutating Microflowmeter
Model Number	FMTE20
Serial Number	8046
Wetted Materials	Stainless Steel, Teflon
Flowrate Range	5-1250 mL/min
Maximum Working Pressure	3447 kPa
Output Signal	0-5 Volt Square Wave
Repeatability	±0.1%
Accuracy	±0.5%
Calibration Factor	10.65 pulses/mL

Table A-14 Dilute Solution Flowmeter Details

Characteristic	Value
Manufacturer	DEA Engineering
Flowmeter Type	Nutating Microflowmeter
Model Number	FMTE20
Serial Number	8047
Wetted Materials	Stainless Steel, Teflon
Flowrate Range	5-1250 mL/min
Maximum Working Pressure	3447 kPa
Output Signal	0-5 Volt Square Wave
Repeatability	±0.1%
Accuracy	±0.5%
Calibration Factor	10.57 pulses/mL

Table A-15 Evaporator Chilled Water Flowmeter Details

Characteristic	Value
Manufacturer	Key Instruments
Flowmeter Type	Rotameter
Series	MR3000
Model Code	3L22
Wetted Materials	Stainless Steel, Viton
Flowrate Range	4-40 gph
Maximum Working Pressure	690 kPa
Maximum Fluid Temperature	65°C
Repeatability	±0.1%
Accuracy	±4% Full Scale

Table A-16 Condenser Inlet Pressure Transducer Details

Characteristic	Value
Manufacturer	WIKA
Model Number	S-10
Serial Number	2603LRK
Wetted Materials	Stainless Steel
Pressure Range	0-3447.4 kPa
Power Supply	10-30 VDC
Output Signal	4-20 mA
Repeatability	±0.05% of span
Accuracy	±0.25% of span
Media Temperature Range	-40°C to 100°C

Table A-17 Absorber Inlet Pressure Transducer Details

Characteristic	Value
Manufacturer	WIKA
Model Number	S-10
Serial Number	2603LRN
Wetted Materials	Stainless Steel
Pressure Range	0-3447.4 kPa
Power Supply	10-30 VDC
Output Signal	4-20 mA
Repeatability	±0.05% of span
Accuracy	±0.25% of span
Media Temperature Range	-40°C to 100°C

Table A-18 Evaporator Inlet Pressure Transducer Details

Characteristic	Value
Manufacturer	WIKA
Model Number	ECO-1
Serial Number	4882574
Wetted Materials	Stainless Steel
Pressure Range	0-689.5 kPa
Power Supply	10-30 VDC
Output Signal	4-20 mA
Repeatability	±0.1% of span
Accuracy	±0.5% of span
Media Temperature Range	-40°C to 100°C

Table A-19 Thermocouple Details

Characteristic	Value
Type	T (Copper-Constantan)
Manufacturer	Omega
Model Number ($1/16^{th}$ in. diameter)	TMQSS-062G-6
Model Number ($1/8^{th}$ in. diameter)	TMQSS-125G-6
Sheath Material	Stainless Steel
Sheath Length	152.4 mm
Accuracy	±0.5°C

Table A-20 Variable Voltage Transformer Details

Characteristic	Value
Manufacturer	Staco Energy Products Co.
Model Number	L1010B
Input Voltage	120 VAC
Output Voltage	0-140 VAC
Maximum Amperage	10 Amps
Maximum KVA	1.4 kVA

Table A-21 Desorber AC Watt Transducer Details

Characteristic	Value
Type	Hall-effect
Manufacturer	Ohio Semitronics, Inc.
Model Number	PC5-0198E
Serial Number	06031222
Sensor Power Supply	120 V
Voltage Range	0-150 VAC
Amperage Range	0-15 Amps
Full Scale Wattage	1500 Watts
Output Signal	4-20 mA
Accuracy	±0.5% Full Scale

Table A-22 Refrigerant and Solution Sight Glasses

Characteristic	Value
Type	Bull's Eye Sight Flow Indicator
Manufacturer	Pressure Products
Drawing Number	G016C26B
Serial Numbers	XBGG-13410, XBGG-13411
Body Material	Stainless Steel
Packing and Gasket Material	Teflon PTFE
Lens Material	Tempered Borosilicate
Maximum Pressure Rating	2068 kPa @ 232°C

A.2 Breadboard Experimental Data Analysis

Table A-23 Example Breadboard System Data Analysis and Uncertainty Calculation

Input	Equations	Output
$T_{Des,DS,Out}$ = 120.4±0.5°C P_{High} = 1669±8.6 kPa $q_{Des,DS,Out}$ = 0	$x_{DS} = f\left(T_{Des,DS,Out}, P_{High}, q_{Des,DS,Out}\right)$	x_{DS} = 32.7±0.2%
$T_{SHX,DS,Out}$ = 63.7±0.5°C P_{High} = 1669±8.6 kPa x_{DS} = 32.7±0.2% $\dot{V}_{DS}$ =140.5±0.7 mL/min	$v_{SHX,DS,Out} = f\left(T_{SHX,DS,Out}, P_{High}, x_{DS}\right)$ $\dot{m}_{DS} = \frac{\dot{V}_{DS}}{v_{SHX,DS,Out}} \cdot \left(\frac{1\ \text{m}^3}{1\text{E6 mL}} \frac{1\ \text{min}}{60\ \text{sec}}\right)$	$v_{SHX,DS,Out}$ = 1.166×10^{-3} ±1.3×10^{-6} m^3/kg $\dot{m}_{DS} = 2.01\times10^{-3}\pm1.0\times10^{-5}$ kg/s
$T_{Rec,Ref,Out}$ = 73.7±0.5°C P_{High} = 1669±8.6 kPa $q_{Rec,Rec,Out}$ = 1	$x_{Ref} = f\left(T_{Rec,Ref,Out}, P_{High}, q_{Rec,Ref,Out}\right)$	x_{Ref} = 99.3±0.03%
$T_{Abs,CS,Out}$ = 42.0±0.5°C P_{Low} = 403±8.6 kPa $\dot{V}_{CS}$ =174±0.9 mL/min $\dot{m}_{DS} = 2.01\times10^{-3}\pm1.0\times10^{-5}$ kg/s x_{DS} = 32.7±0.2% x_{Ref} = 99.3±0.03%	$v_{Abs,CS,Out} = f\left(T_{Abs,CS,Out}, P_{Low}, x_{CS}\right)$ $\dot{m}_{CS} = \frac{\dot{V}_{CS}}{v_{Abs,CS,Out}} \cdot \left(\frac{1\ \text{m}^3}{1\text{E6 mL}} \frac{1\text{min}}{60\ \text{sec}}\right)$ $\dot{m}_{CS} = \dot{m}_{DS} + \dot{m}_{Ref}$ $\dot{m}_{CS} \cdot x_{CS} = \dot{m}_{DS} \cdot x_{DS} + \dot{m}_{Ref} \cdot x_{Ref}$	x_{CS} = 44.1±0.4% $v_{Avs,DS,Out}$ = 1.197×10^{-3} ±2.0×10^{-6} m^3/kg $\dot{m}_{CS} = 2.42\times10^{-3}\pm1.0\times10^{-5}$ kg/s $\dot{m}_{Ref} = 0.41\times10^{-3}\pm1.2\times10^{-5}$ kg/s

Table A-23 Continued

Input	Equations	Output
$T_{Evap,Ref,In}$ = -1.0±0.5°C $T_{Evap,Ref,Out}$ = 11.6±0.5°C P_{Evap} = 409±3.4 kPa $\dot{m}_{Ref}$ =0.41×10^{-3}±1.2×10^{-5} kg/s	$h_{Evap,Ref,In} = f\left(T_{Evap,Ref,In}, P_{Evap}, x_{Ref}\right)$ $h_{Evap,Ref,Out} = f\left(T_{Evap,Ref,Out}, P_{Evap}, x_{Ref}\right)$ $\dot{Q}_{Evap,Ref} = \dot{m}_{Ref} \cdot \left(h_{Evap,Ref,Out} - h_{Evap,Ref,In}\right) \cdot \left(\frac{1000\ \text{W}}{1\ \text{kW}}\right)$	$h_{Evap,Ref,In}$ = 398±1800 kJ/kg $h_{Evap,Ref,Out}$ = 1268±2.4 kJ/kg $\dot{Q}_{Evap,Ref}$ = 360±75 W
$T_{Evap,Coolant,In}$ = 16.2±0.5°C $T_{Evap,Coolant,Out}$ = 12.3±0.5°C $\dot{V}_{Evap,Coolant}$ = 20±1.6 GPH	$v_{Evap,Coolant,In} = f\left(T_{Evap,Coolant,In}, P = 101.3\ \text{kPa}\right)$ $\dot{m}_{Evap,Coolant} = \frac{\dot{V}_{Evap,Coolant}}{v_{Evap,Coolant,In}} \cdot \left(\frac{1\ \text{m}^3}{264.17\ \text{Gal}} \frac{1\ \text{hr}}{3600\ \text{sec}}\right)$ $h_{Evap,Coolant,In} = f\left(T_{Evap,Coolant,In}, P = 101.3\ \text{kPa}\right)$ $h_{Evap,Coolant,Out} = f\left(T_{Evap,Coolant,Out}, P = 101.3\ \text{kPa}\right)$ $\dot{Q}_{Evap,Coolant} = \dot{m}_{Evap,Coolant} \cdot \left(h_{Evap,Coolant,Out} - h_{Evap,Coolant,In}\right) \cdot \left(\frac{1000\ \text{W}}{1\ \text{kW}}\right)$	$v_{Evap,Coolant,In}$ = 1.0×10^{-3} ±8.2×10^{-8} m^3/kg $\dot{m}_{Evap,Coolant}$ = 21×10^{-3} ± 1.7×10^{-3} kg/s $h_{Evap,Coolant,In}$ = 68.0±2.1 kJ/kg $h_{Evap,Ref,Out}$ = 51.9±2.1 kJ/kg $\dot{Q}_{Evap,Coolant}$ = -339±68 W
$\dot{Q}_{Des}$ = 931±7.5 W $\dot{Q}_{Evap,Coolant}$ = -339±68 W	$COP_{Cooling} = \frac{\left\lvert\dot{Q}_{Evap,Coolant}\right\rvert}{\dot{Q}_{Des}}$	$COP_{Cooling}$ = 0.36±0.07

Appendix B Microchannel System Details

B.1 Microchannel System Design

Table B-1 Microchannel System, Thermodynamic Design Point Calculations

Input	Equations	Output
$\dot{m}_{CS} = 2.7\times10^{-3}$ kg/s $x_{cs} = 0.37$ $P_{Low} = 400$ kPa $T_{Abs,CS,Out} = 50.4°C$	$h_{Abs,CS,Out} = f(T_{Abs,CS,Out}, P_{Low}, x_{CS})$ $s_{Abs,CS,Out} = f(T_{Abs,CS,Out}, P_{Low}, x_{CS})$	$h_{Abs,CS,Out} = 2.6$ kJ/kg $s_{Abs,CS,Out} = 0.616$ kJ/kg-K
$s_{Abs,CS,Out} = 0.616$ kJ/kg-K $P_{High} = 1600$ kPa $x_{cs} = 0.37$	$h_{Rec,CS,In,s} = f(s_{Abs,CS,Out}, P_{High}, x_{CS})$	$h_{Rec,CS,In,s} = 4.0$ kJ/kg
$\eta_{pump} = 0.5$ $h_{Abs,CS,Out} = 2.6$ kJ/kg $h_{Rec,CS,In,s} = 4.0$ kJ/kg $\dot{m}_{CS} = 2.7\times10^{-3}$ kg/s	$\eta_{pump} = \frac{h_{rec,CS,In,s} - h_{Abs,CS,Out}}{h_{rec,CS,In} - h_{Abs,CS,Out}}$ $\dot{W}_{Pump} = \dot{m}_{CS}\left(h_{Rec,CS,In} - h_{Abs,CS,Out}\right)$	$h_{Rec,CS,In} = 5.4$ kJ/kg $\dot{W}_{Pump} = 7.6$ W
$\dot{m}_{CS} = 2.7\times10^{-3}$ kg/s $h_{Rec,CS,In} = 5.4$ kJ/kg $\dot{Q}_{Rec,CS} = 152.4$ W	$\dot{Q}_{Rec,CS} = \dot{m}_{CS}\left(h_{SHX,CS,In} - h_{Rec,CS,In}\right)$ $T_{SHX,CS,In} = f(h_{SHX,CS,In}, P_{High}, x_{CS})$	$h_{SHX,CS,In} = 61.9$ kJ/kg $T_{SHX,CS,In} = 63.6$ °C

Table B-1 Continued

Input	Equations	Output
$T_{SHX,CS,Out} = 109°C$ $P_{High} = 1600$ kPa $x_{CS} = 0.37$ $\dot{m}_{CS} = 2.7\times10^{-3}$ kg/s	$h_{SHX,CS,Out} = f(T_{SHX,CS,Out}, P_{High}, x_{CS})$ $\dot{Q}_{SHX,CS} = \dot{m}_{CS}\left(h_{SHX,CS,Out} - h_{SHX,CS,In}\right)$	$h_{SHX,CS,Out} = 269.9$ kJ/kg $\dot{Q}_{SHX,CS} = 562$ W
$\dot{Q}_{Des,CS} = 800$ W $\dot{m}_{CS} = 2.7\times10^{-3}$ kg/s $P_{High} = 1600$ kPa $h_{SHX,CS,Out} = 269.9$ kJ/kg	$\dot{Q}_{Des,CS} = \dot{m}_{CS}\left(h_{Des,Out} - h_{SHX,CS,Out}\right)$ $T_{Des,out} = f(h_{Des,Out}, P_{High}, x_{CS})$ $q_{Des,out} = f(h_{Des,Out}, P_{High}, x_{CS})$	$h_{Des,Out} = 566.2$ kJ/kg $T_{Des,Out} = 128.2°C$ $q_{Des,Out} = 0.14$
$T_{Des,Out} = 128.2°C$ $P_{High} = 1600$ kPa $q_{Rec,Vap,In} = 1$ $q_{Des,Out} = 0.14$ $\dot{m}_{CS} = 2.7\times10^{-3}$ kg/s	$T_{Rec,Vap,In} = T_{Des,Out}$ $h_{Rec,Vap,In} = f(T_{Rec,Vap,In}, P_{High}, q_{Rec,Vap,In})$ $x_{Rec,Vap,In} = f(T_{Rec,Vap,In}, P_{High}, q_{Rec,Vap,In})$ $\dot{m}_{Rec,Vap,In} = \dot{m}_{CS} \cdot q_{Des,Out}$	$T_{Rec,Vap,In} = 128.2°C$ $h_{Rec,Vap,In} = 1672$ kJ/kg $x_{Rec,Vap,In} = 0.876$ $\dot{m}_{Rec,Vap,In} = 0.39\times10^{-3}$ kg/s
$T_{Rec,Ref,Out} = 85°C$ $P_{High} = 1600$ kPa $q_{Rec,Ref,Out} = 1$	$h_{Rec,Ref,Out} = f(T_{Rec,Ref,Out}, P_{High}, q_{Rec,Ref,Out})$ $x_{Ref} = f(T_{Rec,Ref,Out}, P_{High}, q_{Rec,Ref,Out})$	$h_{Rec,Ref,Out} = 1442$ kJ/kg $x_{Ref} = 0.984$

Table B-1 Continued

Input	Equations	Output
$T_{Rec,Vap,In}$ =128.2°C P_{High} = 1600 kPa $q_{Rec,Reflux,Out}$ = 0	$T_{Rec,Reflux,Out} = T_{Rec,Vap,In}$ $h_{Rec,Reflux,Out} = f(T_{Rec,Reflux,Out}, P_{High}, q_{Rec,Reflux,Out})$ $x_{Rec,Reflux,Out} = f(T_{Rec,Reflux,Out}, P_{High}, q_{Rec,Reflux,Out})$	$h_{Rec,Reflux,Out}$ = 381.1 kJ/kg $x_{Rec,Reflux,Out}$ = 0.285
$\dot{m}_{Rec,Vap,In} = 0.39\times10^{-3}$ kg/s $x_{Rec,Vap,In}$ = 0.876 x_{Ref} = 0.984 $x_{Rec,Reflux,Out}$ = 0.285	$\dot{m}_{Rec,Vap,In} = \dot{m}_{ref} + \dot{m}_{Rec,Reflux,Out}$ $\dot{m}_{Rec,Vap,In} \cdot x_{Rec,Vap,In} =$ $\dot{m}_{Ref} \cdot x_{Ref} + \dot{m}_{Rec,Reflux,Out} \cdot x_{Rec,Reflux,Out}$	$\dot{m}_{Ref} = 0.33\times10^{-3}$ kg/s $\dot{m}_{Rec,Reflux,Out} = 60.0\times10^{-6}$ kg/s
$\dot{m}_{Rec,Vap,In} = 0.39\times10^{-3}$ kg/s $\dot{m}_{Ref} = 0.33\times10^{-3}$ kg/s $\dot{m}_{Rec,Reflux,Out} = 60\times10^{-6}$ kg/s $h_{Rec,Vap,In}$ = 1672 kJ/kg $h_{Rec,Ref,Out}$ = 1442 kJ/kg $h_{Rec,Reflux,Out}$ = 381.1 kJ/kg	$\dot{Q}_{Rec} = \dot{m}_{Rec,Vap,In} \cdot h_{Rec,Vap,In} - \dot{m}_{Ref} \cdot h_{Rec,Ref,out}$ $-\dot{m}_{Rec,Reflux,Out} \cdot h_{Rec,Reflux,Out}$	$\dot{Q}_{Rec}$ = 152.4 W
$T_{Cond,Out}$ = 39.61 P_{High} = 1600 kPa x_{Ref} = 0.984	$h_{Cond,Ref,Out} = f(T_{Cond,Ref,Out}, P_{High}, x_{Ref})$	$h_{Cond,Ref,Out}$ = 177.3 kJ/kg

Table B-1 Continued

Input	Equations	Output
$\dot{m}_{Ref} = 0.33\times10^{-3}$ kg/s $h_{Rec,Ref,Out}$ = 1442 kJ/kg $h_{Cond,Ref,Out}$ = 177.3	$\dot{Q}_{Cond,Ref} = \dot{m}_{Ref}\left(h_{Rec,ref,Out} - h_{Cond,Ref,Out}\right)$	$\dot{Q}_{Cond,Ref} = 414$ W
$T_{RHX,High,Out}$ = 30.2°C P_{High} = 1600 kPa x_{Ref} = 0.984	$h_{RHX,High,Out} = f(T_{RHX,High,Out}, P_{High}, x_{Ref})$	$h_{RHX,High,Out}$ = 131.1 kJ/kg
$\dot{m}_{Ref} = 0.33\times10^{-3}$ kg/s $h_{Cond,Ref,Out}$ = 177.3 kJ/kg $h_{RHX,High,Out}$ = 131.1 kJ/kg	$\dot{Q}_{RHX,High} = \dot{m}_{Ref}\left(h_{Cond,Ref,Out} - h_{RHX,High,Out}\right)$	$\dot{Q}_{RHX,High} = 15$ W
$h_{RHX,High,Out}$ = 131.1 kJ/kg	$h_{RHX,High,Out} = h_{Evap,Ref,In}$	$h_{Evap,Ref,In}$ = 131.1 kJ/kg
$h_{Evap,Ref,In}$ = 131.1 kJ/kg P_{Low} = 400 kPa x_{Ref} = 0.984	$T_{Evap,Ref,In} = f(h_{Evap,Ref,in}, P_{Low}, x_{Ref})$	$T_{Evap,Ref,In}$ = -1.4°C
$T_{Evap,Ref,Out}$ = 8.6°C P_{Low} = 400 kPa x_{Ref} = 0.984	$h_{Evap,Ref,Out} = f(T_{Evap,Ref,Out}, P_{Low}, x_{Ref})$	$h_{Evap,Ref,Out}$ = 1212 kJ/kg

Table B-1 Continued

Input	Equations	Output
$\dot{m}_{Ref} = 0.33\times10^{-3}$ kg/s $h_{Evap,Ref,In}$ = 131.1 kJ/kg $h_{Evap,Ref,Out}$ = 1212 kJ/kg	$\dot{Q}_{Evap,Ref} = \dot{m}_{Ref}\left(h_{Evap,Ref,Out} - h_{Evap,Ref,In}\right)$	$\dot{Q}_{Evap,Ref} = 354$ W
$\dot{Q}_{RHX,High} = 15$ W $\dot{m}_{Ref} = 0.33\times10^{-3}$ kg/s $h_{Evap,Ref,Out}$ = 1212 kJ/kg	$\dot{Q}_{RHX,Low} = \dot{Q}_{RHX,High}$ $\dot{Q}_{RHX,Low} = \dot{m}_{Ref}\left(h_{RHX,Low,Out} - h_{Evap,Ref,Out}\right)$	$\dot{Q}_{RHX,Low} = 15$ W $h_{RHX,Low,Out}$ = 1259 kJ/kg
$\dot{m}_{CS} = 2.7\times10^{-3}$ kg/s $\dot{m}_{Ref} = 0.33\times10^{-3}$ kg/s x_{CS} = 0.37 x_{Ref}= 0.984	$\dot{m}_{CS} = \dot{m}_{Ref} + \dot{m}_{DS}$ $\dot{m}_{CS}\cdot x_{CS} = \dot{m}_{Ref}\cdot x_{Ref} + \dot{m}_{DS}\cdot x_{DS}$	$\dot{m}_{DS} = 2.37\times10^{-3}$ kg/s x_{DS} = 0.285
$T_{SHX,DS,In}$ = 128.2°C P_{High} = 1600 kPa $q_{SHX,DS,In}$ = 0.0	$h_{SHX,DS,In} = f(T_{SHX,DS,In}, P_{High}, x_{DS})$	$h_{SHX,DS,In}$ = 381.1.5 kJ/kg
$\dot{Q}_{SHX,CS} = 562$ W $\dot{m}_{DS} = 2.37\times10^{-3}$ kg/s $h_{SHX,DS,In}$ = 381.1.5 kJ/kg	$\dot{Q}_{SHX,DS} = \dot{Q}_{SHX,CS}$ $\dot{Q}_{SHX,DS} = \dot{m}_{DS}\left(h_{SHX,DS,In} - h_{SHX,DS,Out}\right)$	$\dot{Q}_{SHX,DS} = 562$ W $h_{SHX,DS,Out}$ = 144.5 kJ/kg
$h_{SHX,DS,Out}$ = 144.5 kJ/kg	$h_{SHX,DS,Out} = h_{Abs,DS,In}$	$h_{Abs,DS,In}$ = 144.5 kJ/kg

Table B-1 Continued

Input	Equations	Output
$\dot{m}_{CS} = 2.7\times10^{-3}$ kg/s $\dot{m}_{DS} = 2.37\times10^{-3}$ kg/s $\dot{m}_{Ref} = 0.33\times10^{-3}$ kg/s $h_{Abs,DS,In}$ = 144.5 kJ/kg $h_{RHX,Low,Out}$ = 1259 kJ/kg $h_{Abs,CS,Out}$ = 2.6 kJ/kg	$\dot{Q}_{Abs,Sol} = \dot{m}_{Ref} \cdot h_{Abs,Ref,In} + \dot{m}_{DS} \cdot h_{Abs,DS,IN} - \dot{m}_{CS} \cdot h_{Abs,CS,Out}$	$\dot{Q}_{Abs,Sol}$ = 748 W
$\dot{Q}_{Abs,Sol}$ = 748 W T_{Sink} = 37°C $P_{Ambient}$ = 101.3 kPa $\dot{m}_{Abs,Coolant}$=20.9×10^{-3} kg/s	$\dot{Q}_{Abs,Coolant} = \dot{Q}_{Abs,Sol}$ $h_{Abs,Coolant,In} = f(T_{Sink}, P_{Ambient})$ $\dot{Q}_{Abs,Coolant} = \dot{m}_{Abs,Coolant}\left(h_{Abs,Coolant,Out} - h_{Abs,Coolant,In}\right)$ $T_{Abs,Coolant,Out} = f(h_{Abs,Coolant,Out}, P_{Ambient})$	$\dot{Q}_{Abs,Coolant}$ = 748 W $h_{Abs,Coolant,In}$ = 155.1 kJ/kg $h_{Abs,Coolant,Out}$ = 190.9 kJ/kg $T_{Abs,Coolant,Out}$= 45.6°C
$\dot{Q}_{Cond,Ref}$ = 414 W T_{Sink} = 37°C $P_{Ambient}$ = 101.3 kPa $\dot{m}_{Cond,Coolant}$=17.8×10^{-3} kg/s	$\dot{Q}_{Cond,Coolant} = \dot{Q}_{Cond,Ref}$ $h_{Cond,Coolant,In} = f(T_{Sink}, P_{Ambient})$ $\dot{Q}_{Cond,Coolant} = \dot{m}_{Cond,Coolant} \cdot \left(h_{Cond,Coolant,Out} - h_{Cond,Coolant,In}\right)$ $T_{Cond,Coolant,Out} = f(h_{Cond,Coolant,Out}, P_{Ambient})$	$\dot{Q}_{Cond,Coolant}$ = 414 W $h_{Cond,Coolant,In}$ = 155.1 kJ/kg $h_{Cond,Coolant,Out}$ = 178.4 kJ/kg $T_{Cond,Coolant,Out}$= 42.58°C

Table B-1 Continued

Input	Equations	Output
$\dot{Q}_{Evap,Ref} = 354$ W $P_{Ambient} = 101.3$ kPa $T_{Evap,Coolant,In} = 9°C$ $\dot{m}_{Evap,Coolant} = 24\times10^{-3}$ kg/s	$\dot{Q}_{Evap,Coolant} = \dot{Q}_{Evap,Ref}$ $h_{Evap,Coolant,In} = f(T_{Evap,Coolant,In}, P_{Ambient})$ $\dot{Q}_{Evap,Coolant} = \dot{m}_{Evap,Coolant} \cdot \left(h_{Evap,Coolant,In} - h_{Evap,Coolant,Out}\right)$ $T_{Evap,Coolant,Out} = f(h_{Evap,Coolant,Out}, P_{Ambient})$	$\dot{Q}_{Evap,Coolant} = 354$ W $h_{Evap,Coolant,In} = 37.9$ kJ/kg $h_{Evap,Coolant,Out} = 23.2$ kJ/kg $T_{Evap,Coolant,Out} = 5.5°C$

Table B-2 Microchannel System, Component Heat Transfer Calculations

Input	Equations	Output
$\dot{Q}_{Abs}$ = 748 W $T_{Abs,DS,In}$ = 73.2°C $T_{Abs,CS,Out}$ = 50.4°C $T_{Abs,Coolant,In}$ = 37.0°C $T_{Abs,Coolant,Out}$ = 45.6°C	$LMTD_{Abs} = \frac{\left(T_{Abs,DS,In} - T_{Abs,Coolant,out}\right) - \left(T_{Abs,CS,out} - T_{Abs,Coolant,In}\right)}{\mathrm{Ln}\left[\frac{\left(T_{Abs,DS,In} - T_{Abs,Coolant,out}\right)}{\left(T_{Abs,CS,out} - T_{Abs,Coolant,In}\right)}\right]}$ $\dot{Q}_{Abs} = UA_{Abs,Required} \cdot LMTD_{Abs}$	$LMTD_{Abs}$ = 19.7°C $UA_{Abs,Required}$ = 38 W/K
$\dot{Q}_{Cond}$ = 414 W $T_{Cond,Ref,In}$ = 85.0°C $T_{Cond,Ref,Out}$ = 39.6°C $T_{Cond,Coolant,In}$ = 37.0°C $T_{Cond,Coolant,Out}$ = 42.6°C	$LMTD_{Cond} = \frac{\left(T_{Cond,Ref,In} - T_{Cond,Coolant,Out}\right) - \left(T_{Cond,Ref,Out} - T_{Cond,Coolant,In}\right)}{\mathrm{Ln}\left[\frac{\left(T_{Cond,Ref,In} - T_{Cond,Coolant,Out}\right)}{\left(T_{Cond,Ref,Out} - T_{Cond,Coolant,In}\right)}\right]}$ $\dot{Q}_{Cond} = UA_{Cond,Required} \cdot LMTD_{Cond}$	$LMTD_{Abs}$ = 14.3°C $UA_{Cond,Required}$ = 29 W/K
$\dot{Q}_{SHX}$ = 562 W $T_{SHX,DS,In}$ = 128.2°C $T_{SHX,DS,Out}$ = 75.7°C $T_{SHX,CS,In}$ = 63.7°C $T_{SHX,CS,Out}$ = 109°C	$LMTD_{SHX} = \frac{\left(T_{SHX,DS,In} - T_{SHX,CS,Out}\right) - \left(T_{SHX,DS,Out} - T_{SHX,CS,In}\right)}{\mathrm{Ln}\left[\frac{\left(T_{SHX,DS,In} - T_{SHX,CS,Out}\right)}{\left(T_{SHX,DS,Out} - T_{SHX,CS,In}\right)}\right]}$ $\dot{Q}_{SHX} = UA_{SHX,Required} \cdot LMTD_{SHX}$	$LMTD_{SHX}$ = 15.3°C $UA_{SHX,Required}$ = 37 W/K

Table B-2 Continued

Input	Equations	Output
$\dot{Q}_{RHX}$ = 15 W $T_{RHX,High,In}$ = 39.6°C $T_{RHX,High,Out}$ = 30.2°C $T_{RHX,Low,In}$ = 8.6°C $T_{RHX,Low,Out}$ = 18.0°C	$LMTD_{RHX} = \frac{\left(T_{RHX,High,In} - T_{RHX,Low,Out}\right) - \left(T_{RHX,High,Out} - T_{RHX,Low,In}\right)}{\mathrm{Ln}\left[\frac{\left(T_{RHX,High,In} - T_{RHX,Low,Out}\right)}{\left(T_{RHX,High,Out} - T_{RHX,Low,In}\right)}\right]}$ $\dot{Q}_{RHX} = UA_{RHX,Required} \cdot LMTD_{RHX}$	$LMTD_{Abs}$ = 21.6°C $UA_{RHX,Required}$ = 0.7 W/K
$\dot{Q}_{Evap}$ = 354 W $T_{Evap,Coolant,,In}$ = 9.0°C $T_{Evap,Coolant,Out}$ = 5.5°C $T_{Evap,Ref,In}$ = -1.4°C $T_{Evap,Ref,Out}$ = 8.6°C	$LMTD_{Evap} = \frac{\left(T_{Evap,Coolant,In} - T_{Evap,Ref,Out}\right) - \left(T_{Evap,Coolant,Out} - T_{Evap,Ref,In}\right)}{\mathrm{Ln}\left[\frac{\left(T_{Evap,Coolant,In} - T_{Evap,Ref,Out}\right)}{\left(T_{Evap,Coolant,Out} - T_{Evap,Ref,In}\right)}\right]}$ $\dot{Q}_{Evap} = UA_{Evap,Required} \cdot LMTD_{Evap}$	$LMTD_{Evap}$ = 2.2°C $UA_{Evap,Required}$ = 160 W/K
$\dot{Q}_{Rec}$ = 152 W $T_{Rec,Vap,In}$ = 128.2°C $T_{Rec,Ref,Out}$ = 85.0°C $T_{Rec,CS,In}$ = 50.8°C $T_{Rec,CS,Out}$ = 63.7°C	$LMTD_{Rec} = \frac{\left(T_{Rec,Vap,In} - T_{Rec,CS,Out}\right) - \left(T_{Rec,Ref,Out} - T_{Rec,CS,In}\right)}{\mathrm{Ln}\left[\frac{\left(T_{Rec,Vap,In} - T_{Rec,CS,Out}\right)}{\left(T_{Rec,Ref,Out} - T_{Rec,CS,In}\right)}\right]}$ $\dot{Q}_{Rec} = UA_{Rec,Required} \cdot LMTD_{Rec}$	$UA_{Rec,Required}$ = 3.2 W/K $LMTD_{Rec}$ = 47.8°C

Table B-3 Microchannel System Design State Points

State Point	T, °C	P, kPa	x	q	h, kJ/kg
Solution/Refrigerant State Points					
Absorber CS out	50.4	400	0.370	sub-cooled	2.6
Rectifier CS In	50.8	1600	0.370	sub-cooled	5.4
SHX CS In	63.7	1600	0.370	sub-cooled	61.9
SHX CS Out	109	1600	0.370	0.001	269.9
Desorber Out	128.2	1600	0.370	0.14	566.2
Rectifier Vapor In	128.2	1600	0.876	1	1672
Rectifier Reflux Out	128.2	1600	0.285	0	381.1
SHX DS In	128.2	1600	0.285	0	381.1
SHX DS Out	75.7	1600	0.285	sub-cooled	144.5
Absorber DS In	73.2	400	0.285	0.01	144.5
Rectifier Ref Out	85.0	1600	0.984	1	1442
Condenser Ref Out	39.6	1600	0.984	sub-cooled	177.3
RHX High Out	30.2	1600	0.984	sub-cooled	131.1
Evaporator Ref In	-1.4	400	0.984	0.12	131.1
Evaporator Ref Out	8.6	400	0.984	0.94	1212
RHX Low Out	18.0	400	0.984	0.96	1259
Coolant State Points					
Evap Coolant In	9.0	101.3	NA	sub-cooled	37.9
Evap Coolant Out	5.5	101.3	NA	sub-cooled	23.2
Abs Coolant In	37.0	101.3	NA	sub-cooled	155.1
Abs Coolant Out	45.6	101.3	NA	sub-cooled	190.9
Cond Coolant In	37.0	101.3	NA	sub-cooled	155.1
Cond Coolant Out	42.6	101.3	NA	sub-cooled	178.4

B.2 Microchannel System Fabrication Stages

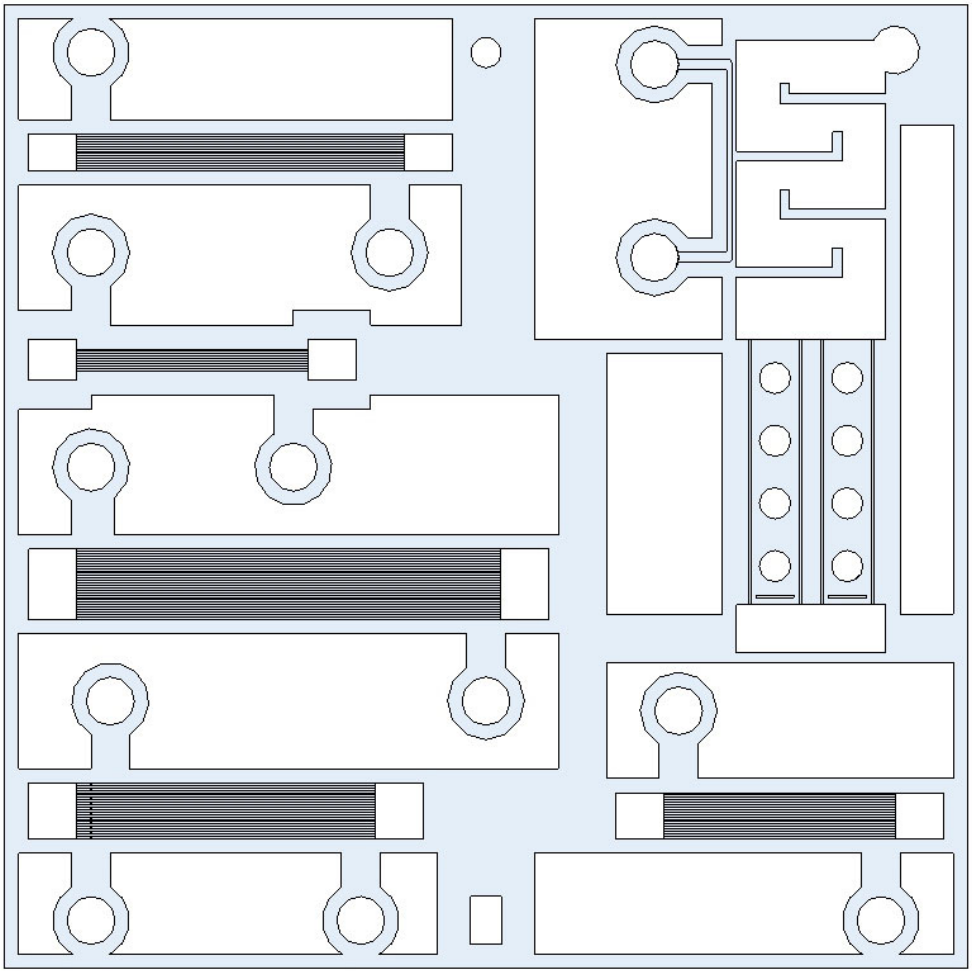

Figure B-1 3-Dimensional CAD Drawing, Shim A

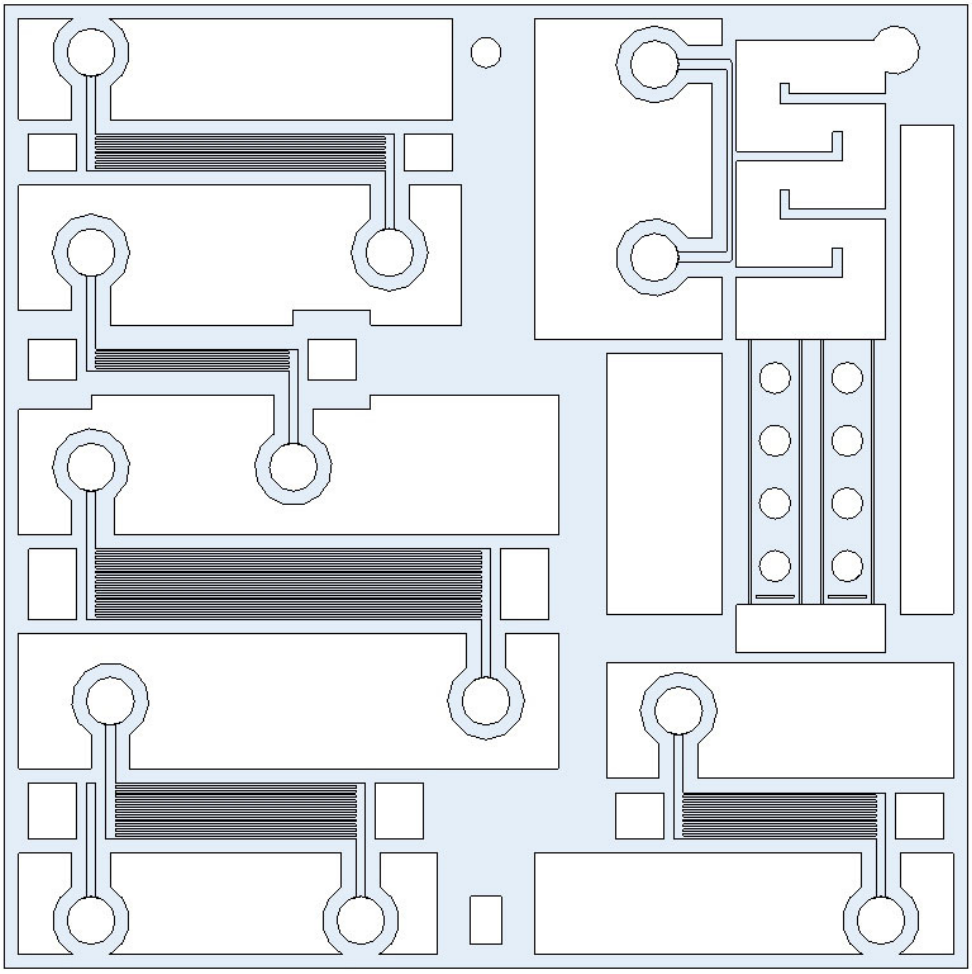

Figure B-2 3-Dimensional CAD Drawing, Shim B

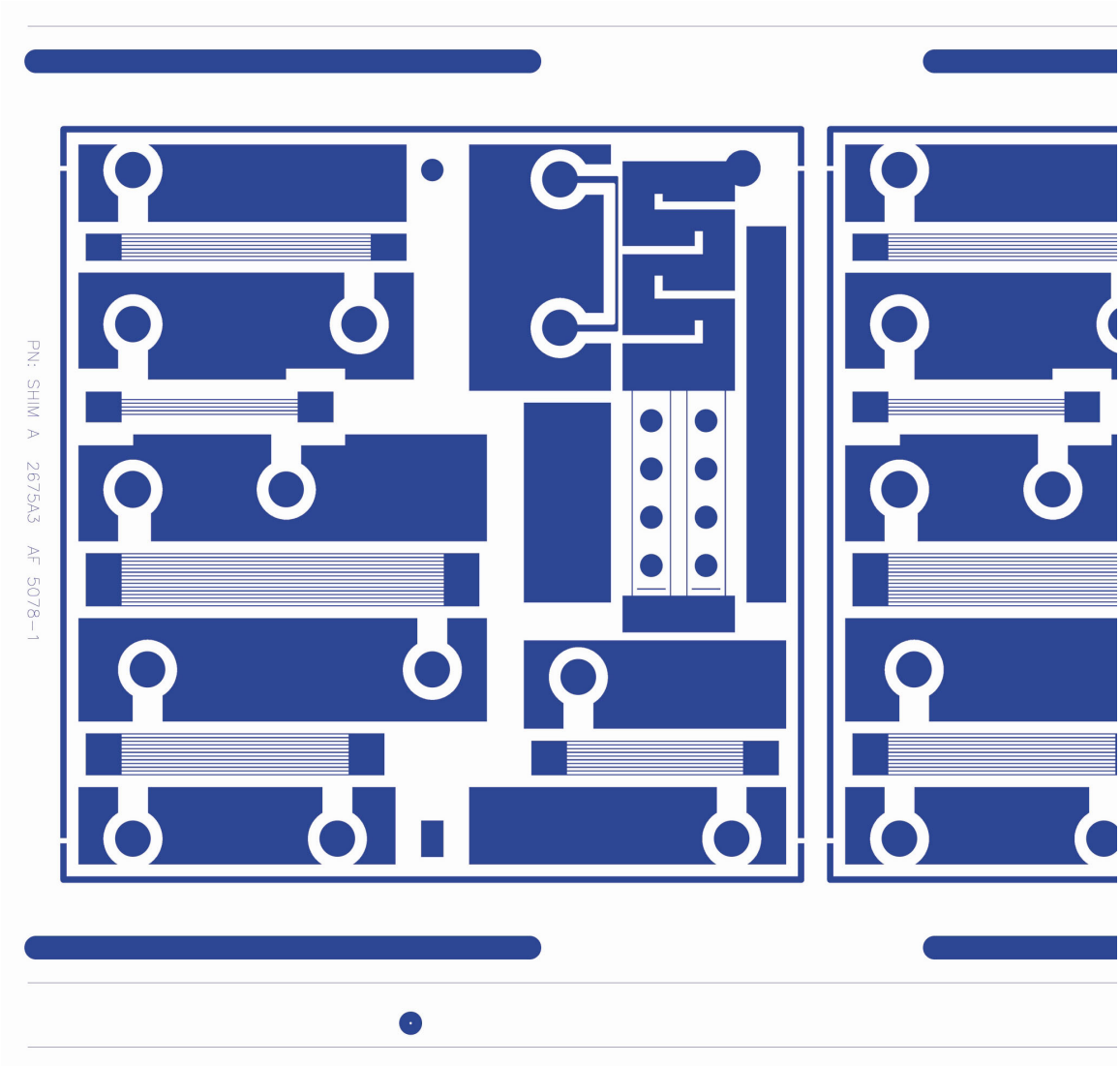

Figure B-3 Mask Artwork, Shim A Front

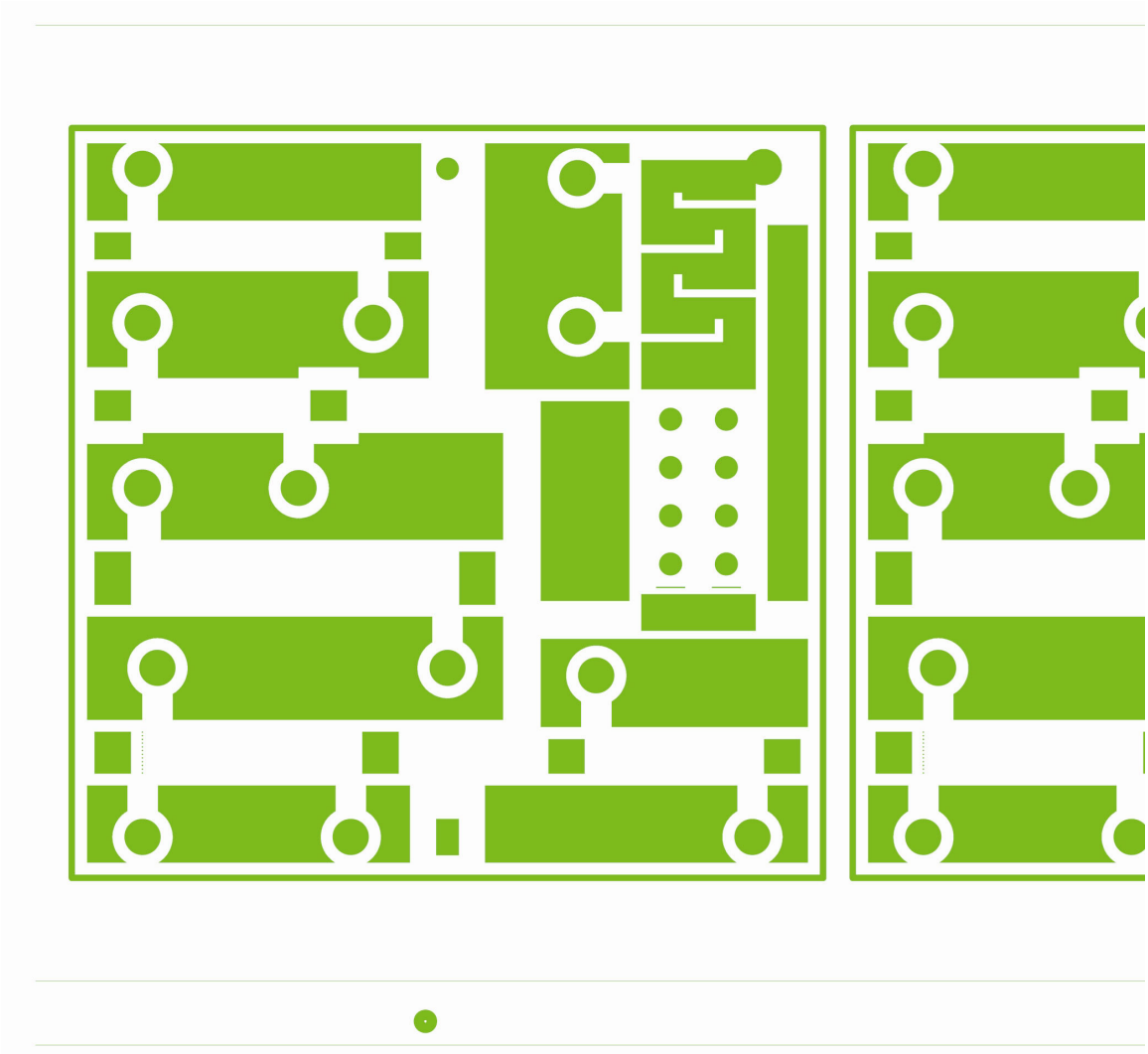

Figure B-4 Mask Artwork, Shim A Back

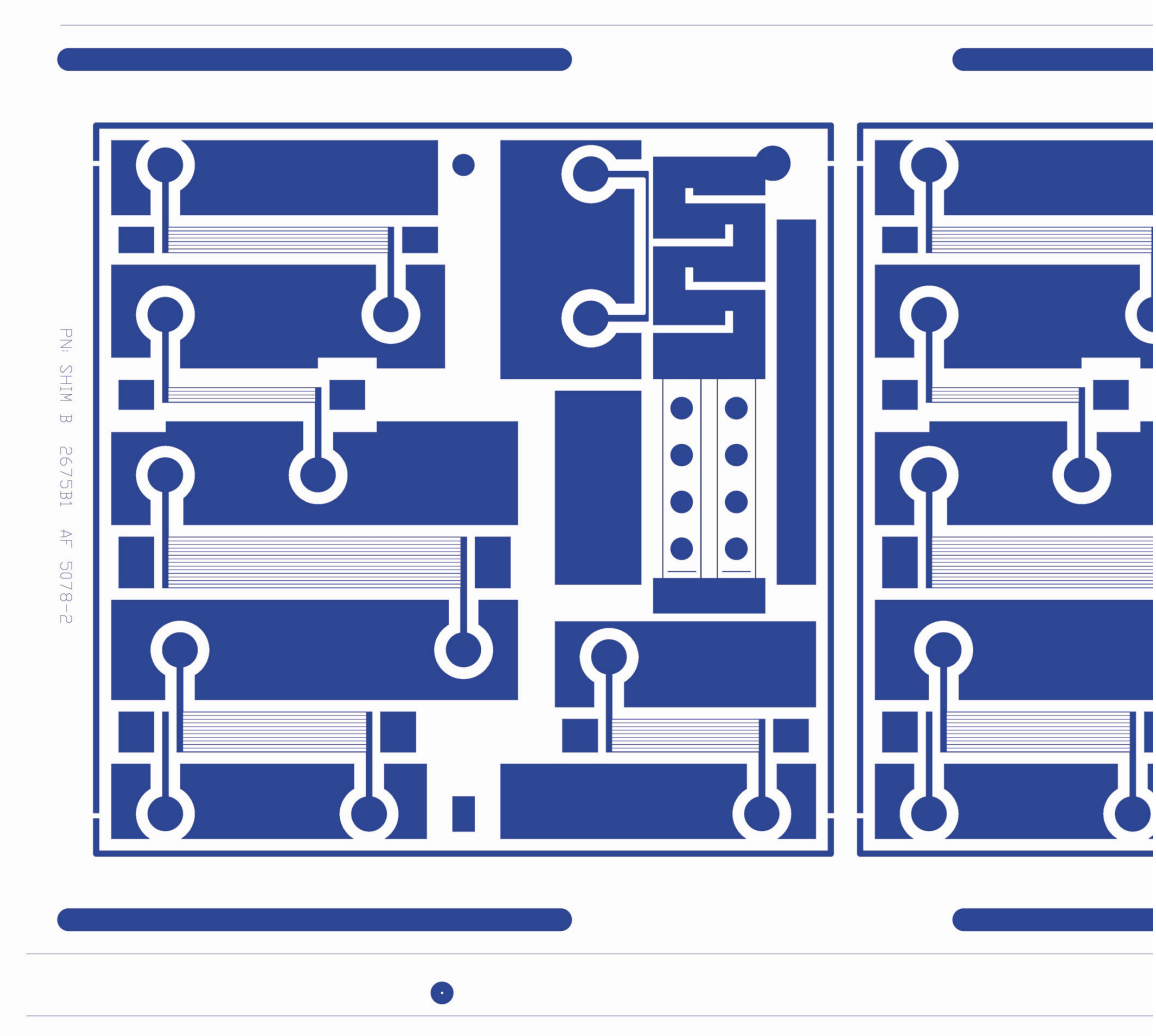

Figure B-5 Mask Artwork, Shim B Front

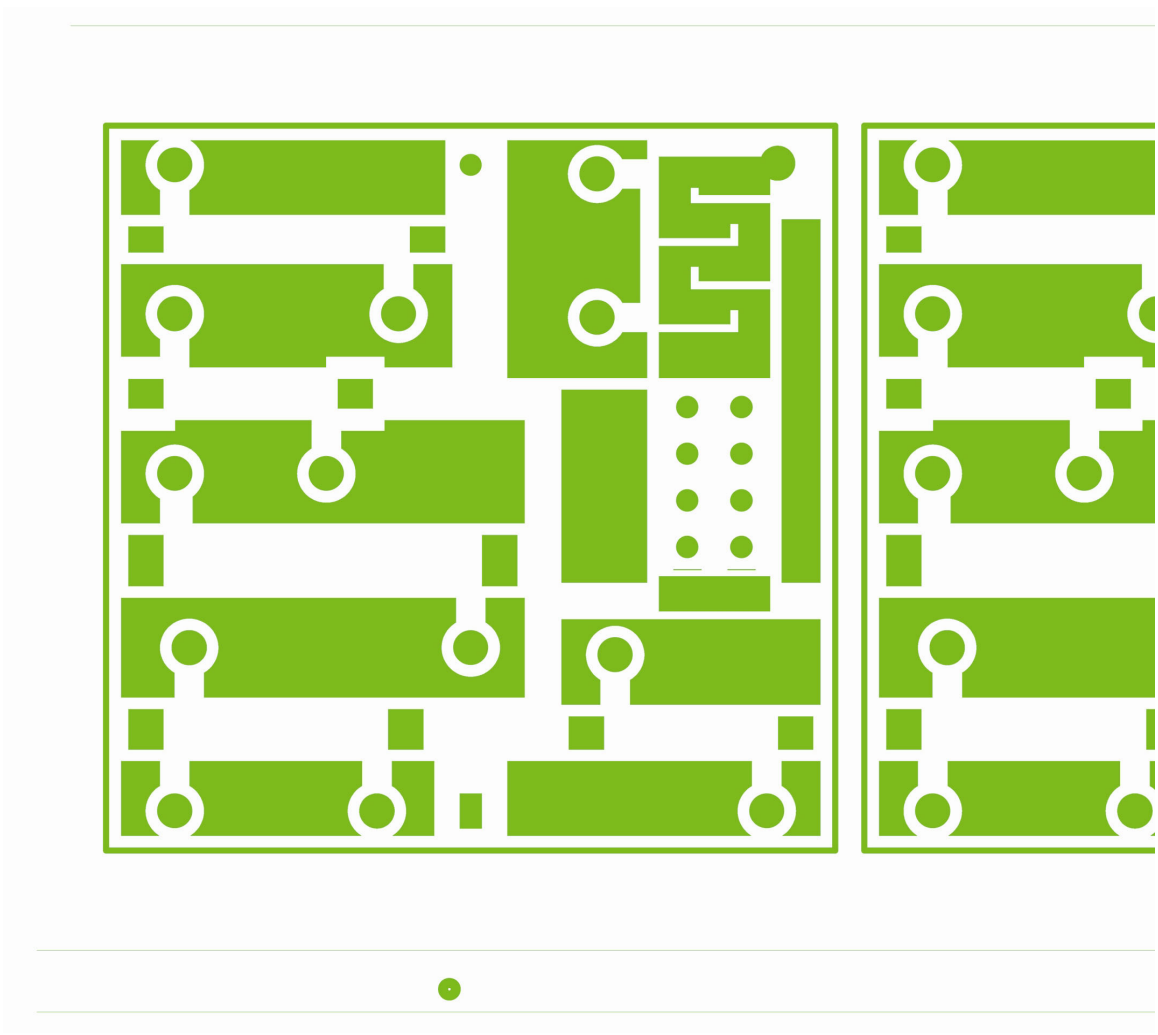

Figure B-6 Mask Artwork, Shim B Back

Figure B-7 Coating and Printing Clean Room

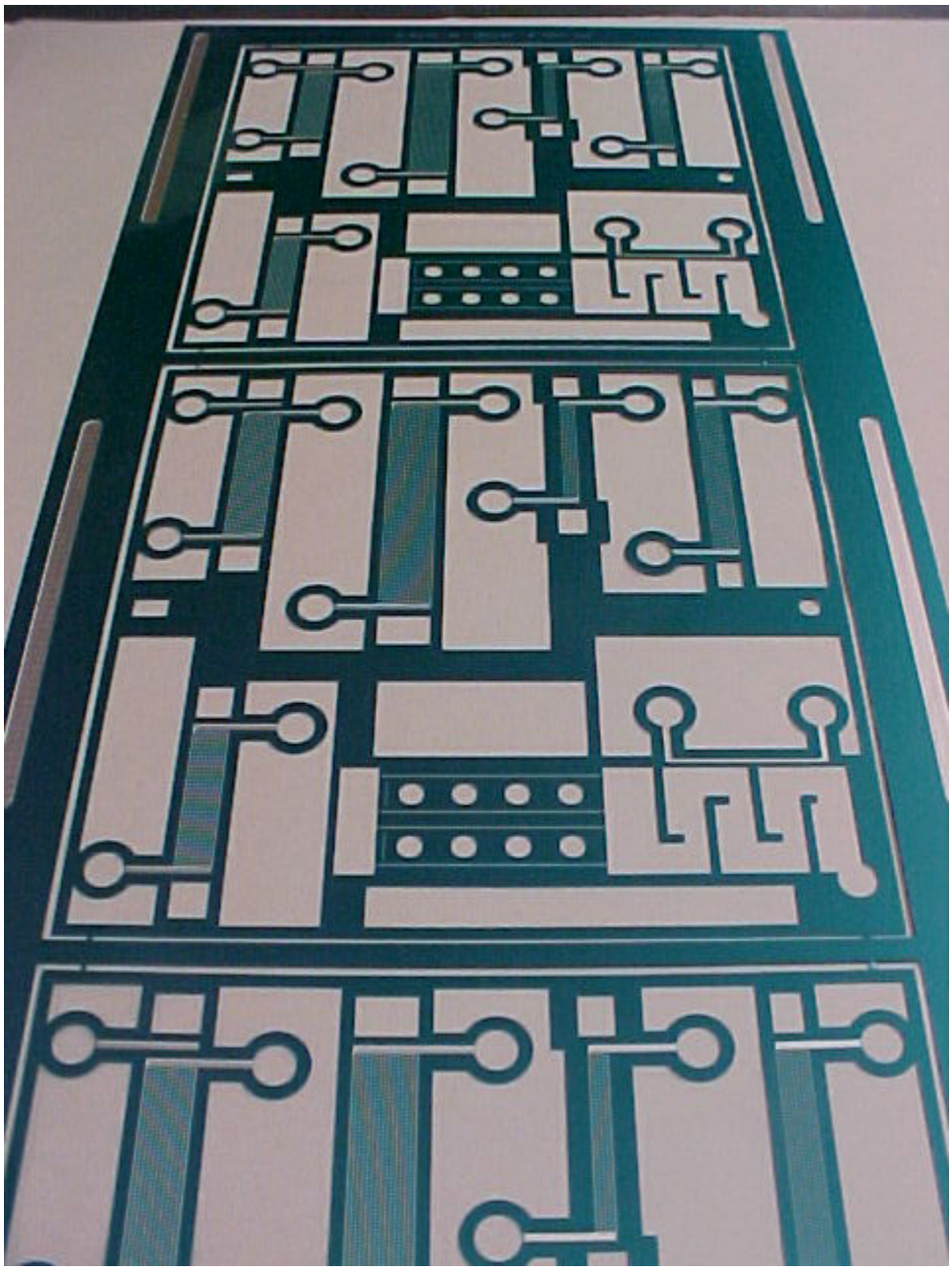

Figure B-8 Photograph of Shim B in tabbed sheet form after etching and before Photoresist is removed

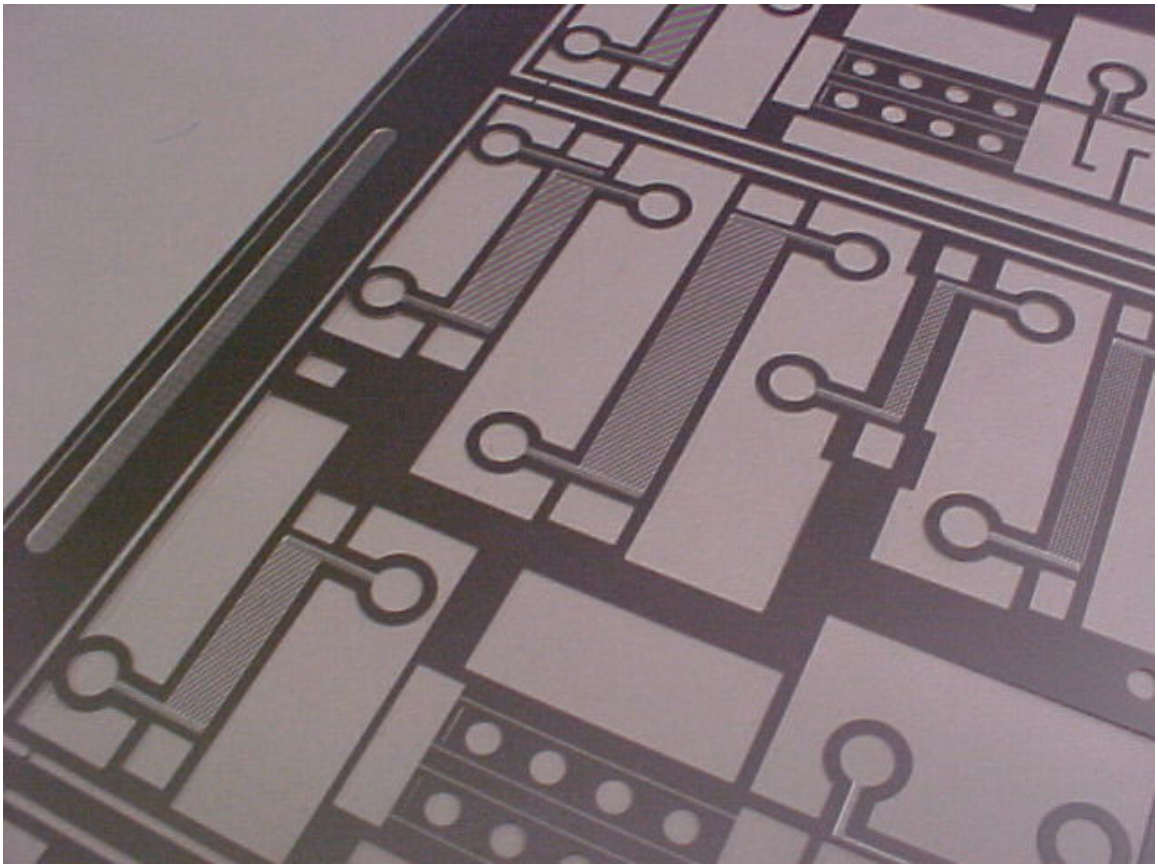

Figure B-9 Photograph of Shim B in tabbed sheet form after Photoresist has been removed

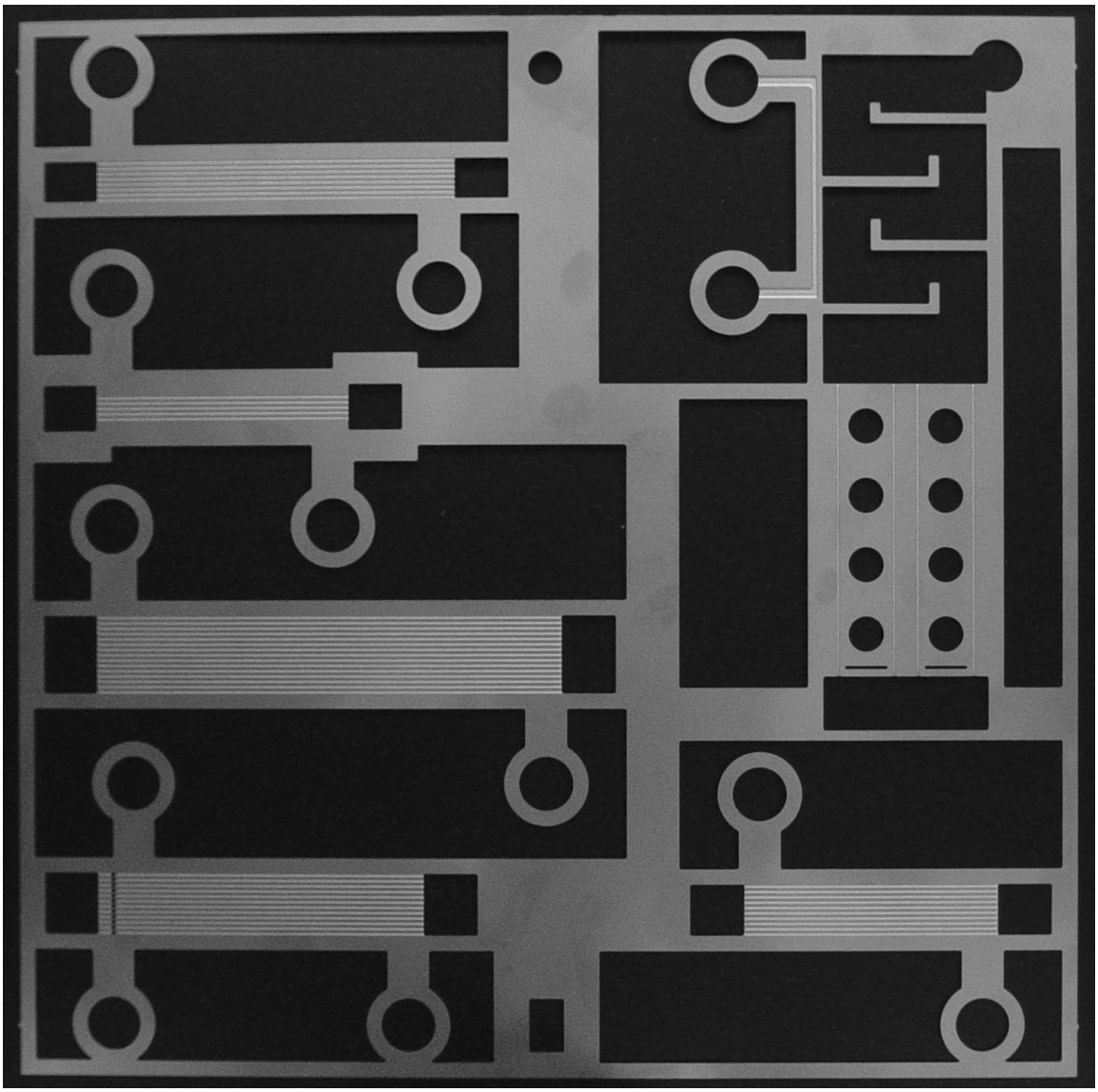

Figure B-10 Photograph of Shim A after being removed from tabbed sheet

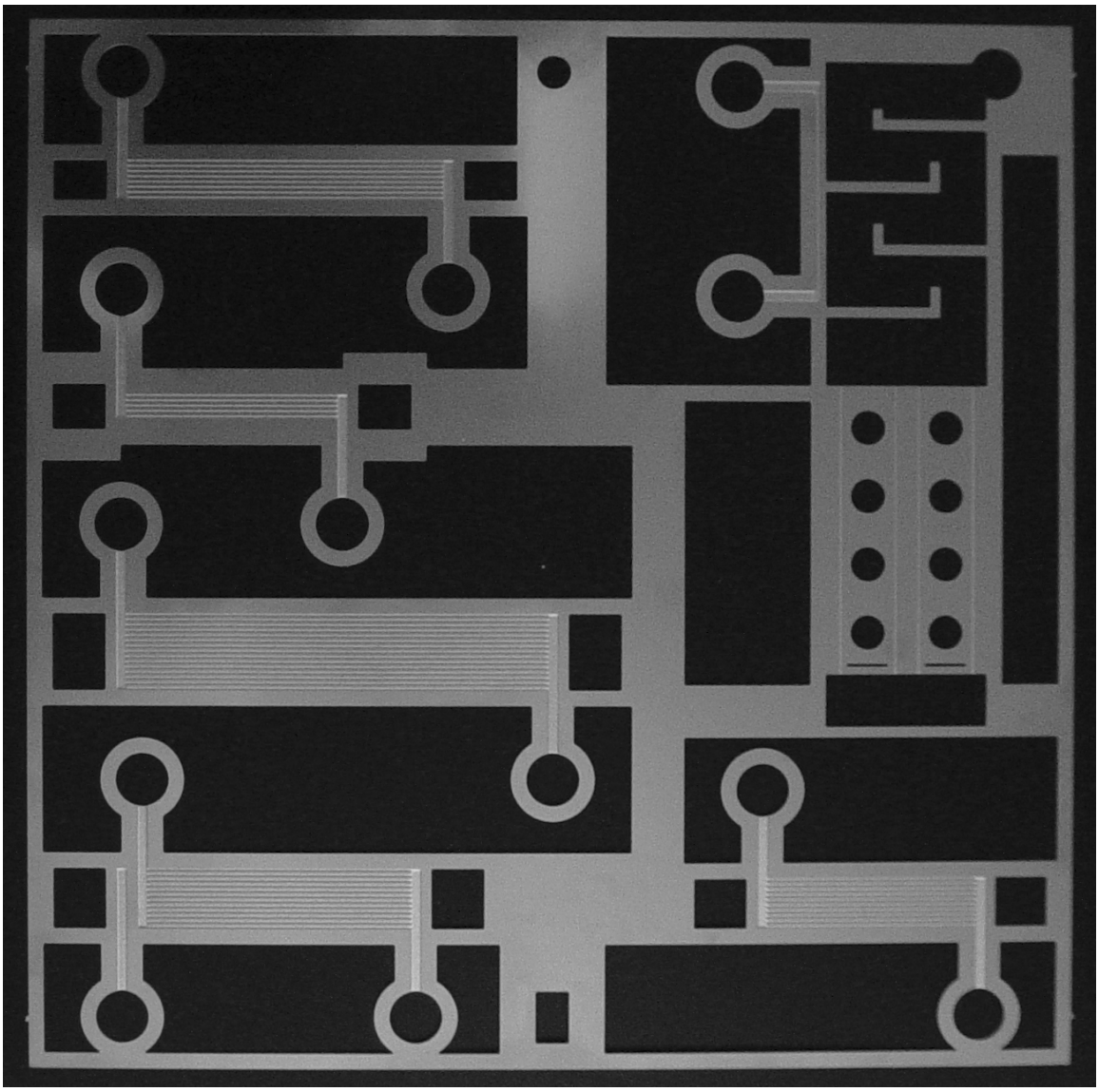

Figure B-11 Photograph of Shim B after being removed from tabbed sheet

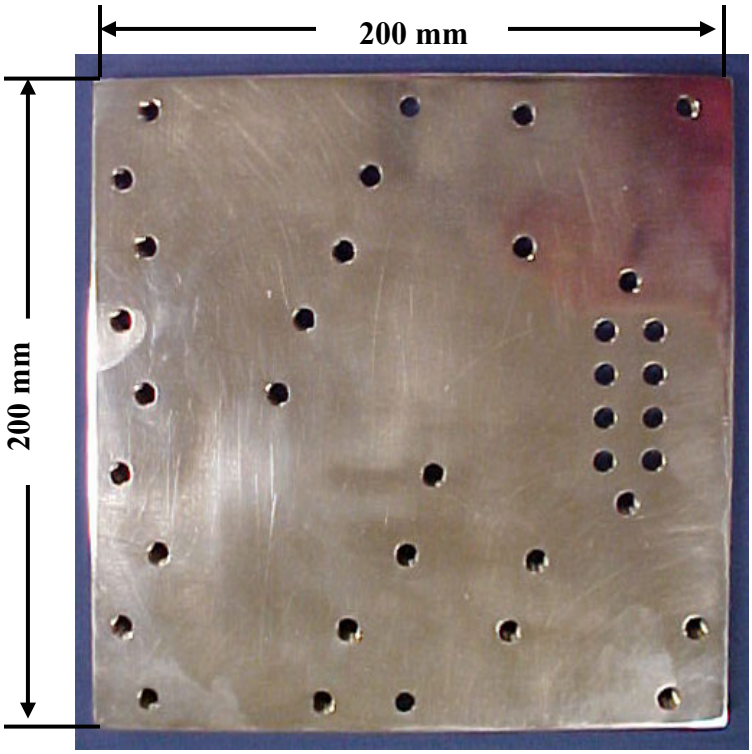

Figure B-12 Photograph of Front Endplate

Figure B-13 Photograph of Back Endplate

B.3 Microchannel System Experimental System Components

Table B-4 Solution Pump Details

Characteristic	Value
Manufacturer	Tuthill Corporation
Pump Type	Magnetic Coupled External Gear Pump
Model Number	DGS.38EEET1NN37000
Serial Number	A31503
Wetted Materials	Stainless Steel, PEEK, Teflon
Maximum Flowrate	76 L/hr
Maximum Differential Pressure	1720 kPa
Temperature Range	-46°C to 176°C
Motor Type	Variable Speed Brushless DC
Motor Voltage	24 VDC
Motor Power	75 W
Maximum Speed	4600 RPM

Table B-5 DC Power Supply Details

Characteristic	Value
Manufacturer	International Power
Model Number	CC
Input	120 VAC
Output	24 VDC
Max Temperature	50°C

Table B-6 Data Acquisition Hardware Details

Characteristic	Value
Thermocouple and Voltage Measurements	
Manufacturer	National Instruments
DAQ	DAQCard-6036E
Signal Conditioning Module	SCXI-1102
Frequency Measurements	
Manufacturer	IOTech
DAQ Model Number	Personal DAQ/56
DAQ Serial Number	262048
Expansion Module Model Number	PDQ2
Expansion Module Serial Number	260689

Table B-7 Refrigerant and Solution Expansion Valve Details

Characteristic	Value
Manufacturer	Swagelok
Valve Type	S Series Needle Metering Valve
Model Number	SS-SS4-VH-NE
Wetted Materials	Stainless Steel, Neoprene, Teflon, Glass Filled PTFE
Temperature Range	-23°C to 121°C
Maximum Working Pressure	13.7 MPa
Orifice Size	0.81 mm
C_V Range	0.0001 to 0.004

Table B-8 Concentrated Solution Flowmeter Details

Characteristic	Value
Manufacturer	DEA Engineering
Flowmeter Type	Nutating Microflowmeter
Model Number	FMTE20
Serial Number	8046
Wetted Materials	Stainless Steel, Teflon
Flowrate Range	5-1250 mL/min
Maximum Working Pressure	3447 kPa
Output Signal	0-5 Volt Square Wave
Repeatability	±0.1%
Accuracy	±0.5% reading
Calibration Factor	10.65 pulses/mL

Table B-9 Dilute Solution Flowmeter Details

Characteristic	Value
Manufacturer	DEA Engineering
Flowmeter Type	Nutating Microflowmeter
Model Number	FMTE20
Serial Number	8047
Wetted Materials	Stainless Steel, Teflon
Flowrate Range	5-1250 mL/min
Maximum Working Pressure	3447 kPa
Output Signal	0-5 Volt Square Wave
Repeatability	±0.1%
Accuracy	±0.5% reading
Calibration Factor	10.57 pulses/mL

Table B-10 Rectifier, Condenser and Absorber Water Pump Details

Characteristic	Value
Manufacturer	Laing
Pump Type	Centrifugal
Model	SM-1212-26
Housing Material	Stainless Steel
Maximum Working Pressure	1034 kPa
Maximum Fluid Temperature	110°C

Table B-11 Evaporator Pump Details

Characteristic	Value
Manufacturer	Laing
Pump Type	Centrifugal
Model	SM-1212-26
Housing Material	Plastic
Maximum Working Pressure	345 kPa
Maximum Fluid Temperature	60°C

Table B-12 Evaporator, Condenser and Absorber Water Flowmeter Details

Characteristic	Value
Manufacturer	Key Instruments
Flowmeter Type	Rotameter
Series	MR3000
Model Code	3L22
Wetted Materials	Stainless Steel, Viton
Flowrate Range	4-40 gph
Maximum Working Pressure	690 kPa
Maximum Fluid Temperature	65°C
Repeatability	±0.1%
Accuracy	±4% Full Scale

Table B-13 Rectifier Water Flowmeter Details

Characteristic	Value
Manufacturer	Key Instruments
Flowmeter Type	Rotometer
Series	MR3000
Model Code	3L19
Wetted Materials	Stainless Steel, Viton
Flowrate Range	0.4-5 gph
Maximum Working Pressure	690 kPa
Maximum Fluid Temperature	65°C
Repeatability	±0.1%
Accuracy	±4% Full Scale

Table B-14 Condenser Inlet Pressure Transducer Details

Characteristic	Value
Manufacturer	WIKA
Model Number	S-10
Serial Number	2603LRK
Wetted Materials	Stainless Steel
Pressure Range	0-3447.4 kPa
Power Supply	10-30 VDC
Output Signal	4-20 mA
Repeatability	±0.05% of span
Accuracy	±0.25% of span
Media Temperature Range	-40°C to 100°C

Table B-15 Absorber Inlet Pressure Transducer Details

Characteristic	Value
Manufacturer	WIKA
Model Number	ECO-1
Serial Number	4897349
Wetted Materials	Stainless Steel
Pressure Range	0-689.5 kPa
Power Supply	10-30 VDC
Output Signal	4-20 mA
Repeatability	±0.1% of span
Accuracy	±0.5% of span
Media Temperature Range	-40°C to 100°C

Table B-16 Evaporator Inlet Pressure Transducer Details

Characteristic	Value
Manufacturer	WIKA
Model Number	ECO-1
Serial Number	4882574
Wetted Materials	Stainless Steel
Pressure Range	0-689.5 kPa
Power Supply	10-30 VDC
Output Signal	4-20 mA
Repeatability	±0.1% of span
Accuracy	±0.5% of span
Media Temperature Range	-40°C to 100°C

Table B-17 Thermocouple Details

Characteristic	Value
Type	T (Copper-Constantan)
Manufacturer	Omega
Model Number ($1/16^{th}$ in. diameter)	TMQSS-062G-6
Model Number ($1/8^{th}$ in. diameter)	TMQSS-125G-6
Sheath Material	Stainless Steel
Sheath Length	152.4 mm
Accuracy	±0.5°C

Table B-18 Variable Voltage Transformer Details

Characteristic	Value
Manufacturer	Staco Energy Products Co.
Model Number	L1010B
Input Voltage	120 VAC
Output Voltage	0-140 VAC
Maximum Amperage	10 Amps
Maximum KVA	1.4 KVA

Table B-19 Plate Heat Exchanger Details

Characteristic	Value
Manufacturer	FlatePlate
Model Number	FP5x12-10
Maximum Temperature	177 C
Maximum Pressure	3100 kPa
Plate Material	316L Stainless Steel
Braze Material	Nickel

Table B-20 Desorber AC Watt Transducer Details

Characteristic	Value
Type	Hall-effect
Manufacturer	Ohio Semitronics, Inc.
Model Number	PC5-0198E
Serial Number	06031222
Sensor Power Supply	120 V
Voltage Range	0-150 VAC
Amperage Range	0-15 Amps
Full Scale Wattage	1500 Watts
Output Signal	4-20 mA
Accuracy	±0.5% Full Scale

Table B-21 Dilute Solution Sight Glass Details

Characteristic	Value
Type	Bull's Eye Sight Flow Indicator
Manufacturer	Pressure Products
Drawing Number	G0A6C04B
Serial Numbers	WAGG-12395
Body Material	Stainless Steel
Packing and Gasket Material	Teflon PTFE
Lens Material	Tempered Borosilicate
Maximum Pressure Rating	4137 kPa @ 204°C

Table B-22 Refrigerant and Concentrated Solution Sight Glass Details

Characteristic	Value
Type	Bull's Eye Sight Flow Indicator
Manufacturer	Pressure Products
Drawing Number	G016C26B
Serial Numbers	XBGG-13410, XBGG-13411
Body Material	Stainless Steel
Packing and Gasket Material	Teflon PTFE
Lens Material	Tempered Borosilicate
Maximum Pressure Rating	2068 kPa @ 232°C

B.4 Microchannel System Experimental Data Analysis

Table B-23 Cycle Data Analysis and Uncertainty Calculations

Input	Equations	Output
$T_{Des,DS,Out}$ = 115.4±0.5°C P_{High} = 1304±17.4 kPa $q_{Des,DS,Out}$ = 0	$x_{DS} = f\left(T_{Des,DS,Out}, P_{High}, q_{Des,DS,Out}\right)$	x_{DS} = 29.9±0.3%
$T_{SHX,DS,Out}$ = 47.7±0.5°C P_{High} = 1304±17.4 kPa x_{DS} = 29.9±0.3% $\dot{V}_{DS}$ =64.8±0.3 mL/min	$\rho_{SHX,DS,Out} = f\left(T_{SHX,DS,Out}, P_{High}, x_{DS}\right)$ $\dot{m}_{DS} = \rho_{SHX,DS,Out} \cdot \dot{V}_{DS} \cdot \left(\frac{1\ \text{m}^3}{1\text{E6 mL}} \frac{1\ \text{min}}{60\ \text{sec}}\right)$	$\rho_{SHX,DS,Out}$ = 880.8±1.2 kg/m^3 $\dot{m}_{DS} = 9.51\times10^{-4}\pm4.9\times10^{-6}$ kg/s
$T_{Rec,Ref,Out}$ = 102.2±0.5°C P_{High} = 1304±17.4 kPa $q_{Rec,Rec,Out}$ = 1	$x_{Ref} = f\left(T_{Rec,Ref,Out}, P_{High}, q_{Rec,Ref,Out}\right)$	x_{Ref} = 94.6±0.2%
$T_{SHX,CS,In}$ = 36.3±0.5°C P_{Low} = 367.2±3.45 kPa $\dot{V}_{CS}$ = 88.2±0.4mL/min $\dot{m}_{DS} = 9.51\times10^{-4}\pm4.9\times10^{-6}$ kg/s x_{DS} = 29.9±0.3% x_{Ref} = 94.6±0.2%	$\rho_{Abs,CS,Out} = f\left(T_{SHX,CS,In}, P_{Low}, x_{CS}\right)$ $\dot{m}_{CS} = \rho_{Abs,CS,Out} \cdot \dot{V}_{CS} \cdot \left(\frac{1\ \text{m}^3}{1\text{E6 mL}} \frac{1\text{min}}{60\ \text{sec}}\right)$ $\dot{m}_{CS} = \dot{m}_{DS} + \dot{m}_{Ref}$ $\dot{m}_{CS} \cdot x_{CS} = \dot{m}_{DS} \cdot x_{DS} + \dot{m}_{Ref} \cdot x_{Ref}$	x_{CS} = 44.7±0.4% $\rho_{Avs,DS,Out}$ = 838.4±1.5 kg/m^3 $\dot{m}_{CS} = 1.23\times10^{-3}\pm5.4\times10^{-6}$ kg/s $\dot{m}_{Ref} = 2.8\times10^{-4}\pm6.2\times10^{-6}$ kg/s

Table B-23Continued

Input	Equations	Output
$T_{Evap,Ref,In}$ = -1.3±0.5°C $T_{Evap,Ref,Out}$ = 16.8±0.5°C $T_{RHX,High,Out}$ = 22.6±0.5°C P_{High} = 1304±17.4 kPa P_{Evap} = 375.3±3.45 kPa x_{Ref} = 94.6±0.2% $\dot{m}_{Ref}$ =2.8×10^{-4}±6.2×10^{-6} kg/s	$h_{Evap,Ref,In} = f\left(T_{Evap,Ref,In}, P_{Evap}, x_{Ref}\right)$ $h_{Evap,Ref,Out} = f\left(T_{Evap,Ref,Out}, P_{Evap}, x_{Ref}\right)$ $h_{RHX,Ref,Out} = f\left(T_{RHX,High,Out}, P_{High}, x_{Ref}\right)$ $\dot{Q}_{Evap,Ref} = \dot{m}_{Ref} \cdot \left(h_{Evap,Ref,Out} - h_{Evap,Ref,In}\right) \cdot \left(\frac{1000\ \text{W}}{1\ \text{kW}}\right)$ $\dot{Q}_{Evap,Ref,Alt} = \dot{m}_{Ref} \cdot \left(h_{Evap,Ref,Out} - h_{RHX,High,Out}\right) \cdot \left(\frac{1000\ \text{W}}{1\ \text{kW}}\right)$	$h_{Evap,Ref,In}$ = 510.1±169.8 kJ/kg $h_{Evap,Ref,Out}$ = 1115±7.2 kJ/kg $h_{RHX,High,Out}$ = 66.4±2.7 kJ/kg $\dot{Q}_{Evap,Ref}$ = 170±48 W $\dot{Q}_{Evap,Ref,Alt}$ = 295±7 W
$T_{Evap,Coolant,In}$ = 12.5±0.5°C $T_{Evap,Coolant,Out}$ = 7.1±0.5°C $\dot{V}_{Evap,Coolant}$ = 10±1.6 GPH	$\rho_{Evap,Coolant,In} = f\left(T_{Evap,Coolant,In}, P = 101.3\ \text{kPa}\right)$ $\dot{m}_{Evap,Coolant} = \rho_{Evap,Coolant,In} \cdot \dot{V}_{Evap,Coolant} \cdot \left(\frac{1\ \text{m}^3}{264.17\ \text{Gal}} \frac{1\ \text{hr}}{3600\ \text{sec}}\right)$ $h_{Evap,Coolant,In} = f\left(T_{Evap,Coolant,In}, P = 101.3\ \text{kPa}\right)$ $h_{Evap,Coolant,Out} = f\left(T_{Evap,Coolant,Out}, P = 101.3\ \text{kPa}\right)$ $\dot{Q}_{Evap,Coolant} = \dot{m}_{Evap,Coolant} \cdot \left(h_{Evap,Coolant,Out} - h_{Evap,Coolant,In}\right) \cdot \left(\frac{1000\ \text{W}}{1\ \text{kW}}\right)$	$\rho_{Evap,Coolant,In}$ =999.4±0.1 kg/m^3 $\dot{m}_{Evap,Coolant}$ = 10.5×10^{-3}± 1.7×10^{-3} kg/s $h_{Evap,Coolant,In}$ = 52.8±2.1 kJ/kg $h_{Evap,Ref,Out}$ = 30.1±2.1 kJ/kg $\dot{Q}_{Evap,Coolant}$ = 239±49 W

Table B-23Continued

Input	Equations	Output
$\dot{Q}_{Des}$ = 708.9±7.5 W $\dot{Q}_{Evap,Coolant}$ = 239±49 W	$COP_{Cooling} = \frac{\left\|\dot{Q}_{Evap,Coolant}\right\|}{\dot{Q}_{Des}}$	$COP_{Cooling}$ = 0.34±0.07

Table B-24 Example Heat Exchanger Data Analysis

Input	Equations	Output
$T_{Abs,DS,in}$ = 42.4°C $T_{Abs,CS,Out}$ = 34.3°C $T_{Abs,Ref,in}$ = 25.7°C $T_{Abs,Coolant,in}$ = 30.2°C $T_{Abs,Coolant,Out}$ = 35.0°C P_{Low} = 367 kPa $P_{Coolant}$ = 101 kPa x_{DS} = 0.299 x_{CS} = 0.447 x_{Ref} = 0.946	$h_{Abs,DS,In} = f\left(T_{Abs,DS,In}, P_{Low}, x_{Abs,DS,In}\right)$ $h_{Abs,CS,Out} = f\left(T_{Abs,CS,Out}, P_{Low}, x_{Abs,CS,Out}\right)$ $h_{Abs,Ref,In} = f\left(T_{Abs,Ref,In}, P_{Low}, x_{Abs,Ref,In}\right)$ $h_{Abs,Coolant,In} = f\left(T_{Abs,Coolant,In}, P_{Coolant}\right)$ $h_{Abs,Coolant,Out} = f\left(T_{Abs,Coolant,Out}, P_{Coolant}\right)$ $\rho_{Abs,Coolant,In} = f\left(T_{Abs,Coolant,In}, P_{Coolant}\right)$	$h_{Abs,DS,In}$ = -6.2 kJ/kg $h_{Abs,CS,Out}$ = -83.4 kJ/kg $h_{Abs,Ref,In}$ = 1175 kJ/kg $h_{Abs,Coolant,In}$ = 126.4 kJ/kg $h_{Abs,Coolant,Out}$ = 146.6 kJ/kg $\rho_{Abs,Coolant,In}$ = 996 kg/m^3

Table B-24 Continued

Input	Equations	Output
$h_{Abs,Coolant,In}$ = 126.4 kJ/kg $h_{Abs,Coolant,Out}$ = 146.6 kJ/kg $\rho_{Abs,Coolant,In}$ = 996 kg/m^3 $\dot{V}_{Abs,Coolant}$ = 16 Gal/hr	$\dot{m}_{Abs,Coolant} = \rho_{Abs,Coolant,In} \cdot \dot{V}_{Abs,Coolant} \cdot \left(\frac{1\ \text{m}^3}{264.17\ \text{Gal}} \frac{1\ \text{hr}}{3600\ \text{sec}} \right)$ $\dot{Q}_{Abs,Coolant} = \dot{m}_{Abs,Coolant} \left(h_{Abs,Coolant,Out} - h_{Abs,Coolant,In} \right)$	$\dot{m}_{Abs,Coolant}$ = 16.8×10^{-3} kg/s $\dot{Q}_{Abs,Coolant}$ = 337 W
$h_{Abs,DS,In}$ = -6.2 kJ/kg $h_{Abs,CS,Out}$ = -83.4 kJ/kg $h_{Abs,Ref,In}$ = 1175 kJ/kg $\dot{m}_{DS}$ = 9.51×10^{-4} kg/s $\dot{m}_{CS}$ = 1.23×10^{-3} kg/s $\dot{m}_{Ref}$ = 2.8×10^{-4} kg/s	$\dot{Q}_{Abs,Sol} = \dot{m}_{DS} \cdot h_{Abs,DS,In} + \dot{m}_{Ref} \cdot h_{Abs,Ref,In} - \dot{m}_{CS} \cdot h_{Abs,CS,Out}$	$\dot{Q}_{Abs,Sol}$ = 428 W
$\dot{Q}_{Abs,Sol}$ = 428 W $\dot{Q}_{Abs,Coolant}$ = 337 W $T_{Abs,DS,in}$ = 42.4°C $T_{Abs,CS,Out,Sat}$ = 38.7°C $T_{Abs,Coolant,in}$ = 30.2°C $T_{Abs,Coolant,Out}$ = 35.0°C	$\dot{Q}_{Abs} = \frac{\left(\dot{Q}_{Abs,Coolant} + \dot{Q}_{Abs,Sol} \right)}{2}$ $LMTD_{Abs} = \frac{\left(T_{Abs,DS,In} - T_{Abs,Coolant,out} \right) - \left(T_{Abs,CS,out,Sat} - T_{Abs,Coolant,In} \right)}{\text{Ln}\left[\frac{\left(T_{Abs,DS,In} - T_{Abs,Coolant,out} \right)}{\left(T_{Abs,CS,out,Sat} - T_{Abs,Coolant,In} \right)} \right]}$ $UA_{Abs} = \dot{Q}_{Abs} / LMTD_{Abs}$	$\dot{Q}_{Abs}$ = 382 W $LMTD_{Abs}$ = 8.0°C UA_{Abs} = 47.7 W/m^2-K

Table B-24 Continued

Input	Equations	Output
$T_{Cond,Ref,In} = 94.8°C$ $T_{Cond,Ref,Out} = 31.4°C$ $T_{Cond,Coolant,In} = 30.3°C$ $T_{Cond,Coolant,Out} = 35.2°C$ $P_{High} = 1304$ kPa $P_{Coolant} = 101$ kPa $x_{Ref} = 0.946$	$h_{Cond,Ref,In} = f\left(T_{Cond,Ref,In}, P_{High}, x_{Ref}\right)$ $h_{Cond,Ref,Out} = f\left(T_{Cond,Ref,Out}, P_{High}, x_{Ref}\right)$ $h_{Cond,Coolant,In} = f\left(T_{Cond,Coolant,In}, P_{Coolant}\right)$ $h_{Cond,Coolant,Out} = f\left(T_{Cond,Coolant,Out}, P_{Coolant}\right)$ $\rho_{Cond,Coolant,In} = f\left(T_{Cond,Coolant,In}, P_{Coolant}\right)$	$h_{Cond,Ref,In} = 1465$ kJ/kg $h_{Cond,Ref,Out} = 108.6$ kJ/kg $h_{Cond,Coolant,In} = 127.2$ kJ/kg $h_{Cond,Coolant,Out} = 147.4$ kJ/kg $\rho_{Cond,Coolant,In} = 996$ kg/m^3
$h_{Cond,Coolant,In} = 127.2$ kJ/kg $h_{Cond,Coolant,Out} = 147.4$ kJ/kg $\rho_{Cond,Coolant,In} = 996$ kg/m^3 $\dot{V}_{Cond,Coolant} = 16$ Gal/hr	$\dot{m}_{Cond,Coolant} = \rho_{Cond,Coolant,In} \cdot \dot{V}_{Cond,Coolant} \cdot \left(\frac{1\text{ m}^3}{264.17\text{ Gal}} \frac{1\text{ hr}}{3600\text{ sec}}\right)$ $\dot{Q}_{Cond,Coolant} = \dot{m}_{Cond,Coolant}\left(h_{Cond,Coolant,Out} - h_{Cond,Coolant,In}\right)$	$\dot{m}_{Cond,Coolant} = 16.8\times10^{-3}$ kg/s $\dot{Q}_{Cond,Coolant} = 339$ W
$h_{Cond,Ref,In} = 1465$ kJ/kg $h_{Cond,Ref,Out} = 108.6$ kJ/kg $\dot{m}_{Ref} = 2.8\times10^{-4}$ kg/s	$\dot{Q}_{Cond,Ref} = \dot{m}_{Ref} \cdot \left(h_{Cond,Ref,In} - h_{Cond,Ref,Out}\right)$	$\dot{Q}_{Cond,Ref} = 382$ W

Table B-24 Continued

Input	Equations	Output
$\dot{Q}_{Cond,Coolant} = 339$ W $\dot{Q}_{Cond,Ref} = 382$ W $T_{Cond,Ref,Out,Sat} = 35.6°C$ $T_{Cond,Coolant,In} = 30.3°C$ $T_{Cond,Coolant,Out} = 35.2°C$	$\dot{Q}_{Cond} = \frac{\left(\dot{Q}_{Cond,Coolant} + \dot{Q}_{Cond,Ref}\right)}{2}$ $LMTD_{Cond} = \frac{\left(T_{Cond,Ref,Out,Sat} - T_{Cond,Coolant,Out}\right) - \left(T_{Cond,Ref,Out,Sat} - T_{Cond,Coolant,In}\right)}{\mathrm{Ln}\left[\frac{\left(T_{Cond,Ref,In,Sat} - T_{Cond,Coolant,Out}\right)}{\left(T_{Cond,Ref,Out,Sat} - T_{Cond,Coolant,In}\right)}\right]}$ $UA_{Cond} = \dot{Q}_{Cond} / LMTD_{Cond}$	$\dot{Q}_{Cond} = 360$ W $LMTD_{Cond} = 2.0°C$ $UA_{Cond} = 179.7$ W/m^2-K
$T_{SHX,CS,In} = 36.3°C$ $T_{SHX,CS,Out} = 89.8°C$ $T_{SHX,DS,In} = 111.6°C$ $T_{SHX,DS,Out} = 47.7°C$ $P_{High} = 1304$ kPa $x_{DS} = 0.299$ $x_{CS} = 0.447$	$h_{SHX,CS,In} = f\left(T_{SHX,CS,In}, P_{High}, x_{CS}\right)$ $h_{SHX,CS,Out} = f\left(T_{SHX,CS,Out}, P_{High}, x_{CS}\right)$ $h_{SHX,DS,In} = f\left(T_{SHX,DS,In}, P_{High}, x_{DS}\right)$ $h_{SHX,DS,Out} = f\left(T_{SHX,DS,Out}, P_{High}, x_{DS}\right)$	$h_{SHX,CS,In} = -73.8$ kJ/kg $h_{SHX,CS,Out} = 239.5$ kJ/kg $h_{SHX,DS,In} = 299.3$ kJ/kg $h_{SHX,DS,Out} = 17.18$ kJ/kg
$\dot{m}_{CS} = 1.23\times10^{-3}$ kg/s $h_{SHX,CS,In} = -73.8$ kJ/kg $h_{SHX,CS,Out} = 239.5$ kJ/kg	$\dot{Q}_{SHX,CS} = \dot{m}_{CS} \cdot \left(h_{SHX,CS,Out} - h_{SHX,CS,In}\right)$	$\dot{Q}_{SHX,CS} = 386$ W

Table B-24 Continued

Input	Equations	Output
$\dot{m}_{DS} = 9.51\times10^{-4}$ kg/s $h_{SHX,DS,In} = 299.3$ kJ/kg $h_{SHX,DS,Out} = 17.18$ kJ/kg	$\dot{Q}_{SHX,DS} = \dot{m}_{DS} \cdot \left(h_{SHX,DS,In} - h_{SHX,DS,Out}\right)$	$\dot{Q}_{SHX,DS} = 268$ W
$\dot{Q}_{SHX,CS} = 386$ W $\dot{Q}_{SHX,DS} = 268$ W $T_{SHX,CS,In} = 36.3$°C $T_{SHX,CS,Out} = 89.8$°C $T_{SHX,DS,In} = 111.6$°C $T_{SHX,DS,Out} = 47.7$°C	$\dot{Q}_{SHX} = \frac{\left(\dot{Q}_{SHX,CS} + \left\|\dot{Q}_{SHX,DS}\right\|\right)}{2}$ $LMTD_{SHX} = \frac{\left(T_{SHX,DS,In} - T_{SHX,CS,Out}\right) - \left(T_{SHX,DS,Out} - T_{SHX,CS,In}\right)}{\mathrm{Ln}\left[\frac{\left(T_{SHX,DS,In} - T_{SHX,CS,Out}\right)}{\left(T_{SHX,DS,Out} - T_{SHX,CS,In}\right)}\right]}$ $UA_{SHX} = \dot{Q}_{SHX} / LMTD_{SHX}$	$\dot{Q}_{SHX} = 327$ $LMTD_{SHX} = 16.0$°C $UA_{SHX} = 20$ W/m^2-K
$T_{Evap,Ref,In} = -1.3$°C $T_{Evap,Ref,Out} = 16.8$°C $T_{Evap,Coolant,In} = 12.5$°C $T_{Evap,Coolant,Out} = 7.1$°C $T_{RHX,High,Out} = 22.6$ $P_{High} = 1304$ $P_{Evap} = 375$ kPa $x_{Ref} = 0.946$ $P_{Coolant} = 101$ kPa	$h_{Evap,Ref,In} = f\left(T_{Evap,Ref,In}, P_{Evap}, x_{Ref}\right)$ $h_{Evap,Ref,Out} = f\left(T_{Evap,Ref,Out}, P_{Evap}, x_{Ref}\right)$ $h_{Evap,Coolant,In} = f\left(T_{Evap,Coolant,In}, P_{Coolant}\right)$ $h_{Evap,Coolant,Out} = f\left(T_{Evap,Coolant,Out}, P_{Coolant}\right)$ $h_{RHX,High,Out} = f\left(T_{RHX,High,Out}, P_{High}, x_{Ref}\right)$ $\rho_{Evap,Coolant,In} = f\left(T_{Evap,Coolant,In}, P_{Coolant}\right)$	$h_{Evap,Ref,In} = 510$ kJ/kg $h_{Evap,Ref,Out} = 1115$ kJ/kg $h_{Evap,Coolant,In} = 52.8$ kJ/kg $h_{Evap,Coolant,Out} = 30.1$ kJ/kg $h_{RHX,High,Out} = 66.4$ kJ/kg $\rho_{Evap,Coolant,In} = 999$ kg/m^3

Table B-24 Continued

Input	Equations	Output
$h_{Evap,Ref,In} = 510$ kJ/kg $h_{Evap,Ref,Out} = 1115$ kJ/kg $\dot{m}_{Ref} = 2.8\times10^{-4}$ kg/s	$\dot{Q}_{Evap,Ref} = \dot{m}_{Ref} \cdot \left(h_{Evap,Ref,Out} - h_{Evap,Ref,In}\right)$	$\dot{Q}_{Evap,Ref} = 170$ W
$h_{Evap,Coolant,In} = 52.8$ kJ/kg $h_{Evap,Coolant,Out} = 30.1$ kJ/kg $\rho_{Evap,Coolant,In} = 999$ kg/m^3 $\dot{V}_{Evap,Coolant} = 10$ Gal/hr	$\dot{m}_{Evap,Coolant} = \rho_{Evap,Coolant,In} \cdot \dot{V}_{Evap,Coolant} \cdot \left(\frac{1\text{ m}^3}{264.17\text{ Gal}} \frac{1\text{ hr}}{3600\text{ sec}}\right)$ $\dot{Q}_{Evap,Coolant} = \dot{m}_{Evap,Coolant}\left(h_{Evap,Coolant,In} - h_{Evap,Coolant,Out}\right)$	$\dot{m}_{Evap,Coolant} = 10.5\times10^{-3}$ kg/s $\dot{Q}_{Evap,Coolant} = 239$ W
$h_{RHX,High,Out} = 66.4$ kJ/kg $h_{Evap,Ref,Out} = 1115$ kJ/kg $\dot{m}_{Ref} = 2.8\times10^{-4}$ kg/s	$\dot{Q}_{Evap,Ref,Alt} = \dot{m}_{Ref} \cdot \left(h_{Evap,Ref,Out} - h_{RHX,High,Out}\right)$	$\dot{Q}_{Evap,Ref,Alt} = 295$ W
$\dot{Q}_{Evap,Ref} = 170$ W $\dot{Q}_{Evap,Coolant} = 239$ W $\dot{Q}_{Evap,Ref,Alt} = 295$ W $T_{Evap,Ref,In} = -1.3$°C $T_{Evap,Coolant,In} = 12.5$°C $T_{Evap,Coolant,Out} = 7.1$°C	$\dot{Q}_{Evap} = \left\lvert\dot{Q}_{Evap,Coolant}\right\rvert$ $LMTD_{Evap} = \frac{\left(T_{Evap,Coolant,In} - T_{Evap,Ref,In}\right) - \left(T_{Evap,Coolant,Out} - T_{Evap,Ref,In}\right)}{\text{Ln}\left[\frac{\left(T_{Evap,Coolant,In} - T_{Evap,Ref,In}\right)}{\left(T_{Evap,Coolant,Out} - T_{Evap,Ref,In}\right)}\right]}$ $UA_{Evap} = \dot{Q}_{Evap} / LMTD_{Evap}$	$\dot{Q}_{Evap} = 239$ W $LMTD_{Evap} = 10.9$°C $UA_{Evap} = 21.9$ W/m^2-K

Table B-24 Continued

Input	Equations	Output
$T_{Rec,Coolant,In} = 30.1°C$ $T_{Rec,Coolant,Out} = 36.5°C$ $P_{Coolant} = 101$ kPa	$h_{Rec,Coolant,Out} = f\left(T_{Rec,Coolant,Out}, P_{Coolant}\right)$ $h_{Rec,Coolant,Out} = f\left(T_{Rec,Coolant,Out}, P_{Coolant}\right)$ $\rho_{Evap,Coolant,In} = f\left(T_{Evap,Coolant,In}, P_{Coolant}\right)$	$h_{Rec,Coolant,In} = 126.4$ kJ/kg $h_{Rec,Coolant,Out} = 153$ kJ/kg $\rho_{Rec,Coolant,In} = 996$ kg/m^3
$h_{Rec,Coolant,In} = 126.4$ kJ/kg $h_{Rec,Coolant,Out} = 153$ kJ/kg $\rho_{Rec,Coolant,In} = 996$ kg/m^3 $\dot{V}_{Rec,Coolant} = 5$ Gal/hr	$\dot{m}_{Rec,Coolant} = \rho_{Rec,Coolant,In} \cdot \dot{V}_{Rec,Coolant} \cdot \left(\frac{1\text{ m}^3}{264.17\text{ Gal}} \frac{1\text{ hr}}{3600\text{ sec}}\right)$ $\dot{Q}_{Rec,Coolant} = \dot{m}_{Rec,Coolant}\left(h_{Rec,Coolant,Out} - h_{Rec,Coolant,In}\right)$	$\dot{m}_{Rec,Coolant} = 5.2\times10^{-3}$ kg/s $\dot{Q}_{Rec,Coolant} = 139$ W
$T_{Rec,DS,out} = 115.4°C$ $T_{Rec,Ref,Out} = 102.2°C$ $T_{Rec,Coolant,In} = 30.1°C$ $T_{Rec,Coolant,Out} = 36.5°C$ $\dot{Q}_{Rec,Coolant} = 139$ W	$\dot{Q}_{Rec} = \dot{Q}_{Rec,Coolant}$ $LMTD_{Rec} = \frac{\left(T_{Rec,DS,Out} - T_{Rec,Coolant,Out}\right) - \left(T_{Rec,Ref,Out} - T_{Rec,Coolant,In}\right)}{\text{Ln}\left[\frac{\left(T_{Rec,DS,Out} - T_{Rec,Coolant,Out}\right)}{\left(T_{Rec,Ref,Out} - T_{Rec,Coolant,In}\right)}\right]}$ $UA_{Rec} = \dot{Q}_{Rec} / LMTD_{Rec}$	$\dot{Q}_{Rec} = 139$ W $LMTD_{Rec} = 75.4°C$ $UA_{Rec} = 1.8$ W/m^2-K

Appendix C Heat Loss Calculation

C.1 Microchannel System Heat Loss Calculation

This section outlines the calculations to determine the heat loss from the experimental system. The details of the calculations can be seen in Table C-1.

The heat losses from the microchannel system and the experimental apparatus used during testing were estimated by approximating the components of the system as several basic geometric shapes. The monolithic stack assembly containing all of the heat exchangers was modeled as a rectangular box. The stack was insulated on all sides with a flexible melamine foam insulation with an insulation thickness of 38 mm. The melamine foam insulation had an operating temperature range of -40 to 177°C. The thermal conductivity of the insulation was 0.0375 W/m-K. The exterior dimensions of the system, including the insulation were 276×276×110 mm.

During testing at nominal conditions of 700 W desorber heat input and 30°C heat sink temperature, and an ambient room temperature of 22.2°C, the surface temperatures of various parts of the system were measured periodically by an infrared thermometer. The temperature on the surface of the insulation covering the diffusion bonded stack varied from 45°C near the desorber to 25°C near the evaporator. For the purpose of this heat loss estimation, an average surface temperature of 35°C was used. The free convection correlation recommended by Incropera and DeWitt (2002) for a vertical flat plate is:

$$Nu_L = \left(0.825 + \frac{0.387 \cdot Ra_L^{1/6}}{\left(1 + \left(0.492/Pr\right)^{9/16}\right)^{8/27}} \right)^2 \quad \text{(C.1)}$$

For the top of the stack, the correlation for an upward facing heated plate was used.

$$Nu_{L_C} = 0.54 \cdot Ra_{L_C}^{1/4} \quad \text{(C.2)}$$

The characteristic length used for this correlation was

$$L_c = \frac{A_s}{P} \quad \text{(C.3)}$$

where A_s is the surface area of the top plate and P is the perimeter. For the bottom of the stack, the correlation for a downward facing heated plate was used.

$$Nu_{L_C} = 0.27 \cdot Ra_{L_C}^{1/4} \quad \text{(C.4)}$$

Using these correlations the free convection heat transfer coefficients for the various surfaces were calculated. The heat transfer coefficients for the vertical sides, top and bottom plates were 3.8, 5.8 and 2.9 W/m^2-K respectively.

The radiation losses from the stack were estimated by assuming the stack is a small surface in a large, isothermal surroundings at the ambient temperature. The surface of the insulation is also assumed to be a gray surface with an emissivity of 0.85. The net radiation exchange between the surface and the surroundings was calculated by:

$$\dot{Q}_{rad} = \varepsilon \sigma A_s \left(T_S^4 - T_{Sur}^4 \right) \quad \text{(C.5)}$$

The total convection loss from the stack was calculated to be 13.8 W while the radiation losses were 18.5 W.

The external tubing connecting the components and the fittings were insulated with silicone foam insulation. The silicone foam had an operating temperature range of -51 to 260°C and a thermal conductivity of 0.0563 W/m-K. The insulation had a thickness of 9.53 mm and an outside diameter of 25.4 mm. There were 26 fittings each 50 mm long and approximately 3 meters of external tubing. The heat losses from the fittings and tubing were calculated by modeling the fittings and tubing as horizontal cylinders. Based on the measurements of surface temperature during the experiments, an average surface temperature of the tubing was 30°C. The recommended correlation for free convection from this geometry is:

$$Nu_D = \left(0.60 + \frac{0.387 \cdot Ra^{1/6}}{\left(1 + \left(0.559/Pr\right)^{9/16}\right)^{8/27}} \right)^2 \qquad \text{(C.6)}$$

The free convection heat transfer coefficient for the tubing was 4.7 W/m^2-K and the estimated convection losses were 12.4 W. The net radiation heat transfer was calculated using Equation (C.5). The radiation losses from the fittings and tubing were 13.8 W.

The solution sump was insulated with polyurethane foam insulation. The polyurethane had an operating temperature range of -29 to 93°C and a thermal conductivity of 0.0433 W/m-K. The insulation was 12.7 mm thick. The solution sump was modeled as a horizontal cylinder with a total diameter, including insulation, of 120 mm and a length of 250 mm. The surface temperature of the insulation on the solution sump was 28°C. The free convection heat losses from this component were calculated by using Equation (C.6). The free convection heat loss from the fittings and tubing was 12.4 W and the radiation losses, calculated using Equation (C.5), were 13.8 W.

The rectifier Surge Tank was insulated with rigid polyurethane foam. The polyurethane had an operating temperature range of -183 to 159°C and a thermal conductivity of 0.0274 W/m-K. The insulation was 25.4 mm thick and had an outside diameter of 92 mm. The reservoir was modeled as a vertical cylinder with a total diameter of 92 mm and a length of 200 mm. The free convection heat transfer coefficient was calculated as recommended by Incropera and DeWitt (2002) by using the vertical flat plate correlation of Equation (C.1). The average surface temperature of the rectifier reservoir was 35°C. The free convection heat transfer coefficient for the rectifier reservoir was 3.5 W/m^2-K and the free convection heat loss was 3.1 W. The radiation heat transfer losses were 4.8 W.

The total calculated heat loss for the system at these operation conditions was 72 W.

C.2 Microchannel System Heat Loss Estimation Calculation Details

Table C-1 Heat Loss Calculation

Input	Equations	Output
$T_{Air} = 22.2°C$ $P = 101$ kPa	$\beta_{Air} = \frac{1}{T_{Ambient}(K)}$ $k_{Air} = f(T_{Air})$ $\rho_{Air} = f(T_{Air}, P)$ $\mu_{Air} = f(T_{Air})$ $\nu_{Air} = \mu_{Air} / \rho_{Air}$ $\mathrm{Pr}_{Air} = f(T_{Air})$	$\beta_{air} = 0.00339$ 1/K $k_{air} = 0.0253$ W/m-K $\rho_{air} = 1.19$ kg/m^3 $\mu_{air} = 18.4 \times 10^{-6}$ kg/m-s $\nu_{air} = 15.4 \times 10^{-6}$ m^2/s $\mathrm{Pr}_{air} = 0.73$
Stack Geometry $L_{Stack} = 0.276$ m $H_{Stack} = 0.276$ m $W_{Stack} = 0.110$ m	$A_{Front} = L_{Stack} \cdot H_{Stack}$ $A_{Back} = L_{Stack} \cdot H_{Stack}$ $A_{Left} = W_{Stack} \cdot H_{Stack}$ $A_{Right} = W_{Stack} \cdot H_{Stack}$ $A_{Top} = W_{Stack} \cdot L_{Stack}$ $A_{Bottom} = W_{Stack} \cdot L_{Stack}$ $A_{Stack} = A_{Front} + A_{Back} + A_{Left} + A_{Right} + A_{Top} + A_{Bottom}$	$A_{Front} = 0.07618$ m^2 $A_{Back} = 0.07618$ m^2 $A_{Left} = 0.03036$ m^2 $A_{Right} = 0.03036$ m^2 $A_{Top} = 0.03036$ m^2 $A_{Bottom} = 0.03036$ m^2 $A_{Stack} = 0.2131$ m^2

Table C-1 Continued

Input	Equations	Output
Vertical Sections β_{air} = 0.00339 1/K T_{Air} = 22.2°C T_S = 35°C H_{Stack} = 0.276 m ν_{air} = 15.4 ×10^{-6} m^2/s Pr_{air} = 0.73 k_{air} = 0.0253 W/m-K	$L_C = H_{Stack}$ $Gr_L = \frac{g\beta(T_s - T_{Air})L_C^3}{\nu^2}$ $Ra_L = Gr_L \cdot Pr_{air}$ $Nu_L = \left(0.825 + \frac{0.387 \cdot Ra_L^{1/6}}{\left(1+(0.492/Pr)^{9/16}\right)^{8/27}}\right)^2$ $\alpha_{Stack,Vertical} = \frac{Nu_L \cdot k_{Air}}{L_C}$	L_C = 0.276 m $Gr_L = 3.7 \times 10^7$ $Ra_L = 2.7 \times 10^7$ Nu_L = 41.84 $\alpha_{Stack,Vertical}$ = 3.8 W/m^2-K
Upward Facing Surface β_{air} = 0.00339 1/K T_{Air} = 22.2°C T_S = 35°C L_{Stack} = 0.276 m W_{Stack} = 0.110 m ν_{air} = 15.4 ×10^{-6} m^2/s Pr_{air} = 0.73 k_{air} = 0.0253 W/m-K	$L_C = \frac{L_{Stack} \cdot W_{Stack}}{2(L_{Stack} + W_{Stack})}$ $Gr_L = \frac{g\beta(T_s - T_{Air})L_C^3}{\nu^2}$ $Ra_L = Gr_L \cdot Pr_{air}$ $Nu_L = 0.54 \cdot Ra_L^{1/4}$ $\alpha_{Stack,Top} = \frac{Nu_L \cdot k_{Air}}{L_C}$	L_C = 0.039 m $Gr_L = 1.1 \times 10^5$ Ra_L = 79000 Nu_L = 9.1 $\alpha_{Stack,Top}$ = 5.8 W/m^2-K

Table C-1 Continued

Input	Equations	Output
Downward Facing Surface $\beta_{air} = 0.00339$ 1/K $T_{Air} = 22.2°C$ $T_S = 35°C$ $L_{Stack} = 0.276$ m $W_{Stack} = 0.110$ m $\nu_{air} = 15.4 \times 10^{-6}$ m^2/s $Pr_{air} = 0.73$ $k_{air} = 0.0253$ W/m-K	$L_C = \frac{L_{Stack} \cdot W_{Stack}}{2\left(L_{Stack} + W_{Stack}\right)}$ $Gr_L = \frac{g\beta\left(T_s - T_{Air}\right)L_C^3}{\nu^2}$ $Ra_L = Gr_L \cdot Pr_{air}$ $Nu_L = 0.27 \cdot Ra_L^{1/4}$ $\alpha_{Stack,Bottom} = \frac{Nu_L \cdot k_{Air}}{L_C}$	$L_C = 0.039$ m $Gr_L = 1.1 \times 10^5$ $Ra_L = 79000$ $Nu_L = 4.5$ $\alpha_{Stack,Bottom} = 2.9$ W/m^2-K
$T_{Air} = 22.2°C$ $T_S = 35°C$ $\alpha_{Stack,Vertical} = 3.8$ W/m^2-K $\alpha_{Stack,Top} = 0.83$ W/m^2-K $\alpha_{Stack,Bottom} = 0.42$ W/m^2-K All Surface Areas	$\dot{Q}_{Stack,Vertical} = \alpha_{Stack,Vertical} \cdot \left(A_{Front} + A_{Back} + A_{Left} + A_{Right}\right) \cdot \left(T_s - T_{Air}\right)$ $\dot{Q}_{Stack,Top} = \alpha_{Stack,Top} \cdot \left(A_{Top}\right) \cdot \left(T_s - T_{Air}\right)$ $\dot{Q}_{Stack,Bottom} = \alpha_{Stack,Bottom} \cdot \left(A_{Bottom}\right) \cdot \left(T_s - T_{Air}\right)$ $\dot{Q}_{Stack,Convection} = \dot{Q}_{Stack,Vertical} + \dot{Q}_{Stack,Top} + \dot{Q}_{Stack,Bottom}$	$\dot{Q}_{Stack,Vertical} = 10.4$ W $\dot{Q}_{Stack,Top} = 2.3$ W $\dot{Q}_{Stack,Bottom} = 1.1$ W $\dot{Q}_{Stack,Convection} = 10.9$ W

Table C-1 Continued

Input	Equations	Output
$T_{Sur} = 22.2°C$ $T_S = 35°C$ $\varepsilon = 0.85$ $\sigma = 5.67 \times 10^{-8}$ W/m^2-K^4 $A_{Stack} = 0.2131$ m^2	$\dot{Q}_{Stack,Rad} = \varepsilon\sigma A_{Stack}\left(\left(T_S + 273\right)^4 - \left(T_{Sur} + 273\right)^4\right)$	$\dot{Q}_{Stack,Rad} = 18.5$ W
$\dot{Q}_{Stack,Convection} = 10.9$ W $\dot{Q}_{Stack,Rad} = 18.5$ W	$\dot{Q}_{Stack} = \dot{Q}_{Stack,Convection} + \dot{Q}_{Stack,Rad}$	$\dot{Q}_{Stack} = 29.4$ W
$D_{Tubing} = 0.0254$ m $D_{Fittings} = 0.0254$ m $L_{Tubing} = 3$ m $L_{Fittings} = 0.05$ m # Fittings = 26	$A_{Fittings} = 26 \cdot \pi D_{Fittings} \cdot L_{Fittings}$ $A_{Tubing} = \pi \cdot D_{Tubing} \cdot L_{Tubing}$ $A_{T\&F} = A_{Tubing} + A_{Fittings}$	$A_{Fittings} = 0.104$ m^2 $A_{Tubing} = 0.239$ m^2 $A_{T\&F} = 0.343$ m^2
$T_{Air} = 22.2°C$ $T_S = 35°C$ D= 0.0254 m $\nu_{air} = 15.4 \times 10^{-6}$ m^2/s $Pr_{air} = 0.73$	$Gr_D = \frac{g\beta\left(T_s - T_{Air}\right)D^3}{\nu^2}$ $Ra_D = Gr_D \cdot Pr_{Air}$	$Gr_L = 18000$ $Ra_L = 13000$

Table C-1 Continued

Input	Equations	Output
$Pr_{air} = 0.73$ $Ra_L = 13000$ $k_{air} = 0.0253$ W/m-K D = 0.0254 m	$Nu_D = \left(0.6 + \frac{0.387 \cdot Ra^{1/6}}{\left(1 + \left(0.559/Pr_{air}\right)^{9/16}\right)^{8/27}} \right)^2$ $\alpha_{T\&F} = \frac{Nu_D \cdot k_{Air}}{D}$	$Nu_D = 4.7$ $\alpha_{T\&F} = 4.7$ W/m^2-K
$\alpha_{T\&F} = 4.7$ W/m^2-K $A_{T\&F} = 0.343$ m^2 $T_{Air} = 22.2$°C $T_S = 35$°C $\varepsilon = 0.85$ $\sigma = 5.67 \times 10^{-8}$ W/m^2-K^4	$\dot{Q}_{T\&F,Conv} = \alpha_{T\&F} \cdot \left(A_{T\&F}\right) \cdot \left(T_s - T_{Air}\right)$ $\dot{Q}_{T\&F,Rad} = \varepsilon\sigma A_{T\&F} \left(\left(T_S + 273\right)^4 - \left(T_{Sur} + 273\right)^4 \right)$ $\dot{Q}_{T\&F} = \dot{Q}_{T\&F,Conv} + \dot{Q}_{T\&F,Rad}$	$\dot{Q}_{T\&F,Conv} = 12.4$ W $\dot{Q}_{T\&F,Rad} = 13.8$ W $\dot{Q}_{T\&F} = 26.2$ W
Solution Sump $D_{Sump} = 0.12$ m $L_{Sump} = 0.25$ m	$A_{Sump} = \pi D_{Sump} L_{Sump} + 2\frac{\pi D^2_{Sump}}{4}$	$A_{Sump} = 0.117$ m^2

Table C-1 Continued

Input	Equations	Output
$\beta_{air} = 0.00339$ 1/K $T_{Air} = 22.2°C$ $T_S = 28°C$ $D_{Sump} = 0.12$ m $\nu_{Air} = 15.4 \times 10^{-6}$ m^2/s $Pr_{Air} = 0.73$ $k_{air} = 0.0253$ W/m-K	$Gr_D = \frac{g\beta(T_s - T_{Air})D^3}{\nu_{Air}^2}$ $Ra_D = Gr_D \cdot Pr_{Air}$ $Nu_D = \left(0.6 + \frac{0.387 \cdot Ra^{1/6}}{\left(1+(0.559/Pr_{air})^{9/16}\right)^{8/27}}\right)^2$ $\alpha_{Sump} = \frac{Nu_D \cdot k_{Air}}{D_{Sump}}$	$Gr_D = 1.4\times10^6$ $Ra_D = 1.0\times10^6$ $Nu_D = 14.7$ $\alpha_{Sump} = 3.1$ W/m^2-K
$\alpha_{Sump} = 3.1$ W/m^2-K $A_{Sump}=0.117$ m^2 $T_{Air} = 22.2°C$ $T_S = 28°C$ $\varepsilon = 0.85$ $\sigma = 5.67 \times 10^{-8}$ W/m^2-K^4	$\dot{Q}_{Sump,Conv} = \alpha_{Sump} \cdot (A_{Sump}) \cdot (T_s - T_{Air})$ $\dot{Q}_{Sump,Rad} = \varepsilon\sigma A_{Sump}\left((T_S + 273)^4 - (T_{Sur} + 273)^4\right)$ $\dot{Q}_{Sump} = \dot{Q}_{Sump,Conv} + \dot{Q}_{Sump,Rad}$	$\dot{Q}_{Sump,Conv} = 2.1$ W $\dot{Q}_{Sump,Rad} = 3.5$ W $\dot{Q}_{Sump} = 5.6$ W

Table C-1 Continued

Input	Equations	Output
Rectifier Surge Tank $D_{Reservoir}$ = 0.092 m $L_{Reservoir}$ = 0.2 m	$A_{Reservoir} = \pi D_{Reservoir} L_{Reservoir} + 2\frac{\pi D^2_{Reservoir}}{4}$	$A_{Reservoir}$=0.071 m^2
β_{air} = 0.00339 1/K T_{Air} = 22.2°C T_S = 35°C $L_{Reservoir}$ = 0.2 m ν_{Air} = 15.4 ×10^{-6} m^2/s Pr_{Air} = 0.73 k_{air} = 0.0253 W/m-K	$Gr_L = \frac{g\beta(T_s - T_{Air})L^3}{\nu^2_{Air}}$ $Ra_L = Gr_L \cdot Pr_{Air}$ $Nu_L = \left(0.825 + \frac{0.387 \cdot Ra_L^{1/6}}{\left(1+(0.492/Pr)^{9/16}\right)^{8/27}}\right)^2$ $\alpha_{Reservoir} = \frac{Nu_L \cdot k_{Air}}{D_{Reservoir}}$	Gr_L = 1.4×10^7 Ra_L = 1.0×10^7 Nu_L = 27.3 $\alpha_{Reservoir}$ = 3.5 W/m^2-K
$\alpha_{Reservoir}$ = 3.5 W/m^2-K $A_{Reservoir}$=0.071 m^2 T_{Air} = 22.2°C T_S = 35°C ε = 0.85 σ = 5.67 × 10^{-8} W/m^2-K^4	$\dot{Q}_{Reservoir,Conv} = \alpha_{Reservoir} \cdot (A_{Reservoir}) \cdot (T_s - T_{Air})$ $\dot{Q}_{Reservoir,Rad} = \varepsilon\sigma A_{Reservoir}\left((T_S + 273)^4 - (T_{Sur} + 273)^4\right)$ $\dot{Q}_{Reservoir} = \dot{Q}_{Reservoir,Conv} + \dot{Q}_{Reservoir,Rad}$	$\dot{Q}_{Reservoir,Conv}$ = 3.1 W $\dot{Q}_{Reservoir,Rad}$ = 4.8 W $\dot{Q}_{Reservoir}$ = 7.9 W

References

Akhilesh, R., A. Narasimhan and C. Balaji (2005), "Method to Improve Geometry for Heat Transfer Enhancement in PCM Composite Heat Sinks," *International Journal of Heat and Mass Transfer* Vol. 48(13) pp. 2759-2770.

Alawadhi, E. M. and C. H. Amon (2003), "PCM Thermal Control Unit for Portable Electronic Devices: Experimental and Numerical Studies," *IEEE Transactions on Components and Packaging Technologies* Vol. 26(1) pp. 116-125.

ANSYS (2007). *ANSYS Academic Research*, ANSYS, Inc.

Ashraf, N. S., H. C. Carter, III, K. Casey, L. C. Chow, S. Corban, M. K. Drost, A. J. Gumm, Z. Hao, A. Q. Hasan, J. S. Kapat, L. Kramer, M. Newton, K. B. Sundaram, J. Vaidya and C. C. Wong (1999), "Design and Analysis of a Meso-Scale Refrigerator, Nashville, TN, USA, ASME, Fairfield, NJ, USA, pp. 109-116.

Bandhauer, T. M., A. Agarwal and S. Garimella (2006), "Measurement and Mmodeling of Condensation Heat Transfer Coefficients in Circular Microchannels," *Journal of Heat Transfer* Vol. 128(10) pp. 1050-1059.

Bishop, P., P. Ray and P. Reneau (1995), "Review of the Ergonomics of Work in the US Military Chemical Protective Clothing," *International Journal of Industrial Ergonomics* Vol. 15(4) pp. 271-283.

Brandner, J. J., E. Anurjew, L. Bohn, E. Hansjosten, T. Henning, U. Schygulla, A. Wenka and K. Schubert (2006), "Concepts and Realization of Microstructure Heat Exchangers for Enhanced Heat Transfer," *Experimental Thermal and Fluid Science* Vol. 30(8) pp. 801-809.

Cheuvront, S. N., M. A. Kolka, B. S. Cadarette, S. J. Montain and M. N. Sawka (2003), "Efficacy of Intermittent, Regional Microclimate Cooling," *J Appl Physiol* Vol. 94(5) pp. 1841-1848.

Chisholm, D. (1973), "Pressure Gradients Due to Friction During the Flow of Evaporating Two-Phase Mixtures in Smooth Tubes and Channels," *International Journal of Heat and Mass Transfer* Vol. 16(2) p. 347.

Determan, M. D. and S. Garimella (2005). *Ammonia-Water Desorption Heat and Mass Transfer in Microchannel Devices*. International Sorption Heat Pump Conference. Denver, CO.

DeVault, R. C. and J. Marsala (1990), "Ammonia-Water Triple-Effect Absorption Cycle," *ASHRAE Transactions* Vol. 96(1) pp. 676-682.

Dillon, C. P. (1995). *Corrosion Resistance of Stainless Steels*. New York, Marcel Dekker, Inc.

DOE (2006). *Multi-Year Research, Development and Demonstration Plan: Planned Program Activities for 2004-2015*, Vol. 2007.

Drost, K. (1999), "Mesoscopic Heat-Actuated Heat Pump Development," *American Society of Mechanical Engineers, Advanced Energy Systems Division (Publication) AES* Vol. 39 pp. 9-14.

Epstein, Y., Y. Shapiro and S. Brill (1986), "Comparison Between Different Auxiliary Cooling Devices in a Severe Hot/Dry Climate," *Ergonomics* Vol. 29(1) pp. 41-48.

Erickson, D. C., R. A. Papar and G. Anand (1996), "Basic GAX Cycle Prototype Results," *Proceedings of the International Ab-Sorption Heat Pump Conference*, Montreal, Canada, pp. 717-724.

Ernst, T. C. and S. Garimella (2007). *Wearable Engine-Driven Vapor-Compression Cooling System for Elevated Ambients*. IMECE. Seattle, Washington.

Ernst, T. C. and S. Garimella (2008). *Demonstration of a Wearable Cooling System for Elevated Ambient Temperature Duty Personnel*. 19th National & 8th ISHMT-ASME Heat and Mass Transfer Conference Hyderabad, India.

Friedel, L. (1980), "Pressure Drop During Gas/Vapor-Liquid Flow in Pipes," *International Chemical Engineering* Vol. 20(3) pp. 352-367.

Garimella, S. (1999), "Miniaturized Heat and Mass Transfer Technology for Absorption Heat Pumps," *International Sorption Heat Pump Conference*, Munich, Germany, pp. 661-670.

Garimella, S. (2004). *Method and means for miniaturization of binary-fluid heat and mass exchangers*. 6,802,364.

Garimella, S. (2006). Condensation in Minichannels and Microchannels. *Heat Transfer and Fluid Flow in Minichannels and Microchannels*. S. G. Kandlikar, S. Garimella, D. Li, S. Colin and M. R. King, Elsevier Science.

Garimella, S., A. Agarwal and J. D. Killion (2005), "Condensation Pressure Drop in Circular Microchannels," *Heat Transfer Engineering* Vol. 26(3) p. 28.

Garimella, S. and T. M. Bandhauer (2001), "Measurement of Condensation Heat Transfer Coefficients in Microchannel Tubes, New York, NY, United States, American Society of Mechanical Engineers, New York, NY 10016-5990, United States, pp. 243-249.

Garimella, S., R. N. Christensen and D. Lacy (1996), "Performance Evaluation of a Generator Absorber Heat Exchange Heat Pump," *Applied Thermal Engineering* Vol. 16(7) pp. 591-604.

Garimella, S., J. D. Killion and J. W. Coleman (2002), "An Experimentally Validated Model for Two-Phase Pressure Drop in the Intermittent Flow Regime for Circular Microchannels," *Journal of Fluids Engineering* Vol. 124(1) pp. 205-214.

Garimella, S., J. D. Killion and J. W. Coleman (2003), "An Experimentally Validated Model for Two-Phase Pressure Drop in the Intermittent Flow Regime for Noncircular Microchannels," *Journal of Fluids Engineering* Vol. 125(5) pp. 887-894.

Garimella, S., D. Lacy and R. E. Stout (1997), "Space-Conditioning Using Triple-Effect Absorption Heat Pumps," *Applied Thermal Engineering* Vol. 17(12) pp. 1183-1197.

Gommed, K. and G. Grossman (1990), "Performance Analysis of Staged Absorption Heat Pumps: Water-Lithium Bromide Systems," *ASHRAE Transactions* Vol. 96(1) pp. 1590-1598.

Gordon, J. M., K. C. Ng, H. T. Chua and A. Chakraborty (2002), "The Electro-Adsorption Chiller: a Miniaturized Cooling Cycle with Applications to Micro-Electronics," *International Journal of Refrigeration* Vol. 25(8) pp. 1025-1033.

Grzyll, L. R. and W. C. Balderson (1997), "Development of a Man-Portable Microclimate Adsorption Cooling Device, Honolulu, HI, USA, IEEE, Piscataway, NJ, USA, pp. 1646-1651.

Henning, T., J. J. Brandner and K. Schubert (2004), "Characterization of Electrically Powered Micro-Heat Exchangers," *Chemical Engineering Journal* Vol. 101(1-3) pp. 339-345.

Herold, K. E., R. Radermacher and S. A. Klein (1996). *Absorption Chillers and Heat Pumps*, CRC Press, Inc.

Hong, S.-H., V. Kenning, C. Call and R. Shekarriz (1999), "Experiments and Modeling of a Mesoscale Laminar Plate Heat Exchanger," *American Society of Mechanical Engineers, Advanced Energy Systems Division (Publication) AES* Vol. 39 pp. 15-23.

Incropera, F. P. and D. P. DeWitt (2002). *Fundamentals of Heat and Mass Transfer*. 5 Ed. New York, Wiley.

Ivester, D. N. and S. V. Shelton (1994), "Varying Heat Exchanger Parameters in the Triple-Effect Absorption Cycle," *Proceedings of the International Absorption Heat Pump Conference*, New Orleans, LA, ASME-AES, pp. 243-250.

Kakac, S., R. K. Shah and W. Aung (1987). *Handbook of Single-Phase Convective Heat Transfer*. New York, Wiley.

Kandlikar, S. G. (1990), "General Correlation for Saturated Two-Phase Flow Boiling Heat Transfer Inside Horizontal and Vertical Tubes," *Journal of Heat Transfer, Transactions ASME* Vol. 112(1) pp. 219-228.

Kandlikar, S. G. and P. Balasubramanian (2004), "An Extension of the Flow Boiling Correlation to Transition, Laminar, and Deep Laminar Flows and Microchannels," *Heat Transfer Engineering* Vol. 25(3) pp. 86-93.

Kandlikar, S. G., S. Garimella, D. Li, S. Colin and M. R. King (2005). *Heat Transfer and Fluid Flow in Minichannels and Microchannels*. 1st Ed., Elsevier Science.

Kandlikar, S. G. and M. E. Steinke (2003), "Predicting Heat Transfer During Flow Boiling in Minichannels and Microchannels, Chicago, IL, United States, Amer. Soc. Heating, Ref. Air-Conditioning Eng. Inc., pp. 667-676.

Kiehne, H. A. (2003). *Battery Technology Handbook*. 2 Ed. New York, M. Dekker.

Klein, S. A. (2006). *Engineering Equation Solver*, F-Chart Software.

Ku, Y.-T. E., L. D. Montgomery, K. C. Wenzel, B. W. Webbon and J. S. Burks (1999), "Physiologic and Thermal Responses of Male and Female Patients with Multiple Sclerosis to Head and Neck Cooling," *American Journal of Physical Medicine and Rehabilitation* Vol. 78(5) pp. 447-456.

Liu, D. and S. V. Garimella (2004), "Investigation of Liquid Flow in Microchannels," *Journal of Thermophysics and Heat Transfer* Vol. 18(1) pp. 65-72.

Lockhart, R. W. and R. C. Martinelli (1949), "Proposed Correlation of Data for Isothermal Two-Phase, Two Component Flow in Pipes," *Chemical Engineering Progress* Vol. 45(1) pp. 39 - 48.

Meacham, J. M. and S. Garimella (2002), "Experimental Demonstration of a Prototype Microchannel Absorber for Space-Conditioning Systems," *International Sorption Heat Pump Conference*, Shanghai, China.

Meacham, J. M. and S. Garimella (2003), "Modeling of Local Measured Heat and Mass Transfer Variations in a Microchannel Ammonia-Water Absorber," *Technical and Symposium Papers Presented At the 2003 Winter Meeting of The ASHRAE, Jan 26-29 2003*, Chicago, IL, United States, Amer. Soc. Heating, Ref. Air-Conditioning Eng. Inc., pp. 412-422.

Meacham, J. M. and S. Garimella (2004), "Ammonia-Water Absorption Heat and Mass Transfer in Microchannel Absorbers with Visual Confirmation," *ASHRAE Transactions* Vol. 110(1) pp. 525-532.

Mishima, K. and T. Hibiki (1996), "Some Characteristics of Air-Water Two-Phase Flow in Small Diameter Vertical Tubes," *International Journal of Multiphase Flow* Vol. 22(4) pp. 703-712.

Paul, B. K., P. Kwon and R. Subramanian (2006), "Understanding Limits on Fin Aspect Ratios in Counterflow Microchannel Arrays Produced by Diffusion Bonding," *Journal of Manufacturing Science and Engineering, Transactions of the ASME* Vol. 128(4) pp. 977-983.

Pfeifer, P., A. Wenka, K. Schubert, M. A. Liauw and G. Emig (2004), "Characterization of Flow Distribution in Microchannel Reactors," *AIChE Journal* Vol. 50(2) pp. 418-425.

Qu, W. and I. Mudawar (2003a), "Flow Boiling Heat Transfer in Two-Phase Micro-Channel Heat Sinks-I. Experimental Investigation and Assessment of Correlation Methods," *International Journal of Heat and Mass Transfer* Vol. 46(15) pp. 2755-2771.

Qu, W. and I. Mudawar (2003b), "Flow Boiling Heat Transfer in Two-Phase Micro-Channel Heat Sinks - II. Annular Two-Phase Flow Model," *International Journal of Heat and Mass Transfer* Vol. 46(15) pp. 2773-2784.

Qu, W. and I. Mudawar (2004), "Measurement and Correlation of Critical Heat Flux in Two-Phase Micro-Channel Heat Sinks," *International Journal of Heat and Mass Transfer* Vol. 47(10-11) pp. 2045-2059.

Rahman, M. M. (1996), "Analysis and Design of an Air-Cycle Microclimate Cooling Device," *Journal of Energy Resources Technology, Transactions of the ASME* Vol. 118(4) pp. 293-299.

Sadasivan, P. and J. H. Lienhard (1987), "Sensible Heat Correction in Laminar Film Boiling and Condensation," *Journal of Heat Transfer, Transactions ASME* Vol. 109(2) pp. 545-547.

Salim, M. (2004), "Thermally Activated Mobile Ejector Refrigeration System Analysis," *Proceedings of the Institution of Mechanical Engineers, Part D: Journal of Automobile Engineering* Vol. 218(9) pp. 1055-1061.

Schubert, K., J. Brandner, M. Fichtner, G. Linder, U. Schygulla and A. Wenka (2001), "Microstructure Devices for Applications in Thermal and Chemical Process Engineering," *Microscale Thermophysical Engineering* Vol. 5(1) pp. 17-39.

Serpente, C. P., M. Kernen, J. S. Seewald and H. Perez-Blanco (1994), "A 2 kW Lithium Bromide Absorption Machine with Heat Recovery and Recirculation for Novel Fluid Testing," *Proceedings of the International Absorption Heat Pump Conference*, New Orleans, LA, pp. 65-71.

Shah, M. M. (1979), "A General Correlation for Heat Transfer During Film Condensation Inside Pipes," *International Journal of Heat and Mass Transfer* Vol. 22(4) pp. 547-556.

Shannon, M. A., M. L. Philpott, N. R. Miller, C. W. Bullard, D. J. Beebe, A. M. Jacobi, P. S. Hrnjak, T. Saif, N. Aluru, H. Sehitoglu, A. Rockett and J. Economy (1999), "Integrated Mesoscopic Cooler Circuits (IMCCS)," *American Society of Mechanical Engineers, Advanced Energy Systems Division (Publication) AES* Vol. 39 pp. 75-82.

Shin, J. S. and M. H. Kim (2005), "An Experimental Study of Flow Condensation Heat Transfer Inside Circular and Rectangular Mini-Channels," *Heat Transfer Engineering* Vol. 26(3) pp. 36-44.

Sobhan, C. B. and S. V. Garimella (2001), "A Comparative Analysis of Studies on Heat Transfer and Fluid Flow in Microchannels," *Microscale Thermophysical Engineering* Vol. 5(4) pp. 293-311.

Tan, F. L. and C. P. Tso (2004), "Cooling of Mobile Electronic Devices Using Phase Change Materials," *Applied Thermal Engineering* Vol. 24(2-3) pp. 159-169.

Taylor, B. N. and C. E. Kuyatt (1994). *Guidelines for Evaluating and Expressing the Uncertainty of NIST Measurement Results*. National Institute of Standards and Technology Technical Note 1297.

Treffinger, P. (1996), "Development and Performance of a Single Stage, High Efficient Absorption Heat Pump for Domestic Heating," *Proceedings of the International Ab-Sorption Heat Pump Conference*, Montreal, Canada, pp. 579-585.

Wang, H., K. Drost and R. Peterson (2004a), "Thermodynamic Performance of a Miniature Expander/Compressor Heat-Actuated Heat Pump, Providence, RI, United States, American Institute of Aeronautics and Astronautics Inc., Reston, VA 20191, United States, pp. 1455-1461.

Wang, H. S. and J. W. Rose (2004), "Effect of Interphase Matter Transfer on Condensation on Low-Finned Tubes a Theoretical Investigation," *International Journal of Heat and Mass Transfer* Vol. 47(1) pp. 179-184.

Wang, H. S., J. W. Rose and H. Honda (2004b), "A Theoretical Model of Film Condensation in Square Section Horizontal Microchannels," *Chemical Engineering Research & Design* Vol. 82(A4) pp. 430-434.

Warrier, G. R., V. K. Dhir and L. A. Momoda (2002), "Heat Transfer and Pressure Drop in Narrow Rectangular Channels," *Experimental Thermal and Fluid Science* Vol. 26(1) pp. 53-64.

Yu, W., D. M. France, M. W. Wambsganss and J. R. Hull (2002), "Two-Phase Pressure Drop, Boiling Heat Transfer, and Critical Heat Flux of Water in a Small-Diameter

Horizontal Tube," *International Journal of Multiphase Flow* Vol. 28(6) pp. 927-941.

Ziegler, F. and G. Alefeld (1994), "Comparison of Multi-Effect Absorption Cycles," *Proceedings of the International Heat Pump Conference*, New Orleans, LA, ASME-AES, pp. 257-264.